

COURSE NOTES
for
WINTER SCHOOL
on
**PROBLEMS OF EHV TRANSMISSION
INCLUDING TRANSIENT PERFORMANCE**

(Dec. 3 - 15, 1984)

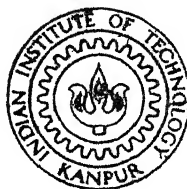
under
Quality Improvement Programme (QIP)

coordinators

(Dr. RAKOSH DAS BEGAMUDRE)

(Dr. RAVINDRA ARORA)

TH
EE EE/1984/D
1984 B 394 p
D
BEG
PRO



DEPARTMENT OF ELECTRICAL ENGINEERING
INDIAN INSTITUTE OF TECHNOLOGY KANPUR

91/

C O U R S E N O T E S

For
Winter School
on

PROBLEMS OF EHV TRANSMISSION INCLUDING TRANSIENTS

(Dec. 3-15, 1984)

Co-ordinators

Dr. Rakosh Das Begamudree Dr. Ravindra Arora

Department of Electrical Engineering
Indian Institute of Technology
Kanpur-208 016
(U.P.) India

EE-1584-BEG-PRO-D

200500

91536

FOREWORD

A state in power transmission has reached in India when the presently planned and installed 400 kV system will be inadequate to handle the needs after 1990. Powers ranging from 3000 MW to 20,000 MW must be transmitted from giant power pools (both hydro and thermal) to load centres 500 to 1500 Km away. The future needs in choice of extra high voltage (ac and dc) is the most difficult decision for Indian power engineers. Thus, the profession of power transmission is going through a very exciting period. With this in view, the Electrical Engineering Department of the I.I.T. Kanpur has organized this Short-Term In-Service Training Programme Course on Problems of EHV Transmission Including Transients. The subject matter is restricted to transmission only and not to interconnection of e.h.v. lines into a network. Thus it refers to the next higher level of voltage that will overlay the existing 220 kV and 400 kV network of lines. The problems that need appreciation and solution are related to high-voltage phenomena such as switching overvoltages, lightning overvoltages, radio noise, audible noise, electrostatic field, shunt and series compensation, protection using digital methods and fault-sensing by travelling waves, characteristics of long air-gap flashover, and many allied topics. Simulation of dc transmission systems for transient performance is also covered. With voltages on the increase, sub-stations are becoming very large and electromagnetic interference to measuring, protection and signal (communication) circuits using conventional co-axial cables is becoming a serious enough problem to replace them with optical fibre cables. Many measurement and control aspects are now being taken over by dedicated microprocessors. An effort has been made to include these two topics in the lecture series. Static Varr systems and high phase order have also been touched upon as future developments indicate that they might find use in India.

A volume such as this is the result of the combined efforts of many individuals. The coordinators wish to acknowledge with gratitude the help of Professors who spared their valuable time and effort to place notes at our disposal readily. The staff of the High Voltage Laboratory did all the chores required in putting this volume together. Without their efforts, we would have been seriously handicapped. We acknowledge our thanks to Sri Ghorupade and Sri Ram Autar. Sri Yogendra Chandra did all the typing, (sometimes very difficult equations). Any error in the final editing is solely the responsibility of the coordinators. The duplicating section of the EE Department and the Graphic Arts section of the I.I.T. deserve our thanks for their cooperation.

We thank the Principal Coordinator, QIP, IIT, and the higher authorities of the I.I.T., for their keen interest and continued encouragement. The Head of the EE Department, I.I.T. deserves our thanks for his part in making this course possible. We finally thank the QIP participants and from the power industry who have given us encouragement by their keen interest and presence.

Short-Term In-Service
Training Programme Course
on Problems of EHV
Transmission Including
Transient Performance.

December-3-15, 1984.

R.D. Begamudre
Ravindra Arora

Coordinators,
Electrical Engineering Department
Indian Institute of Technology
Kanpur-208 016 (UP), India.

CONTENTS

Pages Nos.	Topic
------------	-------

Dr. Ravindra Arora

RA-1-24	Calculation and Measurement of R.I. from High Voltage AC and DC Transmission Lines and Stations.
RA-25-37	Measurement of Radio Interference
RA-38-50	RI Measurements. Meter Response.

Dr. R.D. Begamudre

RDB-1-15	Overview of AC Transmission in India
RDB-16-27	Electrostatic Field and Audible Noise
RDB-28-40	Problems Arising from Overcurrents and Overvoltages
RDB-41-71	Line-Parameter Calculations with Ground.
RDB-72-90	Procedures for EHV Line Designs Part I : Based on Steady-State Operating Limits
RDB-91-106	Part II: Based upon Transient Overvoltages
RDB-107-121	Switching Surge Calculation on Lines
RDB-122-129	Insulation Characteristics of Long Air Gaps.

Dr. P.K. Chatterjee

PKC-1-79	Fiber Optics in Communications
PKC-20-41	Optical Fiber Transmission from Conception to Prominence in 20 years (by M. Schwarz)
PKC-42-48	Overview of Telecommunications Via Optical Fibers (Stewart E. Miller).
PKC-49-59	The Use of Fiber Optics for Communications, Measurement and Control within High Voltage Substations.



Page Nos.	Topic
-----------	-------

Dr. S. Gupta

SG-1-6 plus Figs. and Tables	High Voltage Transformers
------------------------------------	---------------------------

Dr. K.R. Padiyar

KRP-1-5	Modelling and Simulation of HVDC Links for Transients
KRP-6-12	Static VAR Systems.

Dr. Sachchidanand

1-23+Figs.	Digital Simulation of HVDC Systems
------------	------------------------------------

Dr.L.P. Singh

LPS-1-8 2 Papers.	Protective Relaying
----------------------	---------------------

Dr. Ravindra Arora

Page Nos.	Topic
RA-1-24	Calculation and Measurement of R.I. from High Voltage AC and DC Transmission Lines and Stations.
RA-25-37	Measurement of Radio Interference
RA-38-50	RI Measurements. Meter Response

CALCULATION AND MEASUREMENT OF RI FROM HIGH-VOLTAGE AC & DC TRANSMISSION LINES AND STATIONS

Notes on this topic are prepared from the Workshop papers presented by Dr. P. Sarma Maruvada of IREQ, Canada for 'Conference and Workshop on EHV Technology', August 1984, Bangalore.

INTRODUCTION

During normal operation, high-voltage transmission systems produce electromagnetic interference over a wide range of frequencies. This interference generally has its greatest impact on broadcast radio reception (0.535 MHz - 1.605 MHz) and is commonly designated as radio interference (RI). It may also have an appreciable impact on broadcast television reception (54 MHz-216 MHz), in which case it is referred to as television interference (TVI), but from a practical point of view it is RI which is the more important factor to be taken into account in the design of high-voltage transmission lines and stations.

Generation of RI

The main sources of RI on transmission lines and in stations are corona and gap-type discharges which occur on conductors, hardware and insulators. Such discharges occur externally, where air is the dielectric medium, but internal discharges can also be produced inside the dielectric materials used in station equipment such as transformers, circuit breakers, etc.

Corona discharges occur in regions of high electric field surrounding transmission line conductors, stations busbars and the associated hardware. They are due to acceleration of electrons in the high electric field and the resulting cumulative ionization and partial breakdown of air. The nature or 'mode' of corona discharge occurring near a conductor depends to a large extent on the shape of the conductor and the polarity of the voltage applied to it ('negative' or 'positive corona modes'). Irrespective of the conductor polarity, corona modes may be further classified on the basis of temporal variations in the discharge process as well as

in the currents induced in the conductor: glow coronas, in which the variations are very slow or even nonexistent, and pulsative coronas, in which the variations are very rapid. Only pulsative coronas (of either polarity) can give rise to RI.

Negative pulsative corona, generally known as Trichel pulse corona, is characterized by a double-exponential current waveform with a rise time of 5-10 ns, an amplitude of less than 10 nA and a total duration of 150-200 ns. Positive pulsative corona, or positive streamer corona, is also characterized by a double-exponential current waveform with a rise time of some 50 ns, a much larger amplitude of the order of 100 nA and a total duration of about 500 ns. These negative and positive pulsative coronas occur on conductors having the respective polarities of a DC transmission line or during the negative and positive half-cycles of voltage applied to the conductors of an AC transmission line.

Figure 1 shows positive and negative corona current pulse shapes reconstructed in the form of a sketch by Rakoshdas¹. Typical frequency spectra of positive and negative current pulses are shown in Figure 2. The frequency spectrum of the positive pulse has a higher initial amplitude than that of the negative pulse but falls off much faster with frequency. From the point of view of RI, therefore, positive corona pulses are much more important than negative. Thus, only the positive-polarity conductors of a bipolar DC transmission line are assumed to contribute to its RI level. Similarly, only the positive-half-cycle corona is assumed to contribute in the RI level of AC transmission lines. Similar considerations apply to corona-generated RI from AC and DC stations.

In contrast to corona, gap discharges occur between closely spaced conducting, and sometimes insulating, surfaces and represent a complete breakdown of the interelectrode space. The resulting current pulse is characterized by a steep rise time, large current amplitude and very short duration. Gap discharges therefore produce very high levels of RI as well as TVI but fortunately they occur only rarely on high-voltage transmission systems, usually being confined to AC distribution lines...

Corona and gap discharges, and to a lesser extent the internal the partial discharges of equipment, account for the RI from AC stations. In DC converter stations, however, the period turn-on and turn-off of the valves is a predominant source of RI because the switching times in both cases are very short, usually of the order of a few microseconds. During both these operations, transient voltages and currents appear in the system as a result of the redistribution of the energy stored in the reactive elements before a new steady state is reached, but turn-on generates much higher-frequency transients and is therefore the main source of RI from DC converter stations.

In the addition to the sources described above, which generate almost continuous or steady-state RI, the occasional operation of certain types of equipment in both AC and DC stations, such as circuit breakers or disconnecting switches, generates high levels of transient electromagnetic interference but this type of interference is outside the scope of the present discussion.

Calculation of RI

Although the RI levels of both transmission lines and stations are highly variable and can be meaningfully described only by long-term measurements and statistical analysis of data, calculation methods provide a useful physical insight and may reduce the amount of data needed. A brief review of RI calculation methods is therefore given below.

Transmission Lines: The principal source of RI from transmission lines is corona, which occurs randomly along the conductors wherever surface defects, organic or inorganic deposits, raindrops or snowflakes are located. Each corona source in turn injects random current pulses, characterized by fairly constant waveshapes but randomly varying amplitudes and pulse-separation intervals.

The current pulse injected by a corona source divides equally and propagates in both directions, suffering attenuation and distortion as it travels. Thus, at any given point on the

conductor, the resulting current will be composed of trains of random pulses generated at different distances on both sides and consequently undergoing different degrees of attenuation and distortion. In addition, the propagation of currents and voltage on one conductor is influenced by mutual coupling to the other phase conductors in the case of an AC line or to the other pole of DC line. Both conductor and ground impedance characteristics, which vary widely with frequency, must be taken into account in calculating attenuation and distortion effects, which makes RI propagation analysis on multiconductor transmission lines extremely complex.

The most important application of such calculation methods is to predetermine the RI characteristics of a proposed line design but unfortunately it is impossible to count solely on purely analytical methods for this purpose. Measurements are essential, which means that tests must be performed on conductors either in cages or on test lines to obtain the required data.

Empirical methods are also available for predicting the RI performance of a proposed transmission line. These are based on empirical formulae derived from large volume of measured data. Typical formulae for AC transmission lines are summarized by IEEE Committee Report. in 1973 /2/ Appendix I and II.

Stations : No analytical methods are currently available for calculating the RI from high-voltage AC stations although some computational methods exist for determining the RI generated by HVDC converter stations. Reference³ gives one such method which, while basically still valid, has recently been improved with respect to the means of determining the high-frequency equivalent circuits for the different components of the converter station. These improvements, along with the more efficient computer codes now available, promise the development of more accurate prediction methods in the near future.

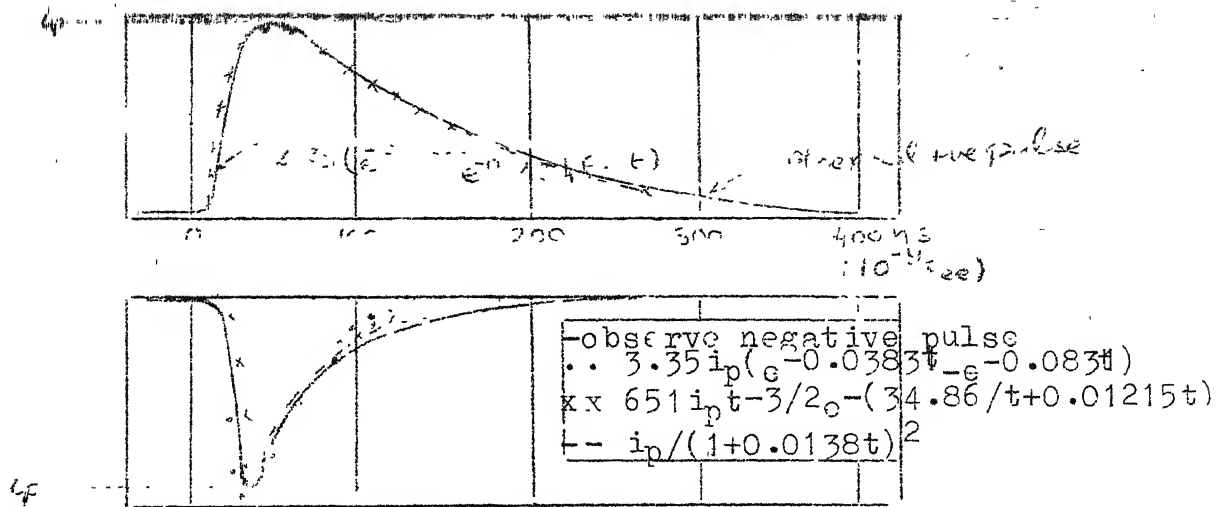


Fig.1. Positive and Negative Corona Current Pulse Shapes.

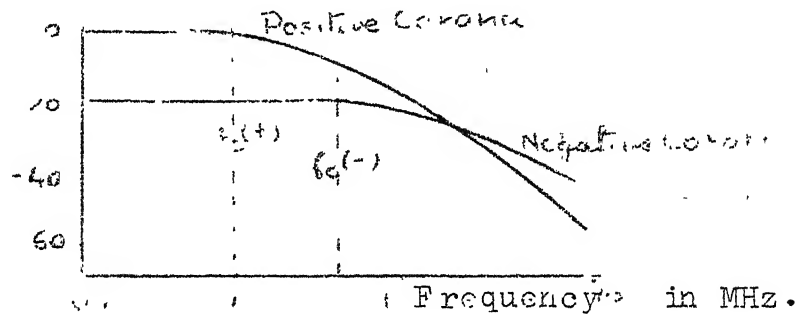


Fig.2 Frequency Spectrum of Positive and Negative Corona Pulses

RI PROPAGATION ANALYSIS

Introduction

Corona on transmission line conductors generates random current pulse trains, which propagate along the line undergoing attenuation and distortion. The objective of the propagation analysis is therefore to determine, from a knowledge of corona generation and the electrical characteristics of the line, the RI currents at any point along the line and subsequently, the RI field strength at points under the line. Some basic concepts involved in the propagation analysis are reviewed below:

A. Power density spectra of random signals. The RI performance of transmission lines is generally expressed as a function frequency. Consequently, the RI propagation analysis should also be carried out in the frequency domains. It is therefore necessary

to determine the most appropriate method of representing the generation, propagation and measurement aspects of RI in the frequency domain.

For periodic or transient signals, uniquely defined in the time domain, Fourier transform techniques are used in order to represent them in the frequency domain. However, since corona-generated RI is characterized by pulse trains, in which both the amplitudes and separation times of the pulses vary randomly, conventional Fourier transform techniques cannot be used. The most appropriate method of representing such signals in the frequency domain is in terms of power density spectrum, which is related to the mean square value of the signal rather than the instantaneous amplitudes. The concept and some properties of the power density spectrum are explained in the following.

Considering a random signal $f(t)$, the average power in the signal is given by

$$P = \lim_{T \rightarrow \infty} \frac{1}{T} \int_{-T/2}^{T/2} f^2(t) dt \quad (1)$$

It is seen that P as defined by (1) also corresponds to the mean square value of $f(t)$, i.e. $\sqrt{f^2(t)}$.

If now it is assumed that $f(t)$ is truncated outside $|t| > T/2$, the Fourier transform of the resulting signal $f_T(t)$ may be defined as $F_T(w)$. The energy E_T of the signal $f_T(t)$ is given by

$$E_T = \int_{-T/2}^{T/2} f_T^2(t) dt \quad (2)$$

By applying Parseval's theorem, we get

$$E_T = \int_{-\infty}^{\infty} f_T^2(t) dt = \frac{1}{2\pi} \int_{-\infty}^{\infty} |F_T(w)|^2 dw \quad (3)$$

But, by definition,

$$\int_{-\infty}^{\infty} f_T^2(t) dt = \int_{-T/2}^{T/2} f^2(t) dt \quad (4)$$

Using (3) and (4) in (1), the average power is given by

$$P = \lim_{T \rightarrow \infty} \frac{1}{T} \int_{-T/2}^{T/2} f^2(t) dt = \frac{1}{2\pi} \int_{-\infty}^{\infty} \lim_{T \rightarrow \infty} \frac{|E_T(w)|^2}{T} dw \quad (5)$$

In the above equation it is seen that as T increases, the energy of $f_T(t)$ and hence $E_T(t)$ and hence $|E_T(w)|^2$ also increase. In the limit as $T \rightarrow \infty$, the quantity $|E_T(w)|^2/T$ may approach a limit. Assuming that such a limit exists, we define $\phi(w)$, the power density spectrum of $f(t)$, as

$$\phi(w) = \lim_{T \rightarrow \infty} \frac{|E_T(w)|^2}{T} \quad (6)$$

The average power P is then given as

$$P = \lim_{T \rightarrow \infty} \frac{1}{T} \int_{-T/2}^{T/2} f^2(t) dt = \frac{1}{2\pi} \int_{-\infty}^{\infty} \phi(w) dw = \int_{-\infty}^{\infty} \phi(f) df \quad (7)$$

where $w = 2\pi f$. It may be noted that, since $|E_T(w)|^2 = E_T(w)E_T^*(w) = E_T(w)E_T^*(-w)$, $\phi(w)$ is an even function of w . Equation (7) may therefore be written as

$$P = \sqrt{f^2(t)} = \frac{1}{\pi} \int_{-\infty}^{\infty} \phi(w) dw = 2 \int_0^{\infty} \phi(f) df \quad (8)$$

It is seen from (6) that the power density spectrum retains only information of magnitude of the frequency spectrum $E_T(w)$ and

that the phase information is lost. It is also clear from (8) that the power spectral density $\phi(f)$ represents average power in the signal $f(t)$ at the frequency f .

Some properties of power density spectra which will be useful later on are summarized below:

- a) If a random signal $f_i(t)$, having a power density spectrum $\phi_i(w)$, is passed through a linear filter defined by a transfer function $H(w)$, the power density spectrum $\phi_o(w)$ of the resulting output signal is obtained as

$$\phi_o(w) = |H(w)|^2 \phi_i(w) \quad (9)$$

- b) If several random signals $f_{i1}(t)$, $f_{i2}(t)$ --- $f_{in}(t)$, having power density spectra $\phi_{i1}(w)$, $\phi_{i2}(w)$ --- $\phi_{in}(w)$ respectively, are passed through a linear filter defined by a transfer function $H(w)$, the power density spectrum $\phi_o(w)$ of the resulting output signal is obtained as

$$\phi_o(w) = \sum_{j=1}^n |H(w)|^2 \phi_{ij}(w) \quad (10)$$

- c) If a random signal $f_i(t)$, having a power density spectrum $\phi_i(w)$ is passed through an ideal bandpass filter tuned to a frequency f_o , having unit gain and a bandwidth Δf , the rms value U_{rms} of the resulting output signal is obtained as

$$U_{rms} = \sqrt{2\phi_i(f_o)} \Delta f \quad (11)$$

where $\phi_i(f_o)$ denotes the power spectral density of the input signal at the frequency of tuning f_o .

The property described in (c) above and the equation (11) give a method of measuring the power density spectrum of a signal using a radio noise meter which has the capability of measuring rms values.

B. RI excitation function: The generation of RI occurs over the entire length of conductors of a transmission line. The generation can be either uniform or nonuniform over the length of the line depending on whether the weather conditions are uniform over the length of the line or portions of the line are subject to different weather conditions. The concept of RI excitation function has been found to be very useful in the analysis of RI from transmission lines in cases of both uniform and nonuniform corona generation.

For the single conductor transmission line shown in Fig.3, consider the movement of a charge q generated by corona in the vicinity of the conductor. The current induced in the conductor due to the motion of the charge may be obtained by applying the Shockley-Ramo theorem* as

$$i = \rho \vec{E} \cdot \vec{v} \quad (12)$$

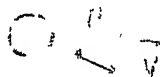


Fig.3.

where, E is the vector electric field, at the point where the charge is located, produced by the application of a unit potential to the conductor, and v is the velocity of the charge. The

*The Shockley-Ramo theorem states that, in a multielectrode system, the current induced in the k th electrode due to the motion of a charge q with a velocity v is given by $i_k = \vec{E}_k \cdot \vec{v}$, where \vec{E}_k is the electric field vector produced at the point where the charge is located by the application of unit potential on the k th electrode and zero potential on all the other electrodes.

electric field is almost radial near the conductor surface where corona occurs, and its magnitude is given by

$$E = \frac{C}{2\pi\epsilon_0} \cdot \frac{1}{r} \quad (13)$$

The current induced in the conductor is therefore obtained as

$$i = \frac{C}{2\pi\epsilon_0} \cdot \frac{1}{r} \cdot v_r \quad (14)$$

where v_r is the radial velocity component of the charge. Equation (14) can be rewritten as

$$i = \frac{C}{2\pi\epsilon_0} \cdot \left(\frac{E}{r} \cdot v_r \right) = \frac{C}{2\pi\epsilon_0} \cdot f \quad (15)$$

In equation (15), $f = \frac{E}{r} \cdot v_r$ is a function only of the space charge movement near the conductor. The current induced in the conductor may therefore be considered as depending essentially on two factors:

- 1) The capacitance of the conductor, which depends only on the conductor configuration, and
- 2) The density and movement of space charge near the conductor, which depends only on the electric field distribution in the conductor vicinity.

The term f in equation (15) is defined as the excitation function.

In the context of RI generation, i represents the random current pulse trains induced in the conductor or, more appropriately, the rms value of the current at a given frequency, which would be measured by a radio noise meter according to equation (11). Consequently, the excitation function is also expressed in terms of a rms value or indirectly in terms of the power spectral density.

The principal advantage of the concept of RI excitation function is that it is independent of the conductor or line geometry. Thus, it can be measured in a simple geometry such as a test cage, and used to predict the RI performance of a practical line configuration.

In the case of a multiconductor line, equation (15) may be generalized to

$$[i] = \frac{1}{2\pi\epsilon_0} [C] [V] \quad (16)$$

where $[i]$ is the vector of currents induced in the different conductors, $[C]$ is the capacitance matrix of the line, and $[V]$ is the vector of the generated RI excitation functions.

RI Propagation on a Single Conductor Transmission Line

Consider an infinitely long single conductor transmission line with uniform corona current injection of J per unit length. For an elemental length of the line, the equivalent circuit shown in Fig.4 applies. From considerations of the voltages and currents as shown in the figure, the following differential equations are obtained:

$$\frac{dV}{dx} = -zI \quad (17)$$

$$\frac{dI}{dx} = -yV + J \quad (18)$$

Since the corona current injected is in the form of random pulse trains, J and, consequently, also I and V are rms values at a given frequency. z and y are the series and the shunt admittance per unit length of the line. According to the basic transmission line theory that $Z_0 = \sqrt{z/y}$ = characteristics impedance of the line and $\gamma = \sqrt{zy} = \alpha + j\beta$ is the propagation constant of the line, α being the attenuation constant and β the phase constant. It may also be recalled that a sinusoidal current $i(f)$ at frequency f , injected at a particular point of the transmission line divides equally as shown in Fig.5

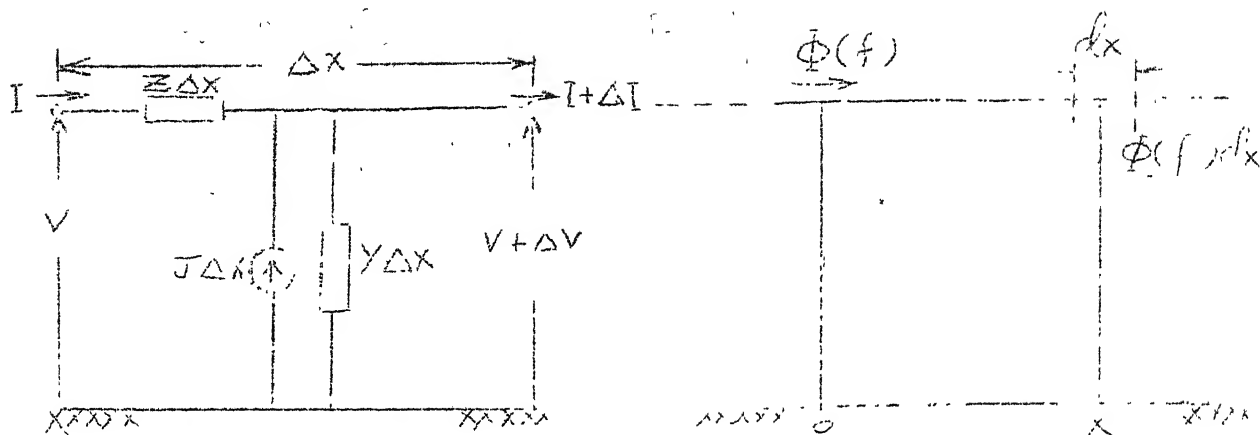


Fig. 4.

Fig. 6

and propagates in both directions. The current $i_x(f)$ at a distance x on either side of the point of injection will then be

$$i_x(f) = \frac{1}{2} i_0(f) e^{-\gamma x} \quad (19)$$

A transfer function $H(f)$ may therefore be defined as

$$H(f) = \frac{i_x(f)}{i_0(f)} = \frac{1}{2} e^{-\gamma x} \quad (20)$$

Returning to the random nature of the corona current injected, the uniform corona generation may be represented by the injection of a current having a power spectral density of $\phi_0(f)$ per unit length. Referring to Fig. 6 the injection of $\phi_0(f)dx$ at x produces at the point of observation 0 a current having a power spectral density

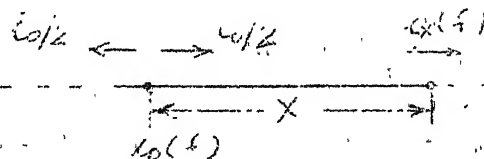


Fig. 5

$$\Delta\varphi(f) = |H(f)|^2 \varphi_c(f) dx = \frac{1}{4} e^{-2\alpha x} \varphi_c(f) dx \quad (21)$$

The power spectral density $\varphi(f)$ of the total current following at 0 is therefore obtained as

$$\varphi(f) = \frac{\varphi_c(f)}{4} \int_{-\infty}^{\infty} e^{-2\alpha x} dx = \frac{\varphi_c(f)}{2} \int_0^{\infty} e^{-\alpha x} dx = \frac{\varphi_c(f)}{4\alpha} \quad (22)$$

The result of equation (22) can be expressed in terms of the corresponding rms values of the currents I and J as (compare Eq. (11))

$$I = \frac{J}{2\sqrt{\alpha}} \quad (23)$$

Equation (23) is thus the required solution to the differential equations (17) and (18).

The last step in the RI analysis of the single conductor transmission line is to calculate the electric and magnetic field components at the ground level from the current obtained in (23),

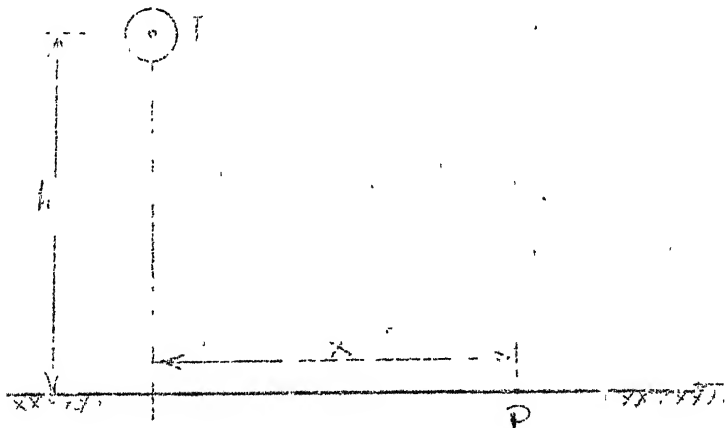


Fig.7

Referring to Fig.7, the magnetic field at any point P is obtained (assuming a perfectly conducting earth) as

$$H = \frac{I}{2\pi} \cdot \frac{2h}{h^2 + x^2} \quad (24)$$

Finally, assuming a TEM mode of wave propagation, the corresponding electric field is obtained as $E = Z_0 H$, where Z_0 is the wave impedance of free space. Since $Z_0 = 120 \pi$, we obtain

$$E = 60 I \cdot \frac{2h}{h^2 + x^2} \quad (25)$$

RI Propagation on a Multiconductor Transmission Line

In analogy to equation (17) and (18), the equations defining the RI propagation on a multiconductor line, including corona generation along the conductors, may be written as

$$\frac{d}{dx} [V] = - [z] [I] \quad (26)$$

$$\frac{d}{dx} [I] = - [y] [V] + [J] \quad (27)$$

where, $[V]$, $[I]$ and $[J]$ are column vectors of the voltage and current on the line and of the corona current densities injected on the conductors, $[z]$ and $[y]$ are square matrices of series impedance and shunt admittance per unit length of the line. The square impedance and admittance matrices comprise, of course, self as well as mutual terms. Thus, equations (26) and (27) represent a set of coupled differential equations which have to be solved simultaneously. Direct solution of these equations is therefore an extremely difficult task.

Modal analysis is used to simplify equations (26) and (27) into a number uncoupled sets of equations which can each be solved as in the case of a single conductor transmission line. In order to further simplify the analysis, the modal decomposition of the equations is carried out assuming a lossless line, and the effect of losses is introduced later for each of the modes in the form of modal attenuation factors.

Now, if $[G]$ represents the 'geometric matrix' of the line, with the matrix elements

$$g_{ii} = \ln \frac{2h_i}{r_i} ; \quad g_{ij} = \ln \frac{D_{ij}}{d_{ij}} \quad (28)$$

where, h_i is the height above ground of the i th conductor, r_i is the radius of the i th conductor, D_{ij} is the distance between the i th conductor and the image of the j th conductor in the ground plane and d_{ij} is the distance between the i th and j th conductors, the impedance and admittance matrices may be written as

$$[Z] = w [L] = \frac{w\mu_0}{2\pi} [G] \quad (29)$$

$$[Y] = w [C] = w \cdot 2\pi\epsilon_0 [G]^{-1} \quad (30)$$

where, $w = 2\pi f$, f being the frequency of voltages and currents, $[L]$ and $[C]$ are the inductance and capacitance matrices of the line.

Also, from (16),

$$[J] = \frac{1}{2\pi\epsilon_0} \cdot [C] [\Gamma] = [G]^{-1} [\Gamma]$$

Substituting (29) to (31) in equations (26) and (27),

$$\frac{d}{dx} [V] = - \frac{w\mu_0}{2\pi} [G] [I] \quad (32)$$

$$\frac{d}{dx} [I] = - w \cdot 2\pi\epsilon_0 [G]^{-1} (V) + [G]^{-1} [\Gamma] \quad (33)$$

Now, let $[M]$ be the modal transformation matrix of G , i.e.

$$[M]^{-1} [G] [M] = [\Lambda]_d \quad (34)$$

where $[\Lambda]_d$ is the diagonal spectral matrix of $[G]$. Also, let

$$[V] = [M] [V_c] \quad (35)$$

$$[I] = [M] [I_c] \quad (36)$$

$$[\Gamma] = [M] [\Gamma_c]$$

$$[J] = [M] [J_c] \quad (37)$$

V_c , I_c and J_c in the equations above are the modal components of the voltage and currents. Substituting (35) - (37) in (32) and (33),

$$\frac{d}{dx} [M] [V_c] = - \frac{w\mu_0}{2\pi} [G] [M] [I_c] \quad (38)$$

$$\frac{d}{dx} [M] [I_c] = - w \cdot 2\pi\epsilon_0 [G]^{-1} [M] [V_c] + [G]^{-1} [M] [\Gamma_c] \quad (39)$$

These equations can be rearranged as

$$\frac{d}{dx} [V_c] = - \frac{w\mu_0}{2\pi} [M]^{-1} [G] [M] [I_c] \quad (40)$$

$$\frac{d}{dx} [I_c] = - w \cdot 2\pi\epsilon_0 [M]^{-1} [G]^{-1} [M] [V_c] + [M]^{-1} [G]^{-1} [M] [\Gamma_c] \quad (41)$$

On further simplification,

$$\frac{d}{dx} [V_c] = - \frac{w\mu_0}{2\pi} [\lambda]_d [I_c] \quad (42)$$

$$\frac{d}{dx} [I_c] = -w \cdot 2\pi\epsilon_0 [\lambda]_d^{-1} [V_c] + [\lambda]_d^{-1} [\Gamma_c] \quad (43)$$

Since $[\lambda]_d$ and $[\lambda]_d^{-1}$ are both diagonal matrices, equations (42) and (43) represent sets of uncoupled differential equations. For an n-conductor system, there will be n sets of differential equations, corresponding to the n modal components, similar to equations (17) and (18). Therefore solutions similar to (23) are obtained for each of the modal components.

By comparing equations (42) and (43) with (17) and (18), the modal characteristics impedance matrix of the line may be obtained as

$$[Z_c] = \sqrt{\frac{w\mu_0}{2\pi} \cdot \frac{1}{2\pi w\epsilon_0}} [\lambda]_d = \frac{1}{2\pi} \sqrt{\frac{\mu_0}{\epsilon_0}} [\lambda]_d = 60 [\lambda]_d$$

Details of application of the modal analysis to actual RI calculations are illustrated by considering a practical example.

Example of RI Calculation

The method of RI calculation described above is illustrated by considering AEP's 765 kV line configuration. The conductor height is assumed to be equal to the average conductor height of 60' (18.288 m), and the influence of ground wires is neglected. The calculation procedure comprises the following steps:

Step 1: The first step is to calculate the maximum bundle gradient for all the three phases of the line. For following the phase number the gradients are:

$$E_1 = E_3 = 19.67 \text{ kV}_{\text{rms}}/\text{cm}$$

$$E_2 = 21.10 \text{ kV}_{\text{rms}}/\text{cm}$$

Step 2: This step involves the determination of the RI excitation functions $\Gamma_1, \Gamma_2, \Gamma_3$ of the three phases, from a knowledge of the maximum bundle gradients of step 1. This requires in turn a prior knowledge of Γ as a function of E for the bundle under consideration, which can be obtained either by testing the bundle in a test cage or on a test line or by using empirical formulas already developed⁴⁻⁶ on the basis of extensive tests. For conditions of heavy rain, reference 4 to 6 propose empirical formulas for determining the Γ for any given conductor bundle. Based on the results of these references, the following values are obtained for

$$\Gamma_1 = \Gamma_3 = 46.5 \text{ dB above } 1 \text{ } \mu\text{A}/\text{m}^{1/2}$$

$$\Gamma_2 = 48.7 \text{ dB above } 1 \text{ } \mu\text{A}/\text{m}^{1/2}$$

$$\text{or } \Gamma_1 = \Gamma_3 = 211.3 \text{ } \mu\text{A}/\text{m}^{1/2} \text{ and } \Gamma_2 = 272.3 \text{ } \mu\text{A}/\text{m}^{1/2}$$

Step 3: for the line configuration under consideration, the geometric matrix $[G]$ defined by equation (28) is obtained as

$$[G] = \begin{bmatrix} 5.15 & 1.05 & 0.51 \\ 1.05 & 5.15 & 1.05 \\ 0.51 & 1.05 & 5.15 \end{bmatrix}$$

Step 4 : This step involves solution of equation (34) to obtain the modal transformation matrix $[M]$ and the diagonal spectral matrix $[\lambda]_d$. Equation (34) may be written as

$$[C] [M] = [\lambda]_d [M]$$

or

$$\begin{bmatrix} g_{11}\lambda & g_{12} & g_{13} \\ g_{21} & g_{22}\lambda & g_{23} \\ g_{31} & g_{32} & g_{33}\lambda \end{bmatrix} \begin{bmatrix} M_{11} & M_{12} & M_{13} \\ M_{21} & M_{22} & M_{23} \\ M_{31} & M_{32} & M_{33} \end{bmatrix} = 0 \quad (44)$$

The above equation has a nontrivial solution only if the determinant of the first matrix is zero, i.e.

$$\begin{bmatrix} g_{11}\lambda & g_{12} & g_{13} \\ g_{21} & g_{22}\lambda & g_{23} \\ g_{31} & g_{32} & g_{33}\lambda \end{bmatrix} = 0 \quad (45)$$

Equation (45) reduces to a cubic equation in λ , the solution of which, using the matrix elements of $-G$ obtained in Step 3, gives the following values of λ :

$$\lambda_1 = 3.91, \lambda_2 = 4.64 \text{ and } \lambda_3 = 6.91$$

Substituting each of these values in (44) gives us the columns of the modal transformation matrix M . For $\lambda_1 = 3.91$, we get

$$\begin{bmatrix} 1.24 & 1.05 & 0.51 \\ 1.05 & 1.24 & 1.05 \\ 0.51 & 1.05 & 1.24 \end{bmatrix} \begin{bmatrix} M_{11} \\ M_{21} \\ M_{31} \end{bmatrix} = 0$$

or

$$\begin{aligned} 1.24 M_{11} + 1.05 M_{21} + 0.51 M_{31} &= 0 \\ 1.05 M_{11} + 1.24 M_{21} + 1.05 M_{31} &= 0 \\ 0.51 M_{11} + 1.05 M_{21} + 1.24 M_{31} &= 0 \end{aligned} \quad (46)$$

Equations (46) is a set of homogenous equations, and only two of the three unknowns can be determined independently. The third unknown has to be chosen arbitrarily. Choosing $M_{11} = 1.0$, the solution of (46) gives $M_{21} = -1.68$ and $M_{31} = 1.00$.

Thus

$$\begin{bmatrix} M_{11} \\ M_{21} \\ M_{31} \end{bmatrix} = \begin{bmatrix} 1.00 \\ -1.68 \\ 1.00 \end{bmatrix}$$

For purposes of normalization, the elements of the column vector above are divided by $\sqrt{M_{11}^2 + M_{21}^2 + M_{31}^2}$. The normalized vector is then given as

$$\begin{bmatrix} M_{11} \\ M_{21} \\ M_{31} \end{bmatrix} = \begin{bmatrix} 0.456 \\ -0.765 \\ 0.456 \end{bmatrix}$$

The other two columns of the $[M]$ matrix are obtained similarly by determining the normalized eigen vectors corresponding to

$\lambda_2 = 4.64$ and $\lambda_3 = 6.91$. The resulting normalized modal transformation matrix is obtained as

$$[M] = \begin{bmatrix} 0.456 & -0.707 & 0.541 \\ -0.765 & 0 & 0.644 \\ 0.456 & 0.707 & 0.541 \end{bmatrix}$$

Step 5: The next step in the calculations is determination of modal components of corona current injections. From equation (43), the equivalent corona current injection is given as

$$[J_o] = [\lambda]^{-1} [\Gamma_o] = [M]^{-1} [\Gamma]^{-1} \quad (47)$$

Since $[M] [\Gamma_o] = [\Gamma]$

Now,

$$[M]^{-1} = \begin{bmatrix} 0.456 & -0.765 & 0.456 \\ -0.707 & 0 & 0.707 \\ 0.541 & 0.644 & 0.541 \end{bmatrix}$$

and

$$[G]^{-1} = \begin{bmatrix} 0.203 & -0.039 & -0.012 \\ -0.039 & 0.210 & -0.039 \\ -0.012 & -0.039 & 0.203 \end{bmatrix}$$

Therefore

$$[M]^{-1}[G]^{-1} = \begin{bmatrix} 0.117 & -0.196 & 0.117 \\ -0.152 & 0 & 0.152 \\ 0.078 & 0.093 & 0.078 \end{bmatrix}$$

Now, if assume RI generation of Phase I,

$$[\Gamma] = \begin{bmatrix} \Gamma_1 \\ 0 \\ 0 \end{bmatrix} = \begin{bmatrix} 211.3 \\ 0 \\ 0 \end{bmatrix} \mu A/m^2$$

$[J_c]$ is then obtained as

$$[J_c] = [M]^{-1}[G]^{-1}[\Gamma] = \begin{bmatrix} 0.117 & -0.196 & 0.117 \\ -0.152 & 0 & 0.152 \\ 0.078 & 0.092 & 0.078 \end{bmatrix} \begin{bmatrix} 211.3 \\ 0 \\ 0 \end{bmatrix}$$

or

$$\begin{bmatrix} J_c^{(1)} \\ J_c^{(2)} \\ J_c^{(3)} \end{bmatrix} = \begin{bmatrix} 24.64 \\ -32.19 \\ 16.54 \end{bmatrix}$$

where the superscripts 1, 2 and 3 represent the mode numbers.

The corresponding modal components of the currents in the conductors are obtained by analogy with equation (23) as

$$\begin{bmatrix} I_c^{(1)} \\ I_c^{(2)} \\ I_c^{(3)} \end{bmatrix} = \begin{bmatrix} J_c^{(1)} / 2\sqrt{\alpha_1} \\ J_c^{(2)} / 2\sqrt{\alpha_2} \\ J_c^{(3)} / 2\sqrt{\alpha_3} \end{bmatrix} \quad (46)$$

where α_1 , α_2 and α_3 are modal attenuation constants⁷. Based on measurements on actual transmission lines, the modal attenuation constants may be assumed as

$$\alpha_1 = 0.173 \times 10^{-4} \text{ Nepers/m (0.15 dB/km)}$$

$$\alpha_2 = 0.115 \times 10^{-3} \text{ Nepers/m (1.0 dB/km)}$$

$$\alpha_3 = 0.691 \times 10^{-3} \text{ Nepers/m (6.0 dB/km)}$$

Substituting these in (48),

$$\begin{bmatrix} I_c^{(1)} \\ I_c^{(2)} \\ I_c^{(3)} \end{bmatrix} = \begin{bmatrix} 2964.6 \\ -1500.0 \\ 314.7 \end{bmatrix} \mu\text{A}$$

Finally, the corresponding phase currents are obtained using equations (36) as

$$\begin{bmatrix} I_1 \\ I_2 \\ I_3 \end{bmatrix} = \begin{bmatrix} M_{11} & M_{12} & M_{13} \\ M_{21} & M_{22} & M_{23} \\ M_{31} & M_{32} & M_{33} \end{bmatrix} \begin{bmatrix} I_c^{(1)} \\ I_c^{(2)} \\ I_c^{(3)} \end{bmatrix}$$

mode \rightarrow 1 2 3

conductor \downarrow

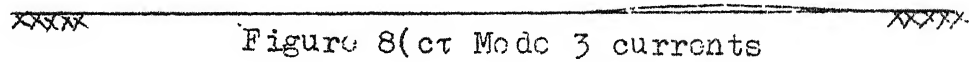
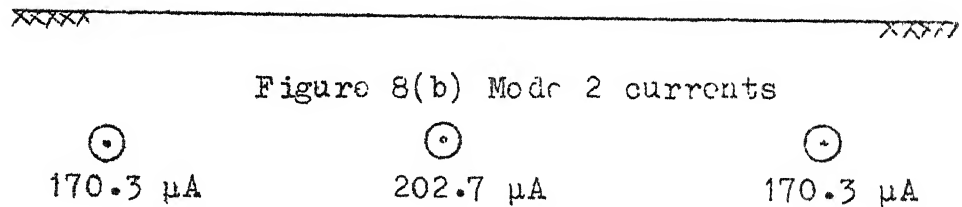
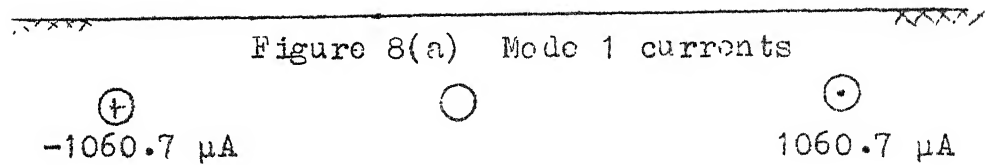
$$\begin{array}{c} 1 \\ 2 \\ 3 \end{array} \begin{bmatrix} 0.456 & -0.707 & 0.541 \\ -0.765 & 0 & 0.644 \\ 0.456 & 0.707 & 0.541 \end{bmatrix} \begin{bmatrix} 2964.6 \\ -1500.0 \\ 314.7 \end{bmatrix} \mu\text{A} \quad (49)$$

It is seen from (49) that each modal current flows in all the three conductors. Thus the modal current $I_c^{(2)}$ for example, results in currents $M_{12} I_c^{(2)}$ flowing in conductor 1, $M_{22} I_c^{(2)}$ in conductor 2 and $M_{32} I_c^{(2)}$ in conductor 3. The modal current distributions in the three conductors can be represented as shown in Figs. 6(a), 6(b) and 6(c).

⊙
1351.9 μA

⊕
-2267.9 μA

⊙
1351.9 μA



In the above, the current components in the three conductors of any given mode are in phase with each other. The current components corresponding to the different modes, however, will not be in phase because of differences in the velocities of propagation of the different modes. Although more sophisticated methods exist⁸ for addition of the different modes, a simple rms addition will be assumed in the following.

Step 6: The next step, after determining the modal RI currents in the different conductors, is to calculate the electric field component of RI under the line. Equation (25) is utilized for this purpose to determine the electric field at any point due to

each of the three modal current distributions. For any point on the ground, at a lateral distance X from the centre phase, the RI field due to the mode 1 current distribution is obtained as

$$E_1 = [F_1(X) \cdot I_1^{(1)} + F_2(X) I_2^{(1)} + F_3(X) I_3^{(1)}] \quad (50)$$

where $I_1^{(1)}$, $I_2^{(1)}$, $I_3^{(1)}$ are the mode 1 currents in conductors 1, 2, 3 respectively and $F_1(X)$, $F_2(X)$ and $F_3(X)$ are field factors given by

$$F_1(X) = \frac{120H}{H^2 + (X-D)^2} ; F_2(X) = \frac{120H}{H^2 + X^2} ; F_3(X) = \frac{120H}{H^2 + (X+D)^2} \quad (51)$$

where H is the conductor height and D is the phase spacing.

For $X = 95'$ (28.956 m)

$$F_1 = 3.87 ; F_2 = 1.87 ; F_3 = 1.02$$

and the modal field is obtained as

$$E_1 = 1351.9 \times 3.87 - 2267.9 \times 1.87 + 1351.9 \times 1.02 = 2368.3 \text{ } \mu\text{V/m}$$

Similarly, the field components at the same point due to the other two modes are obtained as

$$E_2 = 3027.5 \text{ } \mu\text{V/m}$$

$$E_3 = 1212.1 \text{ } \mu\text{V/m}$$

The resultant RI field at the point, due to RI generation on phase I, is obtained as

$$E_a = \sqrt{E_1^2 + E_2^2 + E_3^2} = 4030.4 \text{ } \mu\text{V/m}$$

Steps 5 and 6 will have to be repeated to determine the RI field produced at any given point due to RI generation on phases 2 and 3 respectively of $\Gamma_2 = 48.7 \text{ dB}$ and $\Gamma_3 = 46.5 \text{ dB}$. The resultant

fields at the point under consideration are :

$$E_b = 5437.2 \text{ } \mu\text{V/m}$$

$$E_c = 4030.4 \text{ } \mu\text{V/m}$$

The resultant RI field, due to the RI generation on all three phases, is again assumed to be the r.m.s. sum of the fields E_a , E_b and E_c

$$\text{i.e. } E = \sqrt{E_a^2 + E_b^2 + E_c^2} = 7877.3 \text{ } \mu\text{V/m}$$

$$= 77.9 \text{ dB above } 1 \text{ } \mu\text{V/m}$$

MEASUREMENT OF RADIO INTERFERENCE

The measurement of RI from high-voltage transmission systems is carried out using a radio noise meter, which is basically a calibrated radio receiver that functions as a tuned radio-frequency (RF) voltmeter. The meter comprises an input device which can be antenna or a probe feeding into a tuned RF amplifier. As in the case of a radio receiver, the output of the RF amplifier is mixed with the output of a variable-frequency local oscillator to obtain a fixed intermediate-frequency (IF) signal which is further amplified. The combination of RF and IF stages functions effectively as a calibrated tuned bandpass filter. The IF output is then passed through a detector and appropriate weighting circuits to measure the peak, quasipeak, average or rms values of the interference. A detailed analysis of the radio noise meter response to random pulses is discussed in Ref. 9.

The radio noise meter described above, standardized according to ANSI or CISPR, is used to measure the RI from transmission lines and stations. In making such measurements, particular attention must be paid to the selection of the location, the calibration of the measuring instrument, the background noise level and a number of other factors. A comprehensive guide to the measurement procedure has been published as an IEEE standard¹⁰, which is now undergoing revision to update and extend its range of applicability.

Single-Conductor Line

From the point of view of RI analysis, a single conductor line may represent a single phase AC or a monopolar DC line. In the cases of a single-conductor line, Fabre¹¹ established in a heuristic manner that the geometric mean of the envelopes of the maxima and minima of the RI frequency spectrum of a short open-ended line is identical with the RI frequency spectrum of a corresponding long-line. Holstrom¹² and Perz¹³ provided the necessary analytical proof of the geometric mean method of determining the long-line RI performance from measurements on short open-ended lines.

Considering the case of the open-ended test line at IREQ, which is 273 m long and has a natural resonance frequency $f_0 = 1.1 \text{ MHz}$ Fig 9 shows the frequency spectra of the magnetic field measured at ground level directly below the centre of the line, for a constant uniformly distributed RI excitation function of $\Gamma = 0 \text{ dB}$ above $1 \mu\text{A/m}$ at all frequencies and for different earth resistivities from ∞ to 10,000 ohm-m. The test line comprises a $6 \times 1.6''$ (4.064 cm) conductor bundle at an average conductor height of 12.2m. The earth resistivity is an important parameter since, during long-term testing, the earth resistivity may vary over several orders of magnitude depending on the nature of the soil, the temperature and humidity variations in the soil, etc. The results clearly show that the earth resistivity has a large influence on the amplitudes of the maxima and a much lesser influence on the amplitudes of the minima. The frequencies at which the maxima and minima occur are also reduced with increased earth resistivity, due to the resulting reduced velocity of propagation.

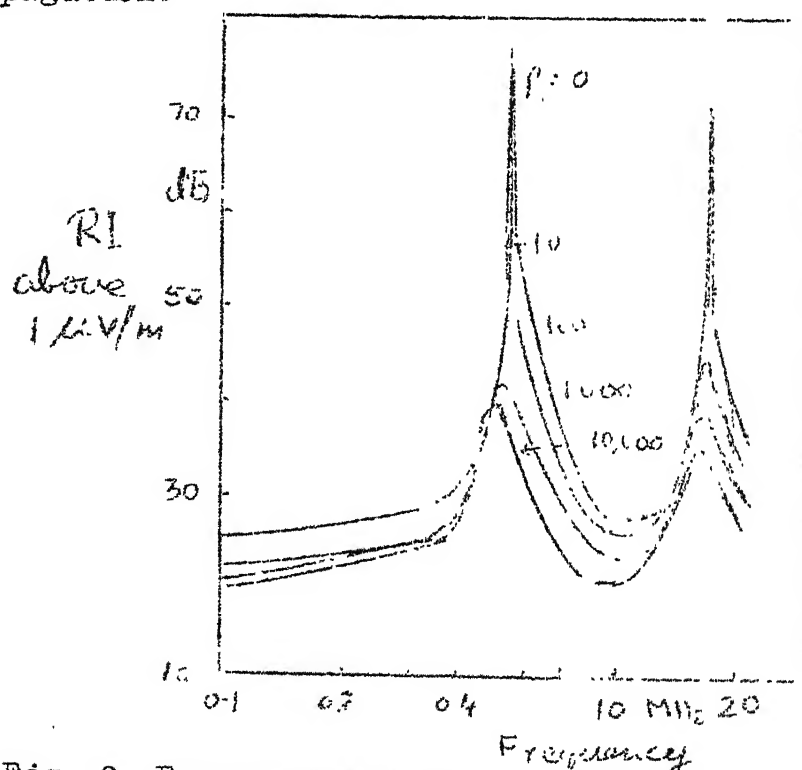


Fig. 9 Frequency spectrum of RI under an open-ended Single-conductor line.

The practical implication of the results of Fig. 9 is in the choice of a measuring frequency for purposes of long-term recording of RI. As pointed out by Lefevre¹⁴, the frequencies near the maxima are not suitable because of the extreme sensitivity of the measurements to slight frequency variations, and measurements near the minima may be affected by ambient noise. Frequencies in between the maxima and minima have therefore been suggested as ideal for long-term measurements. It is seen, however, that frequencies between $(2n-1)f_0/2$, $n=1, 2, \dots$, are also subject to considerable variations in earth resistivity. On the other hand, frequencies between nf_0 and $(2n+1)f_0/2$, $n=1, 2, \dots$ show much less variability due to variations in ρ and therefore appear much better suited for long-term measurements. More precisely, a value of about $(2n+0.6)f_0/2$ seems to be the best measuring frequency.

Another aspect which may affect the accuracy of the geometric-mean approach is the bandwidth of the measuring instrument, especially at low earth resistivities. The geometric-mean method is based on the theoretical maxima and minima of the frequency spectrum. However, the finite bandwidth of the measuring instrument reduces the measured peak compared to the theoretical maximum. For the line considered, for example, at $\rho = 0$ ohm-m, the measured peak with a 5 kHz bandwidth (ANSI) instrument will be about 16 dB lower than the theoretical maximum, resulting in an 8 dB error in the geometric mean. For $\rho = 10$ ohm-m, however, this error is reduced to about 0.3 dB, which is negligible. Thus, for normal values of earth resistivity, the error due to instrument bandwidth is negligible. All the frequency spectra reported in this paper are calculated assuming a measuring instrument having a bandwidth of 5 kHz.

Bipolar DC Line

An example of the two-conductor transmission line is the bipolar DC line, neglecting the influence of any ground wires present. In the case of a bipolar DC line, RI generated by corona on the positive pole predominates completely over that generated on the negative pole, so that for all Practical purposes RI generation on the negative pole can be neglected. Although RI generation occurs only on one conductor, the RI propagation on the bipolar DC line is composed of two distinct modes. In the following, the case of the short bipolar DC test line at IREQ, also 273 m long as in the case of the single-conductor line, is considered. The line comprises 6 x 1.6 conductor bundles on each pole, at a pole spacing of 15.2 m and an average conductor height of 15.4 m. RI measurements with the line either open-ended or terminated are discussed.

As in the case of the single-conductor line, RI measurements may be made on the bipolar DC test line with both ends open. It is not obvious, however, that the geometric mean method, which has been proved analytically for a single-conductor line, applies also to the case of a bipolar DC line. The RI propagation on the bipolar DC line is composed of the ground mode and line mode which propagate with different velocities and different attenuation constants. Although the open-circuited ends of the line produce reflections, they do not give rise to any intermode coupling. The analysis developed is therefore applicable to this case.

The frequency spectra of the RI magnetic field measured at ground level at the centre of the open-ended line, for $T_+ = 0$ dB and $T_- = -\infty$ dB and for three values of earth resistivity are shown in Fig. 10. The two peaks occurring in the region of the maxima correspond to the two modes of propagation. The sharp resonance peaks correspond to the line mode of propagation, and are affected by variations in earth resistivity, although to a

much lesser extent than the ground mode. The lower-amplitude second peaks correspond to the ground mode propagation. The amplitude as well as the frequency of occurrence of the ground mode peaks vary with the earth resistivity, reflecting corresponding changes in modal attenuation and velocity. The dashed lines in the figure correspond to the geometric mean between the maxima for the three values of ρ considered. The solid lines correspond to the actual long-line frequency spectra calculated for $\Gamma_+ = 0$ and $\Gamma_- = -\infty$ dB. The results show that the geometric mean of the maxima and minima does not give the corresponding long-line RI level. At low earth resistivities, the difference between the geometric mean and the long line RI levels is negligible. The error increases, however, with increasing earth resistivity.

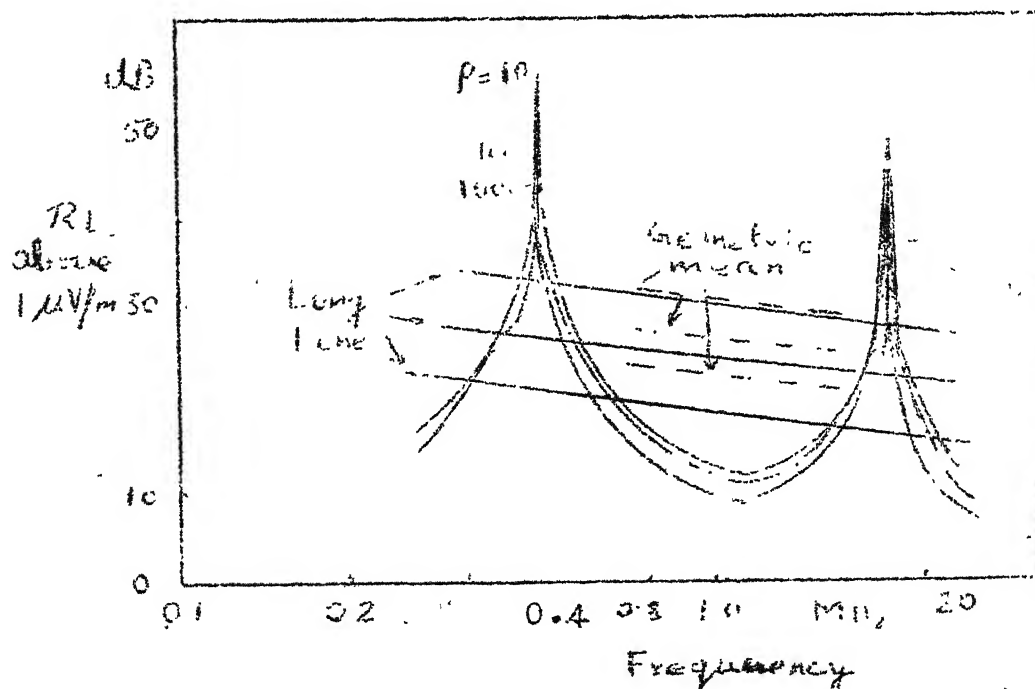


Fig. 10 RI frequency spectrum, at 15 m from positive pole, of an open-ended bipolar DC line.

Three phase AC Line

RI propagation on three phase AC transmission lines is characterized by three modes. The modes are conventionally numbered in the order of decreasing attenuation, with mode 1 having the higher attenuation and mode 3 the least attenuation. For a flat three phase line configuration, the mode 1 - known as the ground mode - corresponds to current flowing out in all the three conductors and returning via earth, mode 2 to current flowing out in one of the outer conductors and returning via the other, and mode 3 to current flowing out in the two outer conductors and returning via the central conductor.

Three phase AC lines are also characterized by RI generation, of about the same order of magnitude, on all the three phases. The corona activity on each phase conductor occurs during a short period around the peak of positive voltage on that conductor. Thus, RI on a three phase line is generated as a result of successive bursts of corona pulses separated from each other by a time interval corresponding to 120° of the applied alternating voltage. For purposes of propagation analysis, however, the RI generation on each conductor should be treated separately. The measuring instrument, on the other hand, integrates the contributions due to the excitation of each conductor. Depending on the type of instrument used, the contributions due to each conductor may be subject to rms addition (rms detector) or to CISPR addition² (QP detector). From a practical point of view, the difference between the two methods of addition is not significant. An rms addition is therefore assumed in the following.

Although only one conductor is excited at a time, currents flow in the other conductors also due to the existence of all the three modes. Thus, in the cases of both short and long lines, a modal analysis of RI propagation should be carried out for the excitation of each conductor, and their contributions added appropriately at the measuring point.

RI measurements on short three phase test lines are generally carried out with the line open-ended. Some attempts have also been made¹⁵ with the line terminated at one end and open at the other. The case of an open-ended line is discussed below. A 732 km long three phase test line, similar to that at Apple Grove is considered for purposes of illustrating the application of the proposed analysis. The line comprises 2 x 1.6" conductor bundles on all three phases, a phase spacing of 10.7 m and an average conductor height of 18.3m.

Figure 11 show the spectra of the RI electric and magnetic fields, at ground level at the centre of the line and at distance of 15 m and 30 m respectively from the outer phase, namely conductor 1.

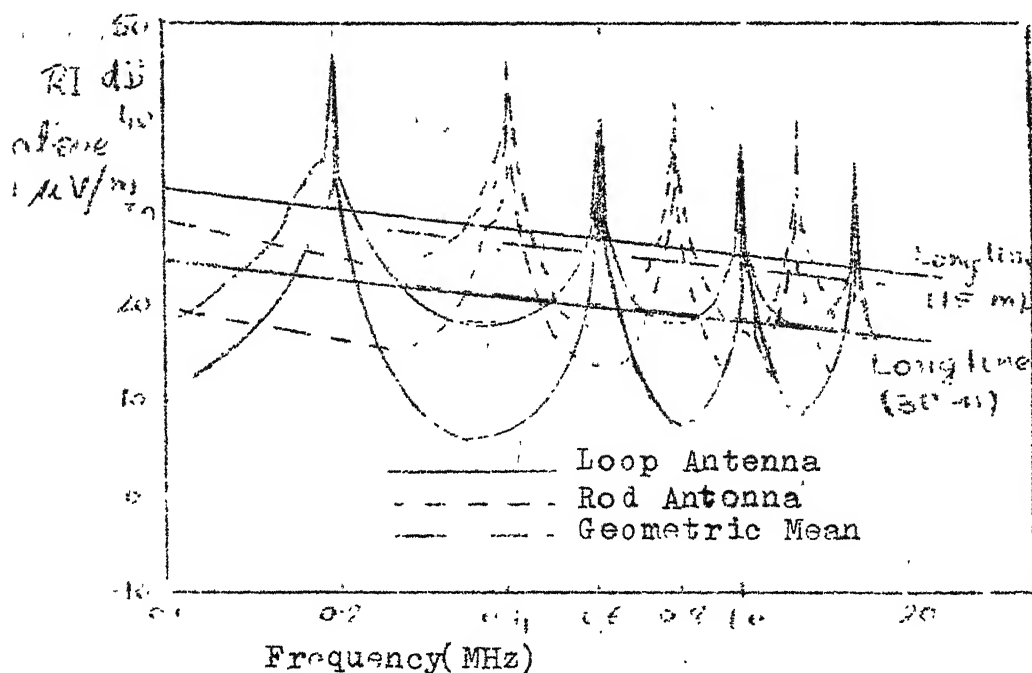


Fig. 11 Frequency spectra of RI electric and magnetic fields, at 15 m and 30 m from conductor 1, for an open-ended three phase test line. $\Gamma_1 = 0$ dB, $\Gamma_2 = \Gamma_3 = \infty$ dB.

REFERENCES

1. B. Rakoshadas, 'Pulses and Radio Influence Voltage of Direct Voltage Corona', IEEE Transactions on Power Apparatus and Systems, Vol. 83, May 1984, pp. 483-491.
2. IEEE Committee Report, 'CIGRE/IEEE Survey on Extra High Voltage Transmission Line Radio Noise', IEEE Transactions PAS, vol. PAS-92, May/June 1973, pp 1019-1028.
3. P.S. Maruvada, T. Gilsig, 'A Method of Calculating the RI from HVDC Converter Stations,' IEEE Transactions on Power Apparatus and Systems, vol. 92, May/June 1973, pp 1009-1018.
4. M.R. Moreau, G.H. Gary, 'Predetermination of the Radio Interference Level of High Voltage Transmission Lines, I- Predetermination of the Excitation Function', IEEE Trans. PAS-91, Jan/Feb. 1972, pp 284-291.
5. Transmission Line Reference Book 345 kV and Above. Published by EPRI.
6. N.G. Trinh, P.S. Maruvada, 'A Method of Predicting the Corona Performance of Conductor Bundles Based on Cage Test Results', IEEE Trans. PAS-96, Jan/Feb. 1977, pp. 312-325.
7. L.O. Barthold, J. Clado, 'The Propagation of High Frequencies on Overhead Lines,' CIGRE Report No. 420, 1964.
8. G.W. Jucette, G.M. Roe, 'Modal Components in Multiphase Transmission Line Radio Noise Analysis,' IEEE Trans. PAS-90, March/April 1971, pp. 801-813.
9. P.S. Maruvada, N. Hylten-Cavallius, N.T. Chinch, 'Radio Noise Meter Response to Random Pulses by Computer Simulation,' IEEE PAS vol. 93, May/June 1974, pp. 905-915.
10. IEEE Std. 430-197, 'Standard Procedures for the Measurement of Radio Noise from Overhead Power Lines,' 1976.
11. M.J. Fabre, 'Etude experimentals et theorique du mecanisme de propagation et de rayonnement de perturbations emises par les lignes a haute tension', Bulletin de la Societe Francaise des Electriciens, Ser. 7, No.31, July 1953, pp 419-423.

12. G.W. Helstrom, 'The spectrum of corona noise near power transmission lines', AIEE Transactions, Part III, Vol. 80, Dec. 1961, pp. 831-837.
13. M.C. Perz, 'Method of evaluating corona noise generation from measurements on short test lines', IEEE Transactions on Power Apparatus and Systems, Vol. PAS-82, Dec. 1963, pp. 833-844.
14. C. Lefevre, 'Etude du champ radioelectrique perturbateur d'une ligne experimentale courts', Rev. Gen. Elect., Vol. 75, No. 5, May 1966, pp. 682-694.
15. C. Gary, M. Moreau, L'Effet de Couronne en Tension Alternative, Eyrolles, Paris, 1976.

APPENDIX - I

RADIO NOISE PREDICTION FORMULAE FOR AC LINES

The basic characteristic equation for all comparative methods (ie: the methods which use empirical relation) can be expressed in the following form:

$$E = E_o + E_g + E_d + E_n + E_D + E_f + E_{fw}$$

E : calculated RN level of a line in dB above 1 μ V/m

E_o : well defined RN reference value followed by correction factors in dB for gradient, diameter, bundle, distance, frequency, and foul weather.

Symbols used in formulas

g_m = maximum gradient kV_{rms}/cm

g_a = average gradient kV_{rms}/cm

d = (Sub) conductor diameter, cm

n = no of subcond. in a bundle.

D = conductor to antenna, or radial distance, m.

h = line height, m

f = frequency, MHz

S = bundle separation, cm.

β = gradient factor ie:

$$\beta = 2(n-1) \sin(\pi/n) \text{ or}$$

$$\beta = 2.0 \text{ for } n=2$$

$$\beta = 3.48 \text{ for } n=3$$

$$\beta = 4.24 \text{ for } n=4$$

400kV-FG(Germany) at 1 MHz

$$E = 53.7 \pm 5 + K (g_m - 16.95) + 40 \log \frac{d}{3.93} + E_n + 20 K_D \log \frac{20}{L} +$$

$$K = 3 \text{ for } 750 \text{ kV class} \quad E_f + E_{fw}$$

$K = 3.5$ for other lines, gradient limit 15-19kV/cm

$E_n = 0.4$ dB for single conductor

$$E_n = 10 \log \frac{n}{4} \text{ for } n > 1$$

$K_D = 1.6 \pm 0.1$ for frequency range 0.5 to 1 MHz

$E_{FW} = \text{zero}$ for fair weather
 $= 17 \pm 3$ for rain.

$E_{line} = E_{max}$ if E_{max} is at least 3 dB higher than the field due to any other phase at that location. If the difference between the two highest values is less than 3 dB,

$$E_{line} = \frac{E_1 + E_2}{2} + 1.5$$

Shiobara (Japan)

In fair weather,

$$E = [(3.7 g_m - 12.2) \pm 3] + 40 \log \frac{d}{2.53} + 20 \log \frac{h}{D^2} - 12(\log f)^2 - 17 \log f.$$

To calculate the maximum RN level in heavy rain, the part of the above equation between bracket [.] must be replaced by one of the following expressions :

$$\begin{aligned} & [10.5 g_p - (g_p/2)^2 - 31] \text{ for } g_p \leq 17 \\ & [4.37 g_p - (g_p/4)^2 + 19.5] \text{ for } g_p > 17 \end{aligned}$$

where g_p is the bottom gradient of the bottom subconductor in kV/cm

$$g_p = \frac{g_m}{1 + \beta d / 2S} \left(1 + \frac{\beta d}{2S} \cos \alpha \right)$$

α = angle between the maximum gradient

$\alpha = 0$ for single and 3-bundle

$= 45^\circ$ for 4 bundle

$= 90^\circ$ for 2 Bundle

Ontario Hydro (Canada)

$$E = E_0 + A \log \frac{g_m}{18.8} + 40 \log \frac{d}{2.54} + B \log \frac{30.5}{D} + 20 \log \frac{c+1}{c+f^2}$$

$$\begin{aligned}
 A &= 146 \text{ for fair weather} \\
 &= 120 \text{ for foul weather} \\
 B &= 40 \text{ for horizontal lines} \\
 &= 32 \text{ for vertical lines} \\
 C &= 1 \text{ for } f \geq 1 \text{ MHz} \\
 &= 0.5 \text{ for } f < 1 \text{ MHz}
 \end{aligned}$$

The RN field intensity reference values at 30.5 m radial distance are :

$$\begin{aligned}
 E_0 &= 34 \text{ dB} \pm 6 \text{ (50\% value, fair weather) horizontal lines} \\
 &= 37 \text{ dB} \pm 6 \text{ (50\% value, fair weather) vertical lines} \\
 &= 63 \text{ dB (max. foul weather) horizontal lines.} \\
 &= 66 \text{ dB (max. foul weather) vertical lines}
 \end{aligned}$$

The ± 6 dB included is the standard deviation

ENEL (Italy)

$$E = 47 + 38(g_a - 15.0) + 40 \log \frac{d}{5.0} + 10 \log n + 30 \log \frac{20}{D} + E_f + E_q$$

$$E_f = \text{zero for } 1 \text{ MHz}$$

$$\text{and } = 20 \log \frac{1 + 0.5^2}{1 + f} \text{ for } 5 \leq f \leq 10 \text{ MHz}$$

$$E_q = \text{correction for elevation}$$

$$= \frac{q}{300} \quad \text{where } q = \text{elevation in metres.}$$

For bundled conductors, g_a is related to max. gradient as :

$$g_a = \frac{g_m}{1 + \beta d/2S}$$

EGU (czechoslovakia)

$$E = 11 + 4.5 g_m - 34 \log D + E_f$$

$$E_f = 0 \text{ for } f = 1 \text{ MHz.}$$

The formula is applicable for g_m between 12 & 20 kV/cm and for (Sub) conductor diameter between 1.92 and 3.31 cm. The distance correction is valid between 10 and 100 m.

For frequencies between 0.15 and 5.0 MHz,

$$E_f = -22 \log f - 15 \log^2 f.$$

Apple Grove : For frequencies between 0.2 and 16 MHz

$$E = 48 + 3.5 (g_m - 17.5) + 30 \log \frac{d}{3.51}$$

$$+ 20 \log \frac{30.7 h}{D^2} + 10 (1-f)$$

RADIO NOISE PREDICTION FORMULAE FOR AC LINES

METHOD	GRADIENT E_g	CONDUCTOR DIAMETER E_d	FREQUENCY E_f	DISTANCE E_D
Germany	$k_g (g_m - g_o)$	$4D \log \frac{d}{d_o}$	$20 \log \frac{1+f_o^2}{1+f^2}$	$20 K_D \log \frac{D_o}{D}$
	$E_n = 10 \log \frac{n}{n_o}$ for number of conductors			
Japan	$3.7 g_m - g_o$	$40 \log \frac{d}{d_o}$	$17(\log f_o - \log f) + 12(\log^2 f_o - \log^2 f)$	$20 \log \frac{h}{h_o} \frac{D_o^2}{D^2}$
Westing-house	$3.5(g_m - g_o)$	$30 \log \frac{d}{d_o}$	$10(f_o - f)$	$20 \log \frac{h}{h_o} \left(\frac{D_o}{D}\right)^2$
Ontario/Hydro	$A \log g_m / g_o$	$40 \log \frac{d}{d_o}$	$20 \log \frac{C+f_o^2}{C+f^2}$	$B \log \frac{D_o}{D}$
Czechoslovakia	$4.5(g_m - g_o)$		$20 \log f_o - \log f + 15(\log^2 f_o - \log^2 f)$	$34 \log \frac{D_o}{D}$
$K_g = 3$ for 750-kV class $K_g = 3.5$ for $g=15-19$ kV/cm (German) $K_D = 1.6$ for frequency range of 0.5 to 1.0 MHz $A = 146$ for fair weather $A = 120$ for four weather				
$B = 40$ for horizontal lines $B = 32$ for vertical lines $C = 1$ for ≥ 1 MHz $C = 0.5$ for < 1 MHz.				

APPENDIX II

RADIO NOISE PREDICTION FORMULAE FOR DC LINES

BPA $E = 51 + 1.5(g - 20.9) + 10 \log \frac{n}{2} + 40 \log \frac{d}{4.577} - 33 \log \frac{f}{0.834} - 40 \log \frac{D}{18.6}$

Reiner
Gehrig

BPA $E = 214 \log \frac{g}{14} - 278 [\log(\frac{g}{44})]^2 + 40 \log \frac{d}{2} - 27 \log \frac{f}{0.834} - 40 \log \frac{D}{30.5}$

Capon

BPA $E = 1.6 g + 40 \log \frac{d}{2} - 40 \log \frac{D}{30.5}$

Gehrig

BPA $E = E_0 + 80 \log \frac{g}{g_0} + 10 \log \frac{n}{n_0} + 40 \log \frac{d}{d_0} + 40 \log \frac{D}{D_0}$

Perry

Germany $E = E_0 + K(g - g_0) + 40 \log \frac{d}{d_0} + 20 \log \frac{1+f_0^2}{1+f^2} + 29.4 \log \frac{D}{D_0}$

IREQ $\Gamma = \Gamma_0 + 1.71 (g - g_0) + 40 \log \frac{d}{d_0} + 30.8 \log \frac{D}{D_0}$

SWEDEN $E = E_0 + 10 \log n + 20 \log r + 1.5 (g - g_0) - 40 \log \frac{D}{D_0}$

$K = 2.65 \text{ } g \leq 23 \text{ kV/cm}$

$= 2.0 \text{ } g \geq 23 \text{ kV/cm}$

INTRODUCTION

Measurements of radio interference from electrical power equipment and lines have been carried out since the early thirties¹. At present, for the range of amplitude modulated broadcasting frequencies, that is around 1 MHz, such measurements are usually carried out with either of two different instruments, the CISPR³ and the ANSI². Both are provided with a tuned band-pass filter at the input, the former for 9 kHz bandwidth, the latter with a (slightly variable) bandwidth around 5 kHz. The output of the filter in both instruments is fed into a detection network consisting of a half-wave rectifier, a weighting circuit, and an indicating meter measuring the arithmetic mean value of the output voltage from the weighting circuit, see Fig. 1.

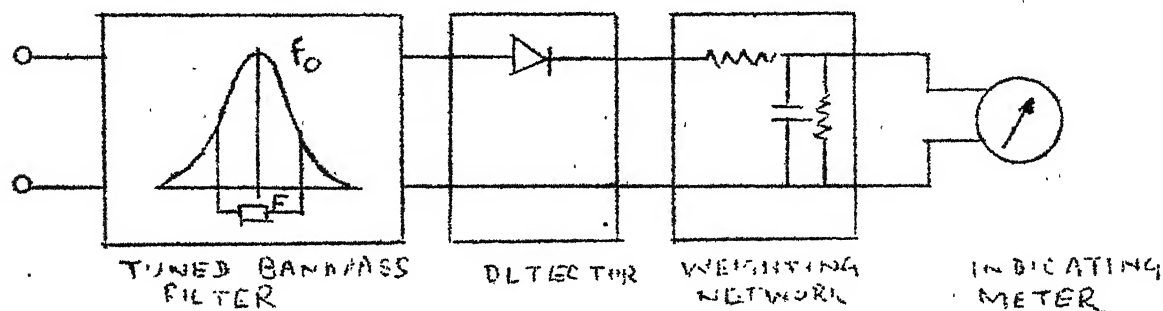


Fig. 1. Schematic diagram of a radio noise meter.

Usually, the instruments are used for 'quasi-peak' reading which means that the weighting circuit is adjusted for 1 ms charging time constant and 160 ms (CISPR) or 600 ms (ANSI) discharge time constant. The mechanical time constant of the indicating instrument is made sufficiently long to filter any rapid variations and give only the mean value. In addition to the quasi-peak, the ANSI instrument also has a peak and an average reading. The peak detector is a slideback voltmeter which measures the peak value of the modulated output of the filter. The average detector, also known as 'Field Intensity' detector, has an RC filter at the output of the detector, which is designed to pass only the very low frequency components (including dc) of the detector output and thus give the average value of the output.

The intention behind the weighting circuit of a quasi-peak detector is to give a reading proportional to the disturbing effect on human being (which is not caused by the program itself). It is an interesting question as to what extent this intention is fulfilled for the various types of radio interference encountered in practice; for example, the character of the noise from a dc converter station or a dc line is entirely different from that from ac equipment and lines, or from household appliances. However, this question has been dealt with elsewhere^{4,5}, and will not be discussed here.

Instead, another problem will be analyzed, namely the prediction of the radio interference from high voltage ac or dc systems by help of mathematical (or semi-mathematical) analysis of test data on equipment, or of data from test cages and test lines, and also from accumulated experience from existing lines of similar but not identical design.

Usually a quasi-peak reading is utilized for such studies, but it goes without saying that the readings from an instrument based on annoyance criteria may not necessarily be suitable for advanced mathematical analysis. Therefore work has been carried out^{6,7} in order to develop a better adapted instrument for this particular case, more specifically an instrument based on the rms value of the noise within the passband. These efforts have not been very successful, essentially due to inherent limitations in the overload characteristics of the instrument.

The authors Sarma and Cavallius have used another approach. A superficial study, based on energy considerations, showed that a conventional quasi-peak meter for pulses in the higher repetition rate, and especially for randomized pulses, might give a reading not too far from the rms value of the pulses. If this would be the case, then the error by using the quasi-peak

meter for line corona studies would be within tolerable limits. With this in mind the response of the two meters in question has been studied in this paper by computer simulation techniques and compared with that of an ideal rms meter.

It could, with some justification, be argued that the radio interference from high voltage power line is a very minor problem. The overwhelming amount of complaints concerning radio interference arises from household apparatus, industrial plants and medium voltage transmission system⁸, in the latter case especially from defective insulators. An instrument, which undoubtedly is reasonably useful for this bulk of instruments might well be used even for the specific case of measurements on high voltage systems.

However, this is not the point. A faulty conclusion at the planning stage, resulting in a too high interference level of an EHV or UHV line, may force reduction of the operating voltage which will have enormous economical consequences. This emphasizes the importance of a correct prediction of the levels. One, or actually the most important, element in such a prediction is the instrument itself, and if its characteristics do not lend themselves to mathematical analysis, excessive errors may occur.

Haber¹⁴ made an analysis of the quasi-peak response of the radio noise meter to periodic impulses with random amplitudes. The analysis is based on the probability density of the input voltage to the detector and weighting circuits. Considering the quasi-peak detector circuit shown in Fig.3, where R_c , R_d are the charge and discharge resistors, U is the positive envelope of the input voltage to the detector circuit, and U_{qp} is the quasi peak output voltage, the charging and discharge current i_c and i_d are given as

$$i_d = \frac{U_{qp}}{R_d} \quad (1)$$

$$i_c = \int_{U=U_{qp}}^{\infty} \frac{U - U_{qp}}{R_c} p(U) dU \quad \text{--- (2)}$$

where, $p(U)$ is the probability density of U .

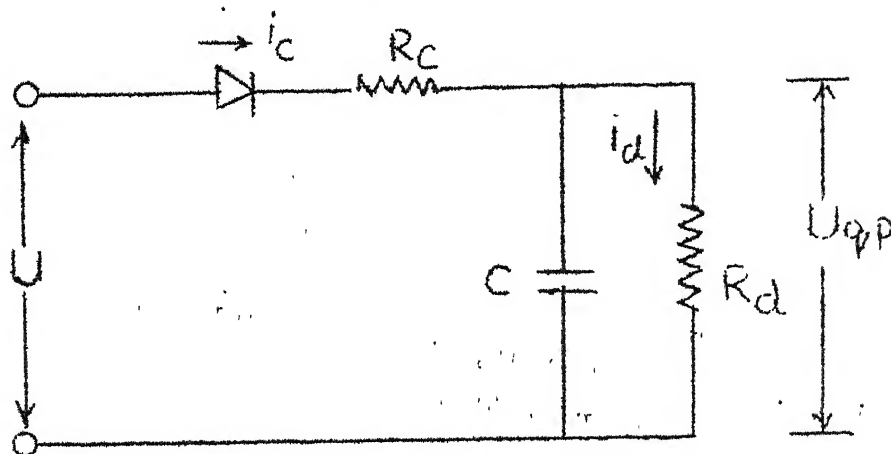


Fig. 2 Quasi-peak detector circuit

In the equation (2), i_c is the average charging current assuming that U_{pq} is very nearly constant. Since the average charging current should be equal to the discharge current, the quasi-peak value U_{qp} is obtained from (1) & (2) as

$$i_c = \frac{R_d}{R_c} \int_{U=U_{qp}}^{\infty} (U - U_{qp}) p(U) dU \quad \text{--- (3)}$$

The probability density function $p(U)$ has been obtained analytically by Haber for periodic pulses having rectangularly distributed amplitudes, and the integral equation (3) is solved to obtain U_{qp} .

The method of analysis described above can be extended to study the more general problem of pulses having amplitudes as well as the separation intervals varying randomly according to specified probability distribution functions. However, an analytical determination of the probability distribution function $p(U)$ for the general case is extremely complex. Consequently, a digital simulation technique is used in this paper to obtain $p(U)$ for any given distribution of the amplitudes and repetition times. The corresponding quasi-peak value is obtained by solving equation (3), and the average and rms values are obtained as

$$U_{ave} = \int_0^{\infty} U p(U) dU \quad (4)$$

$$U_{rms} = \left[\int_0^{\infty} U^2 p(U) dU \right]^{\frac{1}{2}} \quad (5)$$

Some results of the digital simulation study are verified by a hybrid computer simulation of the meter response.

COMPUTER SIMULATION OF RESPONSE

The ideal method of studying the response of a ratio noise meter is to generate voltage pulses similar in shape to corona pulses and having known random amplitude and pulse separation interval characteristics, and feed them directly into the meter. Since no such random pulse generator is presently available, the meter response can not be obtained directly from tests. However, the random pulses as well as the meter characteristics can be simulated either on a digital or on a hybrid computer.

Since the meter can be assumed to be linear up to the detector stage, a pulse input to the meter may be represented

in both simulation techniques by a detector input pulse corresponding to the positive envelope of the first peak of the waveform shown in Fig.2. A rectangular pulse input to the meter having an amplitude U_m and duration T is then represented by a detector input pulse having an amplitude $U_1 = 2U_m \Delta f$, a duration $\tau_1 = 2/\Delta f$ and a form defined by $U_1 a(t)$, where

$$a(t) = \frac{\sin \pi \Delta f t}{\pi \Delta f t}, \quad -\frac{1}{f} \leq t \leq \frac{1}{\Delta f} \quad (6)$$

A random pulse input to the meter is equivalent to a detector input of

$$U(t) = \sum_{i=1}^N h_i a(t - T_i) \quad (7)$$

Where h_i and T_i are the random amplitudes and pulse separation intervals respectively, and N is the number, assumed sufficiently large, of pulses used in the simulation. Equation (10) is not valid in the case when T_i is less than T_1 , since in such a case two or more pulses are superposed within the bandpass filter of the meter. A method of taking into account the superposition of pulses is discussed in the Appendix.

In both methods of simulation, the cases of ac and dc corona pulses are considered separately. A continuous sequence of random pulses represents the case of dc corona. Under ac conditions however, the corona pulses produced during the positive half cycle are the main source of interference. During the period T_p of each cycle, pulses occur only during a time interval T_{cor} centered around the positive peak of the alternating voltage. The duration of T_{cor} depends on the applied voltage, conductor surface conditions, etc.

Digital simulation

In digital simulation, a random detector input pulse train $U(t)$ having specified probability distribution for the amplitudes and the pulse separation intervals is generated, and the probability density distribution $p(U)$ is calculated by random sampling of the pulse train. The calculated distribution $p(U)$ is then used in equations (6), (7) and (8) to obtain the quasi-peak, average and the rms responses of the meter.

Fig.3 shows a typical random pulse train. The amplitudes h_i and the pulse separation intervals T_i are defined by probability functions $p(h)$ and $p(T)$ respectively. For example, experimental evidence shows^{11,12} that the pulse amplitudes have a Gaussian distribution while the pulse separation intervals have an exponential distribution.

Generation of random pulse amplitudes and separation intervals.

Sequences of random numbers corresponding to the pulse heights and separation intervals are generated on the computer using a standard subroutine for computing uniformly distributed random numbers between 0 and 1. Consider, for example, the probability density function $p(X)$ of a random variable X as shown in Fig. 4(a). The corresponding probability distribution function $P(X)$, which is defined as

$$P(x \leq X) = \int_{-\infty}^X p(x) dx \quad (8)$$

is shown in Fig.4(b). The function $P(X)$ varies between the limits 0 and 1. If $P(X)$ is now represented by a random number Y distributed uniformly between 0 and 1, the solution of the equation

$$Y = P(X) \quad (9)$$

gives¹⁵ the desired sequence of random numbers X having the given probability density function $p(X)$.

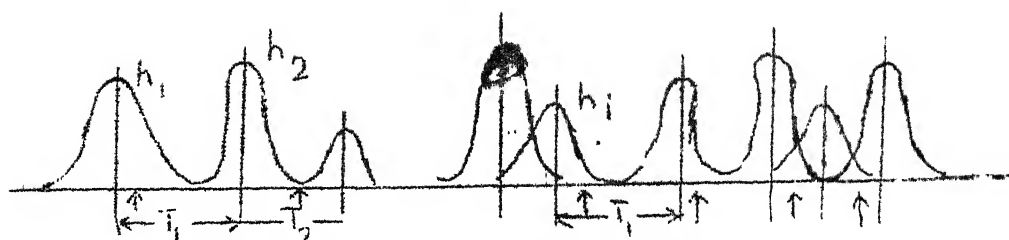


Fig.3. Random pulse train input to the detector.

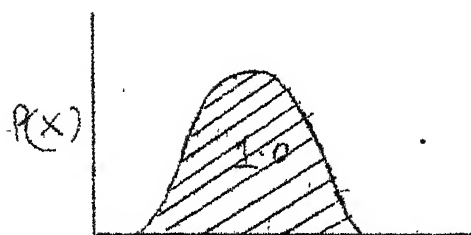


Fig.4(a) Probability density function.

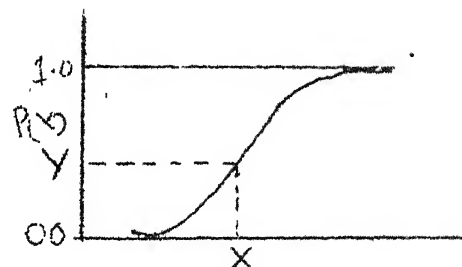


Fig.4(b) Probability distribution function.

Assuming, for instance, that the pulse amplitudes are normally distributed, the probability density function is given as

$$p(\bar{X}) = \frac{1}{\sigma\sqrt{2\pi}} e^{-\frac{(X-\mu)^2}{2\sigma^2}} \quad (10)$$

where μ is the mean pulse amplitude and σ is the standard deviation. The corresponding probability distribution function is given as

$$P(h) = \frac{1}{\sigma\sqrt{2\pi}} \int_{-\infty}^h e^{-\frac{(X-\mu)^2}{2\sigma^2}} dx \quad (11)$$

The sequence of normally distributed pulse amplitudes are then obtained by solving the following integral equation for h

$$Y = p(h) = \frac{1}{\sigma\sqrt{2\pi}} \int_{-\infty}^h e^{-\frac{(x-\mu)^2}{2\sigma^2}} dx \quad (12)$$

For a given values of Y , equations (12) can be solved numerically to obtain the corresponding value of h .

Since only positive pulse amplitudes are considered in this study, it is more appropriate to represent them by a truncated normal distribution function. The probability density function is assumed to be truncated on both sides of the mean at $(\mu-a)$ and $(\mu+a)$, where $(\mu-a) > 0$. The distribution is normalized by making the area under the resultant probability density function equal to 1.0. Equation (12) will then be modified as

$$Y = \frac{P(h) - P(\mu-a)}{P(\mu+a) - P(\mu-a)} = \frac{P(h) - P(\mu-a)}{1 - 2P(\mu-a)} \quad (13)$$

Equation (13) is again solved numerically to obtain h for a given value of Y .

The pulse separation intervals may be represented by the exponential probability density function

$$P(T) = \lambda e^{-\lambda T} \quad (14)$$

where $1/\lambda$ is the mean separation interval.

The sequence of random pulse separation intervals may be obtained using (9) as

$$Y = P(T) = 1 - e^{-\lambda T}$$

$$\text{or} \quad T = -\frac{1}{\lambda} \ln (1 - Y) \quad (15)$$

Equation (14) is then solved explicitly to obtain the random separation times as a function of the uniformly distributed random number Y .

Calculation of $p(U)$. After generating the random detected input pulse train, as shown in Fig.3, by the method described above, the corresponding amplitude probability density function $p(U)$ is calculated by random sampling in each pulse separation interval T_i . The sampling is done by generating again a uniformly distributed random number Y , and selecting the sampling time $t_g = Y \cdot T_i$. The corresponding amplitude of the pulse train is obtained by calculating $U(t_g)$ from equation (10), taking into account the superposition of pulses if necessary. The probability density function $p(U)$ is then obtained by considering a sufficiently large number of samples. Finally, the solution of equations (3), (4) and (5) gives the quasi-peak, average and the rms responses of the meter.

REFERENCES

1. C.R. Barhydt, 'Radio noise meter and its application', Elect. Rev., Vol. 36, pp. 201-205, April 1933.
2. American National Standard C 63.2 - 1963 (R1969), 'Specification for Radio-Noise and Field-Strength Meters, 0.015 to 30 Megacycles/second'.
3. C.I.S.P.R. Publication No. 1, 1961, 'Specifications for C.I.S.P.R. radio interference measuring apparatus for the frequency range 0.15 Mc/s to 30 Mc/s'.

4. C.M. Burill, 'An evaluation of radio noise meter performance in terms of listening experience', Proceedings, Institute of Radio Engineers, Vol. 30, No.10, October 1942, pp. 473-78.
5. O. Nigol, 'Analysis of radio noise from high voltage lines, 1-Meter response to corona pulses' IEEE Transactions on Power Apparatus and Systems, Vol. 83, No.5, May 1964, pp 521-33.
6. F.J. Trebby, 'Development of a Square-law radio noise meter -I'. AIEE Transactions, pt III, Vol. 78, Aug. 1959, pp. 522-28.
7. E.J. Trebby, 'Development of a square-law radio noise meter-II', AIEE Transactions, pt III, Vol. 78, Dec. 1959, pp. 1186-90.
8. C.I.S.P.R. Publication No. 9, 'C.I.S.P.R. limits of radio interference and report of national limits'.
9. C.H. Gary, 'The theory of excitation function: a demonstration of its physical meaning', IEEE Transactions on Power Apparatus and System, Vol. 91, Jan/Feb. 1972, pp. 305-10.
10. David B. Gaselowitz, 'Response of Ideal radio noise meter to continuous sine wave, recurrent pulses, and random noise' IRE Transactions on Radio Frequency Interference, May 1961, pp. 2-11.
11. A Reed, 'Corona pulse characteristics and their relationship to radio noise', Report No. ERB-711,
12. M.H. Khalifa, A.A. Kamal, A.C. Zeitoun, R.M. Radwan, and S. El-Bedwaih, 'Correlation of radio noise and quasi-peak measurements to corona pulse randomness', IEEE Transactions on Power Apparatus and Systems', Vol. 88, No.10, October 1969, pp 1512-1521.

13. Rakosh-Das Bogamudro, 'Radio noise levels in transmission lines and their relation to corona pulse characteristics', Transactions of the Engineering Institute of Canada, Vol.15, No. C-8, Oct. 1970, pp. 1-7.
14. F. Haber, 'Response of quasi-peak detector to periodic impulse with random amplitudes', Trans. IEEE, Vol. WEC-9, March 1967, pp. 1-6.
15. Marek Fisz, Probability theory and mathematical statistics, John Wiley, 1963, pp.145-47.

Dr. R.D. Begamudre

Pages Nos.	Topics
RDB-1-15	Overview of A.C. Transmission in India
RDB-16-27	Electrostatic Field and Audible Noise
RDB-28-40	Problems Arising from Overcurrents and Overvoltages
RDB-41-71	Line-Parameter Calculations with Ground
RDB-72-90	Procedures for EHV Line Designs
	Part I: Based on Steady-State Operating Limits
RDB-91-106	Part II: Based upon Transient Overvoltages
RDB-107-121	Switching Surge Calculation on Lines
RDB-122-129	Insulation Characteristics of Long Air Gaps.

91536

01238

OVERVIEW OF A.C. TRANSMISSION IN INDIA

ENERGY TECHNOLOGY FOR INDIA AND CHOICE OF NEXT HIGHER VOLTAGE FOR POWER TRANSMISSION

This lecture will cover the following topics :

- (a) Energy sources : Transportable and Locally usable:
- (b) Methods of development and their limitations in use :
- (c) Comparison between power situations of India and Canada:
- (d) Power handling capacities and salient features of lines from 400 kV to 1200 kV:
- (e) Examples of power pools in India: Hydro-electric and Thermal:
- (f) Transmission voltage selection for hydro sites:
- (g) Rate of power growth for thermal stations and voltage selection:

SECTION I : Introduction

A student or research worker concerned with power transmission in India must be aware of the energy position in this country. With the extremely rapid pace of development of industry on the lines of North America, Europe, and Japan, which cater mostly to the economic uplift of the urban population, which in turn brings the horrors of over-urbanization, one should not lose one's orientation on what the engineers' efforts are doing for the progress of this country. It is therefore imperative that we understand the nature and extent of our resources, the rate of depletion or conservation of the same, the energy requirement for any given region or the country as a whole, and the methods of planning.

It might be categorically mentioned at the outset that unless new sources of energy are developed rapidly in India, reliance on conventional thermal energy sources will bring the wheels of progress to a complete halt within a century, even if all the hydro potential is developed. By the year 2100, with the never-ceasing rate of increase of population, combined with the depletion of non-renewable natural resources, India will be in dire straits. It has been recognized, without questioning or an understanding of the basic principles laid down by Mahatma Gandhi, that some top people in the electrical power industry have taken it for granted that electrical power forms the basic necessity for the progress of this

country. I will keep away from this debate, but it merits serious thoughts whether the above assumption is true. Be that as it may, the development and use of electrical energy places a very great responsibility on today's planners and managers. This point must be emphasized in college and University curricula. Educational institutions must instruct as much on energy problems as on the control of power by computer methods.

The above is my personal opinion.

Electrical energy sources for industrial and domestic uses can be divided into two broad categories, comprising the following methods of generation:

1. Transportable : (i) Hydro electric, and (ii) Conventional thermal
2. Locally usable (with limited amount of transport):
 - (iii) Conventional thermal in urban load centres:
 - (iv) Nuclear thermal:
 - (v) Wind energy:
 - (vi) Solar Cells, or, photo-voltaic energy:
 - (vii) Solar thermal:
 - (viii) Geo-thermal:
 - (ix) Magneto-hydrodynamic or fluid-dynamic energy:
 - (x) Coal gasification and liquefaction:
 - (xi) Ocean energy: (a) Tidal (b) Wave (c) Thermal gradient
 - (xii) Biomass energy: (a) Forests (b) Vegetation (c) Cow dung.

Sources (iii), (iv), (v), and (viii) can be connected to an existing grid also.

SECTION II : Methods of Power Development and Their Limitations

- 1) Hydro-Electric Power : The known hydro potential in India is 50,000 MW (with 40 GW inside India and 10 GW in Nepal and Bhutan. 30% of potential or about 12 GW lies in the North-Eastern Region in the Brahmaputra Valleys in Arunachala Pradesh and Assam). These can be categorized as (a) High-head (26%) (b) Medium-head (47%) (c) Low-head, (< 30 metres) (7%) and (d) Run-of-the river, (20%). Presently (as of 1980), 18 GW are developed in high-and medium-head stations. Reservoir silting makes the life of a large dam between 50 and 100 years, so that re-location is necessary.

Terracing of fast-moving streams in the Himalayas can be carried out as is the case with Switzerland.

In India, low-head and run-of-the river plants have not been developed, although a lot of planning has taken place for the installation of micro-hydel power stations. This is a rich area for investigation for one who is interested.

2) Coal: The five broad categories of coal in India are : Peat (4500 BTU/Lb), Lignite (6500), Sub-bituminous (7000-12000), Bituminous (14000), and Anthracite (15500 BTU/Lb).

Only non-coking coal is used for power generation, which is estimated as 23 Giga Tonnes (which is 50% of the total deposit of this variety). The present installed capacity in Central India using the available coal in that region is 4000 MW, burning up 12 Million Tonnes annually. The present rate of annual increase in installed capacity is nearly 10%, but this will have to be slowed down to 5% annually. In the U.S.A., which is one of the coal-rich countries in the world, the annual rate of increase in installed capacity is 3.2% for coal-fired stations.

The estimated life of coal deposits in India at different rates of annual growth in installed capacity is as follows:

% Annual Increase	5	6	7	8	9	10
No. of Years for Doubling	15	12	10	9	8	7
Life of Coal Deposit, Years	140	120	108	97	88	80

3) Oil: At present, oil is used exclusively for transportation. Therefore, none is available for electric-power generation.

4) Natural Gas: This rich source of power is not known to exist in India to any great extent for even domestic-cooking use. There are a very limited deposits near oil fields which are used for running gas-turbine electric stations for local use.

5) Coal Liquefaction and Gasification: The efficiency of a conventional thermal station rarely exceeds 25 to 30%. But when the coal is liquefied, because the ash content is removed, it can generate as much power as 7 to 10 times its weight in coal in high-efficiency internal combustion engines. Indian coal contains about 45% ash, so that transport of this ash in coal is very uneconomical. This is further complicated by the large pilferage of coal at stations

where the coal-hauling trains stop and the fact that railway wagons are direly needed for food-transportation. Therefore, with liquefied coal and use of pipe lines, power-generation can take place at load centres with more reliability if pipe lines are maintained properly.

6) Nuclear Energy: Recent events have given this type of energy a lot of publicity which have exposed in some measure, the need as well as the limitations which India faces. France develops 44% of its total national power output in nuclear thermal stations, exporting some to the United Kingdom through the under-sea D.C. cable (about 2000 MW). Fast-Breeder-Reactors are now getting more widely used. In a Liquid-Metal-Fast Breeder Reactor (LMFBR), the fuel is mixed-oxide UO_2 and PuO_2 , which is conserved to some extent by converting U^{238} to U^{239} and then to Pu^{239} . Presently, the breeder ratio is 40%. All reactors use liquid Sodium for heat exchange and no moderator is used as in conventional thermal reactors.

In India, there exist very limited Uranium deposits in Bihar, but the world's major deposit of Thorium lies in Kerala. Research in using this element in nuclear reactors is non-existent in the world on which India borrows heavily for its technological development and utilization. Therefore, India must develop its own research and development plans if its nuclear-energy for the future is to be guaranteed.

7) Wind Energy : It is estimated that 20% of India's power requirements can be met with wind energy development. The Deccan Plateau has winds most favourable for large-scale power production with average wind velocities of 30 Km/hr blowing constantly.

Wind mills or turbines can be of the horizontal-or the vertical-axis types (Darrieus), with further facility for varying the pitch of the vanes to suit wind velocity. These can develop upto 1 MW at any one installation. A power output of 10 MW will require blades of 200 metres in dia and winds of 50 Km/hr. In rural areas, a power of 1 KW to 10 KW requires 1 acre of land.

Wind power is intermittent in nature so that storage facility is necessary. These take the form of storage batteries or compressed air.

Latest improvements are: (a) use of augmenters which create a vacuum on the downstream side of the blades, thereby increasing the power output by a factor which could theoretically reach 100 but at present is about 4; (b) Use of a Venturi duct to enhance the wind velocity by a factor of 3 at the turbine located in the neck, as designed in Portugal; (c) mounting the Venturi duct arrangement on railway tracks to orient the machines along the changing wind directions; (d) the MADRAS system, which uses 7.5 metre dia 30 metre tall cylinders wheeled on a track by the wind to whose axles are attached the generators; and finally, (e) the Tornado System using a wind tower 600m tall and 200m dia using cheap fuel to heat air on the downstream side of the turbine to create the partial vacuum.

For an electrical engineer, the challenge is in devising sophisticated control system in order to generate a constant-frequency constant-voltage from the variable-speed generator, and device circuitry for synchronizing the generators to an existing grid system. This has been accomplished by the Bonneville Power Administration in the U.S.A.

8) Solar-Cell Energy : Primarily, solar cells were used for space-satellites. But, recently, they are finding use for domestic power supply and in industry. As of now, 1 KW can be generated with 5 sq.m. of panel at an insolation level of 400 cal/sq. cm./day. Average Indian insolation level is 600 cal/sq.cm./day. By the year 1986, the U.S. hopes to develop cells which will cost \$1000/KW of peak power. This is the same as the installation cost of a nuclear reactor, but the advantages are obvious. In India, plans for research, development, and manufacture of Silicon solar cells are already taken up by the B.H.E.L. and other plants, since this can be combined with thyristor manufacturer.

9) Magneto-Hydro-Dynamic Power : The largest MHD generator that has successfully completed tests is the AVCO 500 KW unit. Current-collection at temperatures beyond 2000°C has been overcome. Superconducting magnets utilizing liquid-Helium at 4°K give a designed field of 8 Teslas, but the usual field strength used is between 2 to 3 T. Hot liquid-sodium from LMFBR's have also been utilized as

the conductor at about 550°C in order to develop more power from an auxiliary M-F-D generator near the reactor.

10) Fuel-Cell Energy: The first fuel-Cell concept utilized H-O interchange in order to yield a flow of electrons, while at the same time provide drinking-water to astronauts in space programmes, Electric automobiles were developed using the same concept.

The most recent version developed by the Consolidated Edison Co. of New York uses a module operating at 190°C . Each cell develops 0.7V at a current density of 0.25 A/sq.cm. The total voltage output of the installation is 13.8 kV, equal to that of a standard power-station generator. The power output is expected to reach 1 MW.

14) Ocean Energy: Energy from the sea can be developed in 3 different ways. (i) Tidal (ii) Wave (iii) Thermal Gradient.

Tidal Power : The highest tides in the world occur at 40 to 50° latitudes, so that Indian tides are limited. Tides upto 3.5 m exist on the Gujarat Coast, at Bombay, and at Hoogly. The U.K. tidal development is very extensive, and they hope to develop 8000 MW or 10% of the national power requirement by the year 2000. France has successfully put into operation a 2400-MW station at the Rance-River estuary using bulb turbines.

Like wind power, tidal power is intermittent and requires storage systems. Sea water is stored in a reservoir at high-tide periods which will flow through turbines in the conventional way at low-tide periods. In Canada, a unique system exists at the Bay of Fundy on the Atlantic Coast where the power developed at two tidal-power stations is used for running giant pumps for a pumped-storage plant nearby on the St. John River.

Wave Energy: Depending upon wave height, an average power of 25 to 75 KW can be developed per metre of wave length. However, the highest power attained to date is 5 Kw/m of wave. The scheme uses sealed chambers, closed at the top and open to the wave at the bottom. When the crest of the wave passes through such a chamber, it compresses the air in one chamber which flows into another under which the trough of the wave is passing. This compressed air flows

through an air-turbine driving a generator.

The most talked-of scheme is in Japan, where a 200-metre long 30-m wide floating buoy (anchored to the sea bed) has chambers 25 sq.m. in area. With a wave height of 4 m it will generate 30 MW. Each generator is rated 125 KW, 3-ph, 200V, 950 RPM. 6 poles, and 47.5 Hz. The power will be used for extracting Uranium from the sea water which will be utilized in Nuclear reactors yielding ultimately 10 times the power from the wave-power station. Desalination to obtain drinking water is also considered.

Ocean Thermal Power: This scheme utilizes the natural temperature difference existing between the warm surface water (25°C) and the cooler ocean-bed water (5°C). A heat exchanger uses the warm water to convert liquid NH_3 into vapour, which then drives a turbine-generator unit. The cool ocean-bed water is then used in a condenser as in a thermal station, and the fluid is pumped back to the heat exchanger for vaporization of NH_3 . The ocean-bed water is brought up to the surface installation through a pipe 20-m in dia over a height of 500m or more. With giant off-shore structures having been developed for oil-wells, erecting power-generation installations poses no special problems.

SELECTION OF HIGHER TRANSMISSION VOLTAGES FOR INDIA

Section 3 : Comparison of Power Situations in India and Canada

The present highest voltage for transmission in India is 400kV, 3-phase A.C. Nearly all State Electricity Boards have either adopted this level or will be adopting. It is a matter of only 8 or 10 years more when a higher voltage for transmission will be necessary. The C.B.I.P. has already focussed attention of concerned engineers on the need to have planning done on what the next higher voltage should be, whether A.C. or D.C. or a combination of both. Thus, Indian power engineers are now going through an exciting period of planning, and I strongly urge every one to investigate this problem, from theoretical as well as practical point of view. It is always an easy matter to be wise after the event, but no other single problem has such a socioeconomic as well as human bearing as the interconnection of the entire Indian power pool into a National Grid.

At the 1980 Symposium of the C.B.I.P. held at Delhi, several ideas crystallized on this matter. Briefly, the consensus at that Symposium was that it is best to introduce, between 1990 and 2000, (i) 765 kV (800 kV class) as the next higher transmission voltage; (ii) \pm 500 kV D.C. for certain point-to-point transmission; or, (iii) a combination of both.

UHV of 1000-kV class or more might be required beyond the turn of the century.

In considering such an important topic, it is worthwhile drawing a parallel of Indian power situation with that of another country having somewhat similar problems. To me, Canadian power development comes very close to the Indian situation. Briefly, Canada has a population of 2.5 crores and the present installed capacity is 77,000 MW with the following distribution: Conventional thermal 27000MW, Nuclear thermal 6000 MW, and Hydro-electric power of 44000 MW. As compared to this, India has a population of 67.5 crores, installed capacity of 30,000 MW with 40% in conventional thermal and 18000 MW in hydro. The projected rates of growth of installed capacity for the next 20 years are: Canada 2750 MW/year and India 4800 MW/year. The power-doubling will take place in 28 and 7 years, respectively, in the two countries. By the year 2003, the total powers will be equal for both countries at 140000MW.

The situation in the province of Quebec in Canada comes closest to Indian power situation in so far as hydro-electric power is concerned with equal amount of power and distance of transmission as in India. The power from the James Bay area on the La Grande River will be developed as follows:

Station	Delany	Manic-5	LG-1	LG-2	LG-3	LG-4
Power, MW	2550	1000	1140	5300	2300	2600
Cost, M\$	500	750	Total for La Grande : 12,000			

The distance of transmission from any of the La Grande stations to load centres at Montreal and Quebec City will be 675 miles or 1100 Km. The Hydro-Quebec has extensive experience obtained from their 735 kV transmission system over the past 15 years. With such a vast experience, the company investigated using 1200 kV for

the James Bay development, but dropped it in favour of the 735 kV level. These powers and distances are very close to what they are in India for hydro-electric development in the Himalayan and Assam regions, and the Singrauli-Raniganj area to load centres at Kanpur-Delhi-Lucknow, Bombay, and Calcutta.

It is well worth noting that the Hydro-Quebec has not considered the D.C. alternative, in spite of Canadian experience in \pm 400 kV D.C. operating successfully in the Nelson River project in the Province of Manitoba. Also, countries such as the USA, USSR, and Italy who have planned 1000-kV or more, and Sweden, France and the U.K. who have planned 800 kV class lines and for higher voltages have not considered the adoption of D.C. transmission. This is not to imply that D.C. should not be studied for possible adoption in India, but very serious thoughts must be given... Needless to say, Rural Electrification has assumed paramount importance and DC transmission, as it exists today, is most economical for point-to-point transmission of bulk power so that tapping for rural distribution is not possible. Therefore if there are several tapping points and rural lines, the cost of rural electrification must be added to the cost of transmission. As of now, in India, generation cost is Rs. 2500 per KW, transmission Rs. 500 and rural electrification Rs. 2000 per KW, which represents 40% of the total cost. If this is added to D.C. transmission cost, the break-even powers, distances, etc will be different from what they are in North American and European or even South American continents. But D.C. transmission, control of stability by parallel A.C. and D.C. lines, back-to-back asynchronous ties, multi-terminal systems, and so on offer one of the richest fields of study and investigation in India, where such studies are either in the beginning stages or non-existent.

Section 4: Power Handling Capacities and Salient Features of Transmission Lines for 400 kV to 1200 kV

The following voltages have been or being adopted in the world at 400 kV and above, with voltage value expressed between conductors:

3-phase A.C.	: 400,	500,	750,	1000,	1200,	1500 kV
Bipolar D.C.	: 800,	900,	1000,	1200 kV		

The power-handling capacities of these lines (for no series compensation) are normally based on the following assumptions:

- i) A.C. Lines: Equal magnitudes of voltages for sending and receiving ends with a phase displacement of 30° which usually arises from stability considerations.
- ii) D.C. Lines: A current of 1800 Amps is taken to flow in each conductor, which is limited by present state of device technology.

For A.C. lines, based on the above assumption, the allowable power, current, and percentage power loss as a function of distance of transmission are given as follows:

- 1) Power in MW, $P = 0.5 V^2/x L$:
- 2) Current in KA: $I = 0.299 V/x L$:
- 3) % power loss : $p = .50 r/x$.

Here, V = line-to-line voltage in kV.

x = positive-sequence reactance of line, ohm/Km,

r = resistance in ohm/Km at 75°C and 50 Hz,

and L = Line length in Km.

The power-handling capacity and current admissible are inversely proportional to line length at any given voltage level. However, the percentage power loss is independent of line length but depends only on the ratio of resistance to positive-sequence reactance per unit, which is a constant at a given voltage level.

The following table gives the salient features of lines at different voltage levels for calculation purposes:

<u>V, kV</u>	<u>400</u>	<u>750</u>	<u>1000</u>	<u>1200</u>
Av. Height, m	15	18	21	21
Phase Spacing, m	11	14	18	18
Conductor No. and Dia	2x32 mm	4x30 mm	6x46 mm	8x46 mm
Bundle spacing	.4572 m	.4572 m	-	-
Bundle dia	-	-	1.2 m	1.2 m
r , Ohm/Km	.031	.0136	.0036	.0027
x , Ohm/Km	.327	.272	.231	.231
% loss	5.12	2.7	0.85	0.64

For instance, as compared to a 400 kV line, the losses at 750 kV are 52.7%, at 1000 kV are 16.6%, and at 1200 kV are 12.5% for transmitting the same amount of power. These exclude corona

losses. The advantage in using higher voltages is obvious for conserving energy.

The power-handling capacities of line at different voltage levels for A.C. transmission are as follows.

<u>Line length, Km :</u>	<u>400</u>	<u>600</u>	<u>800</u>	<u>1000</u>	<u>1200</u>
<u>Voltage: 400 kV :</u>	670	450	335	270	225 MW/circuit
<u>750 kV</u>	2860	1900	1430	1140	950 MW/circuit
<u>1000 kV</u>	6000	4000	3000	2400	2000 MW/circuit
<u>1200 kV</u>	8640	5760	4320	3460	2880 MW/circuit

The power-handling capacities of D.C. lines at various voltage levels on the assumption of 1.8 kA per pole will be as follows :

<u>Bipolar Voltage, kV</u>	<u>± 400</u>	<u>± 450</u>	<u>± 500</u>	<u>± 600</u>
<u>Voltage between conductors kV</u>	800	900	1000	1200
<u>Power per Circuit, MW</u>	1,440	1,620	1,800	2,160

The powers per circuit given above for A.C. and D.C. lines will be utilized in this lecture to discuss the choice of higher voltage required for transmission of bulk power from Indian power pools to load centres, as is being planned for the country.

SECTION 5 : Examples of Major Power Pools in India

From a plan made for the development of major hydroelectric resources in the Kashmir to Arunachala Pradesh areas covering the entire northern fringes of the country, it appears that the following MW powers have to be transmitted to load centres in the Ganga Valley and the Western Coast (Bombay etc.):

- (1) 2500 MW over 250 Km; (2) 3000 MW over 300 Km;
- (3) 4000 MW over 400 Km; (4) 5000 MW over 300 Km; and
- (5) 12,000 MW over distances of 250 Km, 450 Km, and 1000 Km.

There is considerable doubt as to the time at which some of these power pools will come into operation. Some planners state that the massive power flow from the N.E. Region to other regions of the country will take place in the 90's. Others say that the installed capacity to be added in this region between 1983 and 2001 is only 900 MW. Still others state that the installed capa-

city in the N.E. Region will amount to 20,730 MW by the year 2000 A.D. Therefore it appears that the evacuation of power from such vast pools of resources is still a matter for discussion as regards the time of implementation. This places a greater responsibility on power engineers to be more certain about data in order to plan effectively in India. However, it is certain that these power pools will be developed and higher transmission voltage than 400kV will be necessary. The actual voltages and the number of circuits required will be discussed in the next section.

As is evident from the wide publicity given by the National Thermal Power Corporation, the major power pool for thermal generation is in the Singrauli-Raniganj-Jharia coal fields. As mentioned before, transport of Indian coal from mines to load centres is fraught with drawbacks due to large ash contents, pilferage, and lack of railway wagons. Therefore, as a National policy, the Planning Commission has accepted mine-mouth generation and transmission to load centres as electric power as the only policy. The present installed capacity is 4000 MW with a very rapid annual increase in power which is nearly 16% in the very near future, but which will have to slow down to 5% in course of time. The power generated in this gigantic pool will be transmitted to Bombay, Delhi-Kanpur, and Calcutta areas. The powers transmitted will be nearly equal in the three directions, and in Section 7, the required higher transmission voltages and the number of circuits will be discussed.

SECTION 6 : Higher Transmission Voltage Selection for Hydro-Electric Generation and Evacuation

In the previous Section, the expected power at several major hydro sites and the distance of transmission were given. In Section 4, the power-handling capacity per circuit at several voltage levels was also given. It is now a straight-forward matter to decide on the alternative transmission schemes required and should not tax the intelligence. However, the following Table is given for ready reference.

<u>Power</u>	<u>Distance</u>	<u>Alternative Design Possibilities</u>	
		<u>D.C. Lines</u>	<u>A.C. Lines</u>
2500 MW	250 Km	2 of \pm 400 kV	3 of 400 kV
3000 MW	300 Km	2 of \pm 400 kV	4 of 400 kV or 1 of 750 kV
4000 MW	400 Km	2 of \pm 500 kV	6 of 400 kV, or 2 of 750 kV (70% loaded)
5000 MW	300 Km	2 of \pm 600 kV	6 of 400 kV 2 of 750 kV (75% loaded)
12000 MW	250 Km	8 of \pm 400 kV	12 of 400 kV
		6 of \pm 600 kV	3 of 750 kV
	--		1 of 1200 kV
	450 Km	8 of \pm 400 kV	20 of 400 kV
		6 of \pm 600 kV	6 of 750 kV
	--		2 of 1200 kV
	1000 Km	8 of \pm 400 kV	48 of 400 kV
		6 of \pm 600 kV	12 of 750 kV
			6 of 1000 kV
			4 of 1200 kV

.. From the above table, proper conclusions can be drawn. As an example, for transmitting powers upto 5000 MW for distances between 250 and 400 Km, a voltage level of 400 kV, A.C., will suffice. This also can be accommodated with the technological know-how now available in India, which is a very strong consideration for making decisions. Serious consideration is required for adopting 750 kV and 1200 kV for evacuating a power of 12000 MW over distance from distances from 250 Km to 1000 Km, that is, from the Alakhananda-Bhagirathi complex in the Upper Ganga near Rishikesh, and the Brahmaputra Valley to load centres in Bihar and Bengal and south.

SECTION 7 : Evacuation of Power from Thermal Generation Pool

In Section II, the life of coal deposit available for electric power generation for various rates of annual growth of installed capacity was given. With a present installed capacity of 4000 MW and for various assumed annual rates of increase of installed capacity, the following table has been drawn up to show the power picture for the years 1990, 1995, and 2000.

<u>% Annual Increase</u>	<u>5</u>	<u>6</u>	<u>7</u>	<u>8</u>	<u>9</u>	<u>10</u>
Power in 1990, MW	6520	7160	7870	8630	9460	10,400
Increase over 1980	2520	3160	3870	4640	5460	6400
Power in 1995, MW	8320	9590	11040	12680	14550	16,270
Increase over 1990	1800	2430	3170	4050	5090	6340
Power in 2000, MW	10620	12840	15490	18630	22390	26,930
Increase over 1995	2300	3250	4450	5950	7830	10,210

Therefore, any plans laid down for the choice of voltage and number of circuits would be based on a time-schedule for evacuating the powers, which will not only depend on the total ultimate power but also on the increase with time.

Now, under the assumption that the power from this pool is transmitted equally in 3 directions, some indication of the required transmission circuits can be worked out. The distances to major load centres are: Bombay-1200 Km; Calcutta - 600 Km; and Delhi - 800 Km. We will further assume that all existing and projected 400 kV lines will be fully loaded by the year 1990. The additional lines will overlay the existing 400 kV network. I will restrict to A.C. lines, since as has already been pointed out, major power-producing countries have decided on using A.C. at the 750-kV, or 1000 kV, or 1200 kV levels. I will leave it to you to work out the D.C. alternatives, but keeping in mind that these lines will run in the thickest-populated regions of this populous country and rural electrification and tapping off assume great importance.

By the year 2000, the following transmission lines will be necessary between 1990 and 2000, when the rate of power growth is taken as 5%, 7%, and 10% annually, that is the doubling of power requirement occurs in 15 years, 10 years, and 7 years, respectively.

<u>Direction</u>	<u>% Rate</u>	<u>Voltage Class</u>	<u>No. of Circuits</u> (Required by 2000 A.D.)
Pool to Bombay (1200 Km)	5%	750 kV	2
	7%	750 kV	3
	10%	750 kV	6
		1000 kV	3
		1200 kV	2

<u>Direction</u>	<u>% Rate</u>	<u>Voltage Class</u>	<u>No. of Circuits</u> (Required by 2000 A.D.)
Pool to Calcutta (600 Km)	5%	400 kV	3
	7%	750 kV	1
		400 kV	6
		750 kV	2
	10%	750 kV	3
		1200 kV	1
Pool to Delhi (800 Km)	5%	400 kV	3
	7%	750 kV	2
		750 kV	2
		750 kV	4
	10%	1000 kV	2

From the above table, we can observe that for evacuating power from the Central-Indian generating pool, a voltage in excess of 750 kV is not required. Reliability considerations require two circuits, and 400 kV and 750 kV serve the purpose well. As mentioned in Section III, the vast experience gained by Canada in their 750 kV system and their decision to stick with this voltage class, even after investigating the 1200 kV A.C. and D.C. transmission alternatives, should form food for serious thought to planners for adopting the 750 kV class for Indian conditions. I offer this as my humble suggestion.

ELECTROSTATIC FIELD AND AUDIBLE NOISE

Calculation of Electrostatic Field of A.C. Lines:

Charge of Conductor:

We already described the method of obtaining electrostatic charges on the phase conductors from line geometry and voltage.

This is, for n conductors as shown in Figure 1,

$$\frac{1}{2\pi\epsilon_0} [q] = [P]^{-1} [V] = [M] [V]$$

where

$$[q] = [q_1, q_2, \dots, q_n]$$

$$[V] = [V_1, V_2, \dots, V_n]$$

and

$[P]$ = $n \times n$ matrix of Maxwell's potential coefficients

with $P_{ii} = \ln \left(\frac{2H_i}{R_{eq}} \right)$, and $P_{ij} = \ln \left(\frac{I_{ij}}{A_{ij}} \right)$.

where H_i = height of conductor i above ground

I_{ij} = distance between conductor i above ground and the image of conductor j below ground

A_{ij} = aerial distance between conductors i and j ,

$R_{eq} = (N\gamma R^{N-1})^{1/N}$ = the equivalent bundle radius,

$i, j = 1, \dots, n$

N = number of sub-conductors in bundle,

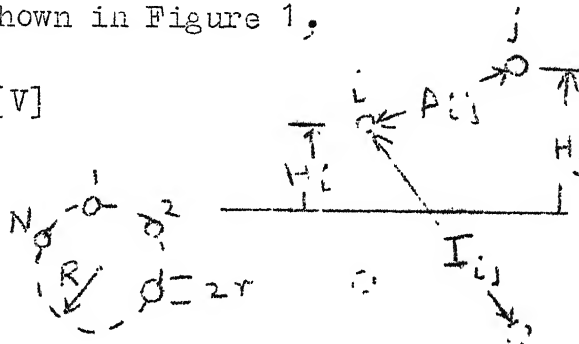
γ = radius of each sub-conductor

and R = radius of bundle.

The line-to-ground voltages V_1 to V_n and bundle charges q_1 to q_n are sinusoidally varying in time. Consequently, the electrostatic field induced at any point near the line is also varying sinusoidally at power frequency. Phasor algebra can be used to combine the several components in order to yield the amplitude of the resulting field.

Electrostatic Field of S/C 3-phase line:

At a point $A(x, y)$ in the vicinity of phase conductor i with coordinates (x, y) referred to an origin, the field strength is



$$E_c = \frac{q_i}{2\pi\epsilon_0} \cdot \frac{1}{D_i}$$

in which

$$D_i^2 = (x-x_i)^2 + (y-y_i)^2$$

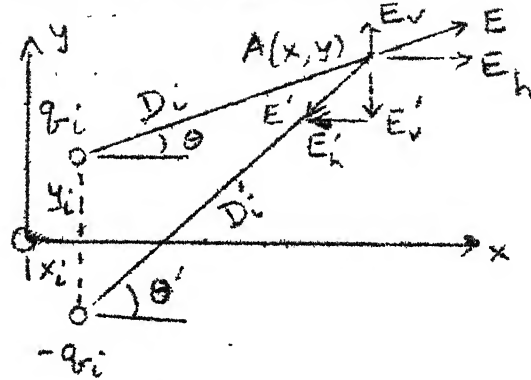
Its horizontal and vertical components are as follows:

Horizontal:

$$E_h = E \cos \theta = \frac{q_i}{2\pi\epsilon_0} \cdot \frac{x-x_i}{D_i^2}$$

Vertical:

$$E_v = E \sin \theta = \frac{q_i}{2\pi\epsilon_0} \cdot \frac{y-y_i}{D_i^2}$$



The contribution from the image charge conductor i can also be calculated. The field components are now in directions opposite to those of the line charge.

$$E_{h'} = \frac{q_i}{2\pi\epsilon_0} \cdot \frac{1}{D_i'} \sin(90-\theta') = \frac{q_i}{2\pi\epsilon_0} \cdot \frac{x-x_i}{(D_i')^2}$$

and

$$E_{v'} = \frac{q_i}{2\pi\epsilon_0} \cdot \frac{1}{D_i'} \cos(90-\theta') = \frac{q_i}{2\pi\epsilon_0} \cdot \frac{y+y_i}{(D_i')^2}$$

where

$$(D_i')^2 = (x-x_i)^2 + (y+y_i)^2$$

The total horizontal and vertical components at A due to both the conductor charge and that of its image are

$$E_{hi} = \frac{q_i}{2\pi\epsilon_0} (x-x_i) \left[\frac{1}{D_i^2} - \frac{1}{(D_i')^2} \right]$$

$$E_{vi} = \frac{q_i}{2\pi\epsilon_0} \left[\frac{y-y_i}{D_i^2} - \frac{y+y_i}{(D_i')^2} \right]$$

Consequently, the total horizontal and vertical components of electrostatic field due to n conductors on the tower will turn out to be:

$$E_{hn} = \sum_{i=1}^n E_{hi}, \text{ and } E_{vn} = \sum_{i=1}^n E_{vi}$$

The total field at point A is

$$E_{tn} = (E_{hn}^2 + E_{vn}^2)^{1/2}$$

Effect of E.S. Field on Humans, Animals, Plants and Vehicles:

The effect of high e.s. field of a e.h.v. or u.h.v. line is important on (a) human beings, (b) animals, (c) plant life, and (d) vehicles. They also have an effect on fences and buried pipe lines located under and near the line. It is clear that when an object of finite size is located under the line, it disturbs the field, the degree of distortion depending upon the size and nature of the object. This is quite an advanced topic and will not be dealt with here and must be investigated case by case. However, it has been found in practical situations that the effects of a distorted field can nevertheless be estimated from a knowledge of the undisturbed field.

(a) Human beings :

The effect of high e.s. field on human beings has been more extensively studied than on any other animals or objects because of its grave and shocking effects which has resulted in loss of life. Consider a farmer ploughing his field while sitting on a tractor and having an umbrella or canopy for shade. He has the chance of being charged by the resulting corona from pointed spikes. When he gets off the vehicle and touches a grounded object, he will discharge himself. Also, when a standing on ground a human body is pure resistance of about 1500 ohms. If a vehicle is parked under a transmission line and has insulated tyres, and a human being touches the chassis, the charge acquired by the vehicle will discharge through the body. If the current is 9 mA, which is known as the let-go current, then he experiences a shock that can cause damage to the body including the brain by impairing muscular action affecting the lungs. For women the let-go current is 6 mA and for children 4.5 mA.

It has been found experimentally that the limit for the undisturbed field is 15 kV/m for human beings to experience shock. An e.h.v. or u.h.v. line must be designed such that this limit is not exceeded. Some power utilities are very conscious of this

responsibility and have purposely increased the minimum clearance over and beyond what is specified from air-gap insulation clearance requirement. As an example, the Bonneville Power Administration in the USA have selected the maximum e.s. field gradient to be 9kV/m at 1200 kV and in order to do so have used a minimum clearance at mid span of 23.2 m whereas they could have chosen 17.2m based on clearance required for switching-surge insulation as prescribed by the National Electrical Safety Council.

(b) Animals:

Experiments carried out in cages under e.h.v. lines have shown that pigeons and hens are affected by high e.s. fields of 30 kV/m. They are unable to pick grain with their beaks properly resulting in large spillage which affects their growth. Pigs and cattle experience shocks when their bodies acquire charge and they then drink water from grounded troughs resulting in a discharge. However, this takes place in fields in excess of 30 kV/m. Therefore, human beings limit the e.s. field of a transmission line and not animals.

c) Plant Life:

Plants such as wheat, rice, sugarcane etc. suffer the following types of damage. At a field strength of 20 kV/m (RMS), the sharp edges of the stalk give corona discharges so that damage occurs to the upper portion of the grain-bearing parts. However, the entire plant does not suffer damage. At 30 kV/m the by-products of corona become intense enough to cause harm. These are emission of N_2O , and ozone. Further, the resistive heating due to increased current prevents full growth of the plant and the grain. Below 20 kV/m the plant is unaffected and this may be considered as the limit. Once again, this is above what is safe from human point of view.

d) Vehicles:

Vehicles parked under a line or driving through acquire electrostatic charge if their tyres are made of insulating material. A parked vehicle might acquire charge because of its capacitance, the larger the vehicle the higher being the charge.

When a human being contacts the vehicle, he has to conduct the discharge current which might amount to the let-go current. It has been found from both experiments as well as by calculation that existing designs of 400 kV are quite safe and no fatalities have been reported so far from parked vehicles acquiring charge. However, if parking lots are located under a line, the recommended safe clearances are 17 m for 345 kV lines and 20 m for 400 kV lines. Lorries will require an extra 3 m clearance.

e) Others:

Fences, buried cables, and pipes are important pieces of equipment that have been investigated for possible danger or damage when they are located in high e.s. fields. Metallic fences parallel to a line must be grounded preferably every 75 m. Pipelines longer than 3.2 km and larger than 15 cm in diameter are recommended to be buried at least 31 m laterally from the centre phase to avoid dangerous eddy currents that could cause corrosion. Sailboats, rain gutters in houses and insulated walls on houses near transmission lines are also subjects of potential danger. The danger of ozone emanation from the transmission-line conductors at high electric fields can also be included in the category of damage to tissues of human beings living near lines.

AUDIBLE NOISE

Mechanism of Generation and Characteristics of Audible Noise:

EHV transmission lines generate audible noise when corona is present on the conductors, which is especially high during foul weather. The noise is broadband extending upto 15 KHz from very low frequency. Corona discharges produce positive and negative ions in the vicinity of the conductors which are alternately attracted and repelled by the periodic reversal in polarity of the a.c. excitation. This motion gives rise to sound-pressure waves at frequencies of double the power frequency and its multiples in addition to the broadband spectrum, as shown in Fig.3. Therefore the noise has a pure tone superimposed on the broadband noise. Due to differences in ionic motions in the case of a.c. and d.c. excitations, d.c. lines exhibit only a broadband noise, and furthermore,

the noise generated from a d.c. line under foul weather is nearly the same as in fair weather. Since audible noise from a transmission line is man-made, it is measured in the same manner as other types of man-made noises such as aircraft noise, ignition noise, transformer hum, etc. We will discuss the meters used and methods of AN measurements in a subsequent chapter.

Audible noise can be a serious problem from 'psychoacoustics' point of view, leading to insanity due to loss of sleep to inhabi-

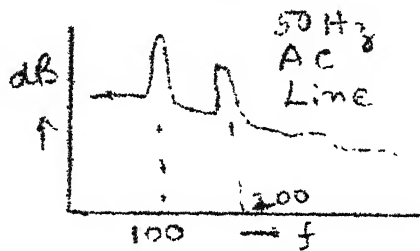


Fig. 3(a)

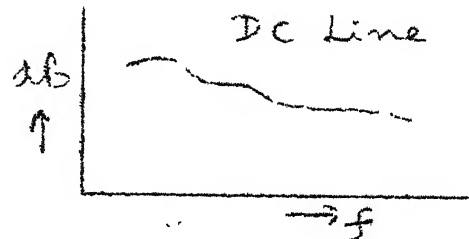


Fig. 3(b)

tants living close to an e.h.v. line. This problem came into focus in the 1960's with the energization of 500 kV lines. Regulatory bodies have not yet fixed limits to AN from power lines since such regulations do not exist for other man-made sources of noise. The limits for AN will be discussed in the next section.

Limits for Audible Noise:

Since no legislation exists for the limit of AN from man-made sources, power companies and environmentalists have fixed limits from public-relations point of view. In doing so like other kinds of interference, human beings must be subjected to listening tests. Such objective tests are performed by every civic-minded power company. The first such series of tests performed from a 500 kV line of the Bonneville Power Administration in the USA has come to be called Perry Criterion for AN limits. The limits taken are as follows:

No complaints	: Less than 52.5 dB (A)
Few complaints	: 52.5 dB(A) to 59 dB(A)
Many complaints	: Greater than 59 dB(A)

Design of line configuration at e.h.v. is now being governed more and more by the need to limit the AN level to above values. At the edge of the right-of-way for the line, where the closest

house may be allowed to exist, nuisance caused by AN is limited to less than 52.5 dB(A) and will be closer to 50 dB(A) as has been done for the BPA 1150-1200 kV line. The design aspect will be considered later on. The audible noise generated by a line is a function of

- a) the surface voltage gradient on the conductors;
- b) the number of sub-conductors in the bundle;
- c) conductor diameter;
- d) lateral distance from the line to the point where noise is to be evaluated; and
- e) atmospheric conditions.

Once again, as in most e.h.v. work, the entire phenomenon is statistical in nature because atmospheric conditions are crucial for operation at these extra high voltages.

While the Perry Criterion is based on actual listening tests and guidelines are formed for limiting values of AN from a line at the location of inhabited places, other man-made sources of noise do not follow such limits. A second criterion which evaluates the nuisance is called the 'Day-Night Equivalent'. This is based not only on the variation of AN with atmospheric conditions but also with the hours of the day and night during a 24-hour period. The reasoning behind this criterion is that a noise level that can be tolerated during waking hours of the day, when ambient noises are high, cannot be tolerated during sleeping hours of the night when little or no ambient noises are present. This will be elaborated upon later on. According to the Day-Night criterion, a noise level of 55 dB(A) can be taken as the limit instead of 52.5 dB(A) according to the Perry Criterion.

Measurement of AN and Meters:

a) Decibel values in AN and addition of sources:

Audible noise is caused by changes in pressure of air or other transmission medium so that it is described by Sound Pressure Level (SPL). Alexander Graham Bell established the basic unit for the SPL as 20×10^{-6} Newton/m² or 20 micro pascals. (2×10^{-4} micro bar). All decibal values are referred to this. In telephone work, we have a flow of current in a set of headphones or receiver. Here the

basic units are 1 mW across 600 ohms which yields a voltage of 775 mV, and current of 1.29 mA. For any other SPL, the decibel value is

$$\text{SPL (dB)} = 10 \log \left[\frac{(\text{SPL})}{(20 \times 10^{-6} \text{ pascals})} \right]$$

This is also termed the 'Acoustic Power Level', denoted by PWL, or simply AN level, AN:

Consider N sources whose decibel levels are $\text{AN}_1, \text{AN}_2, \dots, \text{AN}_N$. In order to add these to determine the resultant sound pressure level and decibel value, the procedure is as follows:

We first calculate the individual sound pressure levels from the given decibel values thus,

$$\text{SPL}_1 = 2 \times 10^{-5} \cdot 10^{\text{AN}_1/10}, \text{SPL}_2 = 2 \times 10^{-5} \cdot 10^{\text{AN}_2/10}, \dots$$

$$\text{SPL}_i = 2 \times 10^{-5} \cdot 10^{\text{AN}_i/10}, \dots, \text{SPL}_N = 2 \times 10^{-5} \cdot 10^{\text{AN}_N/10}$$

The total $\text{SPL} = \text{SPL}_1 + \text{SPL}_2 + \dots + \text{SPL}_i + \dots + \text{SPL}_N$

$$= 2 \times 10^{-5} \sum_{i=1}^N 10^{\text{AN}_i/10}$$

The decibel value of the combination of sources is

$$\begin{aligned} \text{AN} &= 10 \log_{10} (\text{SPL} / 2 \times 10^{-5}) \\ &= 10 \log_{10} \sum_{i=1}^N 10^{\text{AN}_i/10} = 10 \log_{10} \sum_{i=1}^N 10^{0.1 \text{AN}_i} \end{aligned}$$

Formulas for Calculating Audible Noise and use in Design:

Audible noise from a line varies with atmospheric conditions so that there is no one quantity or AN level that can be considered as the level. Designers base their results on two quantities which are designated the L_{50} level and L_5 level. These are defined as follows:

L_{50} Level: This is the AN level as measured on the A-weighted network which is exceeded 50% of the time during periods of rain usually extending over one year.

L_5 Level: Similar to L_{50} but exceeded only 5% of the time.

The latter usually is concerned with heavy rain such as is generated in artificial rain tests so that it is very useful in correlating with the L_{50} level according to some formulas. Since AN measurements were commenced fairly recently, the formulas are an outcome of not only the limited number of test measurements available from actual operating lines, but mainly from 'cage' test results and short-line outdoor experimental projects. As mentioned under limits for AN in earlier, each power company must evolve its own limits since no legislative control exists.

While many empirical formulas exist (Ref. IEEE Task force paper October 1982), we will discuss the use of only one formula here given by the Bonneville Power Administration. Other formulas are given later for the use of a designer. The BPA formula is applicable for the following conditions:

- All line geometries with bundles having upto 16 sub-conductors of diameters in the range 2 cm to 6.5 cm.
- The AN calculated is the L_{50} level in rain.
- The formula is applicable for transmission lines from 230kV to 1500 kV, 3-phase A.C.

The formula for AN level of each phase at the measuring point, as shown in Figure 4. is, ($i=1,2,3$):

$$AN_i = 120 \log_{10} E_{ami} + 55 \log_{10} d - 11.4 \log_{10} D_i - 115.4, n < 3$$

$\Delta b(A)$

and

$$AN_i = 120 \log_{10} E_{ami} + 55 \log_{10} d - 11.4 \log_{10} D_i + 26.4 \log_{10} n - 128.4, n \geq 3$$

$\Delta b(A)$

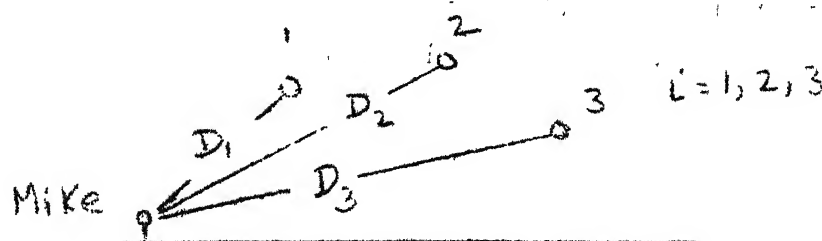


Fig. 4.

Here, E_{ami} = average maximum surface voltage gradient on bundle belonging to phase i in kV/cm,
 d = diameter of sub-conductor, cm,
 n = number of sub-conductors in bundle
 and D_i = aerial distance from phase i to the location of the microphone, metres.

When all dimensions are in metre units, the above become

$$AN_i = 120 \log_{10} E_{mi} + 55 \log_{10} d_m - 11.4 \log_{10} D_i + 234.6, n < 3$$

$$AN_i = 120 \log_{10} E_{mi} + 55 \log_{10} d_m - 11.4 \log_{10} D_i + 26.4 \log_{10} n + 221.6, n \geq 3$$

Day-Night Equivalent Noise Level:

In the previous discussions the AN level of a transmission line has been chosen as the L_{50} level or the value in decible of the audible noise that is exceeded for 50% of the duration of precipitation. This has been tacitly assumed as the nuisance value. However, a more recent criterion which is actively being discussed and applied to other man-made AN sources is called the Day-Night Equivalent Noise Level. This has been applied to aircraft noise, heavy road traffic noise, etc. which leads to litigation among many aggrieved parties and the creators of the noise. According to this criterion, a certain sound level might be acceptable during the day-time hours when ambient noises will be high. But during the night the same noise level from a power line or other man-made noise sources could be found objectionable because of the absence of ambient noises. The equivalent annoyance during nights is estimated by imposing a 10 dB(A) penalty.

Consider an L_{50} level of a power line to be AN and the day-time to last for D hours. The actual 'annoyance' level in terms of the day-night equivalent is specified as

$$L_{dn} = 10 \log_{10} \left[\frac{1}{24} D \cdot 10^{AN/10} + (24-D) \cdot 10^{(AN+10)/10} \right]$$

Example

The L_{50} level of a line is 55 dB(A). The day-light hours are 15 and night-time is 9 hours in duration. Calculate the day-night equivalent.

Solution:

$$\begin{aligned}
 L_{dn} &= 10 \log_{10} \left[\frac{1}{24} (15 \times 10^{5.5} + 9 \times 10^{6.5}) \right] \\
 &= 10 \log_{10} [10^5 (47.43 + 284.58) / 24] = 61.4 \\
 &= 55 + 6.4 \text{ dB(A)}
 \end{aligned}$$

The decibel adder in this case is 6.4 which has increased the SPL by 4.365 times [$10 \log_{10} 4.365 = 6.4$]. The nuisance value of the line has been increased by 5.4 dB(A) by adding the 10 dB(A) penalty for night hours to the AN value for the day-time level. If the day-night hours are different from 15 and 9, a different decibel adder would be necessary.

We also note that the 10 dB(A) penalty added for night time contributes 6 times ($274.58/47.43$).

In evaluating the nuisance value of AN from o.h.v. power lines, we are only concerned about the time duration of rainfall and not the total day-night hours. If rain is not present over the entire 24 hours but only for a certain percentage of the day and night above a minimum rate of rainfall the day-night equivalent will be calculated differently from what is given. Let it be assumed that the percentages of duration of rainfall during the day and night are p_d and p_n .

$$L_n = 10 \log_{10} \left[\frac{1}{24} \left(D \cdot \frac{p_d}{100} \right) 10^{AN/10} + (24-D) \frac{p_n}{100} \cdot 10^{(AN+10)/10} \right] \text{ dB(A) } \dots$$

Example

The following data apply for a line:

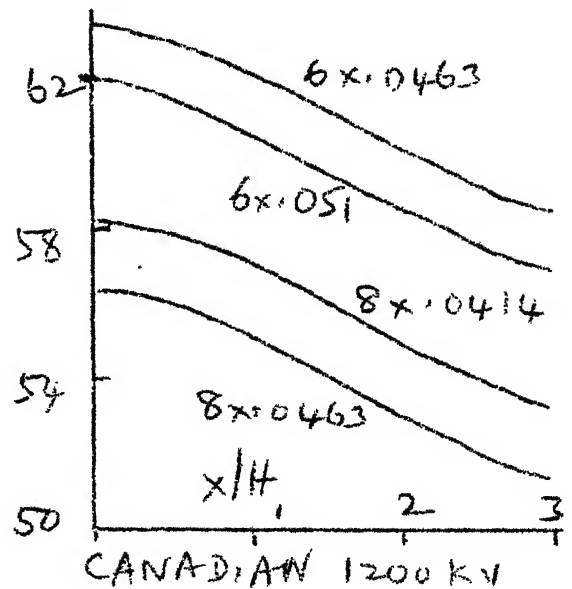
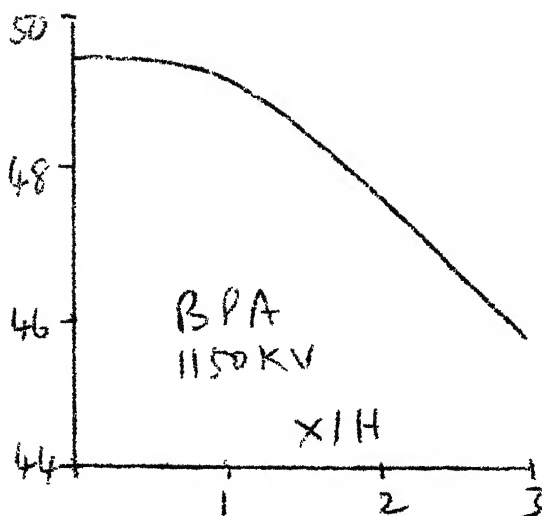
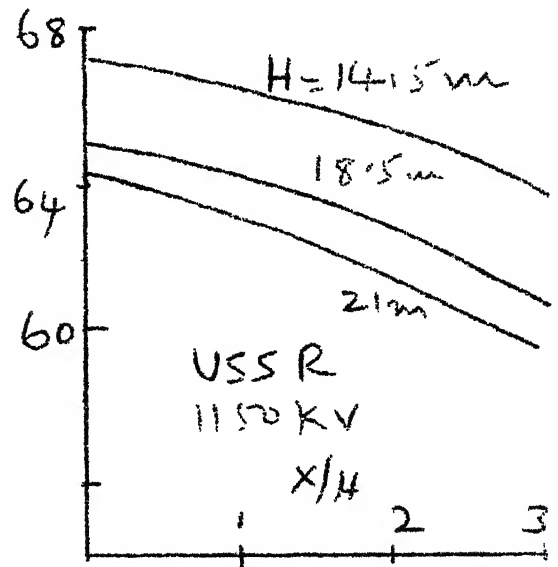
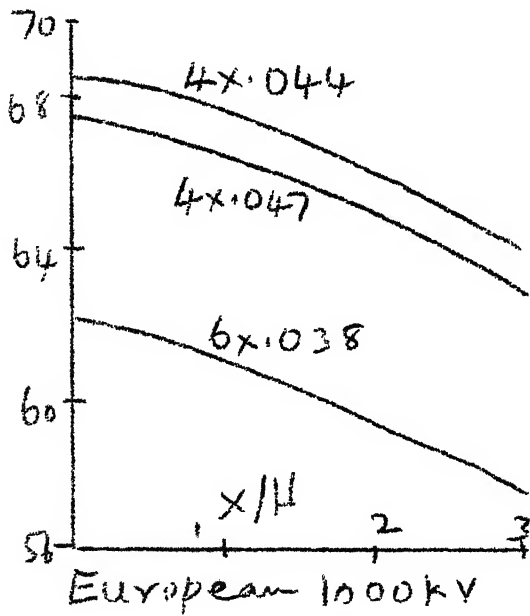
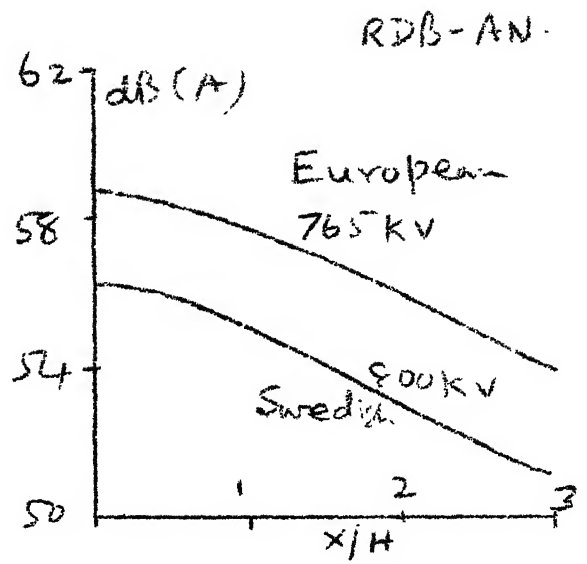
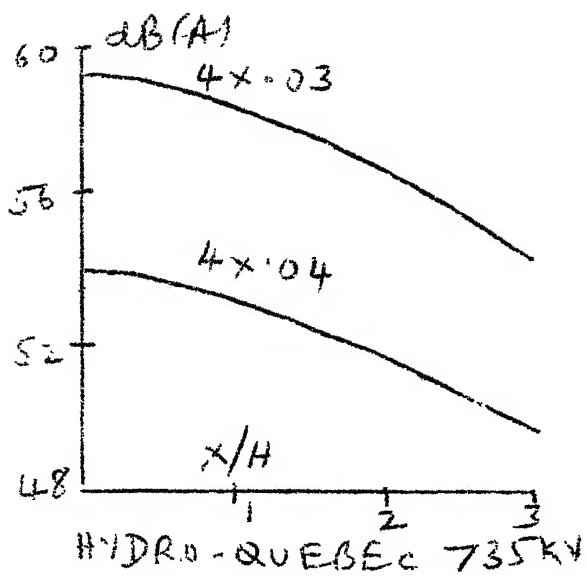
L_{50} level = 55 dB(A). $D=15$, $p_d=20$, $p_n=50$. Calculate the day-night equivalent of AN and DB adder.

Solution:

$$\begin{aligned}
 L_{dn} &= 10 \log_{10} \left[\frac{1}{24} \left(15 \times 0.2 \times 10^{5.5} + 9 \times 0.5 \times 10^{6.5} \right) \right] \\
 &\quad \quad \quad 9.48 \quad + \quad 142.3 \\
 &= 58 \text{ dB(A)}
 \end{aligned}$$

The decibel adder is 3 dB(A).

Again we note that the night-time contribution is nearly 15 times the day-time contribution ($142.3/9.48$).



1000

1000

1000

1000

1000

1000

1000

1000

1000

1000

1000

1000

1000

1000

1000

1000

1000

1000

1000

1000

1000

1000

1000

1000

1000

1000

1000

1000

1000

1000

1000

1000

1000

1000

1000

1000

1000

In the above equation, it was assumed that the L_{50} levels for both day and night were equal. If this is not the case, then the proper values must be used which necessitates very careful experiments to be performed on long-term measurements relating rate of rainfall to the AN level. Such experiments are usually performed with short transmission lines over a ground or in 'cages'.

Some examples of AN levels from EHV Lines:

It might be informative to end this chapter with data of the performance of some line designs in the world based on AN limits.

1. The BPA has fixed 50 dB(A) limit for the L_{50} noise level at 30 m from the line centre in rain for their 1150 kV line operating at 1200 kV. This was based on experience gained from the 500 kV lines upon which Perry established the limit criterion.
2. The AEP, UHV Project of the EPRI, and other designs fall very close to the above values.
3. Operating 750 kV lines of the AEP gave 55.4 dB(A) at 760kV. At their Apple Grove short-line outdoor project, the value obtained at 775kV was 56.5 dB(A), proving that short-line data can be relied upon to provide adequate design values.
4. The Hydro-Quebec Company of Canada gave the following calculated AN levels at 30.5 metres from the line centre.

<u>Voltage</u>	<u>745 kV</u>	<u>735 kV</u>	<u>525 kV</u>	<u>735 kV</u>	<u>525 kV</u>
<u>Conductor</u>	4x1.165"	4x1.2"	2x1.602"	4x1.382"	3x1.302"
<u>Size</u>	(.03296 m)	(.03395 m)	(.0407 m)	(.0351 m)	(.0331 m)
<u>Bundle</u>	18"	18"	18"	18"	18"
<u>Spacing</u>	(.4572 m)				
<u>Phase</u>	41'	45'	34'	50'	34'
<u>Spacing</u>	(12.5m)	(13.72m)	(10.37m)	(15.25m)	(10.37m)
<u>AN level</u>					
<u>dB(A)</u>	60	58.5	57	55	52

PROBLEMS ARISING FROM OVERCURRENTS AND OVERVOLTAGES

In this lecture the nature of problems caused by overcurrents and overvoltages will be described..

- a) Overcurrents are generated by short circuits in the system and due to lightning.
- b) Overvoltages are the result of switching operations, lightning, and resonance conditions.

These are disturbances to a system that must be either removed or suitably protected against.

The following topics will be described here.

1. Short Circuit Current and the Circuit Breaker..
2. Recovery Voltage
3. Interruption of Low Inductive and Capacitive Currents.
4. Overvoltages on Energizing EHV Lines (Closing and Reclosing).
5. Ferro-resonance conditions.

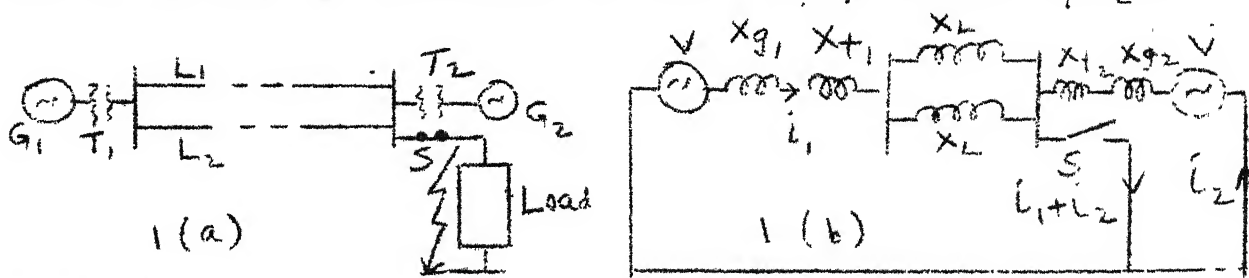
1. Short Circuit Current and the Circuit Breaker

Consider a simple system with 2 generating areas G_1 and G_2 connected through 2 lines and feeding a load, Figure 1(a). Transformers are also included. Let a short-circuit occur at the load bus, necessitating the breaker S to open to isolate the faulted bus. The questions are what are the stresses on the breaker?

The single-line diagram, neglecting all resistances, is shown in Figure 1(b). Usually, the introduction of resistances will change current values by not more than 3 percent. The a.c. components of short circuit currents fed by the two generating areas are

$$i_1 = \frac{V_1}{X_{g1} + X_{t1} + 0.5 X_L} \quad \text{and} \quad i_2 = \frac{V_2}{X_{g2} + X_{t2}}$$

For simplicity in developing the main ideas, we take $V_1 = V_2 = V$



In modern high-speed circuit breakers (2-cycle) contacts separate in about 30 to 40 milliseconds (ms) after initiating the s-c, which is governed by the operating time of the protective system. This time is slightly longer than the subtransient time constant T'' of small and medium-size generators and is nearly equal to that of large turbo-alternators. Therefore, in general, the reactance used is the transient reactance X'_d . For calculating the first peak of s-c current, the reactance to be used is approximately $\frac{2}{3} X'_d$. In terms of the rated power of the generator, the generator reactance used is $X_g = X'_d \cdot V^2/P_g$, where V^2/P_g is the base impedance and X'_d is the per unit value. For turbogenerators of 500 MVA rating, $X''_d = 0.2$ p.u. and $X'_d = 0.3$ p.u. For 1000MVA sets, these will be close to 0.3 and 0.45 p.u. respectively. For smaller sets, they may be approximately 0.15 and 0.2 p.u. respectively.

For transformers, $X_t = P_t V^2/P_t$, where P_t is the p.u. value, P_t is the transformer rating. Usually, $P_t = P_g$ for unit-connected sets and for entire stations. Typically, $P_t = 0.10$ to 0.15 p.u.

For lines, the ohmic values of positive-sequence quantities are given below for estimation purposes only.

<u>System Voltage</u>	<u>220 kV</u>	<u>400 kV</u>	<u>750 kV</u>
<u>No. of conductors</u>	1	2	4
L_1 , mH/Km	1.34	1.03	0.875
R_1 , m-ohm/Km	80	30	15
C_1 , nF/Km	9	11.75	13.5
Z_1 , ohms	380	300	265

In practice, $X'_d + P_t \approx 0.5$ which gives an estimated current of twice the rated current through the high-voltage winding of the transformer.

For very high voltage breakers the new I.E.C. (International Electro Technical Commission) recommends the specification of current rating and not the short-circuit power rating. This gives more information to the designer of the breaker and the system engineers.

When the d-c component is included, the total s-c current will be

$$i = \frac{\sqrt{2}V}{\sqrt{(R^2 + X^2)}} [\cos(\omega t - \phi - \theta) - \cos(\phi + \theta) \cdot e^{-t/T'}]$$

where $\tan \theta = X/R$ and $T' = X/2\pi R$.

The variation of s-c current with full d-c offset is shown in Figure 2. The I.E.C. recommends a time constant $T' = 45$ ms. As an example, consider a 400 kV system with a generation of 2000 MVA. The normal current is 2.8 KA and the s-c current will be about 6 kA, r.m.s. The maximum interrupting current of the breaker occurs 1/2 cycle later, its value is

$$I_i = I_{rms} \sqrt{2} (1 + e^{-10/45}) = 1.8 \sqrt{2} I_{rms}$$

For the above case, $I_i = 1.8 \sqrt{2} \times 6 = 15.3$ KA.

It may be of interest to note that air-blast circuit breakers are available for 80 KA and SF₆ breakers for 90 KA. This shows that a system engineer must keep s-c levels down to what currently available circuit breakers can handle. In 400 kV networks this maximum is 40 KA.

It is evident that the d-c component must decay fast in order that interruption might take place at the first current zero. Since contact separation occurs 30 to 40 ms ($1\frac{1}{2}$ to 2 cycle) after fault initiation, the d-c component decays with 45 ms time constant is adequate to bring it down to about $e^{-10/45} = 40$ percent of maximum value and a current zero can occur.

Single Phase Short Circuits

80 percent of all faults in a system are single phase. However, the s-c current magnitude, recovery voltage and the stresses on the breaker are lower than for 3-phase faults. Even though 3-phase faults occur in 10 percent of the cases, the circuit breaker has to be designed for this type of fault.

The ratio of currents for these two types of fault is

$$I_{1ph}/I_{3ph} = 3/(2 + X_0/X_1),$$

where X_0 , X_1 are the zero-sequence and positive-sequence reactances of the system upto the fault. When the neutral is solidly grounded, $X_0/X_1 \approx 2$, so that the single-phase fault gives 75 percent of the s-c current under a 3-phase fault.

Delayed Current Zero

When faults occur very close to large power stations, (greater than 1000 MVA) it is very difficult for s-c currents to pass through zero quickly because the line reactance is not present. This is a severe condition on the breaker on the h.v. side of the generator-transformer. However, the arc resistance usually contributes on an arcing fault to aid interruption.

For generator breakers, the s-c current is higher than on the h.v. side of transformers usually by one order of magnitude. In order to interrupt, say, 100 KA, air-blast breakers with a higher arc voltage are preferred to SF_6 breakers in order to bring about a current zero. Breakers with multiple interrupters are also used to further increase the arc resistance.

2. RECOVERY VOLTAGE

In addition to interrupting the s-c current, the breaker has to withstand the recovery voltage across its separated contacts. This voltage can have a single frequency or can contain multiple frequencies, depending on the connected network. For single-frequency circuit, it can be written as

$$V_R = \sqrt{2} V_k (\cos \omega t - \cos \omega_0 t),$$

where $\omega_0 = 2\pi f_0 = 2\pi \times$ natural frequency,
and k = constant that depends on the type of fault and the connected network characteristics.

Previously, an amplitude factor giving the ratio of peak value of V_R and the power-frequency voltage peak was used, but the recent I.E.C. recommendation covers only the peak value of the total recovery voltage including the h-f component or components.

The rate of rise of recovery voltage determines the ability of the quenching medium to interrupt the arc, since the rate of rise of dielectric strength must exceed this RRRV. This has given

rise to great controversy in Indian systems, where I.E.C. recommendations are considered too severe to be applied to Indian systems with longer lines and lower natural frequency. The initial rate of rise of transient recovery voltage (ITRV) has oscillations on it caused by the disconnection of lines, transformers, and generators, the number of confusion as to how this is to be determined. These oscillations depend further on the type of fault (1-phase, 2-phase, 3-phase, with and without earth) and the system configuration (solidly earthed, isolated, or earthed through impedances). All these have an effect on the power-frequency and transient component of the recovery voltage.

In so far as determining the characteristic recovery voltage, two types of faults are considered (i) the terminal fault, and (ii) the short-line fault.

Terminal Faults (TF)

These involve the maximum s-c currents, and as mentioned earlier, 3-phase terminal faults yield highest s-c currents and consequently the most severe recovery voltages.

In a 3-phase fault, if the circuit-breaker contacts have a time-delay in opening, the first pole to clear will have the highest recovery voltage. By the time the second pole clears the current, the power-frequency recovery voltage has increased in the first phase since the transient component has not yet decayed. For an unearthed 3-phase fault the first pole to clear may experience a peak recovery voltage of between 1.4 to 1.6 percent the phase voltage after interruption. On the other hand, for a 3-phase fault involving earth, it is $1.5 (\Delta_0 / \Delta_p / (1 + \Delta_0 / \Delta_p))$.

Short-Line Fault (SLF)

In this type of fault, there is a short circuit on a line (usually 1 to 2 Km) between the breaker and fault location. Reflections arriving on this line are superimposed on the source voltage giving rise to highest recovery voltages as shown in Figure 1. Here, the source-side voltage has nearly the same characteristics as for a terminal fault. In many breakers the interrupting capability and maximum breaking current are determined by this type of fault.

It can be shown that the highest rate of TRV in the case of the short-line fault occurs when the faulted phase is the last to clear on a single-phase to earth fault when all 3 poles are set to open. Time delays between opening of poles cannot be avoided if circuit breakers are poorly maintained.

The stresses in a circuit breaker can be reduced by connecting resistances or capacitances in parallel which reduce both the TRV and the peak value of transient voltage under very high s-c currents. Resistances are usually preferred for air blast breakers and capacitances for SF₆ breakers.

Definition of Recovery Voltage (Transient Component)

(a) 2-parameter definition

The transient recovery voltage used to be defined through 2 parameters: (i) the magnitude, and (ii) the rate of rise.

(b) 4-parameter definition

With large interconnections in a system, the 2-parameter definition has been superseded by the 4-parameter definition, which is shown in Figure 4. These are V_1 , V_p , t_1 , t_2 (or V_1/t_1). The initial time t_1 is usually equal to twice the travel time of the wave on the shortest connected line.

The capacitance of the grounding-grid system also helps in some measure to keep the initial rate of rise lower than when it is neglected.

The I.E.C. recommendations for type tests on these two types of faults are given below:

		<u>First Peak of V_R P.U.</u>		<u>dV/dt</u>	<u>Revision</u>
<u>Terminal Fault</u> <u>(TF)</u>	10% Current	1.95	or	5kV/ μ s	5.5-12.6kV/ μ s
		2.25			
	30%	1.95	or	5	5
		2.25			
	60%	1.95	or	2	3
		2.25			
	100%	1.82	or	1	2
		2.1			

	<u>First Peak of V_R P.U. dV/dt</u>		<u>Revision</u>
	100%...	1.82 or	1
	Asymmetry	2.1	2
<u>Single-phase</u>		1.95	2.5 and
		or	3.5
		2.25	
<u>Short-line Fault</u> (SLF)	60% current	0.64	6
	90% current	0.16	9

3. OVERVOLTAGES ON CLOSING OR RECLOSING

Overvoltages caused by switching operations might exceed the insulation level of lines and equipment and cause flashovers. Some measures taken to minimize these overvoltages include (a) insertion of series resistance at the source when switching, (b) surge arresters, (c) draining of trapped charge on line with inductive potential transformers, shunt compensating reactors, or power transformers, (d) closing the breaker poles at the instant when the source voltage is passing through the same polarity as the trapped charge.

Normally, the highest overvoltages occur when unloaded E.H.V. lines are energized or re-energized from an infinite source. The switching overvoltage consists of high-frequency transient component superimposed on the power-frequency voltage.

Consider a 3-phase generating station shown as the voltage V_S in series with a reactance X_S energizing a line of length 1, surge impedance $Z = \sqrt{L/C}$, where L and C are the distributed inductance and capacitance per unit length. For simplicity, ground-return effects are neglected.

The initial voltage on the line is zero when the circuit-breaker S is open while the final voltages due to Ferranti Effect will be

Entrance voltage : $V_R = V_S \cos a l / (\cos a l - \frac{X_S}{Z} \sin a l)$

Open-end voltage : $V_O = V_S / (\cos a l - \frac{X_S}{Z} \sin a l)$

Here, $a = 2\pi f \sqrt{LC}$, $\lambda =$ wave length at power frequency ($= 6000$ Km for 50 Hz). $a = 2\pi / \lambda$.

The ratio Z/X_S is defined as the short-circuit power P_{SC} of the supply to the system.

As an example, for a 2000 MVA 400 kV source with $X_S = 1$ p.u., energizing a 300 Km line with $Z=320$ ohms, $X_S = 400^2/2000 = 80$ ohms, and $Z/X_S = 4$. Also, $2\pi l/\lambda = \pi/10=18^\circ$. The Ferranti Effect gives $V_o = 1.14$ p.u. and $V_c = 1.09$ p.u. The surge-impedance loading is $SIL = 400^2/320 = 500$ MVA, and the short-circuit power is $P_{sc} = 4 \times 500$ MVA = 2000 MVA, which is equal to the source rating since $X_S = 1$ p.u.

When a line is initially energized, it has no trapped charge, but when it is reclosed after clearing a fault, the healthy phases retain a trapped charge. In practice, the overvoltage at the open end when closing on a trapped charge exceeds 3.5 p.u., while it is between 2 and 2.8 p.u. without trapped charge. However, during single-pole reclosure, trapped charge is not present since only the faulted phase is energized. In e.h.v. systems, trapped charge is very rarely present since shunt compensating reactors at both ends help to drain the trapped charge.

Further difficulties are encountered when the three poles do not close simultaneously. This time delay is about 5 ms even in breakers that are properly maintained. When the first breaker pole is closed, capacitive coupling places a voltage on the other two phases which corresponds to about 20% normal trapped charge due to mutual capacitance. The other poles now close on this trapped charge. Although non-synchronous closure appears to yield higher overvoltages than with simultaneous closure, in certain cases, other factors chiefly ground-return currents might actually keep the overvoltage down. Under synchronous closure, earth-return effects are not present, as has been verified from model studies by the author.

Interconnection of the system with more than one generating station yields lower switching-surge magnitudes; however, one must be prepared for the worst.

4. LIMITING OVERVOLTAGES

Overvoltages have been shown to consist of the power-frequency component and a h-f component. In order to limit the steady-state power-frequency component, shunt compensating reactors are used in e.h.v. systems at both ends of a long line. These also are beneficial from switching operations as has been mentioned earlier.

When no compensation is used, the ratio of far-end voltage to the entrance voltage is $V_o/V_e = 1/\cos \alpha l$. But with compensating reactors provided at both ends, and neglecting resistances, the two voltages are:

$$V_e = (\cos \alpha l + \frac{Z}{X_R} \sin \alpha l) V_o$$

$$V_o = V_s / [(1 + 2X_s/X_R) \cos \alpha l + (Z/X_R + ZX_s/X_R^2 - X_s/Z) \sin \alpha l]$$

The travelling-wave or transient component can be reduced by the following schemes:

Reduction of Transient or Travelling Wave Component

(a) When pre-insertion resistors are used, part of the total voltage appears across the resistor which reduces the voltage being fed to the line. The resistance is nearly equal to the surge impedance of line in most cases and is short-circuited or shunted by an auxiliary breaker after a pre-set time of nearly 1/2 cycle. However, the optimum time as well as the optimum value for this pre-insertion resistor must be ascertained from model studies on a Transient Network Analyzer or by Digital Computer calculation. The maximum value of switching surge overvoltage in this scheme occurs at the instant the series resistance is taken out of circuit by the auxiliary breaker.

The optimum value depends upon (i) line lengths, (ii) the series reactance behind the line, i.e., the short-circuit power of the source, (iii) the degree of line compensation, (iv) the insertion time of the resistor, and (v) the surge impedances of the switched line as well as any connected lines. Since the number of connected lines can change during the switching operations, a value higher than the optimum value is usually selected.

(b) The single-resistor scheme can be modified to two-stage or multi-stage closing resistors. This makes it possible to insert a higher resistance in the beginning and then lower this value in steps.

(c) Draining of trapped charge by shunt compensating reactors, and inductive p.t.'s. Transformer-terminated lines remove the trapped charge, but there are serious problems of resonances caused by the non-linearity of the magnetization characteristic when switching in. These have to be investigated in any particular situation.

(d) Reclosing circuit breaker on a line when trapped charge is present at the instant when the polarities of voltage on both sides of the breaker-contacts are the same. Such schemes reduce the overvoltages down to 1.5 p.u.

5. OVERVOLTAGES CAUSED BY INTERRUPTION OF LOW INDUCTIVE CURRENTS

These occur when a normal disconnection of an equipment is made. Overvoltages occur by premature reduction of current to zero when low inductive currents are interrupted. Certain types of breakers use the arc current to aid the flow of arc-extinction medium and therefore the interruption will not take place at low currents. Examples of low inductive currents are given below:

Transformer on no load .. : 2 to 5A

Reactor-loaded transformer: 400A

High-voltage reactors : 100 to 200A

The overvoltage magnitude is usually an interaction between the circuit breaker and the system.

Figure 5(a) shows a source-line-inductive load such as reactors, transformers, or motors. When the switch is opened, an arc is produced and when approaching current zero, it oscillates because of discharge of C_1 and C_2 through the line with a frequency $f_3 = \frac{1}{2\pi} [L(C_1 C_2 / C_1 + C_2)]^{-1/2}$, which is equivalent to C_1 and C_2 is series with L . The arc-quenching medium may blow the current out causing 'current chopping'.

The chopped current now flows through the load inductance L_2 . The stored energy is $(\frac{1}{2} i_a^2 L_2 + \frac{1}{2} V_a^2 C_2)$. It oscillates at the natural frequency $f_2 = \frac{1}{2\pi} (L_2 C_2)^{-1/2}$ which is usually 200 to 400 Hz for a transformer on no load and 1000 Hz for a shunt reactor.

Maximum voltage occurs when all this energy is stored in the capacitance C_2 .

$$V_{2\max}^2 C_2 = V_a^2 C_2 + L_2 i_a^2$$

$$\text{giving } V_{2\max} = [V_a^2 + i_a^2 \frac{L_2}{C_2}]^{\frac{1}{2}}$$

On the source side V_1 builds up with frequency $f_1 = \frac{1}{2\pi} (L_1 C_1)^{-1/2}$ which is between 1000 and 5000 Hz.

If i_a is relatively low, $V_a = \frac{\sqrt{2}}{\sqrt{3}} V_s$ and no overvoltage occurs. If the current is chopped at the peak value, $V_a = 0$, and $V_{2\max} = i_a \sqrt{L_2/C_2}$. With modern grain-oriented laminations in h.v. transformers, because of low saturation, overvoltage is reduced. When no-load current is chopped, the following average overvoltage factors may be expected.

	110kV	220kV	400kV	750kV
P.O.	3	2.5	1.8	1.2

Reactor-loaded transformers yield similar over-voltages. Isolation of shunt reactors with 100 to 200 A and having a surge impedance of 35K to 65K give an overvoltage factor below 2.5. The chopping current in most cases is 20A, maximum. Both surge arresters and series breaking resistors lower these voltages considerably.

6. INTERRUPTION OF CAPACITIVE CURRENTS

When lines are dropped or capacitor banks are switched off, overvoltages are generated. Consider Figure 6 where the line is represented by a lumped capacitance C_2 . Before interruption, $V_1 = V_2$. After the current is interrupted by the breaker, C_2 remains charged to $V_2 = V_s \sqrt{2/\sqrt{3}}$, the peak of the source voltage. However,

the source voltage V_1 changes its value on the power-frequency sine wave and some oscillation due to L_1, C_1 . The breaker voltage is consequently,

$$V_b = V_s \frac{\sqrt{2}}{\sqrt{3}} (1+k). \text{ Usually, } k \geq 1.$$

For $k=1$, the breaker voltage is twice the peak value of source voltage. If the insulating medium has not gained sufficient dielectric strength, the arc may restrike and connect the line back to the source. The phenomenon is just like energizing the line with a trapped charge equal but opposite to the source voltage. A current will therefore flow in the line through the breaker. The circuit is interrupted again at the peak value of voltage and the line holds a negative voltage. There might be renewed restrikes causing switch failures.

It is therefore evident that restrike-free breakers are essential. Modern SF_6 and air-blast breakers meet this requirement. Lines having shunt reactors cause lower frequencies of oscillation and they may aid in proper interruption. But here also restrike-free interruption is necessary.

Capacitor banks also cause the same stresses on the circuit breaker.

7. FERRO-RESONANCE OVERVOLTAGES

Partial resonance conditions occur in power systems when unbalances occur so as to place capacitances in series with inductances. Examples of this type are shown in Figure 7(a) where a 3-phase transformer is fed by a long cable from a substation. Under normal operating conditions, the cable capacitance to ground is energized by the phase voltage and the insulation will withstand this voltage. However, suppose one line is open such as occurs when a fuse blows or when circuit-breaker poles do not act synchronously but one pole makes much later than the other two. The equivalent circuit is shown in Figure 7(b) from which it may be noticed that the cable capacitance is in series with the transformer inductance in the open phase. If the cable is long and its capacitance

high, the resonance frequency may approach power frequency which gives rise to full resonance. The condition when two lines are open is shown in Figure 7(c).

On account of the high voltages, either the cable or the transformer or both may suffer damage to their insulation. In general, the magnetization curve of the transformer works on the non-linear portion so that a mathematical analysis presents difficulties. But either a series approximation to the B-H curve or a step-by-step graphical analysis is possible.

Experiments have shown that grounded-wye primary winding permits longer lengths of cable than any of the other possible connections such as delta or ungrounded -Y, because the three phases are essentially isolated from each other. Furthermore, working the transformer on the linear part of its B-H curve also is less dangerous than when the flux density is on the non-linear portion at the working voltage. Remedies such as switching a transformer with a 5 percent resistive load have also been suggested.

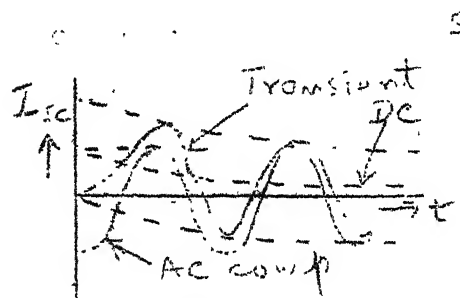


Fig. 2.

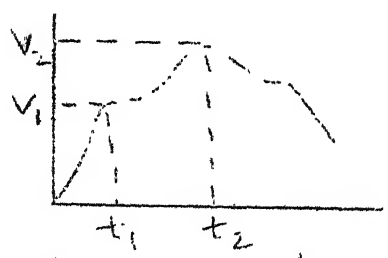
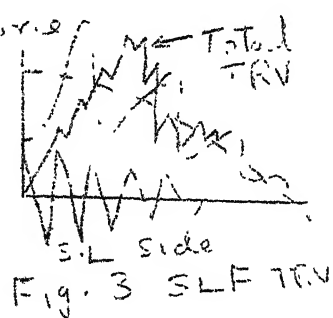
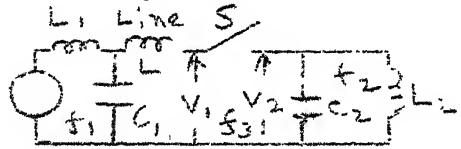


Fig. 4. 2 and 4 - Parameter Representation of TRV.

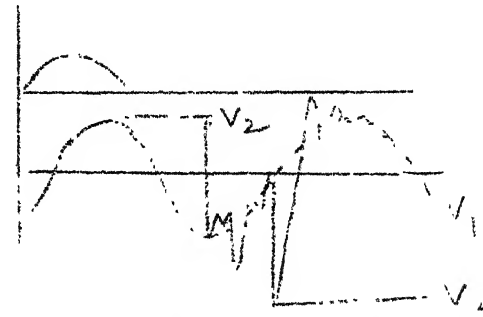
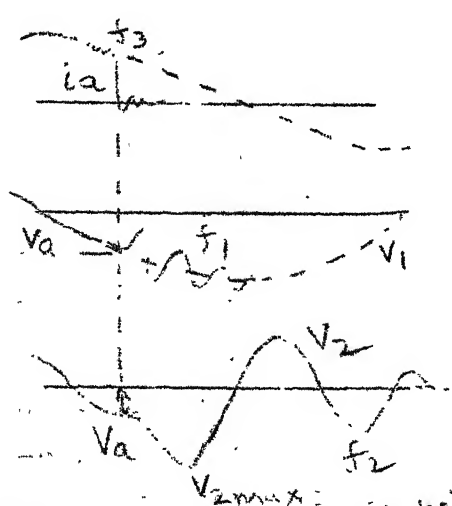


Fig. 6. Interruption of Cap. Curr.

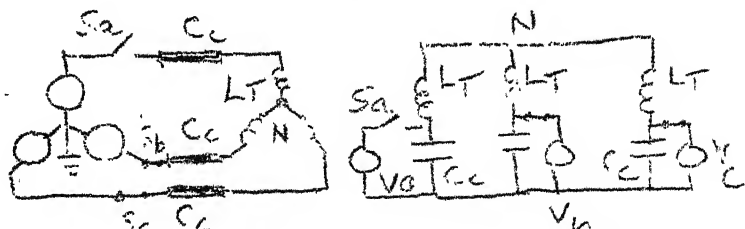


Fig. 7. Conditions for Ferro-Resonance

LINE-PARAMETER CALCULATIONS WITH GROUND

This chapter will cover the following topics :

1. Calculation of conductor resistance with skin effect
2. Line I^2R losses and temperature rise of conductors
3. Properties of bundled conductors
4. Inductance calculation with ground
5. Capacitance calculation with ground
6. Resolution into sequence quantities
7. Modes of propagation on 3-phase lines
8. Ground-return resistance
9. Ground-return inductance
10. Maximum surface-voltage gradient on conductors and corona-inception gradient.

Section 1: Resistance of Conductors and Skin Effect

Conductors used for e.h.v. lines are usually ACSR but with high tensile strength aluminium available, ACAR is becoming increasingly common. The space occupied by steel in ACSR is taken by aluminium in ACAR. When steel is used, due to the high permeability and inductance, no current will flow in it. In ACAR, current flows in the entire metal and more current can be used.

If n_s = no. of strands of Al, d_s = dia of each strand, and ρ_a = specific resistance of Al, the resistance per kilometre will be

$$R = \rho_a \cdot 1.05 \times 10^3 \times \frac{4}{\pi} \times \frac{1}{d_s^2} \times \frac{1}{n_s} = 1333 \rho_a / (d_s^2 n_s), \text{ ohm}.$$

The factor 1.05 accounts for the twist or lay which increase the length of the strand by 5%.

Tables I, II, III provide some relevant data.

Example 1: A Drake conductor 1.108" dia has Al sectional area of 795,000 circular mils. Stranding is 26 Al/7Fe. Its resistance is given as 0.0215 ohm/1000' at 20°C under DC, and 0.1284 ohm/mile at 50°C at 50/60Hz.

1) Take $\rho_a = 2.7 \times 10^{-8}$ ohm-m at 20°C and temperature-resistance coefficient = $4.46 \times 10^{-3}/^\circ\text{C}$; check the values of resistance given.

2) Find % increase in resistance due to skin effect.

Solution : We assume that steel strands do not carry current. Then, for 1000 feet of conductor, strand length is $1.05 \times 1000 / 3.28$ metres.

To convert circular mils to square metres:

$$1 \text{ inch} = 1000 \text{ mils, } 10^6 \text{ circular mils} = \frac{\pi}{4} \text{ sq. in.}$$

$$\therefore 0.79 \times 10^6 \text{ cir-mil} = 0.795 \times \frac{\pi}{4} \times 25.4^2 \times 10^{-6} \text{ m}^2 \\ = 402.83 \times 10^{-6} \text{ m}^2$$

$$1) R_{dc} = 2.7 \times 10^{-8} \times \frac{1.05 \times 1000}{3.28} \times \frac{10^6}{402.83} = 0.02146 \text{ ohm.}$$

$$2) \text{ At } 50^\circ\text{C, } f_{a50} = \frac{1 + 4.46 \times 10^{-3} \times 50}{1 + 4.46 \times 10^{-3} \times 20} = 1.123 \quad 20$$

$$\therefore R_{50} = 5.28 \times 1.123 \times 0.0215 = 0.1275 \text{ ohm at DC}$$

$$\% \text{ increase due to skin effect} = \frac{0.1284 - 0.1275}{0.1275} \times 100 = 0.71\%$$

This is less than 1%. We have assumed that all strands carry current equally.

Resistance of conductor manifests itself in e.h.v. lines in the following forms:

(1) Power-loss; (2) Reduced current-carrying capacity of conductor in high ambient-temperature regions. This is particularly severe in North India in summer when the temperature reaches 50°C in the plains.

3) Conductor resistance governs the attenuation of travelling waves due to lighting and switching, as well as radio-frequency waves generated by corona. For lighting, the resistance is computed at 100-KHz, for switching from 200-2000 Hz, and for radio interference from 0.5 MHz to 10 MHz.

Skin Effect in Round Conductors

The increase in resistance in stranded conductors due to skin effect is analytically difficult to determine. It is easier to do this at the manufacturer's plant by a simple experiment. For round conductors, analytical formulas are available using Bessel Functions.

The ratio $R_{ac}(f)/R_{dc}$ has been tabulated or given in graphical form by the N.B.S., Washington. The controlling parameter is $x = \frac{\pi}{2} \sqrt{f/R_0} = 0.0636\sqrt{f/R_0}$, with R_0 = d.c. resistance of conductor in ohm/mile. The expression for the resistance ratio is as follows:

$$\text{Let } B_{er}(x) = 1 - \frac{x^4}{2^2 \cdot 4^2} + \frac{x^8}{2^2 \cdot 4^2 \cdot 6^2 \cdot 8^2} - \dots$$

$$B_{ei}(x) = \frac{x^2}{2^2} - \frac{x^6}{2^2 \cdot 4^2 \cdot 6^2} + \frac{x^{10}}{2^2 \cdot 4^2 \cdot 6^2 \cdot 8^2 \cdot 10^2} - \dots$$

$$B_{er}'(x) = \frac{d}{dx} [B_{er}(x)]; B_{ei}'(x) = \frac{d}{dx} [B_{ei}(x)]$$

$$\text{Then, } \frac{R_{ac}(f)}{R_{dc}} = \left(\frac{x}{2}\right) \frac{B_{er}(x) \cdot B_{ei}'(x) - B_{ei}(x) \cdot B_{er}'(x)}{[B_{er}(x)]^2 + [B_{ei}'(x)]^2}$$

When using S.I. units, $x = 1.59 \times 10^{-3} \sqrt{f/R_{dc}}$, $R_{dc} = R_0/1610$, ohm/m.

Example: A round-copper conductor 0.5" dia (7/0, 12.7 mm dia) has $f_c = 1.7 \times 10^{-8}$ ohm-m at 20°C. Calculate R_{ac}/R_{dc} as a function of frequency from 100 Hz to 10^5 Hz on a logarithmic base.

$$\text{Solution: } R_0 = 1.7 \times 10^{-8} \frac{1.609 \times 10^3}{\frac{\pi}{4} \times 12.7^2 \times 10^{-6}} = 0.216 \text{ ohm/mile}$$

$$\sqrt{R_0} = 0.465, 0.0636/\sqrt{R_0} = 0.0137$$

$f \rightarrow$	100	300	600	1000	3000	6000	10^4
$x = 0.0137\sqrt{f}$	0.137	0.237	0.335	0.4325	0.749	1.06	1.37
R_{ac}/R_{dc}	$1 + .37 \times 10^{-5}$	$1 + .4 \times 10^{-4}$	$1 + .3 \times 10^{-4}$	$1 + .8 \times 10^{-3}$	1.0017	1.0066	1.0182
			3×10^4	6×10^4	10^5		
			2.37	3.35	4.326		
			1.148	1.35	1.8		

(The increase in resistance is not as much as what is felt to be the case by engineers working with electrical machine slots!)

Section 2 : I^2R Heating Loss and Temperature Rise

The combination of solar irradiation and I^2R heating in summer raises the conductor temperature beyond the maximum of 65°C allowed

(Internal heat developed by I^2R + External heat due to solar irradiation) = Heat lost by (convection to environmental air + radiation). Let W_i , W_s , W_c , and W_r denote these four quantities per metre.

- 1) I^2R heating : $W_i = I^2 R_m$, watts/metre of conductor where R_m = resistance per metre at maximum temperature.
- 2) Solar Irradiation : $W_s = d_m \cdot s_a \cdot I_s$, per metre
 where d_m = diameter of conductor, metre,
 s_a = solar absorption coefficient,
 and I_s = solar irradiation intensity, W/m^2 .

The maximum solar irradiation intensity is in the neighbourhood of $1-1.5 \text{ KW/m}^2$ in July at Delhi at noon time.

The solar absorption coefficient $s_a = 1$ for well-weathered old conductor and 0.6 for new conductor.

- 3) Convection loss, W_c :

$W_c = 5.73 \sqrt{p \cdot v_m / d_m} \cdot \Delta t$, watts/ m^2 of conductor. 1 metre-length of conductor has an area of $(\pi d_m) \text{ sq.m.}$

∴ Per metre length, the convection loss is

$$W_c = 18 \sqrt{p \cdot v_m \cdot d_m} \cdot \Delta t, \text{ watts/m.}$$

Here, p = atmospheric pressure in atmospheres

v_m = velocity of air in m/s

and Δt = temperature rise of conductor above the ambient temperature in $^{\circ}\text{C}$.

- 4) Radiation loss, W_r :

This is given by Stefan-Boltzmann equation

$$w_r = 5.702 \times 10^{-8} \cdot e (T^4 - T_a^4), \text{ watts/m}^2,$$

where e = relative emissivity of conductor surface

= 1 for black body, 0.5 for oxidized Al or Cu.

T = conductor temperature in $^{\circ}\text{K}$,

and T_a = ambient temperature in $^{\circ}\text{K}$.

The radiation loss per metre length of conductor is ..

$$W_r = \pi d_m w_r = 17.9 \times 10^{-8} e (T^4 - T_a^4) d_m, \text{ watts/m.}$$

The heat balance equation now becomes

$$I^2 R_m + d_m \cdot s_a \cdot I_s = 18 \cdot \Delta t \cdot \sqrt{p \cdot v_m \cdot d_m} + 17.9 \times 10^{-8} \cdot d_m (T_f^4 - T_a^4)$$

Example 2 : A 400-kV line in India uses a 2-bundle 'Moose' conductor 0.0318 m dia each. Take $T_a = 40^\circ\text{C}$ and neglect solar irradiation, $p = 1$, $v_m = 1$ m/s, $\alpha = 0.5$, load current = 1000 A/phase (500A/conductor). Area of each conductor 515.7 mm^2 , $\rho_a = 2.7 \times 10^{-8}$ ohm-m at 20°C . Calculate the final temperature of conductor.

Solution : Assume final temperature to be t_f .

$$R_m = 2.7 \times 10^{-8} \frac{1 + 0.0045 t_f}{1 + 0.0045 \times 20} \frac{1}{515.7 \times 10^{-6}} = 0.48 \times 10^{-4} (1 + 0.0045 t_f)$$

$\therefore I^2 R_m = 12 (1 + 0.0045 t_f)$ per metre of each conductor at $I = 500\text{A}$

$$W_c = 18 \sqrt{1 \times 0.0318} (t_f - 40) = 3.21 (t_f - 40)$$

$$\begin{aligned} W_r &= 17.9 \times 0.5 \times 0.0318 (T_f/100)^4 - 3.13^4 \\ &= 2.845 \times 10^{-1} [(273 + t_f)^4 / 10^8 - 95.95] \end{aligned}$$

The equation for t_f turns out to be

$$12(1 + 0.0045 t_f) = 3.21 t_f - 128.4 + 2.845 (273 + t_f)^4 \times 10^{-9} - 27.3$$

$$\text{or } (273 + t_f)^4 = (589.5 - 11.28 t_f) 10^8$$

A trial and error solution gives $t_f = 44^\circ$, [$I^2 R_m = 14.38$, $W_c = 12.84$, $W_r = 1.44$ for $t_f = 44$]

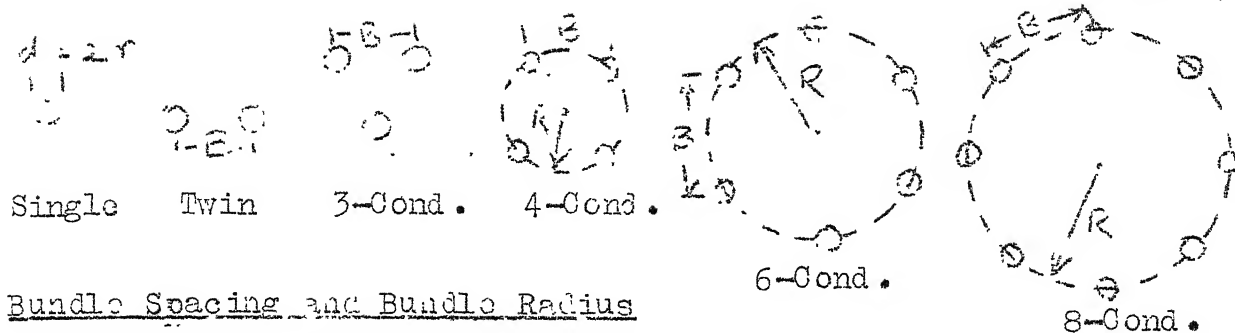
Note: At 40°C , taking solar irradiation contribution to add 10 watts/m, $t_f = 45.5^\circ\text{C}$.

With solar irradiation of 1.16 Kw/m^2 , the contribution is 37 watts/m. $t_f = 54.1^\circ\text{C}$. $\Delta t = 14^\circ$.

[To convert Kw/m^2 to cal/sq.cm./day : $10^4 \text{ cal/sq.cm./day} = 4.86 \text{ Kw/m}^2$].

Section 3 : Some Properties of Bundled Conductors

Bundled conductors are exclusively used for e.h.v. lines, (only one line in the world, that of B.P.A. in U.S.A has used expanded ACSR conductor of 2.5 inch dia for the 525 kV line). Upto now, 18 sub-conductors have been used. Figure 1 shows some of the details that will be used.



Bundle Spacing and Bundle Radius

Normally, the N sub-conductors of a bundle are distributed uniformly on a circle of radius R with spacing B between adjacent sub-conductors. We will call B = bundle spacing and R = bundle radius. The relation is $B/2 = R \sin(\pi/N)$, giving $R = B/2 \sin(\pi/N)$. For $N = 2$ to 18 we therefore have the following relations.

N	2	3	4	6	8	12	18
B/R	2	$\sqrt{3}$	$\sqrt{2}$	1	.7654	.5344	.3472
R/B	.5	.578	.7071	1	1.308	1.874	2.884

Geometric Mean Radius or Equivalent Radius of Bundle

For most important calculations, the bundle of N sub-conductors can be replaced by a single conductor having the equivalent radius $r_{eq} = (N \cdot r \cdot R^{N-1})^{1/N} = r [N \cdot (R/r)^{N-1}]^{1/N} = R(N r/R)^{1/N}$. It is the N -th root of the product of the sub-conductor radius and the distances of this sub-conductor from all the other $(N-1)$ companions in the bundle. These will be

$$r \cdot (2R \sin \frac{\pi}{N}) \cdot (2R \sin \frac{2\pi}{N}) \cdot (2R \sin \frac{3\pi}{N}) \cdot \dots \cdot (2R \sin \frac{N-1}{N} \pi)$$

$$= r \cdot (2R)^{N-1} \cdot (\sin \frac{\pi}{N}) \cdot \dots \cdot (\sin \frac{N-1}{N} \pi) = r_{eq}^N.$$

$$\text{For } N = 2 : r_{eq} = (2 r R)^{1/2}$$

$$N = 3 : r_{eq} = (2^2 R^2 r \sin \frac{\pi}{3} \sin \frac{2\pi}{3})^{1/3} = (3 r R^2)^{1/3}$$

$$N = 4 : r_{eq} = (2^3 R^3 r \sin \frac{\pi}{4} \sin \frac{2\pi}{4} \sin \frac{3\pi}{4})^{1/4} = (4 r R^3)^{1/4}$$

$$\text{The general formula is } r_{eq} = (N r R^{N-1})^{1/N}.$$

Examples : For the 400-kV lines in India, $r = 0.0318$ m, $B = 0.45$ m, $N = 2$. Calculate R and r_{eq} .

Solution : $R = B/2 = 0.225 \text{ m}$. $r_{eq} = (2 \times 0.0318 \times 0.225)^{1/2} = 0.0846 \text{ m}$.

Also, $r_{eq} = \sqrt{r \cdot B} = \sqrt{0.0159 \times 0.45} = 0.0846 \text{ m}$.

For 1200 kV line, $N=8$, $d = 4.6 \text{ cm}$, $R = 0.6 \text{ m}$.

$$r_{eq} = R (N r/R)^{1/N} = 0.6 (8 \cdot 0.023/0.6)^{1/8} = 0.5176 \text{ m}.$$

$$B = .7654 R = 0.46 \text{ m} = 46 \text{ cm}.$$

The equivalent radius is useful for calculation of (a) line charge, (b) inductance, (c) capacitance, and several other line parameters.

Note: The total resistance of an N -conductor bundle = $(1/N)$ times the resistance of each sub-conductor.

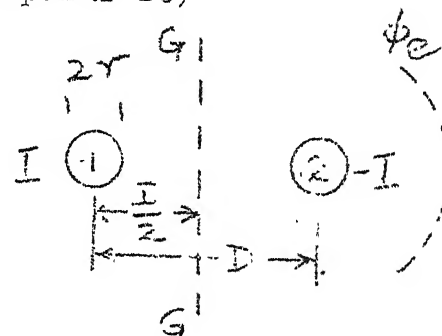
Section 5: Inductance of EHV Lines

Round Conductor

- 1) Inductance due to internal flux : $L_i = \mu_0/8\pi = 0.5 \times 10^{-7} \text{ H/metre}$
- 2) External flux linkage upto distance x : $L_e = \frac{\mu_0}{2\pi} \ln(x/r), \text{H/m}$
 $= 2 \times 10^{-7} \ln(x/r).$

Two-conductor Line (Single Phase or Bipolar DC)

The currents are I and $-I$.
 Consequently, any flux line beyond the conductors such as line ϕ_c will link zero current. Therefore all flux lines must pass between the two conductors. The flux linkage of conductor 1 has two parts : (i) due to its own current, and (ii) due to current in conductor 2.



Flux linkage due to own current I will be

$$\Psi_{11} = \int_r^{D-r} d\Psi_{11} = \frac{I\mu_0}{2\pi} \int_r^{D-r} \frac{1}{x} dx = \frac{I\mu_0}{2\pi} \ln \frac{D-r}{r}$$

Fleming's rule shows that in the space between the conductors, the fluxes produced by I and $-I$ are in the same direction. Therefore, flux linkage of conductor 1 due to current in conductor 2 will be

$$\Psi_{12} = \int_r^{D-r} d\Psi_{12} = \frac{\mu_0 I}{2\pi} \ln \frac{D-r}{r}.$$

∴ Total flux linkage of conductor 1 is

$$\Psi_1 = \Psi_{11} + \Psi_{12} = \frac{I\mu_0}{\pi} \ln \frac{D-r}{r} \approx \frac{I\mu_0}{\pi} \ln \frac{D}{r}, \quad D \gg r$$

Inductance is $L_1 = \Psi_1 / I = \frac{\mu_0}{\pi} \ln \frac{D}{r}$, H/m of conductor 1.

The mid-plane G-G between conductors is a flux line. Therefore, the inductance of any one of the conductors upto G-G will be one half of L_1 . If $D = 2H$, and turning the figure around by 90° , we obtain the configuration of a single conductor above ground.

$$\therefore L = \frac{\mu_0}{2\pi} \ln \frac{D}{r} = \frac{\mu_0}{2\pi} \ln \frac{2H}{r} = 2 \times 10^{-7} \ln \frac{2H}{r}, \text{ Henry/m.}$$

Combining this with inductance due to internal flux linkage gives

$$L_c = 0.5 \times 10^{-7} + 2 \times 10^{-7} \ln \frac{2H}{r} = 2 \times 10^{-7} \left(\frac{1}{4} + \ln \frac{2H}{r} \right), \text{ H/m}$$

For the very large values of H encountered in e.h.v. lines, internal flux linkage can be omitted.

Example : For a 345-kV line, the single ACSR conductor has 1.762 inch dia. For purposes of calculation, use $r = 0.0586$ ft (0.0179 m). Calculate inductance per metre length and % error in neglecting internal flux linkage. $H = 12$ m (40 feet).

Solution $L = 0.05 \mu\text{H/m}$

$$L = 0.2 \ln (24/0.0179) = 0.2 \ln 1341 = 1.44 \mu\text{H/m.}$$

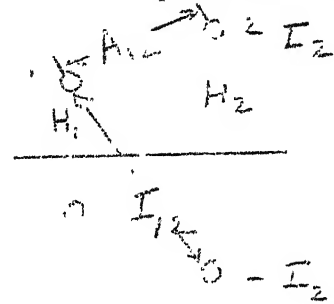
$$\% \text{ error} = 0.05 \times 100/1.44 = 3.5\%$$

Maxwell's Coefficients :

Considering $\Psi_{11} = \frac{\mu_0}{2\pi} I \ln (2H/r)$, the term $\ln(2H/r)$ is called Maxwell's coefficient. Sometimes it may also be written as $\frac{\mu_0}{2\pi} \ln (2H/r)$, but in this lecture it will be $\ln(2H/r)$ which will also occur in capacitance calculation. [Note: For all calculations the average height to be used is $H = \text{minimum height} + \text{Sag}/3$].

When several conductors (phases or poles) are present above ground, each carrying its own current, we can replace ground plane by image conductors carrying currents in opposite directions but of the same value.

Consider flux linkage of conductor 1. Self flux linkage is $\psi_{11} = \frac{\mu_0 I_1}{2\pi} \ln \left(\frac{2H_1}{r} \right)$.



Due to current in conductor 2 :

Current in conductor 2 produces flux in all space. But only the flux flowing beyond A_{12} will link conductor 1. Similarly, due to current $-I_2$ in the image of conductor 2, only the flux flowing beyond I_{12} will link conductor 1.

$$\therefore \psi_{12} = \frac{I_2 \mu_0}{2\pi} \int_{A_{12}}^{\infty} \frac{1}{x} dx + \frac{(-I_2) \mu_0}{2\pi} \int_{I_{12}}^{\infty} \frac{1}{x} dx = \frac{\mu_0}{2\pi} I_2 \cdot \ln \frac{I_{12}}{A_{12}}$$

The mutual Maxwell's coefficient is then $\ln(I_{12}/A_{12})$. In general, between conductors i and j , the mutual coefficient will be $P_{ij} = \ln(I_{ij}/A_{ij})$, $i \neq j$.

For a system of n conductors

$$[\psi]_n = \frac{\mu_0}{2\pi} [P]_{nn} [I]_n = [L]_{nn} [I]_n$$

where $[\psi]_n = [\psi_1, \psi_2, \dots, \psi_n]$ and $[I]_n = [I_1, I_2, \dots, I_n]$.

The elements of Maxwell's Potential Coefficient Matrix are

$$P_{ii} = \ln(2H_i/r_{eq}), \text{ and } P_{ij} = \ln(I_{ij}/A_{ij}).$$

For a bundled conductor, neglecting internal flux linkages, the radius to be used is the geometric mean radius or the equivalent radius $r_{eq} = R(N \cdot r/R)^{1/N}$.

Example:- The dimensions of 400-kV 3-phase horizontal line are : $H = 15$ m, $S = 11$ m between phases, conductor 2-x 3.18 cm, $B = 0.4572$ m (18"). Calculate (a) inductance matrix per Km, considering no transposition. (b) same for fully-transposed line (c) positive-sequence reactance per Km at 50 Hz.

Solution: $r_{eq} = \sqrt{r \cdot B} = 8.53 \text{ cm} = 0.0853 \text{ in.}$ * -11 * -11 - *

$$P_{11} = P_{22} = P_{33} = \ln(30/0.085) = 5.9$$

$$P_{12} = P_{23} = \ln \sqrt{(4H^2 + S^2)/S^2} = 1.0664$$

$$P_{13} = \ln \sqrt{(H^2 + S^2)/S^2} = 0.53$$

$$(a) [L]_{ut} = 0.2 \begin{bmatrix} 5.9 & 1.0664 & 0.53 \\ 1.0664 & 5.9 & 1.0664 \\ 0.53 & 1.0664 & 5.9 \end{bmatrix} \begin{matrix} \mu\text{H/m} \\ \text{mH/Km} \end{matrix} = \begin{bmatrix} 1.18 & 0.213 & 0.106 \\ 0.213 & 1.18 & 0.213 \\ 0.106 & 0.213 & 1.18 \end{bmatrix}$$

$$(b) L_m = \frac{1}{3} (0.213 + 0.213 + 0.106) = 0.177$$

$$[L]_t = \begin{bmatrix} 1.18 & 0.177 & 0.177 \\ & 1.18 & 0.177 \\ & & 1.18 \end{bmatrix} \text{ mH/Km}$$

$$(c) L_+ = L_s - L_m = 1.18 - 0.177 = 1 \text{ mH/Km.}$$

$$\text{At } 50 \text{ Hz, } X_+ = 0.314 \text{ ohm/Km.}$$

Note that self inductance of e.h.v. lines is in the neighbourhood of 1 mH/Km. In general, as the number of sub-conductors is increased, self inductance and positive-sequence inductance reduce so that the series reactance will reduce also. The power-handling capacity will therefore increase.

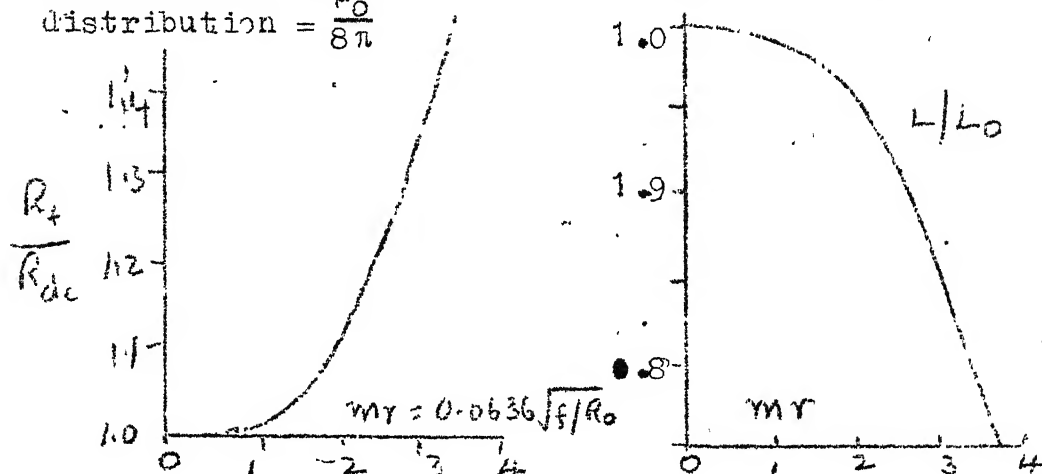
Inductance of Round Conductor with Skin Effect

Resistance increases with skin effect (frequency) but the inductance due to internal flux linkage decreases. This may not be serious for e.h.v. lines where the internal flux linkage is neglected. This inductive reactance at any frequency is

$$X_i = \left(\frac{X}{2} R_o \right) \frac{B_{er}(x) \cdot B_{er}'(x) + B_{oi}(x) \cdot B_{oi}'(x)}{[B_{er}'(x)]^2 + [B_{oi}'(x)]^2}$$

where $x = 0.0636 \sqrt{f/R_o}$, R_o = d.c. resistance, ohm/mile.

In general, the resistance and inductance variations are as depicted in Figure. L_0 = inductance assuming uniform current distribution = $\frac{\mu_0}{8\pi}$



[Please see Westinghouse T and D Reference Book Ch. 2, for actual values].

Section 6 : Line Capacitance Calculation

Let p.d. between conductors = 2V.

Place a unit positive test charge at P.

Then the electric field at P is

$$E_P = \frac{q}{2\pi\epsilon_0} \left(\frac{1}{x} + \frac{1}{2H-x} \right)$$

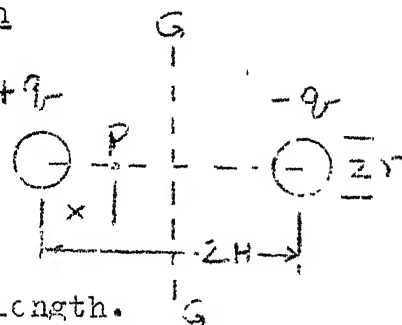
where q = charge on conductors per unit length.

$$\begin{aligned} \text{Consequently, } 2V &= \frac{q}{2\pi\epsilon_0} \int_r^{2H-r} \left(\frac{1}{x} + \frac{1}{2H-x} \right) dx = \frac{q}{\pi\epsilon_0} \ln \frac{2H-r}{r} \\ &\approx \frac{q}{\pi\epsilon_0} \ln(2H/r) \end{aligned}$$

By symmetry, the mid-plane G-G will be at V. The p.d. between positive conductor and ground plane GG (by rotating the figure by 90°) will be $V_g = V$.

$$\therefore V_g = \frac{q}{2\pi\epsilon_0} \ln \frac{2H}{r} = \frac{q}{2\pi\epsilon_0} \ln \left[\frac{\text{Dist of cond. surface from negative charge}}{\text{Dist of cond. surface from positive charge}} \right]$$

Once again, $\ln \frac{2H}{r}$ = Maxwell's potential coefficient P_{11} .



Mutual Potential Coefficients

Potential at location of conductor 1 due to the charges $+q_2$ and $-q_2$ is

$$V_{12} = \frac{q_2}{2\pi\epsilon_0} \ln \frac{\text{Dist. from } -q_2}{\text{Dist. from } +q_2} = \frac{q_2}{2\pi\epsilon_0} \ln \frac{I_{12}}{A_{12}}$$

$$\therefore P_{12} = \ln(I_{12}/A_{12}).$$

For a system of n conductors, the potentials of the conductors will be

$$V_1 = \frac{q_1}{2\pi\epsilon_0} \ln(2H_1/r_{eq}) + \frac{q_2}{2\pi\epsilon_0} \ln(I_{12}/A_{12}) + \dots + \frac{q_n}{2\pi\epsilon_0} \ln(I_{1n}/A_{1n})$$

$$V_n = \frac{q_1}{2\pi\epsilon_0} \ln(I_{1n}/A_{1n}) + \frac{q_2}{2\pi\epsilon_0} \ln(I_{2n}/A_{2n}) + \dots + \frac{q_n}{2\pi\epsilon_0} \ln(2H_n/r_{eq})$$

In matrix form, $[V]_n = [P]_{nn} [q/2\pi\epsilon_0]_n$

$[V]_n = [V_1, V_2, \dots, V_n]$, $[q] = [q_1, q_2, \dots, q_n]$ and elements of potential coefficient matrix are as before

$$P_{ii} = \ln(2H_i/r_{eq}), P_{ij} = \ln(I_{ij}/A_{ij}), i \neq j.$$

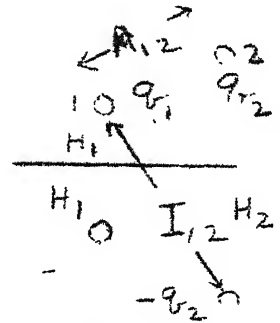
The capacitance matrix is $[C] = 2\pi\epsilon_0 [P]_{nn}^{-1} = 2\pi\epsilon_0 [M]_{nn}$.

We derived the inductance matrix to be

$[L]_{nn} = \frac{\mu_0}{2\pi} [P]$. If internal flux linkages are ignored, we observe that $[L][C] = \mu_0 \epsilon_0 [U] = \frac{1}{c^2} [U]$ where $[U]$ = unit matrix and c = velocity of light. Calculations based on this relation are called 'Light-velocity theory calculations'. The charges q_1 to q_n refer to the total charge of the entire bundle and not of each sub-conductor of the bundle.

Example: For the untransposed 400-kV line, Maxwell's Potential coefficient matrix was

$$[P]_{ut} = \begin{bmatrix} 5.9 & 1.066 & 0.53 \\ & 5.9 & 1.066 \\ & & 5.9 \end{bmatrix} \therefore [M] = [P]^{-1} = \begin{bmatrix} -0.176 & -0.03 & -0.01 \\ -0.03 & 0.180 & -0.03 \\ -0.01 & -0.03 & 0.176 \end{bmatrix}$$



The capacitance matrix is

$$[C] = 2\pi\epsilon_0[M] = \begin{bmatrix} 9.77 & 1.65 & 0.58 \\ -1.65 & 10.02 & -1.65 \\ -0.58 & -1.65 & 9.77 \end{bmatrix} \text{ nF/Km}$$

[Note: $2\pi\epsilon_0 = 10^{-9}/18$]

For a completely transposed line,

$$C_s = \frac{1}{3} (9.77 + 10.02 + 9.77) = 9.85 \text{ nF/Km}, \quad C_m = \frac{-1}{3} (1.65 + 1.65 + 0.58) = -1.29 \text{ nF/Km}.$$

Positive-sequence capacitance $C_+ = C_s - C_m = 11.14 \text{ nF/Km}$. We note that positive-sequence capacitance of e.h.v. lines is in the neighbourhoods of 10-11 nF/Km. With $L_+ \approx 1 \text{ mH/Km}$, the velocity of propagation using positive-sequence quantities is also light velocity. Also, 1) self-capacitances are all positive while mutual capacitances are all negative. This is because a charge of one polarity placed on one conductor induces a charge of opposite polarity on another conductor.

2) the centre phase has higher capacitance to ground than the outer phases, even though the potential coefficients are equal.

Section 7 : Sequence Inductances and Capacitances

This applies only to transposed lines. The mutually interacting inductances and capacitances can be resolved into independent sequence quantities. However, the real meaning of sequence inductances and capacitances is the flux linkage and charge which sequence currents and voltages experience.

Zero Sequence : Here $[I]_0 = [1, 1, 1] I_0$, and $[V]_0 = [1, 1, 1] V_0$

$$[\Psi]_0 = \begin{bmatrix} L_s & L_m & L_m \\ L_m & L_s & L_m \\ L_m & L_m & L_s \end{bmatrix} \begin{bmatrix} 1 \\ 1 \\ 1 \end{bmatrix} I_0 = \begin{bmatrix} 1 \\ 1 \\ 1 \end{bmatrix} (L_s + 2L_m) I_0.$$

The zero-sequence inductance is $L_0 = L_s + 2L_m$.

Positive sequence : $I_1 = I_m \sin \omega t$, $I_2 = I_m \sin (\omega t - 120^\circ)$,
 $I_3 = I_m \sin (\omega t + 120^\circ)$

$$[\Psi_1] = \begin{bmatrix} L_s & L_m & L_m \\ L_m & L_s & L_m \\ L_m & L_m & L_s \end{bmatrix} \begin{bmatrix} \sin \omega t \\ \sin(\omega t - 120^\circ) \\ \sin(\omega t + 120^\circ) \end{bmatrix} \quad I_m = (L_s - L_m) \quad \begin{matrix} \sin \omega t \\ \sin(\omega t - 120^\circ) \\ \sin(\omega t + 120^\circ) \end{matrix}$$

$$\therefore L_1 = L_s - L_m$$

Negative sequence : $L_2 = L_s - L_m$.

Capacitance : The sequence voltages are

$$[V_0] = [1, 1, 1]V, [V_1] = [\sin \omega t, \sin (\omega t - 120^\circ), \sin(\omega t + 120^\circ)]V.$$

$$\text{Using the relation } [q] = 2\pi\epsilon_0 [P]^{-1} [V] = [C][V] = \begin{bmatrix} C_s & C_m & C_m \\ C_m & C_s & C_m \\ C_m & C_m & C_s \end{bmatrix} [V]$$

we obtain, $C_0 = C_s + 2C_m$, $C_1 = C_s - C_m$, $C_2 = C_s - C_m$.

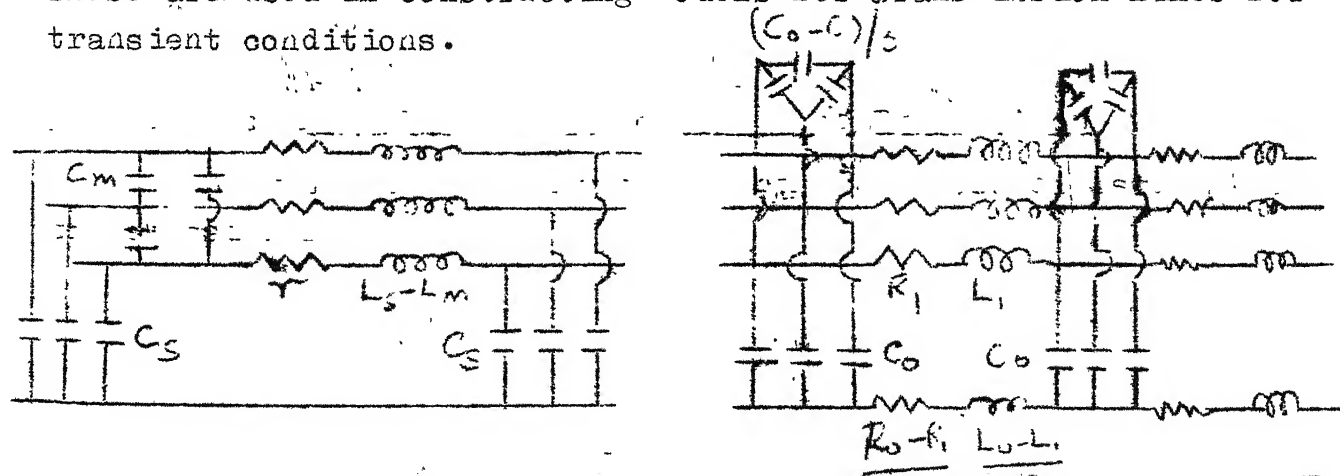
The following properties may be noted:

1. The zero-sequence-inductance is higher than the self-inductance L_s , while L_1 and L_2 are less than L_s .
2. The converse is true for capacitance. Since C_m is a negative quantity, $C_0 < C_s$ while C_1 and C_2 are $> C_s$.
3. In terms of the sequence quantities, the self and mutual quantities are :

$$L_s = \frac{1}{3} (L_0 + 2L_1), \quad L_m = \frac{1}{3} (L_0 - L_1),$$

$$C_s = \frac{1}{3} (C_0 + 2C_1), \quad C_m = \frac{1}{3} (C_0 - C_1)$$

These are used in constructing models for transmission lines for transient conditions.



Section 8 : Line Parameters for Modes of Propagation

When switching or other transient operations are being studied on transmission lines, it is a difficult matter to investigate wave propagation on conductors which are characterized by (a) velocity of propagation, (b) attenuation, and (c) surge impedance, when mutual interaction between the multi-conductors is present. The waves must be de-coupled on transposed as well as untransposed lines. This concept was first applied, following the idea of symmetrical components of Fortescue by G.E. Adams for radio-interference studies. For the fully-transposed line, analytical expressions in closed form for the transformation matrices can be worked out. But an untransposed line can only be handled on numerical basis when all inductances and capacitances are known.

Diagonalization Procedure

The diagonalization procedure will be illustrated through the inductance matrix of a transposed line,

$$[L] = \begin{bmatrix} L_s & L_m & L_m \\ L_m & L_s & L_m \\ L_m & L_m & L_s \end{bmatrix}$$

Step 1 : Evaluate the 'characteristic roots' or eigenvalues from the determinantal equation $|\lambda[U] - [L]| = 0$.

This gives $\begin{vmatrix} \lambda - L_s & -L_m & -L_m \\ -L_m & \lambda - L_s & -L_m \\ -L_m & -L_m & \lambda - L_s \end{vmatrix} = 0$ giving $\lambda_1 = L_s + 2L_m, \lambda_2 = \lambda_3 = L_s - L_m$.

Step 2 : For each of these eigenvalues in turn, we evaluate the eigenvector $[x_n]$, which will be column matrix, according to the equation

$$\{\lambda_n[U] - [L]\} [x_n] = [0]$$

Consider $\lambda_1 = L_s + 2L_m$.

$$\{\lambda_1[U] - [L]\} \begin{bmatrix} x_1 \\ x_2 \\ x_3 \end{bmatrix} = L_m \begin{bmatrix} 2 & -1 & -1 \\ -1 & 2 & -1 \\ -1 & -1 & 2 \end{bmatrix} \begin{bmatrix} x_1 \\ x_2 \\ x_3 \end{bmatrix} = \begin{bmatrix} 0 \\ 0 \\ 0 \end{bmatrix}$$

This gives the three equations for x_1, x_2, x_3 to be $2x_1 - x_2 - x_3 = 0$, $-x_1 + 2x_2 - x_3 = 0$, $-x_1 - x_2 + 2x_3 = 0$. By choosing $x_1 = 1$ the eigenvector is

$\begin{bmatrix} 1 \\ 1 \\ 1 \end{bmatrix}$. Its normalized form is $\frac{1}{\sqrt{3}} \begin{bmatrix} 1 \\ 1 \\ 1 \end{bmatrix}$. By following a similar procedure using the other eigenvalue $\lambda_2 = L_s - L_m$, there results

$$\{ \lambda_2 [U] - [L] \} \begin{bmatrix} y_1 \\ y_2 \\ y_3 \end{bmatrix} = -L_m \begin{bmatrix} 1 & 1 & 1 \\ 1 & 1 & 1 \\ 1 & 1 & 1 \end{bmatrix} \begin{bmatrix} y_1 \\ y_2 \\ y_3 \end{bmatrix} = \begin{bmatrix} 0 \\ 0 \\ 0 \end{bmatrix} \text{ giving } y_1 + y_2 + y_3 = 0$$

Once again taking $y_1 = 1$, we obtain $y_2 + y_3 = -y_1 = -1$.

We now have an infinite number of choices for the values of y_2 and y_3 . These must suit engineering considerations. The most convenient value is to let $y_2 = 0$. Then $y_3 = -1$. The eigenvector is $\begin{bmatrix} 1 \\ 0 \\ -1 \end{bmatrix}$ and its normalized form is $\frac{1}{\sqrt{2}} \begin{bmatrix} 1 \\ 0 \\ -1 \end{bmatrix}$.

Since $\lambda_3 = \lambda_2$, it gives the same equation. We now choose $z_3 = z_1 = 1$ giving $z_2 = -2$. For this case, the eigenvector is $\begin{bmatrix} -2 \\ 1 \\ 1 \end{bmatrix}$ and the normalized form is $\frac{1}{\sqrt{6}} \begin{bmatrix} -2 \\ 1 \\ 1 \end{bmatrix}$.

Step 3: The complete eigenvector vector in normalized form is called the inverse of the transformation matrix:

$$[T]^{-1} = \frac{1}{\sqrt{6}} \begin{bmatrix} \sqrt{2} & \sqrt{3} & 1 \\ \sqrt{2} & 0 & -2 \\ \sqrt{2} & -\sqrt{3} & 1 \end{bmatrix}, \text{ and } [T] = \frac{1}{\sqrt{6}} \begin{bmatrix} \sqrt{2} & \sqrt{2} & \sqrt{2} \\ \sqrt{3} & 0 & -\sqrt{3} \\ 1 & -2 & 1 \end{bmatrix}$$

Step 4: The given inductance matrix is now diagonalized by the multiplication (as can be verified)

$$[T]^{-1} [L] [T] = \begin{bmatrix} L_s + 2L_m & 0 & 0 \\ 0 & L_s - L_m & 0 \\ 0 & 0 & L_s - L_m \end{bmatrix} = [\lambda]$$

The mutually-coupled waves are now de-coupled. The capacitance matrix or the surge-impedance matrix could have been used and yields the same transformation matrices. In this case, the eigenvalues turn out to be equal to the zero, positive, and negative-sequence quantities.

Interpretation of Eigenvector Matrix

1) Corresponding to the first eigenvalue, the eigenvector has the elements $[1, 1, 1]$ which can be interpreted as follows: In the first mode, the voltages, currents, charges, and the accompanying energies are all equal and of the same polarity. In general, the return

current flows in the ground, and the attenuation of energy is high because of ground resistance. It is usually called the 'line-to-ground' mode or 'homopolar' mode. At radio frequencies of 1MHz, attenuation is 6 dB/Km.

2) The second eigenvector is $[1, 0, -1]$ which involves only the outer phases. The centre-phase is not involved in the propagation. One outer is the 'go' and the other is the 'return'. Therefore, ground is not involved. This is called the 'line-to-line mode of 1st kind' or the 'phase-phase' mode. At 1 MHz, attenuation is about 1 dB/Km.

3) The third eigenvector is $[1, -2, 1]$ which can be interpreted as saying that the current 'goes' in the outers and 'returns' in the centre phase. The charge distribution is $[+q, -2q, +q]$ and so on. Ground is not involved and attenuation at 1 MHz for radio-wave propagation is about 0.17 dB/Km. This is called the 'line-to-line mode of the 2nd kind' or the 'inter-phase' mode.

The concept of modes of propagation is also very useful for coupling modes of carrier equipment where attenuation of speech and signals is of concern in determining transmitter and receiver powers.

Velocities of Propagation

We observed that $[L][C] = \frac{1}{g^2} [U]$ for a fully-transposed line. Suppose we pre-multiply by $[T]$ and post-multiply by $[T]$. Then $[T]^{-1}[L][C][T] = [T]^{-1}[L][T] [T]^{-1}[C][T] = [T]^{-1}[U][T] \frac{1}{g^2}$

$$\therefore \begin{bmatrix} L_s + 2L_m & 0 & 0 \\ 0 & L_s - L_m & 0 \\ 0 & 0 & L_s - L_m \end{bmatrix} \begin{bmatrix} C_s + 2C_m & 0 & 0 \\ 0 & C_s - C_m & 0 \\ 0 & 0 & C_s - C_m \end{bmatrix} = \frac{1}{g^2} [U]$$

This gives $(L_s + 2L_m)(C_s + 2C_m) = 1/g^2$
and $(L_s - L_m)(C_s - C_m) = 1/g^2$

This shows that velocities of propagation of waves in all three modes are equal to each other and to light velocity. This is true when ground return inductance is neglected. Usually, in the first or line-to-ground mode, inductance of ground-return reduces

the velocity of that modal component to about 2.5×10^8 m/s or 83% of light velocity.

Untransposed line: Following the steps given before, using numerical values, the eigenvalues and eigenvectors can be worked out.

Section 9: Resistance and Inductance of Ground Return

Under balanced operating conditions of a transmission system, ground-return currents do not flow. Some of the situations where ground-return is involved are :

- (a) Short-circuits : Single line to ground and double line to ground faults.
- (b) Switching Operation.
- (c) Propagation of waves on conductors, (PLC)
- (d) Radio interference studies.

The ground-return resistance increases with frequency of current because the current does not penetrate deeply and area of conduction decreases. But the inductance decreases because the flux lines cannot find as large an area as at low frequencies.

In every case, the soil is inhomogeneous and stratified in several layers with varying conductivities. In this section, the famous formulas of Carson will be given which apply to a single-layer homogeneous soil.

The values of conductivities on the average are :

<u>Moist soil</u>	<u>Loose soil</u>	<u>clay</u>	<u>Bed rock</u>
10^0 mho/m	10^{-1}	10^{-2}	10^{-3} mho/m

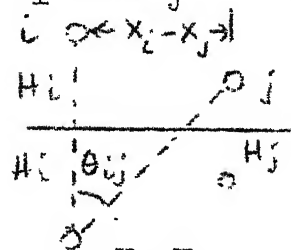
To convert to c.g.s. units, multiply these by 10^{11} . The figure depicts the important parameters involved. X_i and X_j of conductors i and j are referred to any

chosen origin located on ground surface. C_s = soil conductivity in mho/m, f = frequency of current,

$H_z \cdot I_{ij}$ = distance of conductor j

from image of conductor i , metres, $\theta_{ij} = \arctan \frac{X_i - X_j}{H_i - H_j}$

$G = 1.7811$, Euler's number, and $\mu_0 = 4\pi \times 10^{-7}$ H/m.



The most important parameter for the calculation is $r_{ij} = \frac{I_{ij} \sqrt{2 \pi \rho_0 f C_s}}{r_{ij} \sqrt{(8 \pi^2 f C_s)}}$. For usual c.h.v. lines, $r_{ij} < 1$. In c.g.s. units, $r_{ij} = I_{ij} \sqrt{(8 \pi^2 f C_s)}$, with I_{ij} in cm and C_s in c.g.s. units.

Having found r_{ij} , the ground-return resistance and inductance are :

$R_g = 8 \pi f J_r \cdot 10^{-4}$ ohm/Km, $L_g = 4 \cdot J_i \cdot 10^{-4}$ Henry/Km, where, J_r and J_i are calculated as follows

$$J_r = (1-S_4) \frac{\pi}{8} + 0.5 S_2 \cdot \ln(2/G r_{ij}) + 0.5 \theta_{ij} \cdot T_2 - \frac{1}{2\sqrt{2}} W_2.$$

$$J_i = 0.25 + 0.5(1-S_4) \cdot \ln(2/G \cdot r_{ij}) - 0.5 \theta_{ij} \cdot T_4 - \frac{\pi}{8} S_2 + \frac{1}{\sqrt{2}} (W_1 + W_3) - \frac{1}{2} W_4.$$

There are several quantities above which are given by the following infinite series, for $r_{ij} < 1$. For most calculations only 2 or 3 leading terms will be sufficient, as shown by actual calculation for 400 kV line.

$$S_2 = \sum_{K=0}^{\infty} (-1)^K (r_{ij}/2)^{2(2K+1)} \frac{1}{(2K+1)!(2K+2)!} \cos (2K+1)2\theta_{ij}$$

T_2 = same as S_2 with cosine changed to sine.

$$S_4 = \sum_{K=1}^{\infty} (-1)^{K-1} (r_{ij}/2)^{4K} \frac{1}{(K+1)!(K+2)!} \cos 4K \theta_{ij}$$

T_4 = same as S_4 with cosine changed to sine.

$$W_1 = \sum_{K=1}^{\infty} (-1)^{K-1} \cdot r_{ij}^{(4K-1)} \frac{1}{1^2 \cdot 3^2 \cdot 5^2 \cdots (4K-1)} \cdot \cos (4K-3)\theta_{ij}$$

$$W_2 = 1.25 \cdot S_2$$

$$W_3 = \sum_{K=1}^{\infty} (-1)^{K-1} \cdot r_{ij}^{(4K-1)} \frac{1}{3^2 \cdot 5^2 \cdots (4K+1)} \cdot \cos (4K-1)\theta_{ij}$$

$$W_4 = \frac{5}{3} S_4.$$

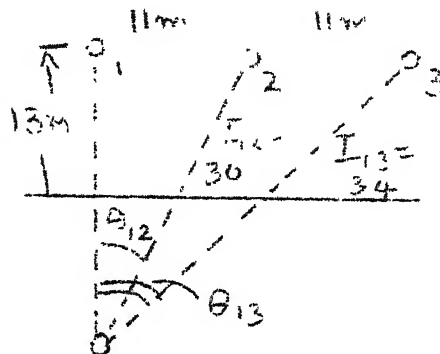
The important and interesting properties of R_g and L_g for a 3-phase horizontal 400-kV line come out to be, nearly

$$[R_g] = R_g \begin{bmatrix} 1 & 1 & 1 \\ 1 & 1 & 1 \\ 1 & 1 & 1 \end{bmatrix} \text{ and } [L_g] = L_g \begin{bmatrix} 1 & 1 & 1 \\ 1 & 1 & 1 \\ 1 & 1 & 1 \end{bmatrix}$$

It is left as an exercise to diagonalize these !.

Example : 400 kV line

The frequency selected is 1 KHz
 which is useful for switching-surge studies. $C_s = 10^{-2}$ mho/m. $\theta_{12} = \tan^{-1}(11/26) = 0.4014$ rad $= \theta_{23}$.
 $\theta_{13} = \tan^{-1}(22/26) = 0.7025$
 $\theta_{11} = \theta_{22} = \theta_{33} = 0$. $r_{ij} = I_{ij} \sqrt{2\pi\mu_0 \times 10^3}$
 r_{ij} : $r_{11} = 0.234$, $r_{12} = 0.27$, $r_{13} = 0.306$.



Self resistance : R_{11} , R_{22} , R_{33} , For this, $\theta_{ij} = 0$.

$$S_2 = \left(\frac{0.234}{2}\right)^2 \cdot \frac{1}{2!} - \left(\frac{0.234}{2}\right)^6 \cdot \frac{1}{3!4!} + \left(\frac{0.234}{2}\right)^{10} \cdot \frac{1}{5!6!} \approx 0.00685$$

$$T_2 = 0. \quad W_2 = 0.00356 = 1.25 S_2$$

$$S_4 = \frac{0.117^4}{2 \times 6}, \text{ which is negligible. } T_4 = 0. \quad W_4 \text{ is negligible.}$$

$$W_1 = \frac{0.234^3}{1^2 \cdot 3} = 0.0043. \quad W_3 = \frac{0.234^3}{3^2 \cdot 5} = 0.00028.$$

$$\therefore J_r = \frac{\pi}{8} + \frac{1}{2} \times 0.00685 \cdot \ln \left(\frac{2}{1.7811 \times 0.234} \right) - 0.00215 + \frac{0.0086}{2\sqrt{2}}$$

$$= 0.4. \quad (\text{Note} = \pi/8 = 0.3925).$$

$$J_i = 0.25 + 0.5 \times 1.61 - \frac{\pi}{8} \times 0.00685 + \frac{0.0046}{\sqrt{2}} \approx 1.055.$$

$$\therefore R_{ii} = 8\pi \times 10^3 \times 10^{-4} \times 0.4 = 1 \text{ ohm/Km}$$

$$L_{ii} = 4 \times 1.055 \times 10^{-4} = 0.422 \text{ mH/Km.}$$

Mutual (1-2) : Calculations give $J_r = 0.3983 \approx .4$, and $J_i = 0.952$

$$\therefore R_{12} = 1 \text{ ohm/Km}, L_{12} = 0.38 \text{ mH/Km}$$

Mutual (1-3) : $J_r = 0.3925$, $J_i = 0.89$

$$\therefore R_{13} \approx 1 \text{ ohm/Km}, L_{13} = 0.356 \text{ mH/Km}$$

$$[R_g] = \begin{bmatrix} 1 & 1 & 1 \\ 1 & 1 & 1 \\ 1 & 1 & 1 \end{bmatrix} \text{ ohm/Km} \quad \text{and} \quad [L_g] = \begin{bmatrix} 0.422 & 0.38 & 0.356 \\ 0.38 & 0.422 & 0.38 \\ 0.356 & 0.38 & 0.422 \end{bmatrix} \text{ mH/Km}$$

$$\text{Average inductance } L_g = \frac{1}{9} (0.422 \times 3 + 0.38 \times 4 + 0.356 \times 2) = 0.39 \text{ mH/Km.}$$

This gives nearly :

$$[R_g] = R_g \begin{bmatrix} 1 & 1 & 1 \\ 1 & 1 & 1 \\ 1 & 1 & 1 \end{bmatrix} \quad \text{with } R_g = 1 \text{ ohm/Km.}$$

$$[L_g] = L_g \begin{bmatrix} 1 & 1 & 1 \\ 1 & 1 & 1 \\ 1 & 1 & 1 \end{bmatrix} \quad \text{with } L_g = 0.39 \text{ mH/Km}$$

It would appear therefore that only one quantity would be necessary for each of these two matrices. This property is usually used by everyone.

Section 10 : Corona-Inception Gradient and Maximum Surface Voltage Gradient on Line Conductors

Corona Inception : Peek's formula for corona-inception gradient on a smooth conductor above a ground plane is still the best for design purposes. This is

$$E_{os} = \frac{30}{\sqrt{2}} \epsilon \left(1 + \frac{0.301}{\sqrt{r \delta}} \right), \text{ kV/cm, r.m.s.}$$

Here, r = conductor outer radius in cm., and S = air-density factor = $\frac{273+t_0}{273+t} \times \frac{p}{760}$ when p is in mm Hg. Indian standards use

$t_0 = 20^\circ\text{C}$ but will consider 27°C in future. [The factor $(273+20)/760 = 0.3855$]. The pressure varies with elevation and temperature. The variation with elevation can be taken as 10 millibars (7.5 mm) per 100 metre change of elevation. Temperature correction is not very important.

On stranded conductors, corona-inception occurs at lower gradients which is known as the nominal smooth-conductor gradient. This is taken into account by using a roughness factor $m = 0.7$ to 0.8 in fair weather, and 0.55 to 0.65 in rain. $E_{or} = m E_{os}$.

Example : For a Moose 0.0318 m dia conductor calculate the corona-inception gradient at elevations of $0, 1000, 2000$, and 3000 m above sea level. Take the temperatures as $40^\circ, 30^\circ, 20^\circ$ and 10°C respectively at these elevations. This usually corresponds to a 400 kV line running in North Indian plains to the Himalayan regions.

Take $m = 0.75$.

h	$^\circ\text{C}$	1000	2000	3000	metres
t	40	30	20	10	$^\circ\text{C}$
p	760	685	610	535	mm
$S = (.3855 \frac{p}{273+t})$	0.936	0.8715	0.8026	0.7288	
E_{os}	25.0	23.4	21.75	19.96	
E_{or}	18.75	17.55	16.31	14.97	

Notice that as elevation increases, corona-inception conditions are more favourable. On hilly terrains, this problem arises even though a conductor may be designed to be corona-free in the plains. [A parallel with Paschen's Law can be found in this. Paschen's Law for breakdown of gaps in uniform fields is $V_b \propto f(pd)$. As p decreases (above the Paschen minimum), for the same gap length, breakdown voltage decreases. Hence the breakdown gradient (V_b/d) also decreases].

Maximum Surface Voltage Gradient on Conductors in Bundle

The surface voltage gradient depends on charges on the sub-conductors of the bundle. This will have to be found first from the equation

$$\left[q/2\pi\epsilon_0 \right] = [P]^{-1} [V] = [M] [V], \text{ where}$$

$$[V] = V [\sin wt, \sin (wt-120), \sin (wt+120)]$$

$[P]$ = Maxwell's potential coefficient matrix,

$$P_{ii} = \ln (2H/r_{cq}), P_{ij} = \ln (I_{ij}/A_{ij}), i \neq j.$$

Since the voltage of any phase conductor is varying with time, the surface voltage gradient will also vary at 50Hz. In e.h.v. lines, the phase separations and heights are very large in comparison to the sub-conductor radii and the spacing between sub-conductors in the bundle. It is therefore assumed that the changes on the other phase conductors and the image conductors have negligible effect on the surface voltage gradient on the sub-conductors of any bundle.

In time, therefore, maximum value of charge occurs when the voltage of that phase passes through its maximum. In a computer programme, depending on the required accuracy, all factors can be incorporated. Therefore, for a 3-phase line, where q_1, q_2, q_3 are total bundle charges,

$$\begin{bmatrix} q_1/2\pi\epsilon_0 \\ q_2/2\pi\epsilon_0 \\ q_3/2\pi\epsilon_0 \end{bmatrix} = V \begin{bmatrix} M_{11} & M_{12} & M_{13} \\ M_{21} & M_{22} & M_{23} \\ M_{31} & M_{32} & M_{33} \end{bmatrix} \begin{bmatrix} \sin wt \\ \sin (wt-120) \\ \sin (wt+120) \end{bmatrix}$$

Considering phase 1, when its voltage passes through maximum or peak value, the voltages of the other two phases are passing through negative half values.

∴ Maximum value of q_1 will occur when

$$(q_1/2\pi\epsilon_0)_{\max} = V [M_{11} - 0.5 (M_{12} + M_{13})]$$

Similarly, $(q_2/2\pi\epsilon_0)_{\max} = V [M_{22} - 0.5 (M_{21} + M_{23})]$

and $(q_3/2\pi\epsilon_0)_{\max} = V [M_{33} - 0.5 (M_{31} + M_{32})]$

Having found the charges, the maximum surface voltage gradients can be found as follows. In the expressions, q denotes this maximum charge. Also, when V is in kV r.m.s., the surface voltage gradient will be in kV/m r.m.s.

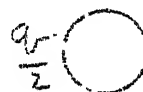
1) single conductor:

$$E_{\max} = \frac{q}{2\pi\epsilon_0} \cdot \frac{1}{r}$$

$$q/2\pi\epsilon_0, r$$



2) Twin conductor: The charge on each conductor = $q/2$.



$$\leftarrow B = 2R \rightarrow$$

In the case of bundled conductor, the surface voltage gradient varies along the periphery of the conductor. When a unit positive test charge is placed at P_o , the forces due to charge on both conductors are in the same direction, while at P_i they are in opposite directions. The maximum anywhere on the periphery occurs at P_o . Due to its own charge, the electric field is $\frac{q}{2\pi\epsilon_0} \cdot \frac{1}{2} \cdot \frac{1}{r}$. Due to the charge on the other sub-conductor of the bundle, the electric field at P_o would be given by $\frac{q}{2\pi\epsilon_0} \cdot \frac{1}{2} \cdot \frac{1}{B+r} \approx \frac{q}{2\pi\epsilon_0} \cdot \frac{1}{2 \cdot B}$. But we have to double this for the reason that when a conducting cylinder is placed in the uniform field of a charge, the stress on the cylinder is twice the stress when it is not present. Assuming that the left sub-conductor is sufficiently far that it produces a uniform field at the location of the right sub-conductor, the field is $\frac{q}{2\pi\epsilon_0} \cdot \frac{1}{2 \cdot B} - \frac{q}{2\pi\epsilon_0} \cdot \frac{1}{2 \cdot R}$.

∴ The maximum surface voltage gradient is

$$E_m = \frac{q}{2\pi\epsilon_0} \cdot \frac{1}{2} \left(\frac{1}{r} + \frac{1}{R} \right) = \frac{q}{2\pi\epsilon_0} \cdot \frac{1}{2} \cdot \frac{1}{r} (1+r/R)$$

3) To derive a general formula, consider the 4 conductors. The charge on each sub-conductor is $q/4 = q/N$.

Due to conductor charge : $E_3 = \frac{q}{2\pi\epsilon_0} \cdot \frac{1}{4} \cdot \frac{1}{r}$

Due to conductor 1: $E_1 = \frac{q}{2\pi\epsilon_0} \cdot \frac{1}{4} \cdot \frac{2}{2R} = \frac{q}{2\pi\epsilon_0} \cdot \frac{1}{4} \cdot \frac{1}{R}$

Due to conductor 2: $E_2 = \frac{q}{2\pi\epsilon_0} \cdot \frac{1}{4} \cdot \frac{2 \cos \frac{\pi}{4}}{2R \sin \frac{\pi}{4}} = \frac{q}{2\pi\epsilon_0} \cdot \frac{1}{4} \cdot \frac{1}{R}$

Also ∴ $E_3 = E_2$

$$\begin{aligned} \therefore E_m = E_1 + E_2 + E_3 + E_4 &= \frac{q}{2\pi\epsilon_0} \cdot \frac{1}{4} \cdot \frac{1}{r} \left[1 + \frac{1}{R} + \frac{1}{R} + \frac{1}{R} \right] \\ &= \frac{q}{2\pi\epsilon_0} \cdot \frac{1}{4} \cdot \frac{1}{r} \left(1 + \frac{3}{R} \right) = \frac{q}{2\pi\epsilon_0} \cdot \frac{1}{N} \cdot \frac{1}{r} \left[1 + (N-1) \frac{1}{R} \right] \end{aligned}$$

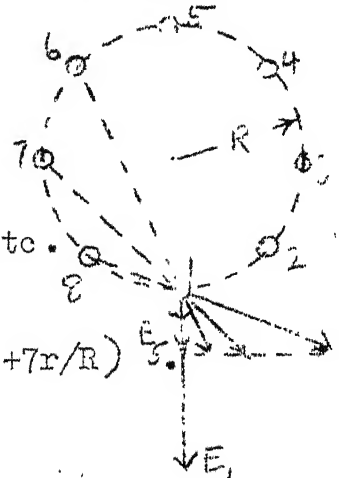
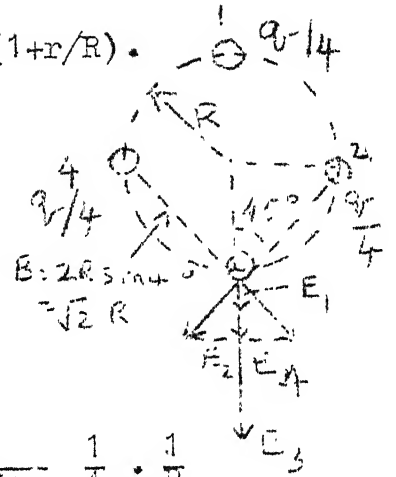
The general formula is $E_m = \frac{q}{2\pi\epsilon_0} \cdot \frac{1}{N} \cdot \frac{1}{r} \left[1 + (N-1)/R \right]$.

Here, q = charge on the total bundle, and (q/N) is the charge on each sub-conductor. For an 8-conductor bundle, the forces are

$$E_1 = \frac{q}{2\pi\epsilon_0} \cdot \frac{1}{8} \cdot \frac{1}{r}, \quad E_5 = \frac{q}{2\pi\epsilon_0} \cdot \frac{1}{8} \cdot \frac{1}{R},$$

$$E_2 = E_8 = \frac{q}{2\pi\epsilon_0} \cdot \frac{1}{8} \cdot \frac{2 \cos 67\frac{1}{2}^\circ}{2R \sin 22\frac{1}{2}^\circ} = \frac{q}{2\pi\epsilon_0} \cdot \frac{1}{8} \cdot \frac{1}{R}, \text{ etc.}$$

$$\therefore E_m = \frac{q}{2\pi\epsilon_0} \cdot \frac{1}{8} \left[\frac{1}{r} + \frac{7}{R} \right] = \frac{q}{2\pi\epsilon_0} \cdot \frac{1}{8} \cdot \frac{1}{r} (1+7r/R)$$



Example : For the untransposed horizontal 400-kV line,

$$[M] = \begin{bmatrix} 0.176 & -0.03 & -0.01 \\ -0.03 & 0.180 & -0.03 \\ -0.01 & -0.03 & 0.176 \end{bmatrix} \cdot \begin{matrix} V=420 \text{ KV, l-l, r.m.s.} \\ =242.5 \text{ KV, l-g, r.m.s.} \end{matrix}$$

For the outer phases : $\frac{q_o}{2\pi\epsilon_o} = 242.5 \times 10^3 [0.176 + 0.5(0.03 + 0.01)]$
 $= 47.53 \times 10^3$

For the centre phase : $\frac{q_c}{2\pi\epsilon_o} = 242.5 \times 10^3 [0.18 + 0.5(0.03 + 0.03)]$
 $= 50.925 \times 10^3 \cdot (7.14\% \text{ more than outer})$

Maximum surface voltage gradients : $r = 0.0159 \text{ m}$, $R=B/2=0.2286 \text{ m}$

Outer phases . $E_{mo} = \frac{q_o}{2\pi\epsilon_o} \cdot \frac{1}{2} \cdot \frac{1}{0.0159} \left(1 + \frac{0.0159}{0.2286}\right)$

$$= 1598 \text{ KV/m} = 15.98 \text{ KV/cm, r.m.s.}$$

Centre phase . $E_{mc} = 1713 \text{ KV/m} = 17.13 \text{ KV/cm, r.m.s.}$

Mangoldt Formula (Markt-Mengele Formula)

For a 3-phase horizontal line, the maximum surface voltage gradient on the subconductors of an N-conductor bundle can be written down in closed form. This is called the Mangoldt formula, also known as Markt-Mengele formula. The average height H to be used for e.h.v. lines is

H=minimum height at midspan + sag/3.

For the horizontal configuration,

$$P_s = P_{11} = P_{22} = P_{33} = \ln(2H/r_{eq}), \quad r_{eq} = R(N r/R)^{1/N}$$

$$P_{m1} = P_{12} = P_{23} = \ln(\sqrt{4H^2 + S^2}/S), \quad P_{m2} = P_{13} = \ln(\sqrt{4H^2 + 4S^2}/2S).$$

$$\text{Now, } \begin{bmatrix} V_1 \\ V_2 \\ V_3 \end{bmatrix} = \begin{bmatrix} P_s & P_{m1} & P_{m2} \\ P_{m1} & P_s & P_{m1} \\ P_{m2} & P_{m1} & P_s \end{bmatrix} \begin{bmatrix} q_1 \\ q_2 \\ q_3 \end{bmatrix} \cdot \frac{1}{2\pi\epsilon_o}$$

For any phase, maximum occurs when the voltage of that phase is at peak value and the other two phases have negative $\frac{1}{2}$ value. This applies to charges also.

For the outer phases: $V_1 = [P_s - 0.5 (P_{m1} + P_{m2})] \frac{q_1}{2\pi c_o}$

$$P_s - 0.5(P_{m1} + P_{m2}) = \ln \frac{2H}{r_{eq}} - 0.5 \ln \left\{ \frac{\sqrt{4H^2 + S^2}}{S} \cdot \frac{\sqrt{H^2 + S^2}}{S} \right\}$$

$$\therefore \frac{q_o}{2\pi c_o} = \frac{V_1}{\ln \frac{2H}{r_{eq}} - 0.5 \ln \left\{ \sqrt{(4H^2 + S^2)(H^2 + S^2)} / S^2 \right\}}$$

The maximum surface voltage gradient is

$$E_{mo} = \frac{q_o}{2\pi c_o} \frac{1}{N} \frac{1}{r} [1 + (N-1) r/R] \text{ where } \frac{q_o}{2\pi c_o} \text{ can be written out in terms of the line-to-ground voltage and the height } H \text{ and phase spacing } S.$$

For the centre phase: $\frac{q_c}{2\pi c_o} = \frac{V}{\ln \frac{2H}{r_{eq}} - \ln \frac{\sqrt{4H^2 + S^2}}{S}}$

$$E_{mc} = \frac{V [1 + (N-1) r/R]}{N \cdot r \cdot \ln \frac{2HS}{r_{eq} \sqrt{4H^2 + S^2}}}$$

For $V = 242.5$ kV, $N=2$, $r = 0.0159$, $r_{eq} = 0.085$, $H=15$, $S=11$, $R=0.2286$, calculation gives 1695 kV/m = 16.95 kV/cm. The previous value was 17.13 kV/Km.

TABLE I.

PARTIAL LIST OF ACSR CONDUCTORS-NORTH AMERICAN MANUFACTURE

Name	Overall Diameter Inches	Area, Circular Mils	Al/Steel Stranding	Approximate current carrying capacity, 50°C Temperature Rise(Amperes)
Ostrich	0.68	300,000	26/7	500
Oricle	0.741	336,400	30/7	530
Lark	0.806	397,500	30/7	600
Hawk	0.858	477,000	26/7	670
Parakeet	0.914	556,500	24/7	730
P. peacock	0.953	605,000	24/7	750
Flamingo	1.000	666,600	24/7	800
Drake	1.108	795,000	26/7	900
Cardinal	1.196	954,000	54/7	1000
Bunting	1.302	1192,500	45/7	1160
Pheasant	1.382	1272,000	54/19	1200
Martin	1.424	1351,500	54/19	1250
Plover	1.465	1431,000	54/19	1300
Falcon	1.545	1590,000	54/19	1380
Chukar	1.602	1780,000	84/19	1600
Kiwi	1.737	2167,000	72/7	2000
Expanded	1.600	1275,000	(50/4)/19	1200
Expanded	1.750	1414,000	(58/4)/19	1280
Expanded	2.320	2294,000	(66/6)/19	2100
Expanded	2.500	3108,000	(62/8)/19	3000

Table II Indian Manufacturer IS:398 (1961)

Coyote	0.625/15.86 mm	128.5 mm ²	26/7
Tiger	0.65/16.52	128.1	30/7
Wolf	0.715/18.3	154.3	30/7
Lynx	0.77/19.53	179	30/7
Panther	0.828/21	207	30/7
Lion	0.875/22.26	232.5	30/7
Goat	1.02/25.97	316.5	30/7
Sheep	1.1/27.93	366.1	30/7
Deer	1.18/29.89	419.3	30/7
Elk	1.24/31.5	465.7	30/7
Moose	1.25/31.77	515.7	54/7

Table III
COPPER CONDUCTOR

Number	Diameter inch/mm	Approx. Current Carrying Capacity, A
7/0	.5/12.7	
6/0	.464/11.785	
5/0	.432/10.97	
4/0	.4/10.16	480
3/0	.372/9.45	420
2/0	.348/8.84	360
0	.324/8.23	310
1	.3/7.62	270
2	.276/7.01	230
3	.252/6.4	200
4	.232/5.893	175
5	.212/5.385	150
6	.192/4.877	125
7	.176/4.47	110
8	.16/4.064	90
9	.144/3.658	
10	.128/3.251	

TABLE IV.

Properties of Some Metals

Metal	Specific Resistance ohm-m	Temperature Coeffi- cient of Resistance per °C	Specific Gravity
Platinum	10.6×10^{-8}	0.003	21.45
Iron	10	0.005	7.86
Molybdenum	5.7	0.0033	10.2
Tungsten	5.5	0.0045	19.3
Aluminium	2.7	0.00446	2.7
Gold	2.4	0.0034	19.3
Copper	1.7	0.00393	8.92
Silver	1.63	0.0038	10.5

PROCEDURES FOR E.H.V. LINE DESIGNS

Part I : Based on Steady-State Operating Limits

This is Part I on e.h.v. transmission-line design. It does not cover system or interconnected network design such as load flow, but only the design of the line from the generating end to the load end. Part II covers line insulation clearances based upon power frequency, lightning, and switching-surge overvoltages.

This lecture will cover the following topics:

- 1) Introduction and problem statement.
- 2) Dimensions of typical e.h.v. lines.
- 3) Design Limits and constraints for
 - (i) current density; (ii) voltage limits; (iii) corona-inception gradient and margins; (iv) Radio Noise; (v) Audible Noise; (vi) Electrostatic field; (vii) corona losses; (viii) Line compensation.
- 4) Design Data and Equations.
 - (i) Decision on voltage and load delivered per circuit;
 - (ii) charge of conductors; (iii) Electrostatic Field;
 - (iv) Conductor Surface Voltage Gradient; (v) Corona-inception gradient; (vi) Radio Noise level; (vii) Audible Noise;
 - (viii) Corona Loss; (ix) Voltage control at Power Frequency.
- 5) Design Examples.
 - (i) 400 kV 400 Km 1000 MW with only shunt reactor compensation;
 - (ii) 400 kV 800 Km 1000 Mw with shunt reactor ^{and} 50% series capacitor compensation;
 - (iii) 750 kV 500 Km 2000 Mw with only shunt reactor compensation.

I. INTRODUCTION

Extra High Voltage (EHV) and Ultra High Voltage (UHV) lines for 400 kV to 1200 kV and higher are being exposed to nature which have important environmental effects so that design constraints have to be not only stringent but also emphasis has to be shifted. Upto the 345 kV level, line designs have been based upon (a) current-carrying capacity (b) use of synchronous condensers and switched capacitors for voltage control at line ends, and (c) insulation clearance at towers and between conductors based upon lightning requirement. Recently, sophisticated/solid state VAR systems are coming into use.

But at the higher voltages (400 kV and above) the important factors to be considered are

- (a) current density because of increased loading;
- (b) bundling, corona-inception gradient and loss;
- (c) shunt-reactor and series-capacitor compensation;
- (d) electrostatic field effects at 50Hz;
- (e) radio interference and audible noise;
- (f) insulation coordination based upon switching-surge levels;
- (g) miscellaneous factors such as ferro-resonance, increased short-circuit current in ground, single-pole reclosing; and
- (h) use of gapless surge arresters for both lightning and switching-surge duty.

This paper gives proposed design procedures for e.h.v. lines (a) to (e) which are steady-state limits, while the second and subsequent part describes insulation design requirements based on transient considerations, mainly the dynamic voltage rise during single-phase-to-ground fault, lightning and switching operations.

Design of an e.h.v. line is always a case-by-case study but it is the purpose of these papers to give the outline of procedures that can be followed and suitably modified. The contents of the papers will be useful for line designers, research workers, managers,

and decision makers. Three examples are worked out to illustrate the application of the procedures to (i) a 400-Km 400 kV line with only shunt-reactor compensation, (ii) an 800-Km 400 kV line with shunt reactor and series-capacitor compensation, and (iii) a 500-Km 750 kV line without series-capacitor compensation.

II. DIMENSIONS OF TYPICAL LINES

Table I gives major dimensions of some typical lines existing and proposed in the world from 400 kV to 1300 kV, A.C. (All dimensions are in metres).

Table I: Dimensions of Typical Lines

No.	Voltage kV	Type	Conductor Details			Height H	Spacing S
			N	r	B or R		
1	400	S/C, Hor.	2	0.0159	B=0.4572	13	11
		S/C, L				13.5, 21.2	13
		D/C				12.4, 21.6	
2	735	S/C, Hor.	4	0.0176 0.015	0.4572	13.8	15.2
3	800	S/C, Hor.	4	0.0204	0.6	18	15
4	1000	S/C, Hor	4 6	0.023 0.019	B=24r	15	17
5	1150	S/C, Hor	8	0.012	0.4	14.5 or 18.5 or 21	23.5
6	1150 ^{MAX}	Delta	8	0.0205	R=0.535	26, 44	24
7	1200	S/C, Hor	6	0.0232	R=0.6	21	18
			6	0.0254			
			8	0.0207			
			8	0.0232			
8	1300	S/C, Hor	4	0.026	B=24 r	17.3	20.5
			6	0.022			
			8	0.019			

III. DESIGN LIMITS AND CONSTRAINTS

The range of values of major design limits and constraints under which lines have to operate are given in this section following typical practice:

- (i) Current Density : 0.75 to 1 A/mm².
- (ii) Voltage Limits : IEC and ISI Standards. Non-Standard
- | | | | | | | |
|-------------------|-----|-----|-----|---------|------|------|
| <u>Nominal kV</u> | 345 | 400 | 500 | 735-765 | 1000 | 1150 |
| <u>Maximum kV</u> | 362 | 420 | 525 | 765 | 1050 | 1200 |
- Suitable compensating equipment must be provided at both ends so that bus voltages should not exceed the maximum stipulated values.
- (iii) Corona-Inception Gradient : In fair weather, the margin between corona-inception gradient on the stranded conductor and the surface voltage gradient at maximum operating voltage is kept between 10% and 30%. Some-lines operate with 0% margin but take measures to counteract high level of radio interference by other means such as increasing the broadcast station signal strengths along the line route if these are few, or increasing the width of line corridor.
- (iv) Radio Noise : The limits for RI are discussed by the author in Reference 1. As of today, no RI limits exist in India. However, following practice used elsewhere, a designer can limit the noise to 40 dB above 1 μ V/m at 1 MHz in order to fix the width of line corridor.
- (v) Audible Noise : Limits for AN are discussed in Reference 2. The most widely-used design criterion is due to Perry of the Bonneville Power Administration in the U.S.A. No limits exist for India and a designer can use a line geometry based upon 53 dB (A) in order to fix the width of right-of-way (R-O-W) for the line corridor.
- (vi) Electrostatic Field : At 50Hz, high electrostatic fields exist which will have adverse effects on human beings, vehicles, animals, plants and food crops, fences and buried pipe lines. (Reference 2). Again, no limits exist in India and a designer should aim at keeping the maximum value of e.s. field in the line vicinity to 15 kV/m, r.m.s.. This is the limit for let-go currents in a normal human being.

- (vii) Corona Losses: These are of importance in rain and is quite a difficult matter to specify at the design stages. There are instances when power stations have been unable to handle full rated load because of very high corona losses. In fair weather, a maximum value of 5 Kw/Km is aimed at.
- (viii) Line compensation : The compensating equipments available to a designer are (a) switched capacitors, (b) shunt reactors, (c) synchronous condensers, (d) series capacitors, and (e) static VAR systems.

These will be described through line-design examples. Series compensation has not been used in India for lines upto 400 Km at 400 kV. But this may be required for increasing the power-handling capacity when a line of 800 Km at 400 kV is considered as has been done in Sweden.

IV. DESIGN DATA AND EQUATIONS

(i) Decision on Voltage and Delivered Load per Circuit :

The choice of suitable EHV level for India has formed the subject matter of many conferences and symposia held by the C.B.I.P. (References 3,4). As a start, with equal voltages at the sending and receiving ends with 30° phase difference, one circuit can handle a power of $P = 0.5 \frac{V^2}{L x}$, where L =line length and x = positive-sequence reactance per phase per unit length. The corresponding percentage power loss in transmission is (neglecting corona loss) $\% p = 50 \frac{r}{x}$, with r =conductor resistance per unit length.

Table II shows average values of r and x used, the power per circuit in Mw, and the % power loss in transmission at various levels from 400 kV to 1200 kV.

Table II : Power-Handling Capacity, P, and % Power Loss, p

System kV	r, ohm/Km	x, ohm/Km	Length, Km	P, Mw(*)	p, %
400	0.031	0.327	400	640	5.1
750	0.0136	0.272	400	2600	2.7
1000	0.0036	0.231	400	5500	0.85
1200	0.0027	0.231	400	8000	0.64

(*) For other line lengths, L, the power-handling capacity per circuit is inversely proportional to L. Multiply P by (400/L).

From the above table it is evident from the last column that to keep the $I^2 r$ -heating loss to a minimum, higher voltages have to be preferred in order to conserve energy. Also, one 1200-kV circuit can handle as much power as 3-750 kV circuits and 12-400 kV circuits for the same distance of transmission. This will decrease the width of line corridor.

(ii) Charge of Conductors:

Many e.h.v. phenomena depend on the 50Hz charge per unit length on the conductors. These are (a) the e.s. field, (b) RI and AN caused by corona which depend on the conductor surface voltage gradient, and (c) corona loss. The charge per unit length on the 3 phase-conductors is given by $[q] = 2\pi\epsilon_0 [M][V]$, where the ~~matrix~~ $[M] = [P]^{-1}$, with $[P] =$ Maxwell's Potential Coefficient Matrix. Its elements are $P_{ii} = \ln(2H_i/R_{eq})$, $P_{ij} = \ln(I_{ij}/A_{ij})$, $i \neq j$, $i, j = 1, 2, 3$. Here, H_i = average height of conductor i = ~~min~~ minimum height + sag/3, A_{ij} = aerial distance between conductors i and j , I_{ij} = distance between conductor i above ground and the image of conductor j below ground, and $R_{eq} = R(N \cdot r/R)^{1/N}$ = geometric mean radius or equivalent radius of the N-conductor bundle with sub-conductor radius r distributed uniformly on a circle of radius R .

The inductance matrix is $[L] = 0.2 [P]$, $\mu H/m$, and the capacitance is $[C] = 2\pi\epsilon_0 [M]$, F/m.

(iii) Electrostatic Field :

The equations for the field at any point (x,y) in the vicinity of the line from an origin placed at any convenient location (usually at ground level under the centre phase) are given as follows:

$$\text{Vertical component : } E_v(i) = (q_i / 2\pi e_o) \left[(H_i - y) / D_i^2 + (H_i + y) / (D_i^1)^2 \right]$$

$$\text{Horizontal component: } E_h(i) = (q_i / 2\pi e_o) (x - x_i) \left[1 / D_i^2 - 1 / (D_i^1)^2 \right]$$

$$\text{where } D_i^2 = (x - x_i)^2 + (y - H_i)^2 \quad \left. \vphantom{D_i^2} \right\} i=1,2,3$$

$$\text{and } (D_i^1)^2 = (x - x_i)^2 + (y + H_i)^2 \quad \left. \vphantom{(D_i^1)^2} \right\} (x_i = \text{horizontal coordinate of phase-conductor } i).$$

$$\text{Total field : } E_t^2 = \left[\sum_{i=1}^3 E_v(i) \right]^2 + \left[\sum_{i=1}^3 E_h(i) \right]^2$$

Each of these is a 50-Hz quantity so that addition of 3 phasors and determining the resulting amplitude is a straight-forward procedure, Reference 5. The charge q_i is that of the entire bundle and is calculated from the known transmission voltage matrix $[V] = V[\sin wt, \sin (wt - 120^\circ), \sin (wt + 120^\circ)]$, and the matrix $[M]$, which depends only on the line dimensions. The voltage to be used is the r.m.s. value of the line-to-ground voltage in kV in which case the amplitudes of vertical, horizontal and total e.s. field will be in kV/m, r.m.s.

(iv) Conductor Surface Voltage Gradient:

On a bundle-conductor, the surface voltage gradient on the sub-conductors will vary along their periphery, Reference 7. The maximum value is very closely given by

$$E_{\max} = (q_i / 2\pi e_o) \cdot (1/N) \cdot (1/r) \cdot [1 + (N-1) r/R].$$

(vii) Audible Noise :

In this paper, the formula developed by the B.P.A. is used.
For $N < 3$, the formula is (Reference 14)

$$AN(k) = 120 \log [E_m(k)] + 55 \log (2 r) + 11.4 \log [D(k)] - 245.4, \text{ dB(A)}$$

For $N \geq 3$ in a bundle, add $26.4 \log (N) - 13.$, dB (A)
to the above expression. For $N=4$, this is 2.894 dB(A). The total
Sound Pressure Level due to all 3 phases is

$$SPL = 10 \cdot \log_{10} \sum_{k=1}^3 10^{0.1 AN(k)}, \text{ dB(A)}.$$

(viii) Corona Loss:

Of the many formulas available, the following is used which is
due to Ryan and Henline, Reference 15.

$$W_L = 4 f C V (V - V_0), \text{ Mw/Km, 3-phase,}$$

where f = frequency in Hz, C = capacitance of line to ground in
F/Km, V = r.m.s. value of power frequency line-to-line voltage in kV
and V_0 = r.m.s. value of corona-inception voltage in kV.

(ix) Voltage control at Power Frequency :

The equations relating the sending-end voltage and current with
those at the receiving end are

$$\begin{bmatrix} V_s \\ I_s \end{bmatrix} = \begin{bmatrix} A & B \\ C & D \end{bmatrix} \begin{bmatrix} V_r \\ I_r \end{bmatrix} \text{ with } A=D, AD-BC = 1.$$

The generalized constants A,B,C,D have the following values,
(with $Z = (r + j \omega l) L$ and $Y = j \omega c L$) :

(a) For only the line : $A=D=\cosh pL$, $B=Z_0 \sinh pL$, $C = (\sinh pL)/Z_0$

$$p = \sqrt{ZY}, \quad Z_0 = \sqrt{Z/Y},$$

r, l, c = distributed resistance, inductance, and capacitance of line
per Km.

$p \cdot Z_0$ = propagation constant and surge impedance of line
and L = line length in km.

The quantities A, B, C, D , p and Z_0 are complex with magnitude and angle.

(b) Shunt-reactor compensation :

When reactors of admittance $(-jB_L)$ each are connected at the two ends of line, the total A, B, C, D constants are

$$\begin{bmatrix} A_T & B_T \\ C_T & D_T \end{bmatrix} = \begin{bmatrix} A & B \\ C & D \end{bmatrix}_{\text{Line}} - jB_L \begin{bmatrix} B & 0 \\ 2A - jB_L B & B \end{bmatrix}$$

(c) Series Capacitor of Reactance $(-jX_c)$ located at ~~line~~ centre

$$\begin{bmatrix} A_T & B_T \\ C_T & D_T \end{bmatrix} = \begin{bmatrix} A & B \\ C & D \end{bmatrix}_{\text{Line}} - j(X_c/2Z_0) \begin{bmatrix} \sinh pL, & Z_0(1+\cosh pL) \\ (\cosh pL-1)/Z_0, & \sinh pL \end{bmatrix}$$

(d) Shunt reactors at line ends and series capacitor at middle

$$\begin{bmatrix} A_T & B_T \\ C_T & D_T \end{bmatrix} = \begin{bmatrix} A & B \\ C & D \end{bmatrix}_{\text{Line}} - jB_L \begin{bmatrix} B & 0 \\ 2A - jB_L B & B \end{bmatrix} - j \frac{X_c}{2Z_0} \begin{bmatrix} \sinh pL, & Z_0(1+\cosh pL) \\ \frac{\cosh pL-1}{Z_0}, & \sinh pL \end{bmatrix} - \frac{X_c B_L}{2} \begin{bmatrix} 1 + \cosh pL, & 0 \\ \frac{2}{Z_0} \sinh pL - jB_L(1+\cosh pL), & 1 + \cosh pL \end{bmatrix}$$

Note: All quantities except B_L and X_c are phasors with a magnitude and angle.

Phase spacing is based on recommended clearances for switching surge. For 400 kV, the phase spacing will be 12m. At 750 kV, the phase-spacing is 15m.

Choice of Conductor Size

A 2-conductor bundle for 400 kV and a 4-conductor bundle for 750 kV will be used with spacings of 45 cm between sub-conductors. The conductor sizes are $r = 0.0159$ for 400 kV and 0.015 to 0.0175 for 750 kV. These sizes will be checked for (a) corona inception gradient (b) margin between this gradient and maximum surface voltage gradient at operating voltage, (c) electrostatic field, (d) RI, (e) AN and (f) corona loss.

(a) Corona inception and Margins : With roughness factor $m=0.7$, $\delta = 1$,

$$\begin{aligned} \text{(i)} \quad E_{or} &= 2140 (1+0.0301/\sqrt{0.0159}) \times 0.7 = 1856 \text{ kV/m for 400 kV} \\ \text{(ii)} \quad E_{or} &= 2140 (1+0.0301/\sqrt{0.015}) \times 0.7 = 1866 \text{ kV/m} \\ \text{(iii)} \quad E_{or} &= 2140 (1+0.0301/\sqrt{0.0175}) \times 0.7 = 1839 \text{ kV/m} \end{aligned} \quad \left. \vphantom{\begin{aligned} \text{(i)} \quad E_{or} &= 2140 (1+0.0301/\sqrt{0.0159}) \times 0.7 = 1856 \text{ kV/m for 400 kV} \\ \text{(ii)} \quad E_{or} &= 2140 (1+0.0301/\sqrt{0.015}) \times 0.7 = 1866 \text{ kV/m} \\ \text{(iii)} \quad E_{or} &= 2140 (1+0.0301/\sqrt{0.0175}) \times 0.7 = 1839 \text{ kV/m} \end{aligned}} \right\} \text{ for 750 kV}$$

400 kV : Using $N=2$, $r=0.0159$, $R=0.225$, $S=12$, and $H=13$, the maximum surface voltage gradient on the centre phase conductor comes to $16.82 \text{ kV/cm} = 1682 \text{ kV/m}$ at the maximum operating voltage of 420 kV, r.m.s. The margin is $\frac{1856-1682}{1856} \times 100\% = 9.4\%$. This may be considered satisfactory.

If 30% margin has to be maintained, the centre-phase gradient has to be limited to $0.7 \times 1856 = 1300 \text{ kV/m}$. This requires conductors of nearly 1.5 inch diameter which is equivalent to at least the Plover of North American manufacture. (Reference 16,17).

750 kV : With $N=4$, $r=0.015$, $R=0.3182 (=0.45/\sqrt{2})$, $S=15$, $H=18$, the centre-phase gradient is $19.9 \text{ kV/cm} = 1990 \text{ kV/m}$. Therefore, with corona-inception gradient calculated as 1866 kV/m , corona has started.

But with $r = 0.0175$, the maximum gradient is $17.4 \text{ kV/cm} = 1740 \text{ kV/m}$, which is lower than the corona-inception gradient of 1839 kV/m . The

margin is $\frac{1839-1740}{1839} \times 100\% = 5.4\%$. In the case of the outer phases the margin comes out to be nearly 10%. These values will be used further to check for RN, AN, etc. Further calculations will be based on $r = 0.0175\text{m}$.

(b) Radio Noise

400 kV : Here, the maximum surface voltage gradients are : centre Phase - 1682 kV/m; outer phases - 1600 kV/m. From the CIGRE formula, at 15 m from the outer phases the RI levels due to the 3 phases come out to be $RI_{(1)} = 45\text{ dB}$, $RI_{(2)} = 42\text{ dB}$, $RI_{(3)} = 36\text{ dB}$. \therefore RI of line is $\frac{1}{2} (45+42+36) = 41\text{ dB}$ at 0.5 MHz and 39 dB at 1 MHz. At the edge of right-of-way, the level is to be limited to 40 dB at 1 MHz. Therefore, the width of R-O-W extends to 15 m from the outer phase.

750 kV : $E_{mc} = 1740\text{ kV/m}$, $E_{mo} = 1650\text{ kV/m}$. At $x = 15\text{ m}$ from outer phase, CIGRE formula gives $RI(1) = 46.5\text{ dB}$, $RI(2) = 43.9\text{ dB}$, $RI(3) = 36\text{ dB}$. \therefore RI = 46.7 dB at 0.5 MHz and 40.7 dB at 1 MHz. This is slightly above 40 dB. At 16.5 metres from outer phase, the RI level works out to be 40 dB. This may be considered as the edge of the R-O-W. While these values can be used for preliminary designs, it might be worth noting that the CIGRE formula has a dispersion of $\pm 6\text{ dB}$ at 0.5 MHz. Therefore, it is fruitless to specify the edge of R-O-W with any great degree of assurance at this stage. Please see Reference 1 for all other considerations, especially, for Signal/Noise ratio basis for setting RI limits.

(c) Audible Noise

400 kV : $AN(1) = 41.3\text{ dB(A)}$, $AN(2) = 42.4$, $AN(3) = 37.7$ at 15 metres from the outer phase.

$$\therefore \text{SPL} = 10 \log [10^{4.13} + 10^{4.24} + 10^{3.77}] = 46\text{ dB(A)}.$$

This is less than the limit of 53 dB(A). The width of R-O-W governed by RI level is therefore used.

750 kV : At 15 metres from the outer phase,

AN(1) = 48, AN(2) = 49 and AN(3) = 44.3 dB(A).

∴ SPL = 52.3 dB(A). The edge of R-O-W at 16.5 metres from outer phase is O.K. from AN point of view.

(d) Electrostatic Field

400 kV:

$$[P] = \begin{bmatrix} 5.64 & .87 & .39 \\ .87 & 5.64 & .87 \\ .39 & .87 & 5.64 \end{bmatrix} \text{ giving } [M] = [P]^{-1} = \begin{bmatrix} .1728 & -.0256 & -.008 \\ -.0256 & .1772 & -.0256 \\ -.008 & -.0254 & .1728 \end{bmatrix}$$

The maximum ground-level field at 420 kV works out to be 8kV/m, r.m.s. This is lower than the limit of 15kV/m. Therefore, the line dimensions are satisfactory. (References 18, 19).

750kV: The maximum ground-level e.s. field works out to 6.7 kV/m.

From the [P] and [M] matrices, the positive-sequence inductance and capacitance are :

400 kV : L = 0.985 mH/Km, C = 10.82 nF/Km

750 kV : L = 0.866 mH/Km, C = 13 nF/Km.

(e) Corona Loss :

Since the corona-inception gradient is higher than the surface voltage gradients, no corona-loss is anticipated in fair weather.

750 kV: When using $r = 0.0175$ metre for the sub-conductors, no corona is present and loss is not of consequence in fair weather.

Important Note : It is emphasized that the design procedures laid down here are not the only set of steps. The method followed in the U.S.R. consists of fixing the conductor size based on current density point-of-view for the load carried and the voltage, and then selecting the spacing between the phases from considerations

of surface voltage gradients. This usually requires conductors larger than used elsewhere. In the U.S.A., line designs for 750 kV and higher (1150 kV) are based on selecting the line clearance from the point of view of keeping the electrostatic field to below 9 kV/m, and then fixing other dimensions.

(f) Line Compensation

The line parameters calculated from final dimensions are :

	<u>L, mH/Km</u>	<u>C, nF/Km</u>	<u>X, ohm/Km</u>	<u>Y, mho/Km</u>	<u>r, ohm/Km</u>
400 kV.	0.985	10.82	0.31	3.4×10^{-6}	0.023
750 kV.	0.866	13	0.272	4.082×10^{-6}	0.0136

Example 1 : 400 kV, 400 Km, 500 MW/circuit

$$Z = 9.2 + j124, \quad Y = j1.36 \times 10^{-3}, \quad Z_0 = \sqrt{Z/Y} = 302.3 \angle -2.1^\circ$$

$$\sqrt{ZY} = pL = 0.411 \angle 88^\circ, \quad \cosh \sqrt{ZY} = 0.917 \angle .36^\circ, \quad \sinh \sqrt{ZY} = .4 \angle 88^\circ$$

For the line : $A = D = 0.917 \angle .36^\circ$, $B = 120.77 \angle 86^\circ$, $C = 1.32 \times 10^{-3} \angle 90^\circ$

Shunt reactors of 50 MVAR at 400 kV may be used at each end with $B_L = 0.3125 \times 10^{-3}$ mho.

$$\therefore A_T = D_T = A - j B_L B = 0.955$$

We select a sending-end voltage of 400 kV, giving a load-end voltage

of $V_R = V_S / A_T = 418.85$ kV which is below the maximum allowable value of 420 kV. $B_T = 120.77 \angle 86^\circ = B$.

$$C_T = C - B_L^2 B - j 2 B_L A = 0.65 \times 10^{-3} \angle 90^\circ$$

$$\therefore \% \text{ compensation} = (1.32 - .63) 100 / 1.32 = 52.3\%$$

With $V_R = 418.85$ kV and $V_S = 400$ kV, the centre and radius of receiving end circle diagram are as follows.

$$\begin{aligned} \text{Centre : } x &= -|(V_R^2 A_T / B_T)| \cos(\theta_B - \theta_A) = -96.8 \text{ MVAR} \\ y &= -|(V_R^2 A_T / B_T)| \sin(\theta_B - \theta_A) = -1384 \text{ MVAR} \end{aligned}$$

$$\text{Radius : } R = |V_R^2 A_T / B_T| = 1387.3 \text{ MVA}$$

For 500 MW, required switched capacitors amount to $Q_0 = 132$ MVAR for unity power factor load. If load power factor is lagging, more capacitive compensation across load will be required. For example, at 0.95 lag, total MVAR in capacitors is 287.

Example 2 : 400 kV, 800 Km, 500 MW/circuit, 50% series capacitor Compensation

$$Z = 18.4 + j248 = 248.6 \angle 85.8^\circ, Y = 2.72 \times 10^{-3} \angle 90^\circ, Z_0 = 302.3 \angle -2.1^\circ,$$

$$pL = \sqrt{ZY} = 0.822 \angle 88^\circ, \cosh pL = 0.6817 \angle 1.765^\circ, \sinh \sqrt{ZY} = 0.733 \angle 88.5^\circ$$

$$\text{For the line : } A = D = 0.6817 \angle 1.765^\circ, B = 221.5 \angle 86.37^\circ, C = 2.424 \times 10^{-3} \angle 90.6^\circ. \text{ For the series capacitor, } X_c = 124 \text{ ohms.}$$

Voltages selected are $V_R = 420$ kV, $V_S = 400$ kV, giving

$$|A_T| = V_S / V_R = 0.9524.$$

$$A_T = A - j B_L B - j \frac{X_c}{2 Z_0} \sinh \sqrt{ZY} - \frac{1}{2} X_c B_L (1 + \cosh \sqrt{ZY})$$

$$= (0.83166 + 116.81 B_L) + j (0.021 - 15.33 B_L)$$

This gives $B_L = 1.0333 \times 10^{-3}$ mho and 165 MVAR at each end at 400 kV.

$$\therefore A_T = 0.9524 \angle 3.13^\circ.$$

$$B_T = B - j \frac{1}{2} X_c (1 + \cosh \sqrt{ZY}) = 117.8 \angle 82.5^\circ$$

$$C_T = C - B_L^2 B - j2 B_L A - j \frac{1}{2} \frac{X_c}{Z_0} \frac{\cosh \sqrt{ZY} - 1}{Z_0} - \frac{X_c B_L}{Z_0} \sinh \sqrt{ZY} \\ + j \frac{1}{2} X_c B_L^2 (1 + \cosh \sqrt{ZY}) \\ = 0.802 \times 10^{-3} \angle 89.7^\circ.$$

Charging current = $C_T V_S = 185 \text{ A}$, MVAR = 128.

% compensation provided by shunt reactors = 67%.

Centre of receiving end circle : -193.5 MW, -1413 MVAR.

Radius $R = 1426 \text{ MVA}$.

Required switched capacitors at load end for 500 MW at unity power factor = 167 MVAR.

Example 3: 750 kV, 500 Km, 2000 MW.

$$A=D=\cosh pL = 0.866, B=129.2 \angle 90^\circ, C=1.945 \times 10^{-3} \angle 90^\circ.$$

$$\text{Try } V_R = V_S = 750 \text{ kV. } A_T = 1 = A - j B_L B \text{ giving } B_L = 1.037 \times 10^{-3} \text{ mho.}$$

At 750 kV, MVAR = 585 at each end

$$C_T = C - j2A B_L - B_L^2 B = 9 \times 10^{-6} \angle 90^\circ$$

% compensation = 95%, This may be too much. For 50% compensation, or 300 MVAR at each end, for $V_R = 750 \text{ kV}$, V_S comes to 700 kV.

For 400 MVAR compensation in shunt reactor at each end, $V_S = 720 \text{ kV}$ for $V_R = 750 \text{ kV}$. This will be selected. From circle diagram, for 2000 MW load at 1.0 p.f., switched capacitors for 500 MVAR are required.

VI REFERENCES

1. R.D. Begamudre : Limits for Interference Fields from EHV and UHV Power Transmission Lines - Part I : Radio Interference. C.B.I.P. Publication No. 170, 51st Research Meeting, Vadodara, January 1984. pp. 5-9.
2. *ibid*, pp. 11-14.
3. Symposium on Selection of Next EHV Transmission Voltage for India. C.B.I.P. Publication No. 142, New Delhi, May 1980.
4. High Voltage AC/DC Transmission. C.B.I.P. Publication No. 154, December 1981.
5. R.D. Begamudre and S. Ganga: Effect of Conductor Size on Problems Relating to 750 kV - 1150 kV Transmission. Proceedings of IInd National Power Systems Planning Conference, Jawaharlal Nehru Technical University, Hyderabad, September 1983, Vol. II.
6. Amruthakala, A : EHV and UHV Transmission Line Design Using Computer Graphics. C.B.I.P. Publication No. 162, 50th Research Meeting, Simla. March 1983.
7. S. Ganga : Calculation of Line Parameters and conductor Surface Voltage Gradients. Proceeding of Ist National Power System Planning Conference. Annamalai University, Sept. 1982. (Also C.P.R.I. Technical Report No. 118, Bangalore).
8. Air Pollution Handbook. McGraw-Hill Book Co.
9. Indian Standard No. IS-2071 Part 1-1974. Methods of High Voltage Testing. p. 16.
10. CIGRE/IEEE Survey of EHV Transmission Line Radio Noise. I.E.E.E. Trans. PA-S, 1972, pp. 1019-1028.
11. Comparison of Radio Noise Prediction Methods with CIGRE/IEEE Survey Results. *ibid*. pp. 1029-1042.
12. CIGRE/CISPR Publication No. 74 on Radio Noise.
13. Sujatha Subhash: RN levels of Existing and Proposed 400 kV Transmission Lines for India. EHV Forum, Institution of Engineers (India), Bombay Centre. Proceedings, December 1980. [Also C.P.R.I. Technical Report No. 101, October 1980.]
14. V.L. Chartier and R.D. Stearns : Formulas for Predicting Audible Noise from Overhead H.V. AC and DC Lines. IEEE Trans. PA-S, January 1981, pp. 121-130. Also, IEEE Trans. PA-S, October 1982, pp. 4090-4099.

15. Edison Electric Institute. EHV Transmission Line Reference Book. 1968. (750 3rd AVE., New York, N.Y. 10017)
16. G. Veena: Voltage Gradient Calculation and Selection of Conductor Size and Configuration for EHV Transmission Lines. C.P.R.I. Technical Report No. 91, Bangalore.
17. R.D. Begamudre : Voltage Gradient Calculation for 345 kV to 1500 kV AC Lines. C.B.I.P. Publication No. 142, New Delhi, May 1980.
18. J. Senthil : Analysis for Design of EHV and UHV 3-phase and 6-phase Lines Based on E.S. Field, AN, and RN. Dept. of EE, IIT Kanpur, June 1984. (M.Tech. Thesis).
19. R.D. Begamudre, Ravindra Arora, J. Senthil : E.S. Field, AN, and RI of 400-1300 kV Lines Existing and Proposed for India, and Comparison of AN Level of 1-phase and 3-phase Test Lines. Conference and Workshop on EHV Technology (Sponsors H.V. Eng. Dept., IISc., Karnataka St. Centre, Inst. of Eng. (Ind.), IEEE, Bangalore Section). Bangalore August 20-23, 1984. Conference Papers Volume.

PROCEDURES FOR E.H.V. LINE INSULATION DESIGNS

PART II : BASED UPON TRANSIENT OVERVOLTAGES

I. INTRODUCTION

Selection of conductor size, bundling, and other geometrical details of an e.h.v. line was the subject of discussion of Part I of this work, Reference 1. The present chapter, discusses insulation requirements based upon overvoltages caused by (a) power frequency, (b) lightning, and mainly (c) switching. These govern (i) insulation clearances, (ii) insulators and air-gap clearances required at towers, and (iii) insulation clearance between phase conductors in the span between towers.

Field studies conducted on an existing system, whose design has already been finalized and put into operation, are only helpful in checking the design adequacy of that particular system, and in addition provide a lot of data for a similar system in future. These field studies can also offer the basis for checking calculated values of overvoltages from model studies, which can take the form of physical models on a Transient Network Analyzer (TNA or ANACOM), and mathematical models using the Digital Computer. As such, all these studies are complimentary to each other. The results of field tests conducted on one system (or TNA and Digital computer study) should ~~not~~ be used for designing a future system elsewhere, as has been proved to be the case in most system designs carried out in North America, where field testing is being continuously undertaken by utilities at great expense. If such were not the case, then only one field test on any one system would have been adequate.

The principles upon which insulation levels are selected are only two: (1) A knowledge of all relevant properties of overvoltages which a system might experience; and (2) a knowledge of insulation characteristics for all types of voltages to which it will be subjected. Both of these factors have been the sub-

ject matter of very extensive, exhaustive, expensive, and enlightened studies all over the world where e.h.v. laboratories have been very active in this field of research and development. As such, only the broad principles will be discussed here to synthesize the present state of the art and provide new formulas to apply to the design of line insulation. Specific cases of a 400-kV line and a 750-kV line will be presented in order to realize the design procedure and to check its adequacy.

No design procedure can be considered as yielding the final result, because all such studies lead to the main objective of evolving a preliminary design for the tower structure details and clearances, which will then make it easy during mock-up studies to verify and finalize the design. EHV line clearances have now become so large that they have reached the saturation region in the gap length - breakdown or withstand voltage relation so that even a slight reduction in the switching overvoltage magnitude brings about a considerable decrease in air-gap clearance required, resulting in economy.

II. DISCUSSION OF ROD-PLANE GAP DESIGN

The basis for selection of air-gap clearances between any given type of electrode geometry can be related to the rod-plane gap properties. As a preliminary example to illustrate the procedure of selection of insulation clearance and the effect on non-linearity in the V_{50} -d relation, where V_{50} = critical flashover (50% probability) voltage in kV and d = gap distance in metres, we assume the positive switching-surge formula of Leroy and Gallet of E.dé F. which is $V_{50} = 3400/(1+8/d)$, Reference 2. We now apply this formula for a 400-kV line and a 750-kV line. The 1 p.u. line-to-ground crest value is $420 \sqrt{2/3} = 343$ kV at the maximum operating voltage of 420 kV, r.m.s., for the 400-kV line, and $750 \sqrt{2/3} = 612.4$ kV crest for the 750-kV line. For switching surge levels of 1.8 p.u. to 3 p.u., the required air-gap lengths are calculated and as a comparison calculations are also made accor-

ding to Paris's formula, Reference 3: $V_{50} = 500 d^{0.6}$. The withstand voltage for all gap lengths is assumed to be $V_{50}/1.15$.

Table I : Rod-Plane Gap clearance for 400-kV and 750-kV Lines
Based upon Positive Switching Surges (voltages in kV,
gap length in metres).

400-kV Line					750-kV Line			
P.U. value K_S	With- stand $V_W = 343 K_S$	CEO $V = 1.15 V_W$	$d_1 =$ $8 / \left(\frac{3400}{V} - 1 \right)$	$d_2 =$ $\left(\frac{V}{500} \right) 1.667$	$V_W =$ 512.4 K_S	CEO $V = 1.15 V_W$	d_1	d_2
1.8	617.4	710	2.1	1.8	1102	1267	4.753	4.712
2.0	686	789	2.42	2.14	1225	1408	5.66	5.62
2.2	754.6	867.8	2.74	2.51	1347	1549	7	6.59
2.4	823.2	946.7	3.09	2.9	1470	1690	7.91	7.61
2.6	892	1025.6	3.455	3.31	1592	1831	9.34	8.7
2.8	960.4	1104.5	3.85	3.75	1715	1972	11.05	9.85
3.0	1029	1183.4	4.27	4.2	1837	2113	13.13	11.04

The above figures reveal the following properties:

- 1) For the 400-kV line, an increase in switching-surge magnitude from 1.8 to 3.0 p.u. (an increase of 66.7% over 1.8 p.u.) requires an increase of 103.3% (2.17 m over 2.1 m) in air-gap when using the Leroy and Gallet formula. Paris's formula gives a 2.4 m increase over 1.8 m or 133.3% for the same range of switching-surge magnitude change of 66.7% over 1.8 p.u.
- 2) For the 750-kV line, the non-linear effect is more pronounced. The gap length has increased from 4.753 m to 13.13 m, an increase of 176%, for 66.7% increase in voltage.

The calculations given above are based on certain important assumptions which have experimental basis, but have serious limitation if applied universally. Therefore, in the opinion of the author, each case must be checked for adequacy on a mock-up in an e.h.v. laboratory. These limitations will be detailed in later

sections. The assumptions made for these calculations are as follows :

- a) The withstand voltage is 15% lower than to 50% flashover voltage V_{50} .
- b) This is based on the well-known and nearly universally-adopted rule that the withstand voltage is 3 standard deviations below the CFO.
- c) The standard deviation is $\sigma = 5\%$ of CFO. These are average values and show wide variations in practice which depend on several important factors such as
 - i) the choice of waveshape of switching surge;
 - ii) the variation of σ with the wavefront time of surge as well as the gap length;
 - iii) atmospheric conditions; and
 - iv) that the flashover probability follows a Gaussian distribution with a known median value and standard deviation.

In addition to the above two formulas, $V_{50} = 3400/(1+8/d)$ and $500d^{0.6}$, which have been used before, there are several other empirical formulas available in the extensive technical literature on the subject of flashover of long gaps, (Reference 4 and bibliography given in Section X). Some of these are quoted below for the CFO or 50% flashover voltage. The values are crest voltages and for positive polarity (except for a.c.) and in kV when the gap length d is in metres.

Gap Geometry	Lightning	D.C.	Power Frequency	Switching Surges
1) Rod-Plane	1.25/50 μ s: 500d 1/50:667d 1.2/50:540d	500d 500d+1	652d ^{0.576} 455d+25	535.5d ^{0.552} 500d ^{0.6} 3400(1+8/d) 100($\sqrt{50d+1}$ -2)
2) Rod-Rod	1.2/50 μ s: 580d	555d	500d	120/400 μ s 687.d ^{0.6} 350/2300 μ s 872.d ^{0.429}

III. CONDUCTOR-TO-TOWER AND CONDUCTOR-TO-GROUND CLEARANCE

The rod-plane gap length required for positive-polarity switching surges ranging from 1.8 p.u. to 3.0 p.u. on a 400-kV line and a 750-kV line have been given in the previous section. The conductor-to-tower clearance is determined through a 'gap factor' $K=1.3$ when the tower structure is above and lateral from the conductor. This means that the CFO for this electrode configuration or geometry is 1.5x the CFO of a rod-plane gap of the same length. This is based on the work of Paris.

Having calculated the conductor-to-tower clearance d , the minimum conductor-to-ground plane clearance will be taken to be $h=4.3+1.4d$ metres, Reference 5.

Accordingly, the following values for conductor-tower and conductor-ground clearances will be typical for the 400kV line and 750-kV line.

Table II. Conductor-Tower and Conductor-Ground Gaps for 400-kV and 750-kV Lines

P.U.S.S.	1.8	2.0	2.2	2.4	2.6	2.8	3.0
Conductor-Tower Gap	$d = (V_{50}/650)^{1.667}$, metres						
400 kV	1.16	1.38	1.62	1.87	2.14	2.42	2.715
750 kV	3.04	3.63	4.25	4.92	5.62	6.36	7.133
Conductor-Ground Gap	$h = 4.3 + 1.4d$						
400 kV	5.924	6.232	6.57	6.92	7.3	7.69	8.1
750 kV	8.56	9.38	10.25	11.2	12.17	13.2	14.29

IV. PHASE-TO-PHASE CLEARANCE

The phase-to-phase clearance required from switching-surge considerations are also designed on the same principles. An average 'gap factor' for conductor-conductor CFO over a ground plane can be assumed to be 1.8 (Reference 5) which allows rod-

plane gap CFO values to be translated to apply to the conductor-conductor gap which will be $V_{50}=900 d^{0.6}$. In this case, we have to design the required gap on the basis of expected maximum phase-to-phase switching-surge magnitude. This will be taken to range from 2.5 to 3.5 p.u. with 1 p.u. = 343 kV for the 400-kV line and 612.4 kV for the 750-kV line. Then, the following clearances between phases far from the tower will be typical.

Table III : Phase-to-phase Clearance for 400-kV and 750-kV Lines (voltages in kV crest, d in metres)

P.U.S.S.	2.5	2.7	2.9	3.1	3.3	3.5
<u>400-kV Line</u>						
V_W , kV crest	857.5	926	995	1063	1132	1200
$V_{50}=1.15V_W$	986	1065	1144	1223	1302	1381
d, rod-plane $(\frac{V_{50}}{500})^{1.667}$	3.1	3.5	3.97	4.44	4.93	5.43
d, cond.-cond. $(\frac{V_{50}}{900})^{1.667}$	1.164	1.324	1.492	1.67	1.85	2.04
<u>750-kV Line</u>						
V_W	1531	1653.5	1776	1898	2021	2143
V_{50}	1761	1902	2042	2183	2324	2465
d _{r-p}	8.15	9.27	10.44	11.66	12.95	14.28
d _{c-c}	3.06	3.48	3.92	4.38	4.86	5.36

Once again, these are based on the assumptions that (a) the withstand voltage is 3% lower than the CFO, and (b) the standard deviation = 5% of CFO. This has serious limitations.

From these discussions, it should be evident that design of insulation clearances is based on an immense amount of experimental investigations. The sections to follow will discuss the need for correction factors to be applied to the previous type of calculations before the final choice of insulation clearances is made.

Before this is carried out, we must check whether the previous air-gap clearances from conductor-to-tower are adequate for

power-frequency and lightning voltages.

V. CLEARANCES FOR POWER FREQUENCY AND LIGHTNING

In carrying out the check for the adequacy of the above-calculated clearances based on positive switching-surge considerations, several governing criteria are postulated below:

- 1) Extreme angle of swing of insulators from vertical will be
 - a) for Power Frequency : 60°
 - b) for Lightning Impulse : 30°
 - c) for Switching Surge : 15°

They are based on the assumption that power-frequency excitation is continuous and maximum swing under a severe storm is 60° . Lightning strokes and insulator swing are based on observed probability of simultaneous occurrence, as also for switching operations. During thunderstorm activity, wind gusts are less severe than in storms and the maximum angle of swing is assumed to be 30° . Switching surge flashover, which is assumed to occur once in 500 operations at the ~~30~~-level postulated earlier, is taken to occur when the maximum swing of insulator is 15° . These are probability events and must be ascertained on a case-by-case study. Projects especially devoted to such study are therefore of the utmost importance, Reference 6.

The practice in the USSR is not to allow any swing when considering the clearance required for switching surges. This is based on the assumption that the probability of swing occurring simultaneously with maximum possible switching surge is nil, (Reference 7).

- 2) The ratio of minimum air-gap length inside the tower window to the length of insulator string is usually 1 from switching-surge consideration.

These will form the bases for checking design adequacy for power-frequency and lightning voltages.

An example of a 2 p.u. switching surge on the 750-kV line will be discussed. With surge-suppression resistors in breakers, this is a valid value. The procedure for other p.u. values and other voltages are similar. From previous calculations it has been observed (see Table II) that the required average clearance to tower is 3.63 metres. With an insulator length L and 15° swing, the width of tower window is $2(3.63 + L \sin 15^\circ)$ while the depth is $(L + 3.63)$. Drawing a circle for the window, there results $2(3.63 + L \sin 15^\circ) = L + 3.63$ giving $L = 7.525$ m (24.7 ft). The size of window is $7.525 + 3.63 = 11.155$ m (36.6 ft). The actual tower window could be of any shape provided it accommodates these clearances. A length of 7.525m for the insulator will accommodate about 45 discs and hardware.

From data available of insulator flashover tests, for 2 p.u. switching surge of 1224 kV on the 750-kV line, the required insulator length based on dry flashover is 4.3m (14 ft) with 26 discs. Allowing 40% more for wet flashover, the insulator length can be increased to 6 metres and 36 discs. Under dry conditions the ratio of insulator length to the minimum strike distance is $4.3/3.63 = 1.185$ while the final value is $6/3.63 = 1.65$. This gives the distance from the bottom of the top cross-arm to the lower brace of the tower window to be 9.63 m, while the strike distance to the side is still kept at 3.63 m at maximum swing of 15° . With 6m length for insulator and 15° swing allowed, the clearance from the rest position of insulator to the side is $3.63 + 6 \sin 15^\circ = 5.2$ m and the tower width will be a minimum of 10.4m. Thus, the horizontal and vertical distances of the tower window are nearly equal (10.4m, 9.63m). Conditions will be different if a double 90° -V string is employed for the centre phase in the window.

In practice, a leakage distance of 2.25 to 2.54 cm/kV (0.9-1.0 in/kV), r.m.s. line-to-ground voltage, is used for power frequency, Reference 8. An average $5\frac{3}{4} \times 10$ " disc gives a leakage distance of 31.8 cm (12.5 in) so that the 36-disc string has a leakage distance of 11.45m (37.5 ft) giving 2.44 cm/kV. $(750/\sqrt{3} \times 450 = 0.96 \text{ in/kV} = 2.44 \text{ cm/kV})$.

Now, consider a swing of 60° . The CFO voltage for a rod-plane gap at 50 Hz is taken to be $652 d^{0.576}$, crest, which gives a withstand voltage for the conductor-tower gap (with $\sigma = 5\%$, $K = 1.3$, and $V_{50} = 1.15 V_W$) $V_W = (1.3 \times 652 / 1.15) d^{0.576}$. The required gap for a voltage of 612.4 kV crest at 50 Hz will then be given as $d = (612.4 \times 1.15 / 1.3 \times 652)^{1/0.576} = 0.831 \text{ m}$. However, at 60° swing and 6 m length of insulator in a 5.2 m half-window, the clearance is zero since $6 \sin 60^\circ = 5.2$. Therefore, under the assumptions postulated, the tower window has to be widened to a minimum of $5.2 + 0.831 = 6.031$ metres from the rest position of insulator to the sides giving a horizontal width of 12.1 m (39.7 ft) while retaining a depth of 9.63 m (31.6 ft). This permits a maximum swing of 23.6° of the 6-m insulator string while still retaining 3.63 m clearance required for switching surge condition.

For lightning, allowing a swing of 30° , the resulting strike distance is $6.03 - 6 \sin 30^\circ = 3.03 \text{ m}$ (10 ft). The CFO under lightning for a rod-plane gap is taken to be $V_{50} = 500d$. Corresponding withstand voltage, with gap factor of 1.3 and $V_W = V_{50} / 1.15$, for the 3.03-m gap is $V_W = (650 \times 3.03 / 1.15) = 1713 \text{ kV}$. This is 2.5 p.u. which is considered as adequate. Dillard and Hileman, Reference 9, find a CFO voltage of about 1750 kV crest for a 10-foot strike distance inside the tower window which gives a withstand voltage of 2.5 p.u. based on 30° down, $\sigma = 5\%$ of CFO and 1 p.u. = 612.4 kV, crest. Their observations for a 1100-kV tower yield $\sigma = 1\%$ for dry flashover and $V_{50} = 574d$, kV.

Allowing 30° swing of the 6-foot insulator for switching surge condition and increasing the tower width will make the design still safer for lightning. With $\sigma = 1\%$, the withstand voltage is also higher for the same gap length. Their p.u. lightning surge allowed is 1.96 p.u.

The above discussions raise many questions for which satisfactory answers must be provided by e.h.v. laboratories and investigators under Indian conditions, since the extremely large number

of variables involved are local to the line environment. This strengthens the need to treat each line design on its own merits.

VI. VARIATION OF CRITICAL FRONT TIME, CFO AND GRADIENT WITH GAP LENGTH FOR ROD-PLANE GAP

It has been mentioned in the introduction that the wavefront time at which the minimum CFO under positive switching-surge occurs will vary with the gap length for all electrode geometries. For rod-plane gaps, from best available data from all over the world upto 25 m gaps, Reference 10, this author has formulated the following relations for the salient properties of CFO:

a) Time-to-crest at Minimum CFO:

$t_{fc} = 43.65 d^{1.0215}$, μs (with d in metres). It applies for gaps from 3 to 15 metres, the best fit occurring between 4 and 13 m. This range in gap length covers the requirements for switching surge magnitudes considered in Section II for a 400 kV line between 2.4 to 3 p.u., and for 750 kV line between 1.8 to 3.0 p.u. over-voltages.

b) Minimum CFO:

$$V_{50m} = (355-15d)d, \text{ kV crest.}$$

c) Average Gradient at Minimum CFO:

$E_{50m} = V_{50m}/d = 355-15d$, kV/m, crest, It might be of some interest to compare these values with Paris's formula : $V_{50} = 500d^{0.6}$.

$d, \text{ m}$	4	6	8	10	12
$(355-15d)d, \text{ kV}$	1180	1590	1880	2050	2100
$500d^{0.6}, \text{ kV}$	1149	1465	1741	1990	2221

The discrepancy is believed to be due to the fact that Paris used the same wave-front time for the positive switching surge for all gap lengths upto 8m which had the timings 120/4000 μs . When conducting such tests it is evident that a switching surge generator capable of delivering a variable waveshape must be available in an e.h.v. laboratory. The gap length determined on the basis of $V_{50} = 500 d^{0.6}$ will be slightly longer.

VII VARIATION OF STANDARD DEVIATION AND WITHSTAND VOLTAGE

In previous sections, the standard deviation in flashover voltage was uniformly assumed to be $\sigma = 5\%$ of CFO for all gap lengths, voltage waveshapes (power frequency, lightning, and positive switching surge), and all gap geometries (rod-plane, conductor-to-tower, and conductor-conductor). Experiments performed all over the world show this to be not the case. The results are so erratic about this quantity that it is impossible to take a single value for σ , as concluded by Watanabe, Reference 11. The proposed Swedish 800 kV system was designed on the basis of $\sigma = 8\%$ and using Paris's formulas, Reference 5. In view of lack of agreement on this topic, the IEEE has recommended a value of $\sigma = 5\%$, Reference 10. The British Columbia Power Authority in Canada has tested 500-kV tower insulation and found $\sigma = 6$ to 8.6% of CFO in wet tests and 5% under dry tests for the tower-window gap, Reference 8. Recent tests conducted on 1200-kV tower insulation by joint US-USSR efforts have yielded σ values between 3.5% and 7.5% of CFO, Reference 12. The second assumption made earlier was that the withstand voltage is 3σ lower than V_{50} , the critical or 50% probability of flashover voltage. This figure has been accepted nearly all over the world, with some exceptions who prefer 2σ lower than V_{50} , giving a larger probability of flashover since the gap length based on $(V_{50} - 2\sigma)$ is now smaller.

VIII. NETWORK TRANSIENT STUDIES

The second item to be ascertained with confidence is the expected maximum switching-surge magnitude for a given system on a probability basis. So much has been done on this topic and is still being carried out that it is impossible to give the expected values for phase-to-neutral and phase-to-phase switching surges on a universal basis. This is a case-by-case study.

Appendix I gives a summary of a typical TNA study carried out on a 500 kV/230 kV system as reported in Reference 13. This indicates exhaustive studies as the need for design. Appendix I does

not give the expected phase-to-phase voltages. This may reach a maximum of 3.34 p.u. in studies reported by Wilson in Reference 14. Several studies conducted under the author's guidance on TNA's have been reported to the C.B.I.P. and elsewhere; References 15-17.

Evaluation of phase-to-phase switching-surge magnitudes is gaining increasing importance in view of the fact that for voltages of 500 kV and higher, the rope and chainette concepts in line construction are being considered where phase conductors are supported by insulator strings from each other while the tower structures are removed to the sides, References 18,19.

IX. CONCLUSIONS.

1. A systematic method for synthesizing all available formulas for estimating air-gap clearances of e.h.v. lines is presented, and their limitations discussed.
2. Conductor-to-tower, conductor-to-ground, and conductor-to-conductor clearance for a 400-kV ~~and~~ 750-kV line are worked out according to Paris's formulas and compared with others where necessary.
3. Equations derived by the author for (a) variation of critical wave-front time at minimum 50% flashover voltage, (b) the minimum value of 50% or critical flashover voltage, and (c) the average voltage gradient at the minimum CFO with gap length for a rod-plane gap are given, and they are compared with the work of others for CFO using constant wave-front time for all gap lengths.
4. The paper discusses the need for carrying out insulation tests on towers on a case-by-case basis in order to determine the values of all controlling parameters required to determine even a preliminary design which can be tested in an e.h.v. laboratory for design adequacy and for evolving the final design.

5. Clearances designed on the basis of switching-surge requirements are checked for adequacy under power-frequency and lightning voltages, and in one example of a 750-kV line it is shown that insulation clearance at tower designed entirely for switching surge may not be adequate for other types of voltages.
6. Atmospheric correction factors are not dealt with in the paper.

X. REFERENCES AND BIBLIOGRAPHY

[Items 1-19 are referred in the paper]

1. R.D. Begamudre : Procedures for Designing EHV Lines Based upon Steady-State Limits. (This volume).
2. G. Gallot and G. Leroy: IEEE Conference Paper No. C73-408-2, 1973. (Also Review Lecture, Proc. 3rd International Conf. on Gas Discharges, 1974).
3. L. Paris: Influence of Air Gap Characteristics on Line-to-ground Switching-surge Strength; IEEE Transactions, Power Apparatus and Systems, 1967, pp. 936-947.
4. J.M. Meek and J.D. Craggs: Electrical Breakdown in Gases. Cambridge University Press. 1978.
5. The Swedish 800-kV system. CIGRE Proceedings, 1974, Paper No. 31-11. Also 1978, Paper No. 31-03.
6. Edison Electric Institute: EHV Transmission Reference Book, 1968.
7. Design of the EHV 1150-kV AC Transmission Line of the USSR. CIGRE, 1976, Paper No. 31-03.
8. H.S.H. Goff, D.G. McFarlane, and F.J. Turner: Switching-Surge Tests on Peace River Transmission-Line Insulation. IEEE Trans. PAS. 1966, pp. 601-613.
9. J.K. Dillard and A.R. Hileman: UHV Transmission Tower Insulation Tests. *ibid*, 1970, pp. 1772-84.
10. IEEE Working Group on Insulator Switching Surges (Lightning and Insulator Subcommittee): Guide for Application of Insulators to Withstand Switching Surges. *ibid*, 1975, pp. 58-67. (Also the extensive list of references in this paper).
11. Y. Watanabe: Switching Surge Flashover Characteristics of Extremely Long Air Gaps. *ibid*, 1967, pp. 933-936.
12. F.S. Young, E.M. Schneider, Y.M. Gutman, and N.N. Tikhodcyev: USA-USSR Investigation of 1200-kV Tower Insulation. *ibid*, 1980, pp. 462-470.

13. J. Sabath, H.M. Smith, and R.C. Johnson: Analog Computer Study of Switching Surge Transients for a 500-kV system. *ibid*, 1966, pp. 1-9.
14. D.D. Wilson: Phase-phase and Phase-neutral Switching Surges on 500-kV Open-ended Lines, *ibid*, 1969, pp. 660-665.
15. R.D. Begamudre, S. Subhash, K.S. Meera, and M. Kanya Kumari: Effect of Line-coil Representation in a TNA on Switching Transients of Transmission Lines. Central Board of Irrigation and Power, 51st Research Meeting, Vadodara, 1984, and C.B.I.P. Publication No. 170, pp. 15-22.
16. S. Subhash, K.S. Meera and K.S. Jyothi: Digital Computation and Model TNA Investigations of Switching Surges of 3-phase Transmission Systems. C.B.I.P. Publication No. 162. pp. 63-71, 50th Research Meeting, Simla, 1983.
17. S. Subhash, K.S. Meera, and M. Kanya Kumari: Switching Over-voltage Study on Transmission Lines with Complex Terminations by TNA Models and Digital Calculation, *ibid*, pp. 73-81.
18. J.E. Dulus and R.Y. Shuping: Design of 500 kV Transmission Line Cross-Rope Suspension Structures. Proc. American Power Conference, Chicago, 1982, pp. 665-670.
19. R.L. Retallack: The Chainette Structure Concept. *ibid*, pp. 660-664.
20. S. Annestrand, E.F. Bossuyt, and N. Dag Reppen: Insulation Performance Analysis of a 500-kV Transmission-line Design, *IEEE Trans.*, PAS, 1970, pp. 429-437.
21. IEEE Working Group on Switching Surges: Switching Surges: Part IV-Control and Reduction on A.C. Transmission Lines. *ibid*, 1982, pp. 2694-2702.
22. R. Cortina, M. Sforzini, and A. Taschini: Strength Characteristics of Air Gaps Subjected to Interphase Switching Surges. *ibid*, 1970, pp. 448-452.
23. A.R. Hileman, P.R. Leblanc, and G.W. Brown: Estimating the Switching Surge Performance of Transmission Lines. *ibid*, 1970, pp. 1455-1469.
24. G.L. Wagner and J.W. Bankoske: Evaluation of Surge-Suppression Resistors in H.V. Circuit Breakers. *ibid*, 1967, pp. 698-707.
25. R.N. Newsom, et.al.: Staged Tests on the TVA-SCEC 500-kV Interconnection Between Johnsonville and West Memphis. *ibid*, 1967, pp. 1389-1399.

26. IEEE Substation Committee Working Group 78.1: Safe Substation Grounding - Part II. *ibid*, 1982, pp. 4006-4023.
27. IEEE Committee Report: Report on Industry Survey of Protective Gap Applications in H.V. Systems. *ibid*, 1967, pp. 1432-1437.
28. N. Giao Trinh and Claire Vincent: Statistical Significance of Test Methods for Low Probability Breakdown and Withstand Voltages. *ibid*, 1980, pp. 711-719.
29. J.G. Kassakian and D.M. Otten: On the Suitability of a Gaussian Stress Distribution for a Statistical Approach to Line Insulation Design. *ibid*, 1975, pp. 1624-1628.
30. H. Patrunke, et.al.: Switching of Transformers, Reactors and Long Transmission Lines. Field Tests in German 420-kV Networks. CIGRE 1980 Session. Paper No. 13-08
31. G. Köppl and E. Ruoss: Switching Overvoltages in EHV and UHV Networks. *Brown Boveri Review*, 1970, pp. 554-561.
32. E. Ruoss and P. Djurdjevic: Network Analyzers for Studying Transient Phenomena in HV Networks. *ibid*, 1968, pp. 734-739.
33. S.H. Sarkinen and D.A. Bradley: Impulse Tests on UHV Air Gap Configurations. *Proc. American Power Conference*, 1982, pp. 678-682.
34. G.D. Friedlander: UHV-Onward and Upward. *IEEE SPECTRUM*, Feb. 1977, pp. 56-65.
35. A Study of the Design Parameters of Transmission Lines above 1000 kV. CIGRE, 1972, Paper 31-15.
36. R.D. Begamudre: Design Characteristics of Air-Gap Insulation of EHV and UHV Transmission Lines. *Proceedings of Winter School on H.V. Technology and Laboratory Measurements. I.I.T., Kanpur, EE Dept. December 1982.*
37. E. Ruoss: Overvoltages on Energizing H.V. Lines. *Brown Boveri Review*, 1979, pp. 262-270.

SWITCHING SURGE VOLTAGES FROM MODEL STUDIES ON T.N.A.

D: SOURCE TRANSFORMER TERTIARY EFFECT

1. Switching Open Ended Line:

a)	High-side energizing with trapped charge	3.0
3.3 i)	With transformer tertiary	3.3
3.3 ii)	Without tertiary	3.3

b) High-side energizing = dead line without

trapped charge:

2.1	i)	With transformer tertiary
2.6	ii)	Without tertiary

1.P.U.
on all
, -1, -1)

c) Low-side Energizing of transformer and Line:

2.7	i) Without transformer	2.8	tertiary
2.0	ii) Without transformer	2.0	

iii) With shunt reactor connected to tertiary for 50% compensation

E. Lightning Arrester

Arrested at sending end set to spark at:

hc	a) 2.0 p.u.
2.0	b) 1.5 p.u.

Arrester included at receiving end,
and set to spark at 1.5 p.u.

In all cases where overvoltages exceeded 2.0
2.3 p.u., 1200 ohms was included

G. High-Speed Reclosing After Fault Clearing:
(With trapped charge) 5.6

•

$$\begin{array}{cc} 4 & 5 \\ 2 & 3 \end{array}$$

SWITCHING SURGE CALCULATION ON LINES

Insulation design of e.h.v. lines is based primarily on clearances required to withstand switching-surge overvoltages caused when a sinusoidal source with practically infinite short-circuit capability is switched to energize a line. Conditions are very severe during re-energization when trapped charge from a previous de-energization operation is held by the line capacitance.

Before analyzing the transmission network by mathematical models (usually using the digital computer) it may be informative to engineers to provide an idea of the per unit values of overvoltages caused by switching operations. The most severe overvoltage conditions occur when re-energizing open-ended transmission lines, but an analysis of most types of terminal conditions of a system must be carried out for possible resonance conditions. Table I is a summary of Switching-surge voltages reported on a 500 kV/230kV system with an autotransformer, with or without tertiary windings. These values were obtained by the authors of that paper on one particular system and do not apply universally. Each system must be studied on a case-by-case basis.

The analysis in this chapter begins with single-phase circuits and then will indicate the procedure for extending to 3-phase circuits. Even for 1-phase analysis, it is simplest to commence with a lumped-parameter circuit and then observe the changes necessary to deal with a distributed-parameter transmission line. An actual system will consist of combinations of lumped parameters (such as generator series inductance, transformer leakage inductance, shunt reactors, etc) and distributed-parameter lines. This is the chief difficulty in analyzing switching surge problems.

At the outset it is made clear that there exist a very large number of methods for analysis. The more important ones are given here which are (a) the method of Laplace Transforms; (b) the method of Fourier Transforms. The former leads to (i) travelling-wave method, and (ii) standing-wave method.

It is emphasized at the outset that the interested reader should derive all equations on his/her own.

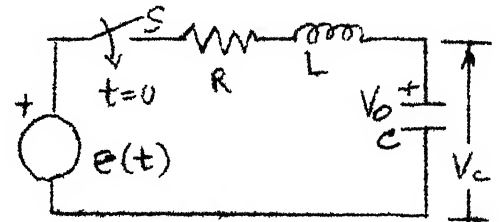
SINGLE-PHASE CIRCUITS AND LINES

I. Single-Frequency Lumped-Parameter Circuit

Ideas involved in analyzing and understanding the behaviour of voltage at the open end of a long line with distributed parameters when switched by a step or sinusoidal voltage input can be very easily illustrated by considering a series R-L-C circuit with lumped parameters. The circuit is shown in Figure 1.

We assume that the capacitor is initially charged to a voltage V_0 and no current exists in the circuit prior to closing the switch S.

The problem is to determine the current and the voltage V_c across the capacitor as functions of time t .



The Laplace Transforms of the quantities are :

Source voltage : $E(S) = E/S$ for step, $\frac{E_m}{S^2 + \omega^2} (S \cos \phi - \omega \sin \phi)$ for an input of $e(t) = E_m \cos (\omega t + \phi)$.

The angle ϕ denotes the point on the wave at the instant of switching from the peak value of the sinusoidal wave of frequency $f = \omega/2\pi$.

Resistance voltage : $R I(s)$, $I(s)$ = Laplace Transform of current.

Inductance voltage : $e_L = L \frac{di}{dt}$, $E_L(S) = L_S I(s)$, with no initial current.

Capacitor voltage : $e_c = \frac{1}{C} \int_0^t i dt + V_0$; $E_c(s) = \frac{1}{Cs} I(s) + \frac{V_0}{S}$.

The general equation for the current and voltage V_c will be, with $\alpha = R/2L$ and $\omega_0^2 = 1/LC - \alpha^2$ or $\alpha^2 + \omega_0^2 = 1/LC$,

$$I(s) = \frac{sE(s) - V_0}{L} \cdot \frac{1}{s^2 + \frac{R}{L}s + \frac{1}{LC}} = \frac{sE(s) - V_0}{L[(s + \alpha)^2 + \omega_0^2]}$$

APPENDIX - I SWITCHING-SURGE VOLTAGES FROM MODEL STUDIES ON T.N.A.

RDB-106

A. Switching an Open-ended Line

1. Switching from High Voltage Side (500kV)

a) With trapped charge on line: 2,260 MVA source short circuit power 13,600 MVA Infinite Bus at source	3.5 3.8 4.1	i) With transformer tertiary ii) Without tertiary	3.0 3.3
b) Without trapped charge on line: 2,260 MVA source short circuit power 13,600 MVA	2.1 2.6	i) With transformer tertiary ii) Without tertiary	2.0 2.1
c) De-energizing without fault: No restriking in breaker	1 P.U. trapped on all lines(+1, -1, -1)	c) Low-side Energizing of transformer and line:	
d) De-energizing or unfaulted line: with re-strike in breaker	2.7	ii) With transformer tertiary Without tertiary	2.8 2.0
e) De-energizing line with a line to ground fault (270 Kms)	1.3	iii) With shunt reactor connected to tertiary for 50% compensation	2.6

2. Switching from Low-Voltage Side (220KV)

Transformer has no tertiary, line has no trapped charge since transformer drains the charge in 5 to 10 cycles.

B. SWITCHING A TRANSFORMER TERMINATED LINE

High-voltage side closing; source transformer has no tertiary

C. SERIES CAPACITOR COMPENSATION:

Upto 50%
No charges
in overvoltage
magnitudes.

D. SOURCE TRANSFORMER TERTIARY EFFECT

1. Switching Open Ended Line:

a) High-side energizing with trapped charge			
i) With transformer tertiary	3.5		3.0
ii) Without tertiary	3.8		3.3
b) High-side energizing a dead line without trapped charge:	4.1		
i) With transformer tertiary	2.1		2.0
ii) Without tertiary	2.6		2.1
c) Low-side Energizing of transformer and line:	1 P.U.		
trapped on all lines(+1, -1, -1)			
ii) With transformer tertiary	2.7		2.8
Without tertiary			2.0
iii) With shunt reactor connected to tertiary for 50% compensation	1.3		2.6
E. <u>Lightning Arrester</u>			
Arrester at sending end set to spark at:			
a) 2.0 p.u.			3.0
b) 1.5 p.u.			2.6
Arrester included at receiving end, and set to spark at 1.5 p.u.			2.2
F. <u>Surge Suppressing Resistor in Breaker</u>			
In all cases where overvoltages exceeded 2.3 p.u., 1200 ohms was included			2.0
G. <u>High-Speed Reclosing After Fault Clearing:</u> (With trapped charge)			3.6
H. <u>Effect of Non-Synchronous Operation of Circuit breaker poles</u>			
a) Breaker poles close within 1/2 cycles			2.4
b) Breaker poles close on 1 cycle			3.5

$$\text{and } V_c(s) = \frac{1}{cs} I(s) + \frac{V_o}{s} = \frac{s E(s) - V_o}{LC s[s + \alpha^2 + w_o^2]} + \frac{V_o}{s}$$

(a) Step Response : The inverse transform with $E(s)=E/S$ gives

$$V_c(t) = (E - V_o) \left[1 + e^{-\alpha t} \frac{\sqrt{\alpha^2 + w_o^2}}{w_o} \sin(w_o t - \phi_o) \right] + V_o$$

where $\tan \phi_o = w_o/\alpha$.

This expression applies when $R < 2\sqrt{L/C}$, giving an oscillatory condition. As a check we observe that at $t = 0$, the expression reduces to V_o and at $t = \infty$, it is E , the step input.

For the very important and worst case, when $V_o = -E$,

$$V_c(t) = 2E \frac{1}{w_o \sqrt{LC}} e^{-\alpha t} \sin(w_o t - \phi_o) + E.$$

For very lightly - damped circuit, $\alpha \ll w_o$ and $\phi_o \approx 90^\circ$.

$$\therefore V_c(t) = E [1 - 2 e^{-\alpha t} \cos w_o t].$$

This reaches a maximum of nearly $3E$ when $w_o t = 180^\circ$, i.e. one half-cycle later based on the natural frequency $f_o = w_o/2\pi$. When the trapped charge is zero, i.e. $V_o=0$, the maximum is $2E$.

Therefore it should be evident that the capacitor must be designed with an insulation level of 3 p.u. in order to take care of its initial voltage being equal and opposite to the input step. This is a case which parallels the voltage at the open end of a line when switched by a sinusoidal source at its peak value while the line holds a trapped voltage.

In switching transmission lines, the voltage is high when series resistance is not used in the circuit breaker. A resistance-switching scheme brings the voltage to not more than 2 p.u. Thus, it is important to note the effect of varying R on the capacitor voltage in this simple circuit also. Normally, in transmission lines, the value of resistance used is a little over the surge-impedance of the line, i.e. $R \approx \sqrt{L/C}$. In this circuit, let $R = 2\sqrt{L/C}$ which is the critical-damping case giving $w_o = 0$. for

the step input, $V_c(s) = \frac{E-V_0}{LC} \frac{1}{s(s+\alpha)^2} + \frac{V_0}{s}$

and the inverse transform is $V_c(t) = (E-V_0)[1-e^{-\alpha t}(1+\alpha t)] + V_0$.
For the case when $V_0 = -E$, $V_c(t) = E-2E e^{-\alpha t}(1+\alpha t)$. By differentiating with respect to t , the maximum occurs when $t = 0$. Therefore the capacitor voltage will not exceed the initial voltage. At $t = \infty$, its voltage is equal to the step.

(b) Sinusoidal Excitation : $e(t) = E_m \cos (wt + \phi)$.

The responses are

Current

$$I(t) = \frac{E_m \cos (wt + \phi + \psi_1)}{\sqrt{R^2 + (wL - \frac{1}{wc})^2}} - \frac{V_0}{wL} e^{-\alpha t} \sin w_0 t$$

$$+ \frac{E_m e^{-\alpha t}}{w_0 L [\frac{w^2 R^2}{L^2} + (\frac{1}{LC} - w^2)^2]} \left[-\left\{ (w^2 - \frac{1}{LC}) \sin \phi + 2\alpha w \cos \phi \right\} w_0 w \cos w_0 t \right.$$

$$\left. + \left\{ \frac{1}{L^2 C^2} + \left(\frac{R^2}{2L^2} - \frac{1}{LC} \right) w^2 \right\} \cos \phi \right.$$

$$\left. + \alpha w \left(\frac{1}{LC} + w^2 \right) \sin \phi \right] \sin w_0 t \}.$$

where $\alpha = \frac{R}{2L}$, $w_0^2 = \frac{1}{LC} - \alpha^2$, $\tan \psi_1 = \frac{\frac{1}{wc} - wL}{R}$

The capacitor voltage is, with $\tan \phi_0 = w_0/\alpha$,

$$V_c(t) = \frac{E_m \cos (wt + \phi + \psi_1)}{w_c \sqrt{R^2 + (wL - \frac{1}{wc})^2}} + \frac{V_0 e^{-\alpha t}}{w_0 \sqrt{LC}} \cos (w_0 t - \phi_0)$$

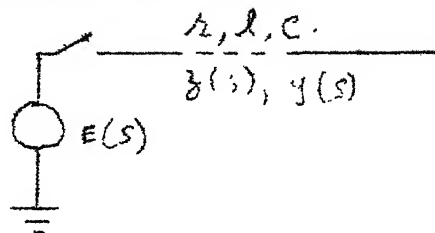
$$+ \frac{E_m \cos \phi \cdot e^{-\alpha t}}{w_0 LC [\frac{w^2 R^2}{L^2} + (\frac{1}{LC} - w^2)^2]} \left[w_0 (w^2 - \frac{1}{LC}) \cos w_0 t - \frac{R}{2L} (w^2 + \frac{1}{LC}) \sin w_0 t \right]$$

$$+ \frac{E_m \sin \phi \cdot e^{-\alpha t}}{w_0 LC [\frac{w^2 R^2}{L^2} + (\frac{1}{LC} - w^2)^2]} \left[\frac{R}{L} \left(\frac{1}{LC} + \frac{R^2}{4L^2} \right) \cos w_0 t - \left(w^2 + \frac{R^2}{2L^2} - \frac{1}{LC} \right) \sin w_0 t \right]$$

II. Single-Phase Line Energized by Source : Open-ended

1) No trapped charge, no series impedance

Let $x = 0$ at the open end and $x=L$ at the source end for the line of length L . Then it is clear that at $x=0$, the current is zero, and at $x=L$, the voltage is $E(s)$.



The differential equations for the line are :

$$dV(x,s)/dx = z(s) \cdot I(x,s), \text{ and}$$

$d I(x,s)/dx = y(s) \cdot V(x,s)$, where $z(s) = r + ls$ and $y(s)=cs$, which are called the impedance and admittance operators per unit length. The quantities r, l, c are the series resistance, inductance, and shunt capacitance of the line to ground per unit length. We have omitted the shunt conductance g per unit length, but in a general analysis, this also can be included when the effect of corona losses have to be taken into account. Let $p^2 = z(s) \cdot y(s)$.

The voltage and current are functions of both x and s , the L-transform operator. For ease in writing, we will omit x and s in the brackets.

The general solutions can be assumed to be $V = A e^{px} + B e^{-px}$, and $I = (p/z) (A e^{px} - B e^{-px})$. The quantity $(z/p) = \sqrt{z/y} = Z_0$ which is the surge-impedance of the line. p is the propagation constant per unit length. They are both in operational form. The quantities A and B are not functions of x but possible functions of s .

By using the boundary conditions, we obtain

$$V(x,s) = E(s) \cdot \cosh px / \cosh pL$$

$$\text{and } I(x,s) = E(s) \cdot \sinh px / Z_0 \cdot \cosh pL.$$

In particular, at the open end, $V_0 = E(s) / \cosh pL$.

(a) Travelling-wave Solution

A travelling-wave is described through a velocity of propagation and an attenuation factor. These are obtained as follows: The propagation factor can be written as

$$p^2 = (r+ls) / cs = lc(s^2 + (r/l)s) = lc[s + r/2l]^2 - r^2/4l^2$$

If resistance is very low, we can write this approximately as $p \approx \sqrt{lc} (s + a) = s/v + a$, where v = velocity of propagation and a = attenuation factor per unit length. Note that $a = r/2lv = r/2Z_0$, where the surge impedance is $Z_0 = lv = 1/cv = \sqrt{l/c}$. These expressions are valid only if the resistance is negligible and for low attenuation.

Now, $V_0 = E(s) / \cosh pL = 2E(s) / (e^{pL} + e^{-pL})$.

This can be written in a series expansion form

$$\begin{aligned} V_0(s) &= 2 E(s) [e^{-pL} - e^{-3pL} + e^{-5pL} - e^{-7pL} + \dots \text{to infinity}] \\ &= 2 E(s) [e^{-aL} \cdot e^{sL/v} - e^{-3aL} \cdot e^{s \cdot 3L/v} + \dots]. \end{aligned}$$

Let e^{-aL} be denoted as A_0 = attenuation of voltage or current when travelling over one line length L , and $L/v = T$, the time taken to travel over one line length. Then,

$$V_0(s) = 2 E(s) [A_0 \cdot e^{sT} - A_0^3 \cdot e^{s \cdot 3T} + A_0^5 \cdot e^{s \cdot 5T} - \text{etc}]$$

The inverse transform of $F(s) \cdot e^{s \cdot kT}$ has the same shape as the inverse transform of $F(s)$ but its appearance at any point is delayed in time by (kT) .

(i) Step Response

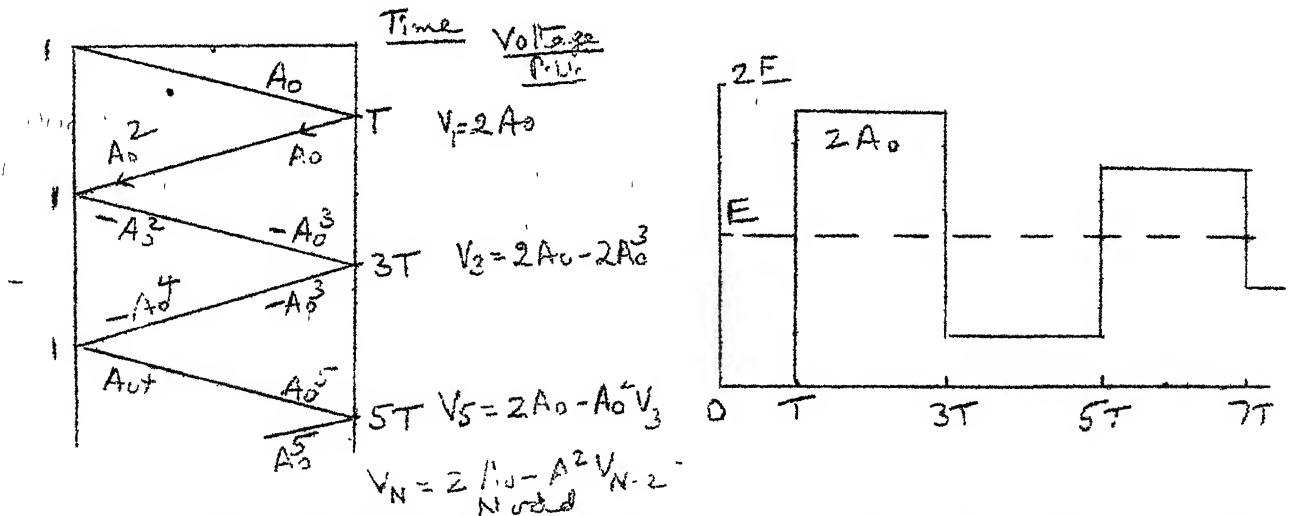
Let us consider the conditions at the open end of line when the input is a step of height E . Then, the following sequence of events will take place.

At $t=T$, the step arrives at the open end with an amplitude $A_0 E$ after having travelled over a distance L . It is accompanied by a current wave. At the open end, the current will be zero so that the current will be zero.

a backward-travelling wave from the open end to the source. The voltage reflects positively and the open-end voltage doubles to $2A_0E$ which is the inverse transform of the first term in $V_0(s)$. The reflected voltage wave, A_0E , arrives at the source after a time T with an amplitude A_0^2E , and since the source voltage is constant, this will be totally reflected back into the line negatively. At $t = 3T$, this voltage ($-A_0^2E$) arrives at the open end with an amplitude ($-A_0^3E$) which doubles and reflects back. The voltage at the open end at $t = 3T$ is then $2E(A_0 - A_0^3) = 2EA_0(1 - A_0^2)$.

The reflections and voltage doubling keep on repeating indefinitely until reduced to negligible value for the n -th reflection to ignore further values.

The sequence of events can be kept track on a lattice diagram called the Bewley Lattice Diagram, and the time variation can be plotted easily. This is shown in Figure 3.



Several important properties may be noted from these events.

- 1) The highest voltage for which line insulation at the open end must be designed is $2A_0E$ when trapped charge is absent. In transmission lines, the value of A_0 is about 0.9 depending upon line and ground resistance and line length. $\therefore V_{0(\max)} = 2E$.
- 2) When trapped charge is present, $V_{0(\max)} = 3E$. In practice the maximum value is about $2.8E$. We may note that this value was obtained for the lumped-parameter single-frequency R-L-C series circuit also.

- 3) The periodic-time of the voltage wave is $4T$. It therefore appears that the phenomenon is taking place as if it has the frequency $f = 1/4T = v/4L$. This has great importance when calculating the line parameters with ground return. The ground-return resistance and inductance are frequency-dependant so that the frequency to be used for evaluating them depends on the length of line being switched. The following frequencies for line lengths from 100 Km to 800 Km apply, based on light velocity.

L =	100	200	300	400	600	800, Km
f =	750	375	250	187.5	125	94, Hz.

When ground-return inductance is neglected, this is valid. But usually, the velocity is 83% light velocity in practice.

- 4) The time during which the maximum voltage will be present is $2T$. For a 300-Km line, this is 2 ms or 2000 μ s. The wave front is very steep, practically vertical, for a step. We can now appreciate that a switching-surge waveform of 250 μ s/2500 μ s is very nearly approached during these operations although the actual waveform will depend on many factors.
- 5) As a mathematical exercise, the final value of open-end voltage will be

$$V_o(\infty) = 2E(A_o - A_o^3 + A_o^5 \text{ ---}) = 2E A_o / (1 + A_o^2).$$

and not E . This is because of the approximation made in the value of p .

$$\text{For } A_o = 0.9, \quad V_o(\infty) = (1.8/1.81) E = 99.5\% E.$$

$$\text{For } A_o = 0.8, \quad V_o(\infty) = (1.6/1.64) E = 97.5\% E.$$

ii) Sine Wave Response

The principles given for the step response can be easily extended when the source is sinusoidal and is switched on to the open-ended line. For preliminary discussion, consider the source voltage to be switched-on to the line when it has a peak value.

Its equation is $e(t) = E_m \cos \omega t$. If it is switched at any other point on the wave, we will have to take $e(t) = E_m \cos (\omega t + \phi)$ where ϕ = the angle after the peak at the instant of switching. For now, let $\phi=0$. The sequence of events will now be as follows:

- 1) At $t=T$, the voltage reaching the open end is $E_m(\cos \omega x_0)$. A.
- 2) This doubles up giving $V_1 = 2A E_m(\cos \omega x_0)$.
- 3) The reflected wave is $A \circ E_m$ which will reach the source whose internal impedance is taken to be zero. Therefore, the reflected wave is $-A^2 E_m$. This will reach the open end at $t = 3T$ with value $-A^3 E_m$. In addition, the source will send the voltage $E_m \cos (\omega x_2 T)$ which has the value at the open end of $A E_m \cos (\omega x_2 T)$.
- 4) Following the procedure, it is then easy to write the sequence of voltages received at the open end at various times.

$$t = T : V_1 = 2A E_m$$

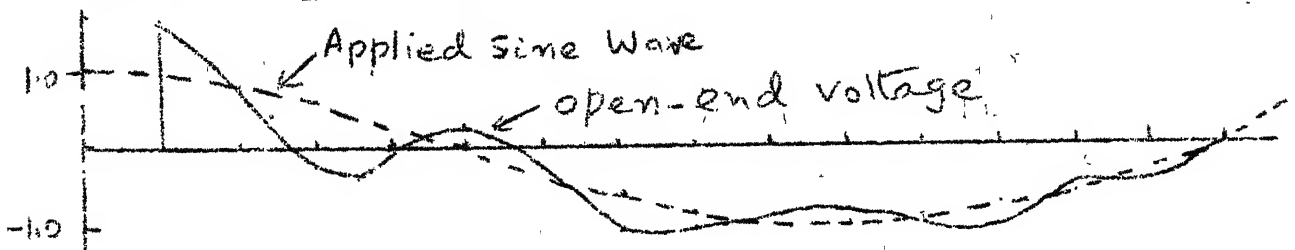
$$t = 2T : V_2 = 2A E_m \cos \omega T$$

$$t = 3T : V_3 = 2A E_m \cos (\omega x_2 T) - A^2 V_1$$

$$t = 4T : V_4 = 2A E_m \cos (\omega x_3 T) - A^2 V_2$$

$$t = 5T : V_5 = 2A E_m \cos (\omega x_4 T) - A^2 V_3$$

$$t = NT : V_N = 2A E_m \cos \omega x(N-1)T - A^2 V_{N-2}$$



The figure shows the resulting open-end voltage for a 400 kV line of $L=300$ Km with the following line parameters :

$R = -452 \frac{\Omega}{km}$ including ground return, $L_1 = 1.51 \text{ mH/km}$

$C_1 = 9.2 \text{ nF/km}$, $Z_0 = 404$, $\alpha L = LR/2Z_0$, $A = e^{-\alpha L} = 0.845$

If the point-on-the wave switching is to be included, we would only add ϕ in the cosine term.

(b) Standing-wave Solution

The Laplace-Transform of open-end voltage is

$$V_0(s) = E(s) / \cosh pL \quad \text{with } p^2 = (r + ls) \text{ cs, when } g = 0.$$

In the travelling-wave method, an attempt was made to separate p into an attenuation term and a time-shift term. In the method of standing waves, the inverse transform is evaluated directly by the method of residues. This yields an infinite number of frequency terms just as the travelling-wave method gave an infinite number of reflection terms.

(i) Step Input : For this case,

$$V_0(s) = \frac{E}{s} \frac{1}{\cosh pL}$$

The first step is to find the location of the poles at which the denominator becomes zero. It is easy to see that a simple pole exists at $s = 0$. The residue at this pole is

$$V_0(0) = V_0(s) \cdot s \cdot e^{st} \Big|_{s=0} = \frac{E}{\cosh \sqrt{(r+ls)cs}} \Big|_{s=0} = E, \text{ the step}$$

The second term in the denominator is $\cosh pL$ which will become zero whenever $pL = \pm j(n+1)\frac{\pi}{2}$, with $n=0, 1, 2, \dots, \infty$. Thus, we have an infinite number of poles. In such a case, the residue is evaluated by the equation

$$V_0(n) = \frac{E}{s} \frac{e^{st}}{d(\cosh pL)/ds} \Big|_{pL = \pm j(n+1)\frac{\pi}{2}}$$

Now, when $pL = \pm j(2n+1)\frac{\pi}{2}$, $p^2 L^2 = -(2n+1)^2 \pi^2 / 4$

or $L^2 (r+ls) \text{ cs} = -(2n+1)^2 \pi^2 / 4$.

This is a quadratic equation in s and the values of s are found from

$$L^2 c s^2 + L^2 r c s + (2n+1)^2 \pi / 4 = 0$$

which yields $s = -a + j w_n$ where $a = r/2l$ and $w_n^2 = (2n+1)^2 \pi^2 / 4L^2 lc - a^2$.

The term a is the attenuation factor and w_n is the natural radian frequency. The first natural frequency is with $n=0$, ($v=1/\sqrt{lc}$),

$$w_0/2\pi = \frac{1}{4L\sqrt{lc}} \sqrt{1 - 4a^2 L^2 lc / \pi^2} = \frac{1}{4(L/v)} \left(1 - \frac{4a^2 L^2}{\pi^2 v^2} \right) \approx \frac{1}{4T}$$

when a is negligible,

This can be seen to correspond to the travelling wave case.

The residues at each pole can be evaluated now.

$$\text{Now, } \frac{d}{ds} \cosh pL = (\sinh pL) \cdot L \cdot \frac{dp}{ds}.$$

$$(a) \text{ with } pL = j(2n+1)\frac{\pi}{2}, \sinh pL = j \sin (2n+1)\frac{\pi}{2} = j(-1)^n.$$

$$(b) L \frac{dp}{ds} = \frac{L}{2} \frac{2lcs + rc}{\sqrt{(r+ls)cs}} = \frac{L^2}{2} \frac{2lc(-a+jw_n)+rc}{j(2n+1)\frac{\pi}{2}}$$

$$\text{But } 2lc a = rc.$$

$$\therefore \left. \frac{d}{ds} \cosh pL \right|_{pL=j(2n+1)\frac{\pi}{2}} = j(-1)^n \frac{j L^2 w_n lc}{j(2n+1)\pi} = j(-1)^n \frac{L^2 w_n lc}{(2n+1)\pi}$$

This gives the residue at any pole $s = -a + jw_n$ to be

$$V_0(n+) = \left. \frac{E e^{st}}{s \frac{d}{ds} \cosh pL} \right|_{s=-a+jw_n} = \frac{(-1)^n E e^{-at} \cdot e^{jw_n t} (2n+1)\pi}{j(-a+jw_n) \cdot L^2 w_n lc}$$

$$= -(-1)^n \frac{E e^{-at} (2n+1)\pi}{2L^2 lc w_n} \cdot \frac{e^{jw_n t}}{w_n + ja}$$

Similarly, at $s = -a - jw_n$, which is the complex conjugate of $s = -a + jw_n$, the residue will be equal to the complex conjugate of the residue $V_0(n+)$.

Then, $V_o(t) = \frac{E_m}{(m^2+n^2)} \cos (wt + \phi - \psi)$

$$+ E_m \sum_{k=0}^{\infty} \frac{(-1)^k \cdot (2k+1) \pi e^{-at}}{L^2 l c w_k (p_2^2 + 4a^2 w_k^2)} \left[\cos \phi \left\{ w_n (p_2 - 2a^2) \cos w_k t - a (2w_k^2 + p_2) \sin w_k t \right\} + w \cdot \sin \phi \cdot (p_2 \cos w_k t - 2a w_k \sin w_k t) \right]$$

It consists of a steady-state response term, and transient response terms which decay with the time constant $\tau = 1/a = 2l/r$.

III FOURIER-TRANSFORM METHOD

This method applied to propagation of lightning and switching surge response of distributed-parameter lines when in combination with lumped parameter circuit elements is of recent origin. The lumped parameters are series impedance of source, shunt reactors, series resistances used in circuit breakers, loads, substation transformers etc.

We will illustrate the method for obtaining the voltage at the open end of a line. This was derived as $V_o(s) = E(s)/\cosh pL$, where p is a function of the distributed line parameters r, l, g, c . In the Fourier-Transform Method we write $S = a + jw$. Then,

$$V_o(a+jw) = E(a+jw) / \cosh L \sqrt{\{r+l(a+jw)\} \{g+c(a+jw)\}}$$

1) Step Response: Here, $E(a+jw) = E/s = E/(a+jw)$. $\cosh pL$ can be expanded and written as $M+jN$. Then, $V_o = E / \{ (a+jw) (M+jN) \} = E / \{ (aM-wN) + j(aN+wM) \}$. This is separated into its real part p and j -part, Q . $P = E(aM-wN)/D$, $Q = -E(aN+wM)/D$, where $D = (aM-wN)^2 + (aN+wM)^2$.

Finally, the time response is calculated from the Inverse Fourier Transform using either P or Q :

$$V_o(t) = F^{-1}[V_o(a+jw)] = \frac{2}{\pi} e^{at} \int_0^{\infty} \left\{ \begin{array}{l} (P \cdot \cos wt) \\ (-Q \cdot \sin wt) \end{array} \right\} \sigma_f \cdot dw,$$

where σ_f is called the 'sigma factor' which helps in the convergence of the integral. The integral is evaluated numerically

according to the following procedure.

- a) The limits for integration are changed to w_i and w_f , instead of 0 and ∞ .
- b) The sigma factor is written as $\sigma_f = \sin(\pi w/w_f)/(\pi w/w_f)$.
- c) A trapezoidal rule can be used by evaluating the ordinates at w and $(w+\Delta w)$ by selecting a suitable increment Δw in frequency. Then the integral can be written as the sum, with $n=(w_f-w_i)/\Delta w$,

$$V_o(t) = \frac{2e^{at}}{\pi} \sum_{k=1}^n [P(w_k) \cdot \cos w_k t \cdot \sigma(w_k) - P(w_{k-1}) \cdot \cos w_{k-1} t \cdot \sigma(w_{k-1})] \cdot (w_f - w_i)/n$$

where $w_{k-1} = w_i$ at $k=1$.

- d) The integration or summation depends on the value of the exponent a . This imposes very serious restrictions and a very large number of trials must be made before the final choice for the value of a is decided upon. One rule is to commence with the value $(a T_f) = 4$, where T_f is the final value of time upto which calculations are of interest. For example, if $T_f = 20$ ms (1 cycle time on 50 Hz basis) $a = 4/20 \times 10^{-3} = 200$. In some cases, the calculation may proceed in stages and a different value of a may be selected. For example, if T_f is to be 40 ms, a value of 200 during the first 20 ms of the calculation may be used and then a value of 100 for the next 20 ms.
- e) The integral also depends on the final value of w . Again, the choice is based on trial and error. One rule is that w_f should be greater than the reciprocal of the fastest rise time of the voltage involved in the problem. The step is the worst voltage for this method and any value of w_f that yields the proper response for a simple problem will give adequate results for all other types of excitation.

The values of M and N can be worked out to be as follows :

$$M = \left[\frac{1}{2} (\sqrt{J^2 + K^2} + J) \right]^2, \quad N = \left[\frac{1}{2} (\sqrt{J^2 + K^2} - J) \right]^2, \quad \text{where } J = L^2 \{ (r+la)(g+ca) - lc w^2 \}, \quad \text{and } K = L^2 \{ (r+la) cw + (g+ca)lw \}.$$

2) Sine Wave Excitation

For this case, $e(t) = E_m \cos (w_0 t + \phi)$, where $w_0 = 314$ for $f = 50$ and $\phi =$ angle on the wave at the instant of switching from the positive peak. Then, with $s = a + jw$, and $E(s) = E_m [\cos \phi \cdot s - w_0 \cdot \sin \phi] / (s^2 + w_0^2)$,

$$V_0(a + jw) = E_m [\cos \phi \cdot (a + jw) - w_0 \cdot \sin \phi] / [\{ (a + jw)^2 + w_0^2 \} (M + jN)]$$

This can be split into the real part, P, and j-part, Q, and the previous procedure followed for evaluating the inverse Fourier Transform giving $V_0(t)$.

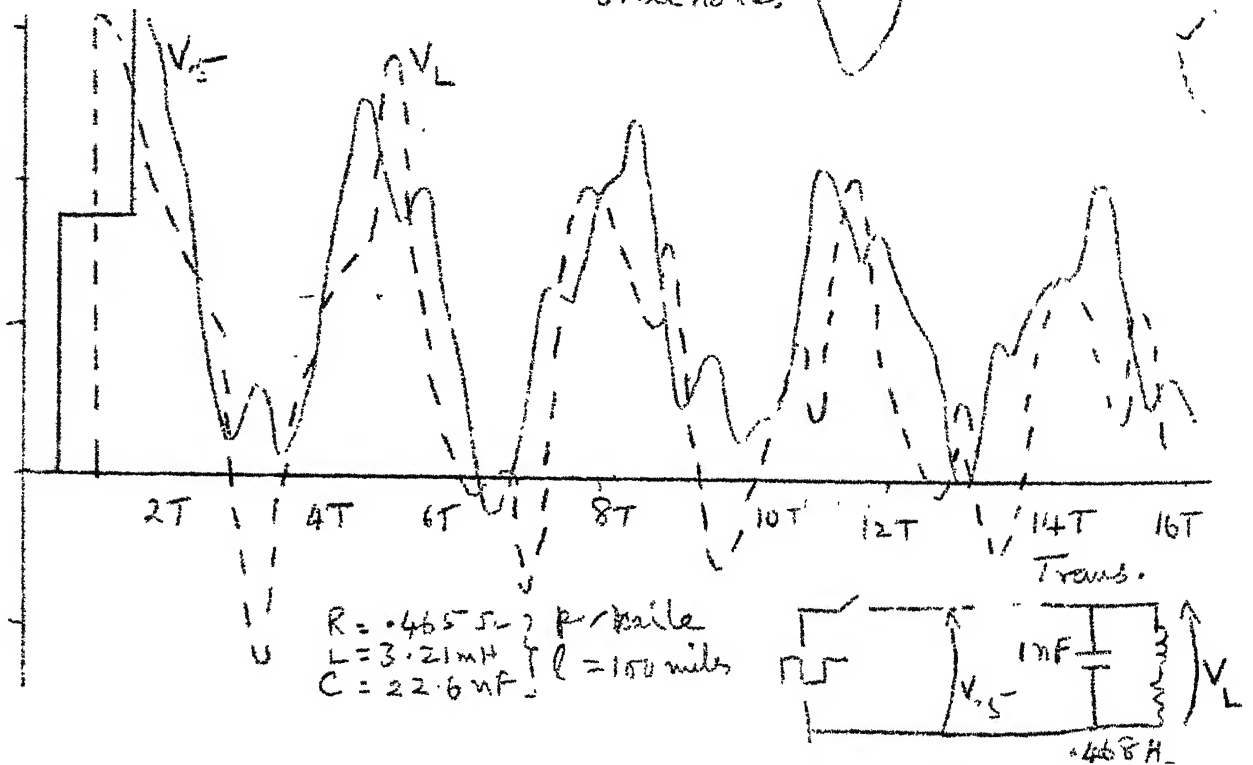
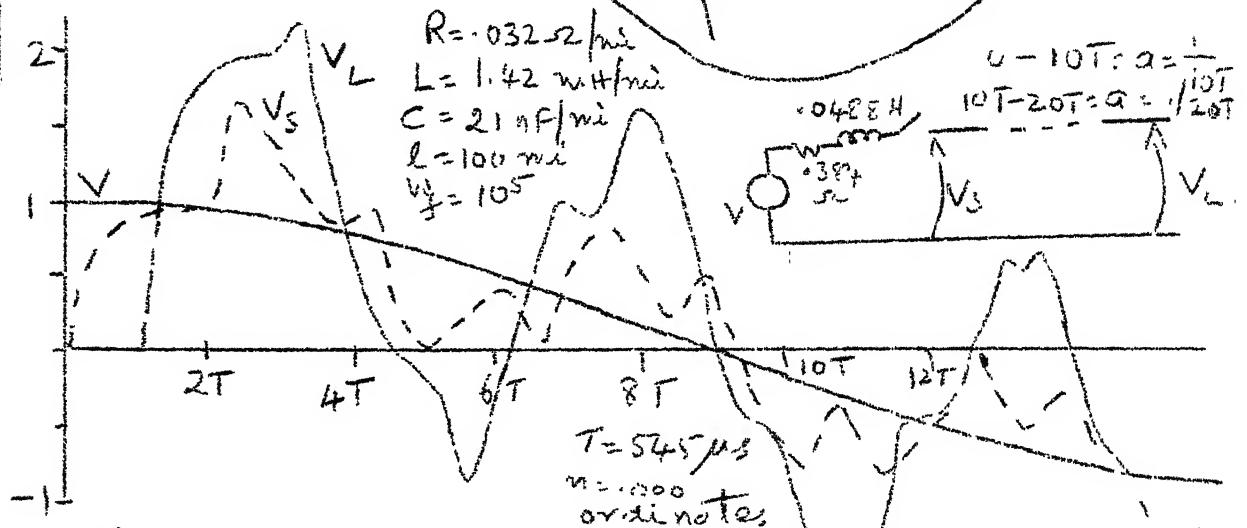
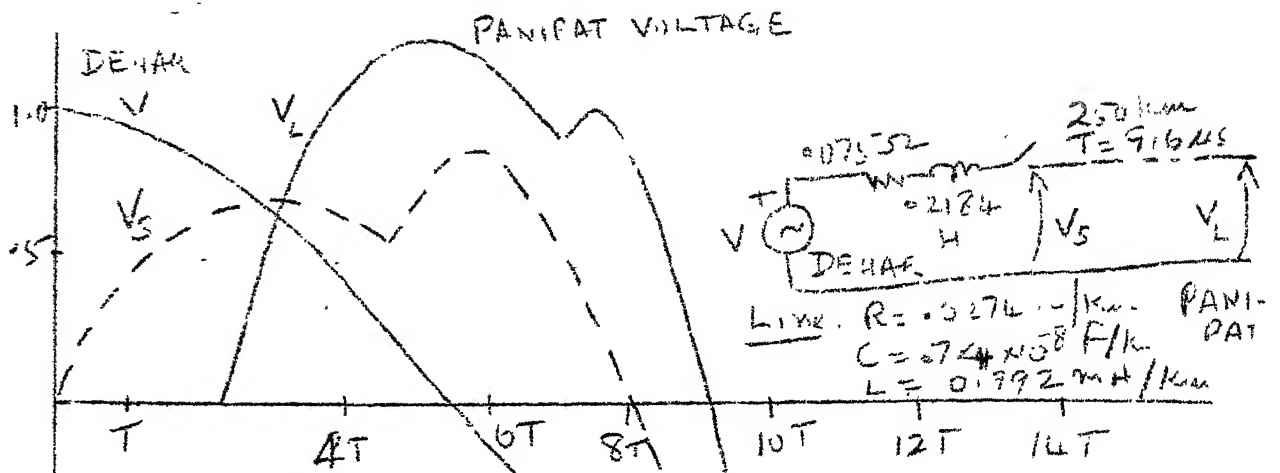
An example of switching a 400-kV line from Dohar Power Station to the Panipat Receiving Station of the Northern Regional Electricity Board is given in the figure for sinusoidal excitation when $\phi = 0$.

Please see the next page.

Another example is worked out when the far end of the line is terminated in a large transformer or a receiving station which can be replaced by a combination of capacitance and a parallel branch consisting of an inductance and resistance.

IV THREE-PHASE SYSTEMS

The above methods considered only a single-phase system. The extension to 3-phases can be carried out by first splitting the mutually-interacting systems into 3 mutually-independent systems by diagonalization procedures outlined in a previous chapter by using the transformation matrix $[T]$, and its inverse $[T]^{-1}$. The writing is very lengthy and is not given here.



INSULATION CHARACTERISTICS OF LONG AIR GAPS

1. Types of Electrode Geometries Used in EHV Lines

In e.h.v. transmission systems, all external insulation is air (and in recent years SF_6). Air gaps have reached lengths upto 20 metres and will continue to increase. In this chapter we will consider the insulation properties of only long air gaps."

The breakdown and withstand voltages of airgaps is controlled by the geometry of electrodes which have to be insulated by the gap. The electric field distribution in all cases is non-uniform. The figure shows some electrodes.

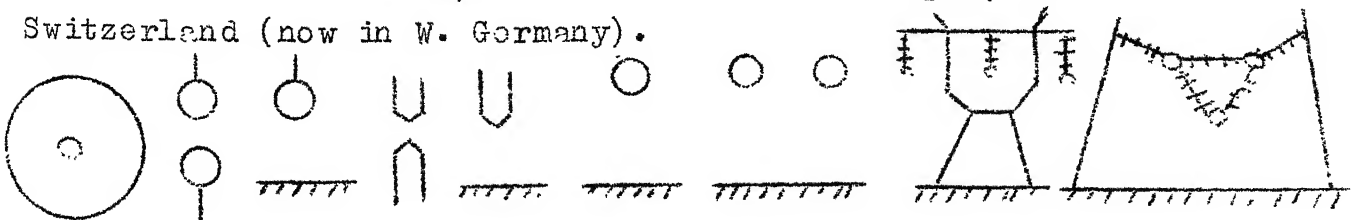
2. Types of Voltages in EHV Lines

The above gaps are subjected to several types of voltage wave-shapes. The breakdown and withstand voltages have to be ascertained for all these waveshapes. They are: (a) Power Frequency AC; (b) DC (+ and -); (c) Lightning impulses (+, -); (d) Switching Surges (+, -).

In both indoor and outdoor h.v. labs, experiments at great expense have been and are being conducted, and along with these, theoretical models for breakdown are also being evolved. Once these mechanisms are theoretically understood, it will reduce the expense involved in setting up large-scale experiments, as well as help in proper design of experiments and interpretation of the results.

3. Breakdown Characteristics

The following empirical relations between the 50% flashover voltage value and the gap length are nearly valid for design purposes. They are based mostly on the work of Paris of Italy, Leroy and Gallet of E. de F., Watanabe and Udo of Japan, and Feser of Switzerland (now in W. Germany).



Positive Polarity CFO (d in metres, voltage in kV crest).

Rod-Plane: Lightning Impulse : $1.25/50\mu s$ - $V_{50} = 550 d$, kV
 $1/50$ - $667 d$
 $1.2/50$ $540 d$

D.C.

Power Frequency

$$V_{50} = 500 d$$

$$V_{50} = 652 d^{0.576}$$

$$V_{50} = 455 d + 25$$

Switching Surges

120/4000 μs

$$V_{50} = 535.5 d^{0.552}$$

$$(3 < d < 9)$$

$$V_{50} = 500 d^{0.6}$$

$$V_{50} = 100(\sqrt{50d+1}-2.5)$$

$$V_{50} = 3400/(1+8/d)$$

Many attempts have been made to explain these equations which are based entirely on experimental results. The theoretical models have been based on vastly different basic assumptions, and a serious worker still has the opportunity to consolidate these several assumptions and put together better models. Briefly, the basic mechanism of breakdown appears to be:

- (i) Before breakdown is reached, there is an intense corona envelope formed on the highly-stressed electrode. This is particularly intense on the positive rod. This spherical corona envelope is assumed to have a diameter ranging from 20 cm to 1 metre.
- (ii) The corona gives rise to leader channels of about 1-3 mm in diameter such that the radial electric field is 20 kV/cm with a charge of about 0.5 to 1 $\mu c/cm$. These leaders fork out in all directions, but the one that eventually causes sparkover propagates along the axis of the gap. It is preceded by a leader-corona at its tip. The axial electric field in the leader column is about 5 kV/cm.

- (iii) When the leader-corona has reached a length of 4.5 to 5 m in a 7 m-gap, or about 65-70% length, the influence of the leader on the plane cathode is so intense that there is a jump-phase where the acceleration of the leader is high enough to bridge the gap and sparkover occurs. In a rod-rod gap, a negative leader propagates from the negative rod also to meet the positive-leader.

The following theoretical equations are available based on various assumptions for positive switching surges.

I. Lemke's Model ($d < 10\text{m}$)

$$V_s = 450 [1 + 1.33 \ln (d - \ln d)], \text{ kV.}$$

II. Waters' Model

$$V_s = (1.5 \times 10^6 + 3.2 \times 10^5 d)^{0.5} - 350, \text{ kV}$$

III. Alexandrov's Model ($r=0.9\text{m}$)

$$V_s = 1260 r (1 - r/d)^{0.5}, \tanh^{-1} \sqrt{1 - r/d}, \text{ kV.}$$

All the three models yield nearly the same value for V_s for d upto 10m, while II and III agree upto 20 m. It is therefore surprising how widely-different assumptions can lead to close results. They also come close to experimental formulas quoted earlier.

4. Positive Switching-Surge Flashover : Saturation Problem

The positive switching surge flashover and withstand voltage characteristics of long gaps are the most important and interesting because an air gap is weakest for this type of voltage wave-shape. The s.s. magnitude determines by and large the gap length required in tower windows, insulator lengths, phase-to-phase clearance and conductor-to-ground clearance. The problem is complicated since the CFO voltage depends upon.

- (a) the wavefront time of the switching surge, and
- (b) the presence of insulators in the tower window.

Therefore, no two laboratories agree on the CFO value of a given gap length. From a very large number of experimental results available, some important observations are worth noting. These are as follows:

1. The CFO voltage of tower windows with insulator strings inside varies with the switching-surge wavefront time.
2. The CFO voltage also varies with the percentage of space filled by the porcelain with higher permittivity than air.
3. The CFO voltage depends on the ratio of length of the shortest distance in air between conductor and tower to the length of the porcelain insulator. A ratio of 0.85 to 1 is usually used.
4. The first tower-window insulation strength was established by J.W. Kalb of the Ohio Brass Co. of U.S.A. under switching surges. According to his experimental findings for a 525-kV tower with 24 discs in the insulator string, minimum CFO occurred at a wavefront time of 250 μ s.
5. Subsequent results obtained from all over the world at many voltage levels have yielded the wavefront time for minimum CFO ranging from 55 to 300 μ s.
6. Since Kalb's experiments, the standard waveshape for switching surge has been accepted as 250/2500 μ s for line equipment testing.
7. This does not necessarily mean that insulation structures tested using the standard waveshape will yield the worst s.s. strength. Each airgap clearance has to be tested individually with varying front times to ascertain minimum CFO.
8. The widths of tower structures used in experiments have a considerable effect on the CFO voltage, as well as the length of conductor used on either side of a tower mock-up in an c.h.v. laboratory. This is because pre-breakdown phenomena depend on the presence of metallic parts near the conductor.
9. The CFO does not increase linearly with the gap length. A saturation phenomenon takes place [CFO varies as $3400/(1+8/d)$].

10. If this is true, then even if d is increased to infinity, the maximum voltage the gap can support is 3400 kV crest.
11. This implies that with a 1.5 p.u. switching surge, the crest value of power-frequency voltage is about 2250 kV giving a line-to-line voltage of $2250 \sqrt{3}/\sqrt{2} = 2800$ kV. With a factor of safety of 1.25, this gives a ceiling voltage for ac transmission to be about 2240 kV.
12. One of the objectives of the ASEA-AEP 1500kV project is to establish the validity of this assumption.
13. It therefore still remains to see whether theoretical models can explain this.
14. This can be compared to what happens under lightning voltages in nature. If there be such a thing as saturation phenomenon, voltages of the order of 100 to 1000 MV observed in lightning might not be present in order to flashover air gaps from cloud to ground from 500 to 5000 metres. This is where Alexandrov's model and other theories of breakdown under lightning voltages can help to understand breakdown mechanisms occurring under switching surges:

5. Critical Flashover Voltage, Withstand Voltage, and Statistical Considerations.

While all laboratories report the 50% flashover voltage, a designer is really interested in the withstand voltage. This quantity is an ambiguous one. According to statistical considerations, the withstand value in reality gives probability of flashover of .2% and not 0%. Therefore, laboratories must also provide this information. It can be observed that in order to determine the voltage that will give a flashover of 1 in 500, at least 500 shots must be given at each voltage level close to the so-called withstand voltage. Some designers use a .1% probability of flashover which requires 1000 shots to be given at voltages close to this probability.

In order to obviate such a procedure, the experimentalists use the assumption that breakdown probabilities follows a Gaussian distribution with a known mean value (50% flashover voltage) and a standard deviation σ . Then the withstand voltage is 3 σ below the CFO.

In addition to this probability, other factors in design also require to be investigated on a statistical basis, especially meteorological conditions. These give rise to oscillation of conductors, relative air density, rain fall rates, and the magnitude of switching surges. From these considerations it should be clear that a very large number of experimental conditions must be varied in order to establish confidence in design procedures. It has been recognized, however, that a flashover to external insulation is not catastrophic to the system. Its severity is the same as a single line to ground fault or a phase-phase fault.

6. Paris's Work and Gap Factors

After a great deal of experimental work, Dr. Paris of the ENEL and CESI in Italy formulated his great theory which has formed the basis for line designs in Europe. According to him, the following results are observed.

- 1) the CFO of any gap geometry varies as $d^{0.6}$.
- 2) For two gap lengths for the same electrode geometry,

$$V_1/V_2 = (d_1/d_2)^{0.6}$$

- 3) For the same gap lengths in two different electrode geometries, with one of them taken as rod-plane gap,

$$V/V_{r-p} = K, \text{ called the gap factor.}$$

Here, all voltages are the 50% flashover voltages.

For example, $r-p = 500 d^{0.6}$ and $V_{r-r} = 687.5 d^{0.6}$

$\therefore K$ for rod-rod gap is $687.5/500 = 1.375$.

- 4) For the more common electrode geometries used, the following table gives the gap factors

Rod-plane	K=1.0
Rod-rod	1.375
Conductor to cross arm end	1.55
Rod-tower structure	1.05
Conductor-plane	1.15
Conductor-window	1.2
Conductor to structure	1.3

The values of K given above apply when there are no insulators present in a tower window. Since the height of insulator H_i in relation to the air-gap strike distance d can vary in designs used at different places in the world, the EHV-UHV Project of U.S.A. initiated a very worthwhile set of experiments. Their finding is that the exponent is not 0.6 but close to 0.75 for a H_i/d ratio of 1.

The steps to be followed in line designs based on Paris's formulas will be the following:

- (i) From network transient studies (using physical modelling on a TNA or mathematical modelling on a Digital Computer) ascertain expected maximum value of per-unit switching surge on the system studied. Let this be V_{ss} . For example, suggested levels are 2.5 p.u. to 1.5 p.u. for transmission levels of 345 kV to 1150 kV. [1 p.u. = crest value of line-to-ground power-frequency voltage at maximum operating voltages of 362kV to 1200 kV, r.m.s., line-to-line].
- (ii) Assume a suitable value of the standard deviation σ . This is usually taken to be 5% or 8% of CFO.
- (iii) Assume withstand voltage to be $V_{50}(1-3\sigma)$. This should equal V_{ss} .
- (iv) The CFO is then $V_{50} = V_{ss}/(1-3\sigma)$.
- (v) This must equal Paris's value of $500 k d^{0.6}$.

(vi) The required air gap clearance is

$$d = (V_{50}/500K)^{1/0.6} = [V_{ss}/(1-3\sigma) \cdot 500K]^{1/0.6}$$

We may remark here that the IEEE suggests $\sigma = 5\%$ while the I.E.C. suggests $\sigma = 6\%$ of the CFO voltage V_{50} .

(vii) Once the line-to-tower clearance is calculated through suitable gap factor K , the line-to-line clearance is taken to be $1.7d$ and the minimum conductor-to ground clearance is $(4.3+1.4d)$.

Example: A 400-kV line (420 kV maximum) has a maximum switching surge of 2.5 p.u. when resistor switching is used and trapped charge is neglected. Assume V_w to be 3σ below V_{50} with $\sigma = 5\%$ V_{50} . Allow a further 5% to cover differences between laboratory and field conditions and take

$$V_w = \frac{1}{1.05} (V_{50} - 3\sigma V_{50}) = 0.8095 V_{50}.$$

Design the clearance between conductor and tower and between phases. Take a factor of safety of 1.2.

Solution : 1 p.u. crest voltage = $420 \sqrt{2/\sqrt{3}} = 343$ kV.

∴ Switching surge crest value $V_{ss} = 1.2 \times 2.5 \times 343 = 1029$ kV.

$K = 1.2$ from the table for conductor to tower window.

$$\therefore d = \left(\frac{1029}{0.8095 \times 1.2 \times 500} \right)^{1.667} = 3.33 \text{ metre.}$$

Line-to-line clearance is typically $3.33 \times 1.7 = 5.7$ m.

Line-to-ground clearance is a minimum of $4.3 + 1.4 \times 3.33 \approx 9$ m.

[Note ∴ The UPSEB conductor-tower clearance is nearly $132'' = 11'$ = 3.3 metres, and phase-spacing is 11m. The minimum clearance to ground at mid span is 9 m.].

Dr. P. K. Chatterjee

Page Nos. Topic

PKC-1-19 Fiber Optics in Communications

PKC-20-41 Optical Fiber Transmission from Conception to
Prominence in 20 Years (By M. Schwarz)

PKC-42-48 Overview of Telecommunications via Optical
Fibers (Stewart E. Miller)

PKC-49-59 The Use of Fiber Optics for Communications,
Measurement and Control **within High Voltage**
Substations.

1000

1000

1000

1000

1000

1000

1000

1000

1000

FIBRE OPTICS IN COMMUNICATIONS

After completing extensive field trials in several countries, Fibre optic communications systems have started entering commercial services. In the next few years the number of new services will become impressive. World fibre sales, are stated to be presently about £ 120 million per year, and that are expected to rise to 1500 million by 1990. Field trials of various new applications are in progress at present. Also research and development efforts are on to find better and more economic materials, optical fibres, optical sources and detectors, and fibre components. On the other hand, applications in a variety of communications, control and measurement systems are being investigated.

The major advantages of fibre optics are : availability of very large bandwidth, immunity to electromagnetic induction and r.f. interferences, absence of ground loops, less volume and weight, good mechanical strength and abundance of raw materials. These virtues have made fibre optics very attractive for civilian as well as military uses (both tactical and strategic). Today the case for fibre optics rests not only on its high reliability and bandwidth capability under noisy electromagnetic conditions, but also on price.

Optical fibres today have excellent transmission properties. The economical multimode graded-index fibres are available with losses of 1 to 3 dB/Km according to the light wavelength. Whereas single mode fibres have a loss of less than 1 dB/km permitting a spacing of 20km between repeaters at a bit rate of 565 Mbps. In such a case, approximately 16 TV programs or some 8000 telephone calls can be transmitted simultaneously. The wavelength regions of interest are the 0.8-0.9 μm short wavelength* region has readily available reliable sources (LEDs and Laser diodes) and excellent detectors. Operating close to 1.3 μm , two properties of the fused silica fibre permit much longer distances (repeaterless) and higher data rates. First, the fibre loss is greatly reduced and second, pulse spreading (owing to material dispersion) becomes zero. At longer wavelength of 1.55 μm the fibre loss becomes even smaller, and 1.3-1.55 μm long wavelength ranges. The short wavelength

but material dispersion is non-zero. In a Bell Lab experiment, signal has been transmitted over a unrepeated distance of 119 Km at 1550 nm with a transmission rate of 420 Mbps. The bit error rate achieved was 10^{-9} . However, reliable sources and low noise detectors are still not readily available in the long wavelength region.

The most important fibre fabrication methods in current use for the communications field are variants of two: outside vapour phase oxidation (OVD) and inside vapour phase oxidation (IVD). Using IVD method high quality single-mode fibre of 20 km length and using OVD method high quality single mode as well as multimode fibres of 40-50 km length have been reported to be produced in research laboratories. Also a minimum attenuation figure of 0.16dB/km for a single mode fibre at 1550 nm has been reported. Researchers feel that using $\text{GeO}_2\text{-SiO}_2$ glass system smaller losses cannot be obtained. So attention has turned to other glass systems, both oxides and nonoxides and predictions have been made of much lower losses. For example, for fluoride glasses, especially those based on ZrF_4 , predicted losses approach 10^{-13} dB/km, and rapid progress is being made towards these figures (1980 - more than 10^4 dB/km, 1982 - about 30 dB/km). Very large repeater spacings - greater than 1000 km at 10^{-3} dB/km - is being visualized using these fibres.

The sources used in optical fibre networks are Laser diodes and Light emitting diodes (LED). The semiconductor material which emits light in the short wavelength range (0.85/0.9 μm) is GaAlAs. A laser diode using this material is reported to have an extrapolated life of more than 10^5 hours. LEDs and Laser diodes commonly used in this region are CW double heterostructure (DH) surface and edge emitting types. The typical light output for a LED is 100 μW and Laser diode is 5-6 mW, with spectral widths of 40nm and 1 nm, respectively. A suitable semiconductor material for use in the long wavelength region is the quaternary alloy, InGaAsP. LEDs using this alloy are efficient, fast, and very reliable. The quaternary laser diodes are still not as reliable, although narrowstripe buried hetero-structure (BH) lasers are reported to be highly reli-

able, ~~their~~ mean time to failure (MTTF) at room temperature could be expected to exceed 10^7 hours. However, certain problems still remain with BH lasers aged over long period of time. These include the occurrence of rapid degradation after long term stable operation.

Silicon photo detectors are a natural choice in the 0.85-0.9 μ m range having a typical maximum responsivity in excess of 0.6A/W occurring just above 900 nm. However, Ge photo detectors have to be used at 1.3 μ m wavelength region ~~with~~ significantly increased dark current. Both PIN as well as Avalanche Photo Diode (APD) detectors are used in fibre optics, the choice depends upon the repeaterless length. Whereas silicon APD is a commercially available detector with excellent photodetector properties, germanium APDs have high excess noise introduced by avalanche gain. Very sensitive InGaAs PIN photodetectors have also been demonstrated offering a possibility of a common material ^{te} technology for both emitting and receiving devices at long wavelengths.

Fibre optic components like connectors, attenuators, directional couplers, splitters, multiplexers, demultiplexers, etc. having very good properties are commercially available, but, further development to reduce their costs is necessary. Similarly, splicing tools should be made more economical.

Considerable improvement in the space requirements, reliability and cost of components for optical communication systems is possible if the individual optical, optoelectronic, and electronic components can be combined to form integrated optical devices. Among other things, they may some day help to make full use of the bandwidth of the optical fibre.

Availability of very large bandwidth has made application of optical fibre in telecommunications highly attractive, but, this also makes it possible to use optical fibres for a wide bandwidth robust modulation technique, like spread-spectrum modulation (SSM) and multiplexing for special applications, like data networks, etc. Wavelength ~~division~~ multiplexing (WDM) is another new technique having considerable attention in fibre optics due to its great potentiality.

Applications particularly suited to fibre optics, excluding telecommunications, include: process control, remote monitoring, CCTV, CATV, data processing, single and multichannel modem replacement, mixed speech and data systems (ISDN), local area networks (LAN), railway signaling, power system applications, etc.

OPTICAL FIBRE

Three types of fibres : (1) Step-Index (Multimode)

(2) Graded-Index

(3) Single Mode

$$n_2 = n_1(1-\delta) \text{ where } \delta = \frac{n_1 - n_2}{n_1} = 0.01 \text{ to } 0.02$$

At. 850 μm : (i) Silica ($\text{GeO}_2/\text{P}_2\text{O}_5$ doped core, SiO_2 or $\text{SiO}_2/\text{B}_2\text{O}_3$ clad)

Refractive index : Core (n_1) = 1.469 Cladding (n_2) = 1.452

Diameter : Core = 50 μm Cladding = 55-60 μm outer dia = 125 μm

Max. theoretical NA = 0.22, $\text{NA} = \sqrt{n_1^2 - n_2^2} = \sin \phi_{1\text{max}}$, $\phi_1 = 13^\circ$

Modal dispersion = 57 ns/km (Theoretical) Practical = $\frac{1}{3} \times 57$

(ii) Plastic clad silica (multimode step index)

$n_1 = 1.452$ $n_2 = 1.405$ Core dia = 150 μm Cladding dia = 230 μm

Max. N.A. = 0.37 (Theoretical) $\phi_1 = 22^\circ$ outer dia 230 μm

Modal dispersion = 165.0 ns/km (Theoretical) Practical = 30

Multimode Graded Index : $\text{GaO}_2/\text{P}_2\text{O}_5$ doped core
(.850 μm) SiO_2 or $\text{SiO}_2/\text{B}_2\text{O}_3$ clad

$n_1 = 1.475$ core dia = 50 μm $n_2 = 1.452$ cladding dia = 55 μm
outer dia = 125 μm

Max. N.A. = 0.26 (Theoretical) } Central region of Core
 $\phi_1 = 15^\circ$

Modal dispersion < 0.5 ns/km (experimental)

Single Mode : GeO_2 doped core SiO_2 cladding

$n_1 = 1.462$ core dia = 3.3 μm $n_2 = 1.452$ cladding dia = 45 μm
outer dia = 125 μm

Max. N.A. = 0.17 (theoretical) $\phi_1 = 10^\circ$ Modal dispersion = 0

The relation between core and cladding refractive indices for a step-index multimode fibre is $n_2 = n_1 (1 - \delta)$ where $\delta \ll 1$, typically $\delta = \frac{n_1 - n_2}{n_1} = 0.01$ to 0.02 .

For the graded-index fibres, the core has a graded index which usually decreases radially from maximum value n_1 at the centre of the core according to the law $n = n_1 (1 - \alpha \gamma^2)$ where α is a constant and γ is the distance from axis. A particular and popular core is the parabolic gradation:

$$n_\gamma = n_1 \left[1 - \left(\frac{\delta}{a^2} \right) \gamma^2 \right], \quad 0 \leq \gamma \leq a$$

In the single-mode fibre, the core radius a is very small ($a \approx 2 - 5 \mu\text{m}$) which enables propagation of a single mode only. The number of modes of propagation in an optical fibre is given by

$$N = 0.5 \left(\frac{\pi d (N.A.)}{\lambda} \right)^2$$

where $d = 2a$ is the diameter of the core, and $NA = (n_1^2 - n_2^2)^{\frac{1}{2}}$.

Thus, for a given combination of refractive indices, as the diameter of the core is reduced, fewer modes propagate. When eventually the diameter becomes of the same order of magnitude as the wavelength of light, then only a single mode will propagate.

The r.m.s. width of the impulse response for a step-index fibre is proportional to δ , whereas for the graded-index fibre it is proportional to δ^2 .

Propagation thru' Fibres : (Ray Theory)

We consider the step-index fibre:

$n_1 > n_2$ From Snells' law

$$n_1 \sin \phi_1 = n_2 \sin \phi_2$$

$$\text{or } n_1 \cos \theta_1 = n_2 \cos \theta_2$$

No real angle θ_2 exists if $n_1 \cos \theta_1 > n_2$

For this inequality to hold, there will not be any refracted ray in the cladding region. For the rays to be confined to the core region the angle θ_1 must not exceed the critical incident angle θ_c ,

where $\cos \theta_{ic} = n_2/n_1$.

Also $n_0 \sin \theta_0 = n_1 \sin \theta_1$.

Assuming $n_0 = 1$

$$\sin \theta_0 = n_1 \sin \theta_1$$

Let $\theta_0 = \theta_m$ when $\theta_1 = \theta_{ic}$. Therefore, $\sin \theta_m = n_1 \sin \theta_{ic}$

$$= n_1 \sqrt{1 - \cos^2 \theta_{ic}} = n_1 \sqrt{1 - \frac{n_2^2}{n_1^2}}$$

$$\text{or, } \sin \theta_m = \sqrt{n_1^2 - n_2^2}$$

This means that a cone of light incident on fibre with conical semiangle less than θ_m will be accepted and propagated through the fibre. $\sin \theta_m$ is the measure of the light gathering power of the fibre and is known in optics as the Numerical Aperture (N.A.). Thus

$$NA = \sqrt{n_1^2 - n_2^2}$$

This indicates that the maximum light acceptance angle of the fibre is independent of its physical dimensions, and can be made large. Secondly, the fibre cross-section can be made small to increase flexibility.

It is to be noted that total internal reflection is a necessary but not a sufficient condition for propagation of light rays in optical waveguides. At each point of reflection the ray undergoes a phase change. It is these phase shifts which impose an additional constraint. Their evaluation becomes necessary to satisfy the condition that optical paths (phase difference) between two normal planes for parallel rays should differ by an integer multiple of 2π . This condition can be applied to the ray undergoing multiple reflections in an optical waveguide.

It can be seen from the figure that the wavefronts are also equiphase planes. For the two rays 1 and 2, points A and C are on an equiphase plane while points B and D are on another equiphase plane. Now when the two rays travel from one equiphase plane to the other, their path difference (including the phase shifts in ray 2 due to reflections at C and D) should be integer multiple of 2π .

Let the phase shifts due to reflections at C and D be ϕ (same phase shift at both interfaces as the refractive indices of the two media are the same at both C and D), and to express various distances in terms of d and θ_1 , we have

$$\begin{aligned} AB &= BC \cos \theta_1 \\ &= (CF - BF) \cos \theta_1 \\ &= \left(\frac{d}{\tan \theta_1} - d \tan \theta_1 \right) \cos \theta_1 \\ &= (\cos^2 \theta_1 - \sin^2 \theta_1) \frac{d}{\sin \theta_1} = S_1 \end{aligned}$$

and $CD = \frac{d}{\sin \theta_1} = S_2$

Therefore, phase change due to only path difference is $n_1(S_2 - S_1)k$, where k is propagation constant in free space ($k = \frac{2\pi}{\lambda} = \frac{2\pi}{\lambda_0} \frac{c}{v} = \frac{2\pi}{\lambda_0} n_1$). Thus, the equiphase condition can be expressed as

$$n_1 (S_2 - S_1) k + 2\phi = 2N\pi$$

where N is an integer. Hence, only rays at discrete values of angle θ_1 satisfying the above equation can propagate. These discrete values of θ_1 correspond to the various waveguide modes.

Two types of rays exist in optical fibres :

(i) meridional rays

and (ii) skew rays

Meridional rays confine to a single (meridional) plane and pass thru' guide axis. Skew rays do not confine to a single plane and do not pass thru' the guide axis.

It can be easily shown that the path length of the meridional ray is $P(\theta_1) = L \sec \theta_1$

where L is the axial length of the guide. The path length and therefore, the transit time of a ray is a function of the angle of the ray. This differential delay between the permitted modes reduces the information capacity of the guide. The number of reflections of a meridional ray can be shown to be

$$N(\theta_1, d) = \frac{L \tan \theta_1}{d}$$

The number of reflections plays an important part as each reflection is associated with some loss. The number of reflections per unit length is

$$N_m = \frac{\tan \theta_1}{d}$$

Skew Rays:

Consider Fig.1.3(a) which shows a typical skew ray AXY. Here X and Y are the two reflection points at the core and the cladding interface. XC is normal to the reflecting surface at the point X and ϕ_1 is the angle of reflection the ray makes with the normal XC. YP is perpendicular from Y to the cross-sectional plane containing XC. YP is therefore parallel to the axis and P like Y also lies on the interface. Angle γ is called the azimuthal angle for the ray. Angle θ_1 , the angle between the ray and the reflecting surface is called internal axial angle. These angles, i.e., θ_1 , γ and ϕ_1 are maintained for a particular ray through successive reflections.

Figs. 1.3 (b) and (c) give the different views of the relevant angles in detail. It can be seen that the angles γ and β are in perpendicular planes. Plane YPW is perpendicular to plane WXP, as PW is perpendicular to XC, therefore, triangle XWY is a right angled triangle. Therefore,

$$\begin{aligned} \cos \phi_1 &= \frac{XW}{XY} = \frac{XW}{XP} \cdot \frac{XP}{XY} \\ &= \cos \gamma \cos \beta \\ &= \cos \gamma \sin \theta_1 \text{ as } \beta = \frac{\pi}{2} - \theta_1 \end{aligned}$$

$$\sin \theta_1 = \frac{1}{\cos \gamma} \cdot \cos \phi_1 \quad \dots\dots (1)$$

We know for total internal reflection

$$\cos \theta_1 > \frac{n_2}{n_1}$$

$$\sin \phi_1 > \frac{n_2}{n_1}$$

$$\text{or } \cos \phi_1 < \left(1 - \frac{n_2^2}{n_1^2}\right)^{\frac{1}{2}} \quad \dots\dots (2)$$

Using eq. (1), we have

$$n_1 \sin \theta_1 < \frac{1}{\cos \gamma} (n_1^2 - n_2^2)^{\frac{1}{2}}$$

Applying Snell's law

$$n_0 \sin \theta_0 < \frac{1}{\cos \gamma} (n_1^2 - n_2^2)^{\frac{1}{2}}$$

If n_0 is unity and θ_M is the maximum value of the angles θ_0 , i.e., the maximum acceptance angle, then

$$\sin \theta_M = \frac{1}{\cos \gamma} (n_1^2 - n_2^2)^{\frac{1}{2}}$$

$$\text{or } \sin \theta_M = \frac{\sin \theta_m}{\cos \gamma} \quad \dots \quad (3)$$

where θ_m is the maximum acceptance angle for meridional rays as discussed earlier.

Thus we see that skew rays can be accepted at wider angles than the meridional rays. For $\gamma = 0$, i.e., for the maximum value of $\cos \gamma$ (unity), the ray becomes a meridional ray. As γ varies from 0 to $\frac{\pi}{2}$, the rays tend to travel more along the surface. At $\gamma = \frac{\pi}{2}$, the ray travels along the surface. For any angle $\theta_0 > \theta_m$ there is a range for which the skew rays are accepted. It is interesting to note that for any numerical aperture, θ_M can be equal to 90° for $\gamma = \frac{\pi}{2} - \theta_m$. As an example, let $\theta_m = 30^\circ$. Therefore, $NA = 0.5$. Then for $\gamma = 90^\circ - \theta_m = 60^\circ$, we get $\theta_0 = 90^\circ$. Hence, there will be a cone of light of semi-conical angle of 30° , followed by a dark band and then a ring of light due to skew rays the width of which depends upon angle γ . Thus θ_M depends upon γ and the refractive indices, and there exists an angle γ for which ray at any θ_0 is accepted.

The unit path length for a skew ray is

$$l_s = \sec \theta_1 = l_m$$

where, l_m is the unit path length of a meridional ray. The number of reflections (n_s) per unit length for a skew ray work out to be,

$$n_s = \frac{\tan \theta_1}{d \cos \gamma}$$

$$\text{or } l_s = \frac{n_m}{\cos \gamma}$$

Thus the number of reflections increase in case of the skew rays over the meridional rays. If $\gamma = \frac{\pi}{2}$, the number of reflections is infinite giving a true helical path along the interface.

Attenuation Mechanisms :

The mechanisms for linear losses are:

- (a) material absorption
- (b) material scattering
- (c) mode coupling to the radiation field
- (d) radiation due to bends, and
- (e) leaky modes.

Material absorption: Many glass compositions would show negligible material absorption in the wavelength regions of interest if no foreign elements were present. However, traces of transition metal or hydroxyl ions have a profound effect. Both the glass type and the state of oxidation of these impurities influence the absorption.

Material Scattering : Several linear scattering mechanisms can be distinguished in most fibre waveguides. The most fundamental, Rayleigh scattering, is always present due to the inhomogeneities, small in comparison to the guided wavelength, which are produced in the guide during glass melting and fibre drawing. Rayleigh scattering can normally be identified by its proportionality to λ^{-4} and by its angular dependence proportional to $(1 + \cos^2 \theta)$.

When the inhomogeneities are comparable in size to the guided wavelength, Mie-scattering can be observed.

Mode Coupling Scatter : Variations in core diameter or core/cladding refractive index difference along the length of a fibre waveguide can influence the transfer of power from one mode to another and hence to the radiation field.

Radiation due to Bends: All dielectric guides, other than those that are absolutely straight, will radiate.

Leaky Modes : It has been shown that there is a class of modes which are not completely guided, but will slowly leak. These modes are in two classes both of which can be represented by highly skewed rays.

Dispersion in Optical Fibres:

Inter-Modal Dispersion: In optical fibres only certain modes, each having its own velocity of propagation, are allowed which correspond to discretely defined angles of incidence of rays in the fibre. Owing to the range of different group velocities of these excited modes, there is a spread in the arrival times of power transmitted in the individual modes which results in a wider, dispersed pulse at the output. This is known as intermodal dispersion or group delay dispersion, and in multimode fibres is the dominant dispersion mechanism. The delay difference between an axial ray and a ray incident at the maximum angle is given by

$$\Delta \tau = \frac{n_1 L}{c} \left(\frac{1}{\cos \theta} - 1 \right)$$

Thus, for $n_1 = 1.45$ and $\theta = 8^\circ$ (corresponding to $\delta = 0.01$),

$\Delta \tau = 47$ n sec./km. In practice the spread obtained is less due to mode coupling between higher and lower order modes and higher order and radiating modes. This results in less power throughput.

Intermodal dispersion may be greatly reduced, however, without associated power losses or reduced launching efficiency by arranging for the energy transmitted in the higher order modes to travel faster than the lower order modes such that the increased velocity compensates the longer distance traversed by the higher order modes to travel faster than the lower order modes. Since the modal group velocity is an inverse function of refractive index this may be achieved in practice by the fabrication of fibres having a gradual decrease in refractive index from the centre of the core to the core/cladding interface. In a fibre having an optimized profile and small relative refractive index ($\delta \ll 1$), neglecting other dispersive mechanisms, the maximum delay difference (τ_{\max}) per km. between fastest and slowest modes

is given by $\tau_{\max} = \frac{n_1 \delta^2}{8c}$ per km.

Thus, for $n_1 = 1.45$ and $\delta = 0.01$, the delay spread is 0.06 ns/km. Practical values are more than this.

Material Dispersion : Material dispersion becomes the dominant fibre bandwidth-limiting mechanism when intermodal dispersion is negligible. Material dispersion, which is also known as wave length dispersion, arises as a result of the refractive index variation of the fibre with the wavelength of the signal source. Practical sources used in optical fibre transmission systems have a finite spectral linewidth and since the fibre refractive index is different for different frequency components of the source there is a finite range of group velocities which results in a spreading of a pulse propagating in the fibre. The pulse spread ($\Delta\tau_m$) due to material dispersion is proportional to the second derivative of the refractive index w.r.t. wavelength,

$$\Delta\tau = \frac{\lambda}{c} \frac{d^2 n}{d\lambda^2} \Delta\lambda \cdot L$$

For GaAlAs laser of line width 4 nm centred at 900 nm, the material dispersion is 0.35 ns/km. For an LED this is 3.5 n sec/km.

It has been shown that the second derivative of n and hence the material dispersion falls to zero at a wavelength in the region 1.2 - 1.4 μm and then increases with wavelength but with a change of sign (i.e., longer wavelengths are delayed w.r.t. shorter wavelengths).

Waveguide Dispersion : There is a third dispersive mechanism known as waveguide dispersion. This arises as a result of the λ dependence of the group velocity in each mode. This is obtained as about 6.6 p sec/nm. km. Cancellation of waveguide dispersion with material dispersion may take place a little above 1.3 μm when the latter changes sign.

Electro-Optic Transducers : (Light Sources)

Light Emitting Diodes (LED's)

Laser Diodes

GaAlAs LED's emit in the 0.85 μm to 0.9 μm region

GaInAsP/InP LED's emit in the 1.25 μm to 1.3 μm region.

LED's are simple to construct, extremely easy to modulate, and

LED's work by spontaneous radiation.

LED's have linear characteristics, so more suitable for analog systems.

LED's have smaller light power output than lasers.

LED's are incoherent sources - spectral width is of the order of 40 nm.

LED's can be modulated directly.

Lasers to be used for fibre optics must be of CW type.

They have much higher output than LED's. Lasers are more coherent sources than LED's - 1 to 4 nm spectral width.

If a LED is operating with a binary input, the light output will be between zero and some maximum.

In the case of laser, some spontaneous emission occurs at low currents where the device behaves just like an LED. As the current is increased a threshold is reached, I_{th} , beyond which lasing occurs.

The threshold current of lasers vary with temperature and time, and differs from time to time. This causes the operating point to vary if the drive current is held constant. So some kind of feedback control is necessary to keep I_{th} under control. The above control system provides real time feedback at d.c. and low frequencies, and mean power feedback at high frequencies.

Photo Detectors : (Opto-Electric Transducers)

Photo detectors used in fibre optics are of two types:

PIN Photo detectors

APD Photo detectors

In the APD the electrical output signal from the photodetector goes through multiplication within the device due to the avalanche process created by the presence of high electric fields.

Noise at the output of the detectors appear from several sources :

- (a) Fundamental quantum noise which is simply shot noise in the photon current. In effect, it results from the random time of arrival of the photons. It has the important property that it depends on the signal level.
- (b) Multiplication noise, or additional shot noise in multiplication. This results from the statistical nature of the multiplication process in photo multipliers.
- (c) Dark current or leakage current, independent of illumination, that increases the above shot noise effects.
- (d) Thermal noise in the amplifier.
- (e) Noise in the transmitted signal or generated in the transmission medium.

Si - mostly used in the 0.85 - 0.9 μm region

Ge - used in the 1.3 - 1.55 μm region

APD's can have fast response - from well below 1 n. sec. to a few n. secs.

The receiver circuit must provide a steady reverse bias voltage for the photodiode.

For PIN - a bias voltage of 5 to 80 V with extremely low current - it is not critical.

For APD - A bias voltage of 100 to 400 V is needed - it is critical since the multiplication factor depends on this critically.

A remedy to this is to bias the APD with a d.c. constant current source.

LED:

	<u>Operating Voltage(V)</u>	<u>Mean current(a)</u>	<u>Reference O/P Power (dBm)</u>	<u>λ (nm)</u>	<u>Window Fibre (Reference)</u>	
					<u>Core Dia (μm)</u>	<u>N.A.</u>
Edge Emi- tting	1.8	0.15	-14.0	850	82	0.48
LED Burrus	1.6	0.3	-10.0	900	63	0.48
LED Burrus	1.6	0.3	-7.0	900	63	0.48
LED Burrus	1.6	0.3	-5.2	900	63	0.48
LED Surface emitting	1.6	0.1	-7.9	820	(250)	(0.39)

Lasers :

	<u>Max. Output Power (mW)</u>	<u>Typical Drive Current (mA)</u>	<u>Typical Threshold current (mA)</u>	<u>Typical Forward voltage at I_{th} (V)</u>	<u>λ (nm)</u>	<u>Spectral Width (nm)</u>	<u>Rise Time (psec)</u>
	2	185	150	1.8	860	1	
	1	110	80	1.8	850	2	
GaAlAs DH (in 50 μ m 125 μ m fibre) NA=0.2, Graded Index	2	115	90	2.0	830	2.5	100
	7 (into NA=0.5)	185	150	1.85	850	1	

PIN :

<u>Area (mm²)</u>	<u>Bias Voltage (V)</u>	<u>Sensitivity (A/W)</u>	<u>Dark Current (nA)</u>	<u>Capaci- tance (pF)</u>	<u>Core Dia(μm)</u>	<u>N.A.</u>	<u>Typical Quan- Spectral tum Response η(%) range(nm)</u>
	10	0.3	0.15	1	190	0.48	
0.8	45	0.6/0.15 (900)(1060)	10	2.5	Rise Time=3/5 ns (900)(1060)	400-1100	83/17 (900) (1060)
5	45	0.6/0.15	30	6		5/8	400-1100 83/17
50	45	0.6/0.15	70	35		10/18	400-1100 83/17
100	45	0.6/0.15	300	70		10/22	400-1100 83/17

ASD:

Area(mm ²)	Bias Voltage(V)	Gain	Sensitivity A/W	Dark Current	Cap. (pF)	Rise Time (ns)	η
0.5	275-425V	120	75/18	.50 nA	2	2/2	400-1100 85/18
0.2	180-250V	150	65	.15 nA	1.6	0.5/	400-1100 60/
7	275-425	75	45/25	.10 nA	10	2/	400-1150 85/40

Optical Detectors :

Important requirements to be fulfilled by photodetectors used in fibre optics:

- High response at the wavelength of emission.
- Sufficient bandwidth or speed of response.
- Minimum additional noise introduced by the detector.
- Low susceptibility of performance characteristics to change in ambient conditions.
- Compatibility in size, power supply requirements and coupling to the fibre.

PIN Photodiode:

When the incident photon energy $h\nu$ becomes greater than the band gap, the photon can excite an electron from the valence band to the conduction band (absorption). Every semiconductor becomes absorptive at some critical wavelength. This limit is known as the absorption edge.

$$\lambda_c = \frac{h\nu}{\Delta E}$$

Material	Energy gap, ΔE (eV)	λ_c (μm)
Pb S	0.34 - 0.37	3.35 - 3.65
Ge	0.67	1.85
Si	1.14	1.09
GaAs	1.43	0.87
Ga P	2.26	0.55

Optical power incident on the photo diode gets absorbed and produces electron-hole pairs resulting in mainly displacement current. The number of electron-hole pairs produced depends mainly on the quantum efficiency of the diode.

Quantum efficiency (η) of the diode is defined as the fraction of electrons emitted when a single photon of energy $h\nu$ is received by the photodetector; where h is the Plank's constant and ν is the frequency of the propagated light.

In the PIN photodiode there is often a trade-off between the quantum efficiency and the speed of response. For higher quantum efficiency long absorption region is required. For high speed we require short drift times, thus a short absorpition region resulting in a trade-off between η and the speed of response.

An ideal photodiode, i.e., one which produces one electron for every photon incident on it, operating at 1 μm wavelength will have the responsivity of about 0.8 amp. per watt.

Responsivity (R) is defined as the average emitted current divided by the average incident power

$$R = \frac{e}{h\nu} \cdot \eta \text{ coulombs/joule (=amps/watt)}$$

where e is the electron charge in coulombs.

Since the optical power levels we are interested in detecting can be as low as a few nanowatts, the photoelectron current will be a few nanoamperes or less. Thus the amplifier stages used after the detector which generate thermal noise, limits the performance of the optical receivers. Thus it is desirable to have a mechanism to increase the detector responsivity before amplification.

Avalanche photodiodes (APD) provide such a mechanism.

The doping profile is adjusted to result in a narrow region to the left of the intrinsic (i) region where high electric fields exist. Carriers which drift into this region can be accelerated to velocities which are sufficiently high to generate new electron-hole pairs through the process of collision ionization. These new carriers can in turn generate additional pairs. The result is an effective amplification of the photodiode output current. But, unfortunately, this amplification is random. The variance of this random process is made as small as possible by proper device design. As stated above the speed of response of a PIN detector is governed by the time it takes for carriers to cross the 'i' region. For

APD the speed of response is governed by the time it takes for carriers to cross the 'i' region plus the time required for multiplication process in the high field region. In practical APD's there is a trade off between the gain and the bandwidth (response speed).

PIN Photodiode Model :

The PIN photodiode circuit and its incremental equivalent circuit is shown

C_d = Diode Junction Capacitance

R_S = Diode Series Resistance

R_L = Physical Load Resistor

The diode as can be seen is essentially a current source. The ~~small~~ series resistance is negligible in most applications. The load is the amplifier to be used with the photodiode modeled as a resistor in parallel with a capacitor followed by an ideal, infinite impedance amplifier. If $A(f)$ is the amplifier gain and $I(f)$ the detector current at a frequency f , the output voltage is given by:

$$V(f) = I(f) Z(f) A(f)$$

where $Z(f) = \frac{1}{\frac{1}{R_T} + j2\pi f C_T}$

is the impedance of the load, and

$$R_T = \frac{1}{\frac{1}{R_L} + \frac{1}{R_A}}$$

and $C_T = C_A + C_d$

If the optical power falling on the detector with responsivity R (amps/watt) is $p(t)$ watts, then the amplifier output voltage is

$$v(t) = p(t) R * h_{\text{diode}}(t) * h_{\text{amp}}(t)$$

where $h_{\text{diode}}(t)$ is the detector impulse response, and $h_{\text{amp}}(t)$ is the load amplifier impulse response.

It is to be noted that $p(t)$, the received optical power varies in time at a baseband rate and not at an optical rate. Further, the model assumes that the detector output current is a linearly filtered version of the received optical power.

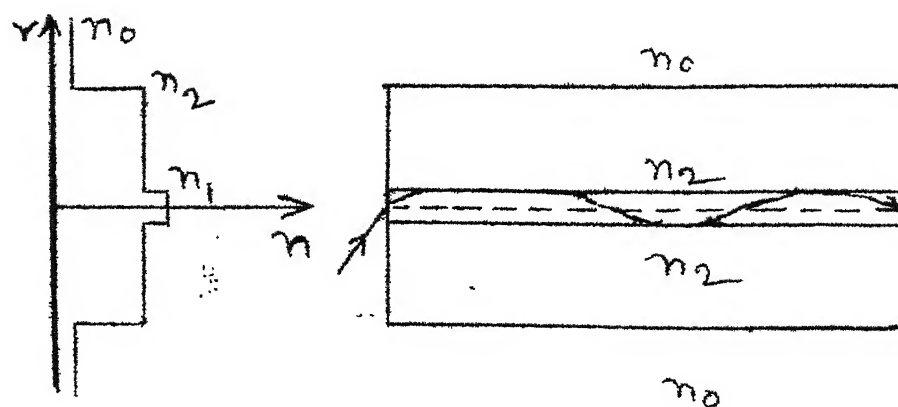
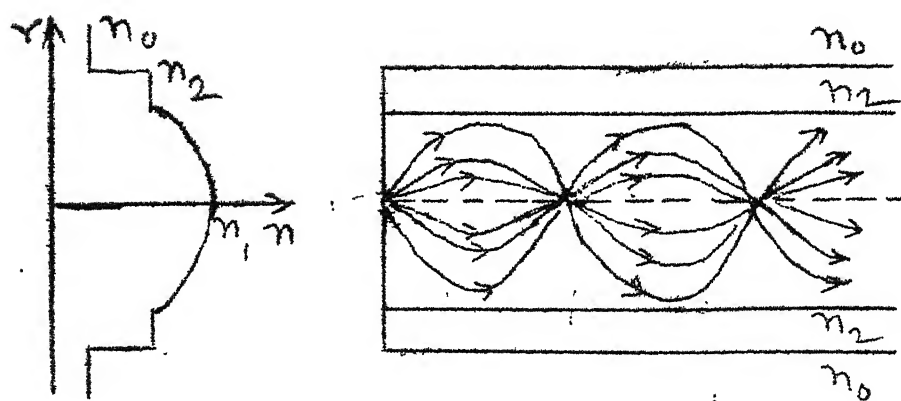
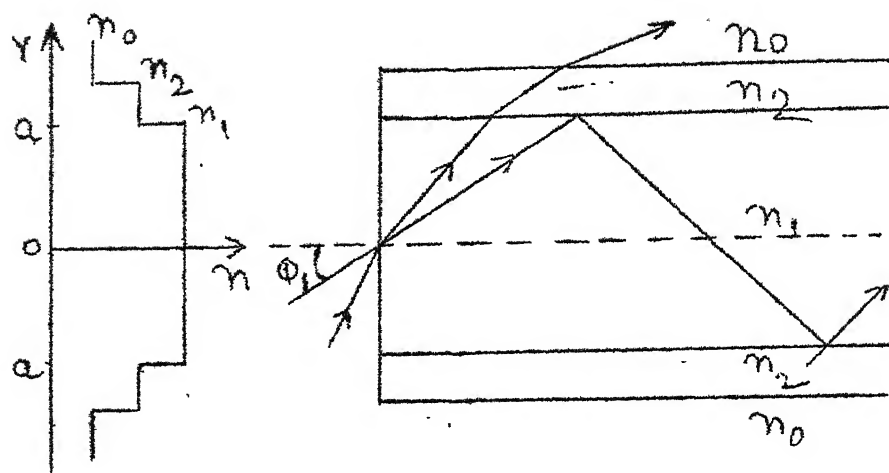
APD Model

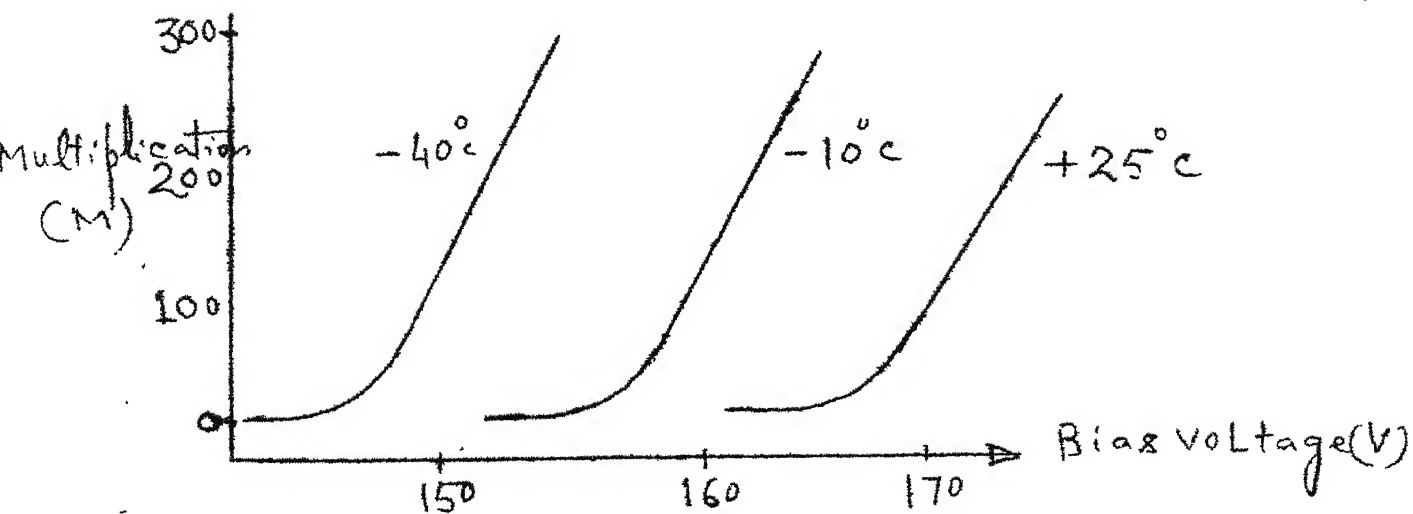
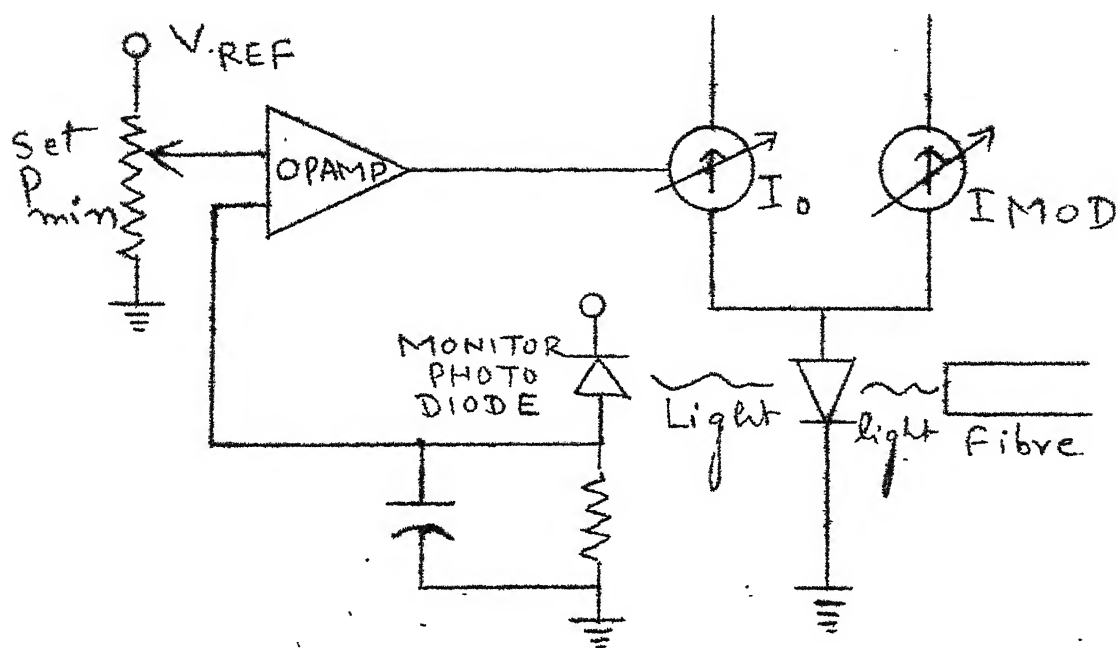
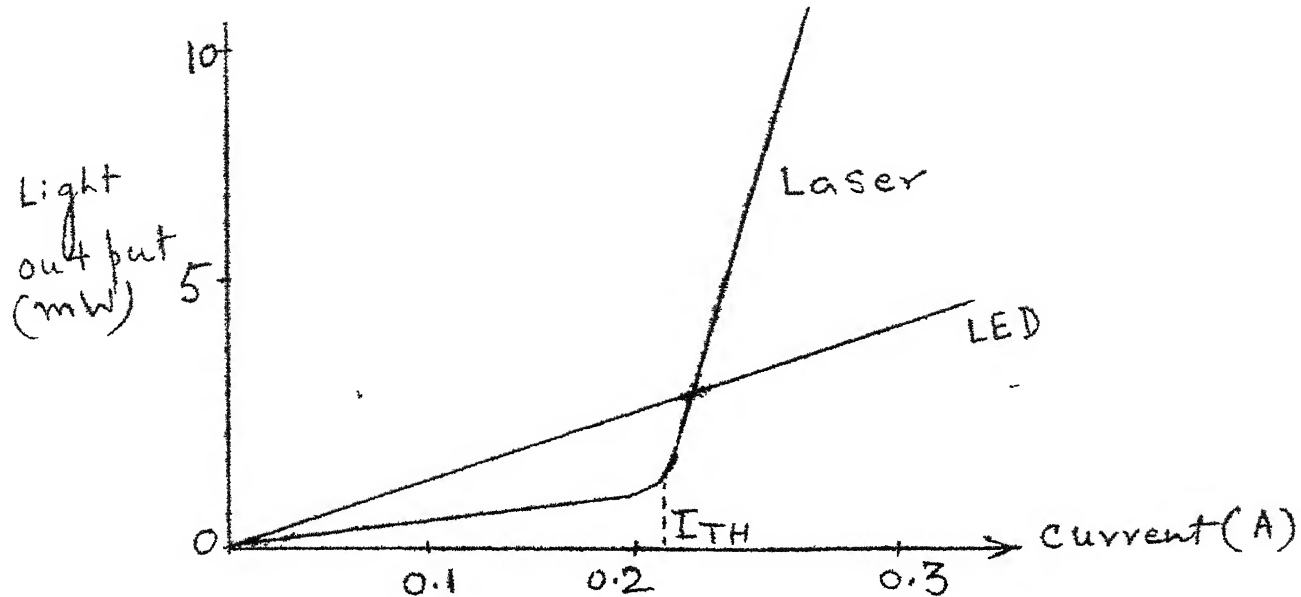
The above is a schematic of an APD biasing circuit. The APD responsivity is a strong function of the bias voltage. Therefore, power supply has to be controlled by a temperature compensating circuit to maintain a fixed avalanche gain, because temperature variation varies the detector breakdown voltage. The equivalent circuit of an APD is identical to that of a PIN diode. Since the avalanche gain is bias sensitive, saturation can occur if the applied signal variations are very large, therefore caution must be exercised.

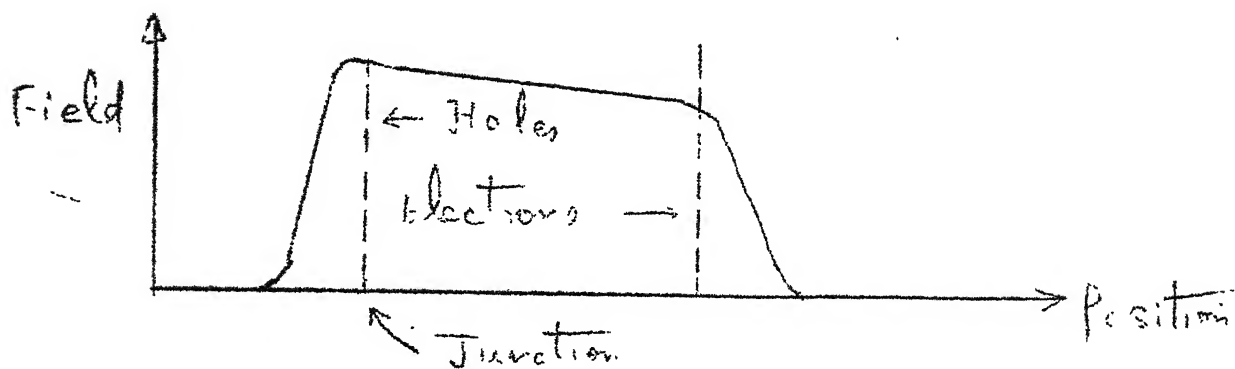
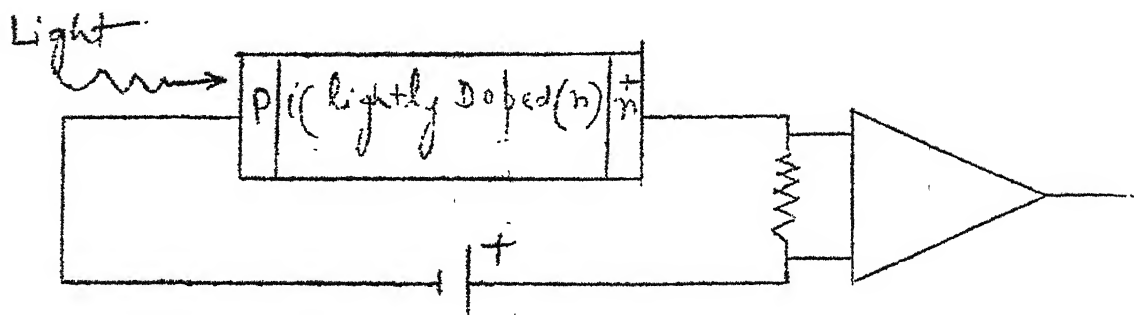
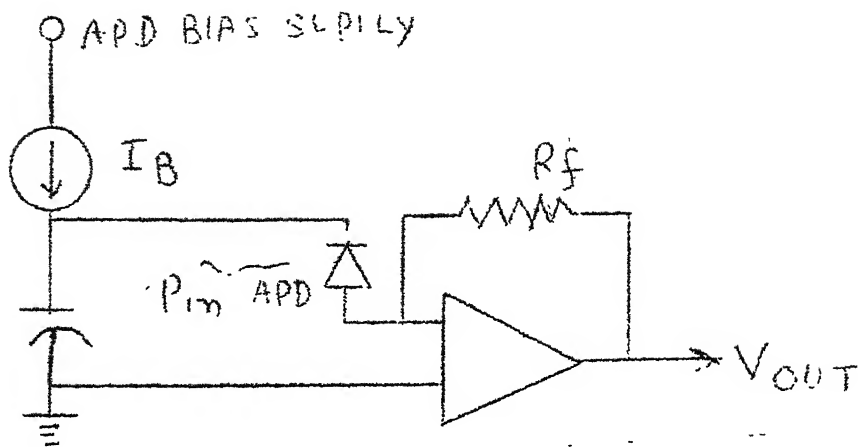
Noise in Photodiodes :

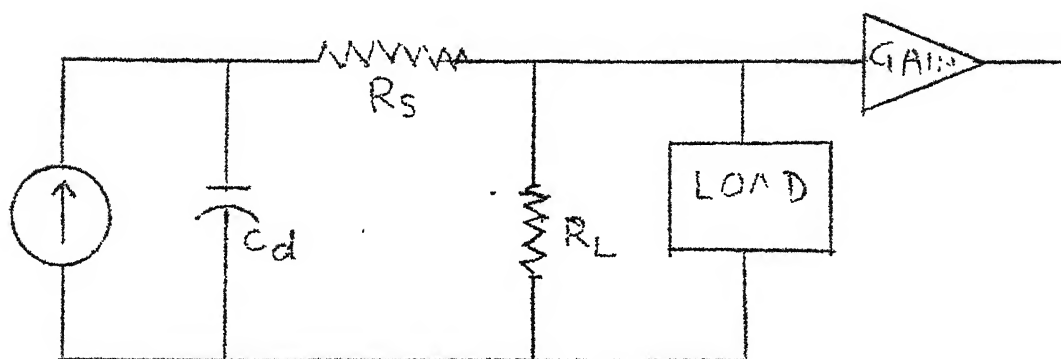
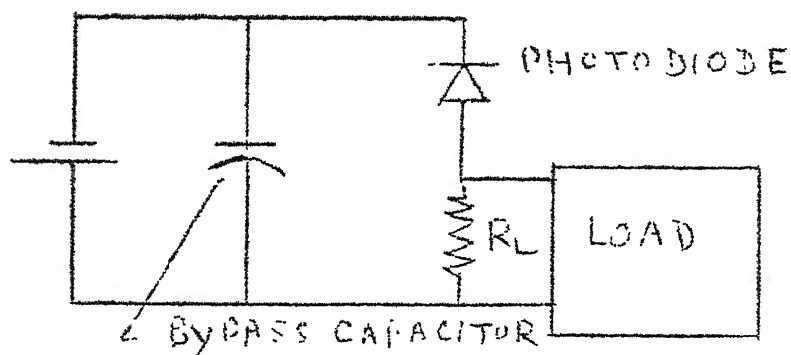
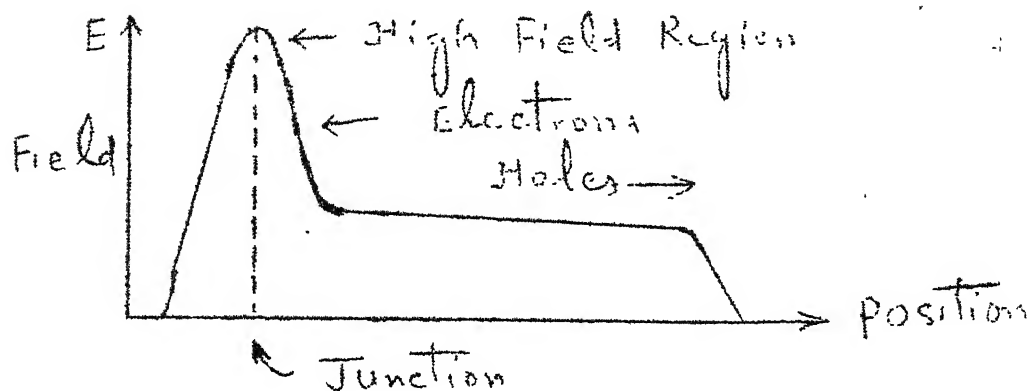
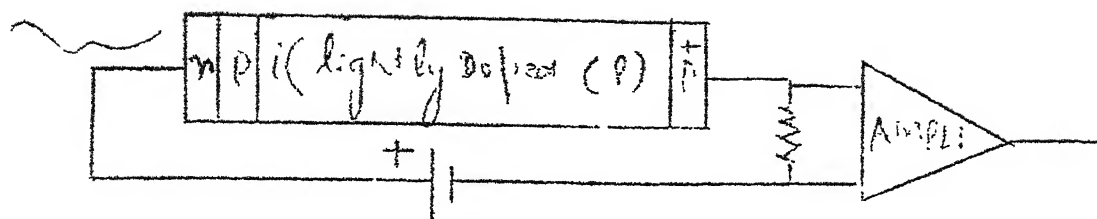
Various sources of noise associated with the detection and amplification process for an APD are depicted on next page

Normally when the photodiode is without the internal avalanche gain, thermal noise arising from the detector load resistance and from active elements of the amplifier dominate. When internal gain is employed, the relative significance of thermal noise reduces.



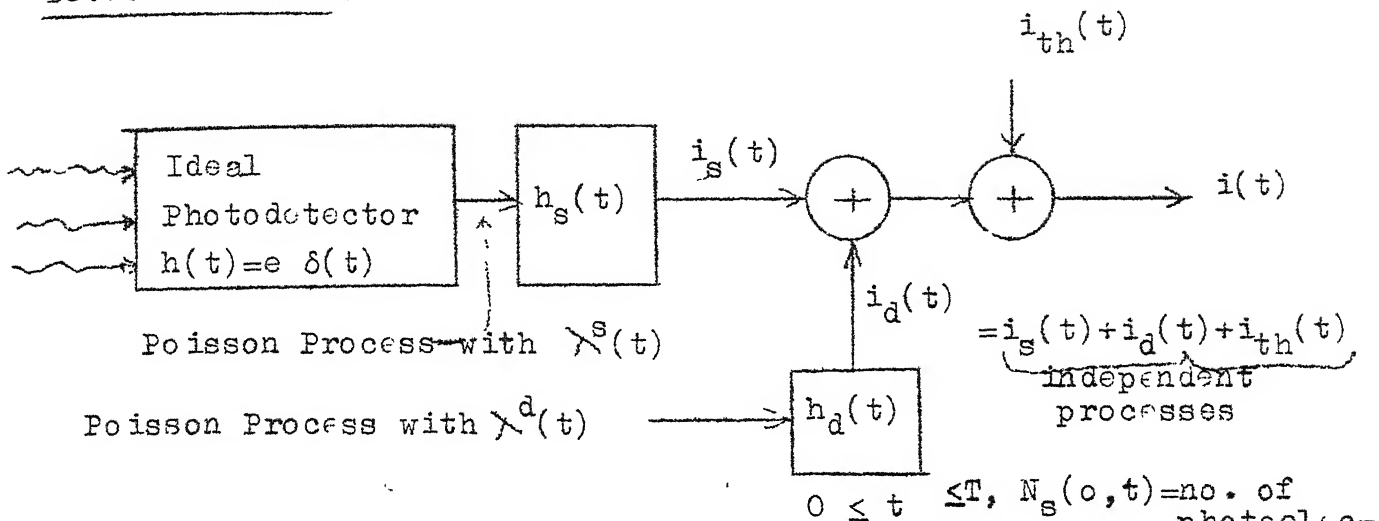






(EQUIVALENT CIRCUIT)
 C_d = DIODE JUNCTION CAPACITANCE
 R_s = DIODE SERIES RESISTANCE
 R_L = PHYSICAL LOAD RESISTOR

Detector Model :



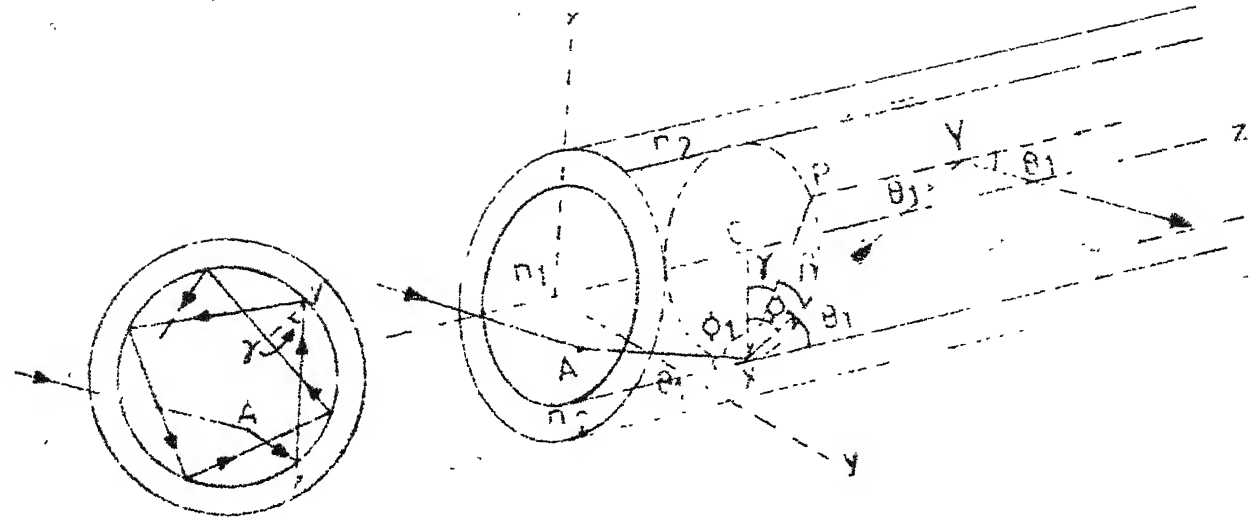
$$i_s(t) = \sum_{j=1}^{N_s(o,t)} e h_s(t-z_j),$$

$$i_d(t) = \sum_{j=1}^{N_d(o,t)} e h_d(t-z_j)$$

Inhomogenous Poisson Process with intensity $\lambda^s(t)$, e = electron charge

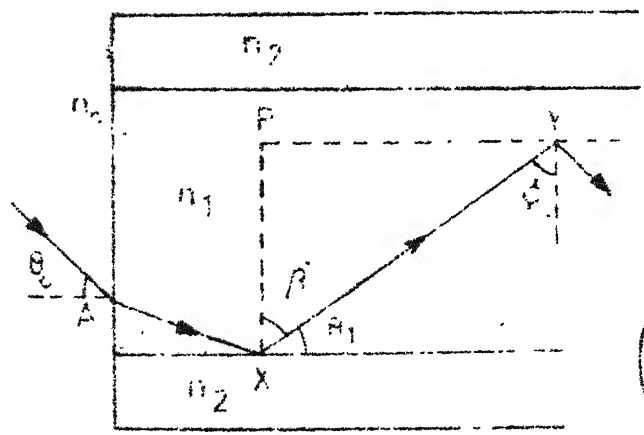
$0 \leq t \leq T$, $N_s(o,t)$ = no. of photoelectrons generated during (o,t) interval

$N_d(o,t)$ is an inhomogeneous Poisson counting process with intensity $\lambda^d(t)$.

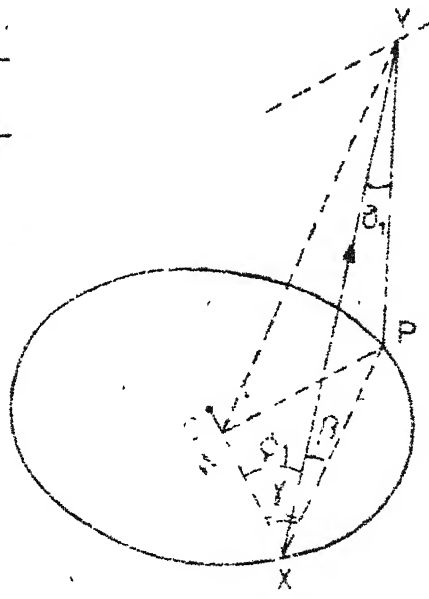


Cross-Sectional View

(a) Typical Skew Ray



(b)



(c)

Fig.1-3 Skew Ray and Associated Angles

OPTICAL FIBER TRANSMISSION FROM CONCEPTION TO PROMINENCE IN 20 YEARS

(M. Schwarz)

The Transmittal of information by optical means, such as smoke and fire signals, dates back to prehistoric times. However, little advance in these methods appears to have occurred until 1791 when Chappe invented and demonstrated the optical telegraph [1]. This system was widely used in France and in other parts of Europe for more than 60 years. In 1870 the physicist John Tyndall demonstrated that light could be guided along a curved path in water. Subsequently, in 1910, Hondros and Debye [2] laid the foundation for understanding this behaviour when they analyzed dielectric waveguides in their studies of the propagation of radio waves.

In 1880, A.G. Bell invented and patented the 'Photophone', which he used to transmit speech signals at distance of a few hundred meters. This system used intensity-modulated sunlight reflected from a ~~mirror~~, atmospheric transmission, and a solenium detector. However, because the system lacked a well-controlled medium, a dependable optical source, and a sensitive detector, Bell's Photophone lost out to another, somewhat better known, Bell invention—the telephone.

Technical development in the field of optical communications again seemed to cease until the invention and realization of the laser in 1959 and 1960. The prospects of a controlled source capable of transmitting enormous amounts of information, at a time when the importance of information in the society of the future was just being recognized, led to major research efforts to uncover a low-loss, well-controlled, guided optical medium. The breakthrough occurred in 1966 when K.C. Kao and G.A. Hockham [3] of STL proposed a clad glass fiber as a suitable dielectric waveguide. They predicted that a loss of 20 dB/km should be attainable in such fibers. These remarkable predictions, at a time when the lowest loss in fibers was about 1000 dB/km, led to increasing research in glass materials and processing efforts in many parts of the world. By 1968, bulk silica samples had been prepared with losses as low as 5 dB/km [4]. In 1970, F.P. Kapron, D.B. Keck, and R.D. Maurer

[5] of Corning Glass Works reported on a doped-silica clad fiber that achieved the 20 dB/km loss bogey. That same year, just eight years after the development of the first semiconductor injection laser (GaAs, low temperature, pulse operated only), T. Hayashi and others [6] at AT&T Bell Laboratories achieved continuous, albeit short-lived, operation at room temperature and optical confinement, with an AlGaAs double-heterostructure device which was lattice-matched to a GaAs substrate.

As promising as these developments were, there still seemed to be enormous obstacles to making optical fiber transmission practical. Some of the major issues at that time were:

- Could the loss be reduced to the range of a few dB/km or less to gain a regenerator spacing advantage over competing wideband technologies, such as COAX?
- Could fibers be produced at sufficiently low cost to make optical fiber transmission economically attractive
- Could fibers be drawn with sufficient strength to survive manufacture, cabling, installation, and field use?
- Could fiber dimensions and index-of-refraction profile be controlled well enough to permit satisfactory transmission characteristics and reasonable splice losses?
- Could splicing be performed in the hostile field environment with sufficient alignment accuracy, freedom from contamination, and stability to allow stable system performance?
- Could practical optical fiber connectors be designed?
- Could injection laser lifetimes, then measured in minutes, be extended to the tens of thousands of hours needed for real systems?
- Could laser light be coupled without large loss into optical fibers?

In the succeeding 13 years, affirmative answers were reached to these questions, and to other vital ones which had not even been identified. An excellent objective historic account of optical fiber communications has been provided recently by T. Li[7].

In this admittedly personalized and not so objective account, I will review the progress made in optical fiber transmission, with emphasis on the medium, while pointing out :

- the set of optical and physical materials, properties, and discoveries which jointly make optical fiber communications practical : and
- that scientific and engineering knowledge and tools, along with the necessary incentive, were in place by this time which supported a period of remarkable progress.

LOW LOSS FIBERS: OPENING THE DOOR

As previously indicated, the lowest-loss optical fiber that has been made by 1965 had a loss of about 1000 dB/km. As engineers we sometimes throw such numbers around with great abandon without giving enough thought to their significance. To put things in the perspective of that time (1965), let us assume that we wanted to transmit a signal via an optical fiber over distance of 1 km (a short distance by telecommunications standards), without amplification or regeneration. Since the weakest signal we can possibly detect corresponds to a single photon, and assuming a source wavelength $\lambda = 1\mu\text{m}$, the minimal detectable energy E_d is

$$E_d = h\nu = (6.625 \times 10^{-27})(3 \times 10^{14}) \text{ ergs} \quad (1)$$

$$E_d = 20 \times 10^{-20} \text{ joules} \quad (2)$$

Assuming a 1000-dB average loss in transmission, the required average input energy E_i , is

$$E_i = E_d \times 10^{100} = 20 \times 10^{80} \text{ joules} \quad (3)$$

to get, on the average, one photon out!

One of the many ways to show that this number is absurdly large is to note that the total world energy production in 1981 was 284.51-quadrillion BTU [8]. Hence, it would take Y years

$$Y = \frac{20 \times 10^{80} \text{ joules}}{(284.51 \frac{\text{BTU}}{\text{yr}}) \times 10^{15} \times 1054.8 \frac{\text{joules}}{\text{BTU}}} \quad (4)$$

$$Y = 6.67 \times 10^{60} \text{ years} \quad (5)$$

to produce enough energy, at the 1981 rate, to average 1 photon out of the 1-km fiber length. (Of course the fiber would have disintegrated in the first millisecond).

The previous calculation indicates the significance of the Kao-Hockham prediction that losses of less than 20 dB/km were possible in optical fibers. In their 1966 paper [3] they concluded that, 'Theoretical and experimental studies indicate that a fiber of glassy material constructed in a cladded structure represents a practical optical waveguide with important potential as a new form of communications medium... The crucial material problem appears to be one which is difficult but not impossible. Certainly, the required loss figure of around 20 dB/km is much higher than the lower limit of loss figure imposed by fundamental mechanisms'.

In order to make this prediction, Kao and Hockham had to establish the theoretical waveguide and materials properties of the optical-fiber dielectric medium, and demonstrate that the materials and dimensional requirements were realizable. Kao [9] points out that 'dimensional tolerance requirements had to be established on simulated fibers', and that 'instruments to measure optical loss had sensitivities several orders less than that was required'. In spite of these difficulties, rapid progress was made, including vastly improved optical loss measuring instrumentation. Figure 1 shows the enormous progress that has been made in fiber loss versus calendar year.

It has already been noted how the Kao-Hockham results simulated fiber research in many countries. F.P. Kapron, D.B. Keck, and R.D. Maurer [5] achieved the goal of 20-dB/km attenuation in 1970. In

reviewing this work in 1979. Maurer [10] points out that there were two key decisions made early in their research work. 'One was to use glasses consisting primarily of silica, with oxides added to the extent necessary to increase the refractive index. These glasses have provided the lowest attenuations yet achieved and have excellent physical properties. The other decision was to use vapor phase processes for manufacturing the glass preform, or rod from which the fiber is drawn. Vapour phase processes have not only provided the necessary purity but, in addition, have turned out to be surprisingly flexible when adapted to new ways of making the preform. As a result both ideas seem to have stood the test of time and remain at the heart of today's technology'.

The choice of glasses made principally of silica was very important from the physical properties point of view, and because of the cost and availability of silicon tetrachloride. High-silica glasses tend to be chemically stable and durable, and if properly formed and free of inclusions and surface damage, can be even stronger than steel. The vapor phase process normally starts with reasonably pure liquid chlorides, such as silicon tetrachloride and germanium tetrachloride, which are vaporized in bubblers and carried by the oxygen carrier gas through a hot zone in which the oxides are formed. This process results in a substantial purification by a factor of 1000 or more with respect to iron, copper, and other transition metal ions, because of the large difference in vapor pressures involved. This self-purification process, and the avoidance of container-induced contamination associated with melt operations performed in other glass-forming methods, continue to make vapor-phase methods extremely attractive for low-loss fiber fabrication.

At this time, the principal methods for fabricating fiber preforms, from which the optical fiber is drawn, are: the Outside Vapor Deposition (OVD) process [11,12], the Modified Chemical Vapor Deposition (MCVD) process [13], the Vaporphase Axial Deposition (VAD) process [14], and the Plasma Chemical Vapor Deposition (PCVD) process [15]. Perhaps because it has resulted in high-quality multimode and singlemode (SM) production fibers and is well understood [16-18]

the MCVD process is widely used throughout the world for fiber manufacture. Figure 2 is a schematic of the vaporphase MCVD process.

Based on results obtained thus far, it appears that there may be little to choose between the alternative process, insofar as producing low losses is concerned. Figure 3 shows the loss versus wavelength for a good, but not champion, multimode high-silica fiber produced by such a process. However, there may be some differences in the area of profile control, and hence bandwidth reproducibility for multimode fibers and 'zero dispersion wavelength' for SM fibers. These factors, and the cost of fiber production, are likely to determine the preferred process in the future.

Optical Fiber Bandwidth

Step index multimode optical fibers, such as shown in Fig. 4(a), with relative index of refraction difference $\Delta = 0.01$, have a bandwidth distance product of about 10 or 20 MHz. km. The bandwidth distance product of such fibers is in fact proportional to Δ^{-1} . The relatively small bandwidth of such fibers is due to the differences in path length of the different rays supported by the multimode guide. In 1964, S.E. Miller [19] made the important proposal that the refractive index be graded, as in Fig 4(b), to reduce intermodal dispersion. By proper choice of index profile (a near parabolic profile) the maximum bandwidth versus wavelength is proportional to Δ^{-2} . Since Δ is of the order of 0.01, a very significant increase in bandwidth over the step index case is possible. However the bandwidth is very sensitive to the index profile, that is, small distortions greatly reduce the bandwidth. In addition, the bandwidth versus wavelength curve is very sharp (see Fig. 5.), and the location of the peak depends on the dopant concentrations.

These sensitivities have made it difficult to repeatedly achieve bandwidths close to the maximum theoretical value of multimode fibers in production. Figure 5 shows the bandwidth versus wavelength characteristic of the champion multimode fiber which had the largest bandwidth yet attained [20]. This fiber was made by the VAD process. However, in production it has been difficult to consistently attain high bandwidth with the VAD process, due to the difficulty of con-

trolling the involved aerodynamics. This may result in the VAD process being used principally for SM fibers (and perhaps low-bandwidth multimode fibers, that is, ≤ 500 MHz. km), since the index profile is less critical for SM fibers.

Based on manufacturing results reported to this date, high yields ($> 90\%$) of multimode fiber with bandwidths of more than 1500 MHz. km have not been obtained with any known process. With the shift of systems to the long wavelength region and the consequent reduction in loss, bandwidth becomes the factor limiting the repeater spacing of multimode systems. This is the case even though mode-mixing, that is, the exchange of energy between modes due to fiber nonuniformities, results in bandwidth decreasing with fiber length (L) more slowly than L^{-1} . Nevertheless, the need for greater bandwidth leads to the use of SM fiber, such as that shown in Fig. 4(c). In the wavelength range in which the fiber supports a single mode, intermodal differential delays are eliminated. Fiber bandwidth becomes dependent on waveguide dispersion and material dispersion, as well as optical source bandwidth. In the wavelength region where material dispersion and waveguide dispersion essentially cancel one another, fiber bandwidth can be extremely large. Furthermore, with an appropriate choice of core diameter, profile shape, and Δ , the 'zero dispersion' crossover can be controlled such that production fiber bandwidth remains high at the selected system wavelength. Figure 4(d) shows a depressed cladding SM fiber. One of the advantages of this fiber is that the required Δ value can be attained with a lower dopant concentration, and hence a lower Rayleigh scattering loss. Figure 6 illustrates a quadruply clad fiber which has < 2 ps/nm. km dispersion in the entire wavelength range between 13-16 μm [21]. Such a fiber is well-suited for simultaneous transmission of many wavelengths (wavelength division multiplexing (WDM)).

Physical Strength of Optical Fibers

In the early 1970's, just after the announcement of the first low-loss optical fiber, the physical and chemical properties of fibers received much increased attention. Until that time, most

of the research on the strength of glass fibers, and the achievements made, related to fibers in the millimeter to few centimeter length range. Cable and manufacturing engineers changed all that by telling their ceramist and metallurgist colleagues something like,

"I've got to make cables in kilometer lengths. I need to know and design for the minimum strength/strain capability of kilometer lengths of fibers, not the maximum strength of short lengths!"

It was already well known that glass fibers under tension behave nearly like linear elastic solids until a critical stress intensity for the material is reached [22], at which point brittle failure occurs. The stress intensity is highest at crack tips of flaws; hence fiber strength depends on the flaw distribution. The distribution of flaw size depends very strongly on the material and processing history of the sample, and consequently can have a large range [23]. Figure 7 shows the strain capability of high-silica fiber versus the maximum flaw size. The maximum flaw size alone (weakest link phenomenon) determines the fiber strength, and since the maximum flaw size will increase statistically with the length, it is clear why measurements on short lengths provide little information on the strength of long fibers. From the figure it can be seen that the maximum allowable flaw size to achieve 1% strain is of the order of 1 μm . To provide a feeling for what this means, if someone took a pristine sample of newly-formed high-silica glass and lightly ran their fingers on the surface, the strain capability would drop to a few tenths of a percent, indicating a maximum flaw size in the 5 μm range!

The foregoing indicates one of the fundamental issues in the physical properties of glass, namely, the statistical nature of its strength. The second important strength issue, known as static fatigue, is that water can degrade the strength of glass [24]. Both of these phenomena are fundamental consequences of the atomic structure of glass: therefore, they can be altered in extent, but not in kind, by composition and processing changes [23].

It is noteworthy that high-silica glasses, relative to other glasses, have very-high tensile strength versus flaw size, as well as good static fatigue behavior. That is, the very same material systems which are capable of yielding low-loss low-cost fibers also possess the best physical properties. Nevertheless, optical fibers in contrast to metallic conductors have a statistical distribution of strengths, as opposed to an essentially deterministic strength. The question asked by our cable engineer in the early 70's was: how could one assure a minimum level of tensile strain on which to base cable design and manufacture? The answer, which was and is employed in most optical-fiber cable manufacturing processes, was to employ proof testing [24-26]. In proof testing, every segment of the fiber is exposed to a short-term tensile strain test, in some cases in-line with the fiber draw process. This truncates the fiber strain distribution on the low side and provides the design engineer with a tensile strain capability equal to or greater than the proof strain. Today, typical proof strain values in fiber manufacture are in the .5% - 15% range.

Even if fibers can be drawn with the large strain capability, it is almost impossible to handle them directly without introducing flaws in the process. This led to the idea of inline coating of the fiber, the most successful versions of which have been polymer coatings. In this process, the freshly drawn fibers are passed through a die containing a liquid polymer, which is subsequently cured thermally or by UV radiation, for example. The central idea is that contact with the fiber surface by particular matter is avoided; hence, abrasion- and handling-induced flaws are avoided. Once the coating has set up, the fiber can be fed over capstans, placed on reels, stranded into units, and cabled.

In order to obtain very-high strength fibers, many factors need to be controlled [18,23,27]: Fig. 8 summarizes some of these. By paying careful attention to these factors, very-high-strength fibers have been fabricated. Figure 9 [18] summarizes some of the highest fiber strengths obtained to date. The 500 ksi (1 ksi = 1000 lbs/in

strength which corresponds to about 5% strain indicates a maximum flaw size of about $0.04 \mu\text{m}$. The result associated with the light - guide sea trial, reported by Runge [28] - that 101 km of fiber in $\geq 2.5\text{km}$ lengths had been assembled and spliced and passed proof test of 200 ksi-is particularly significant.

Gabling and Splicing

In the early 1970's there were strong concerns about achieving high fiber survival rate in optical cable manufacture. This is not hard to understand for those who have seen the machinery in a conventional cable-manufacturing plant. Getting $\sim 100 \mu\text{m}$ diameter fibers through such processes without breaks seemed to be an incredible task. It was a very difficult job, but in-line coating techniques and proof testing provided the strength and handling properties required to make cable manufacture practical.

Another problem 'unique to optical fibers', called microbending was discovered [29,30]. It was observed that small deflections of the fiber axis (in the submicron range or larger) with periods of about 1 mm can cause large losses (tens of dB/km) in graded index multimode fibers. At the time, there was concern as to whether it would be possible to avoid such tiny bends in cabled fibers. However, it was soon realized that coating design could play an important role in controlling microbending. Gloge [31] demonstrated that hard or soft coatings, and combinations thereof, could be used to control microbending.

Two basically different cable design approaches were taken. In the first approach, tight mechanical coupling exists between the fibers and the cable sheath. This approach, which is similar to conventional cables, has the advantage that it is easy to match the 'fiber length' to the sheath length in manufacture. However, it requires that the cable sheath take installation loads with little elongation, since the fibers usually have relatively small elongation to break when compared to copper (about 1% for fibers compared to more than 20% for copper). The tight mechanical coupling approach led to the use of thick fiber coatings to prevent microbending

loss due to the effects of pressure from other cable components on the fibers. Figure 10(a) shows the cross section of a typical coated fiber used in the 'tight configuration'. The dimensions are dominated by the coating and hence optical cables with this type of coated fiber tend not to be space efficient. A second cable design approach places the fibers in loose structures, as shown in Fig. 11. Since the fibers are loose, they need not be pressed on by other cable members, and the inherent fiber stiffness can prevent microbends. Such designs can employ thinner coatings as shown in Fig. 10(b). However, manufacture of cables with loosely coupled fibers requires care to avoid introducing excessive fiber length mismatch with the sheath length. For example, if the fibers are 'too long' they will tend to buckle and bending losses can result. On the other hand, if the fibers are too short, they will break under tensile loading. Figure 12 taken from [32], shows a number of high-density cables (with a large number of fibers per unit cross section). The highest-density and lowest-weight fiber is achieved by the ribbon-based cable shown in Fig. 12(e). High-density and low weight/fiber are important cable characteristics for duct-type installations.

Figure 13 shows the cross section of an undersea cable with a tightly coupled embedded core with 12 SM fibers. Added losses due to cabling of 18.2 km of this cable were negligible [33].

In the early 1970's, the problem of finding methods of splicing fibers loomed almost as large as the problems of attaining low fiber loss, adequate fiber strength, and low microbending loss. Although a number of different mechanisms can contribute to splice loss, the difficulty of the problem can be understood with the help of Fig. 14 [32]. In the case of a multimode fiber with a 50 μm core diameter, the transverse offset between the two fibers has to be less than about 8 μm to keep the loss below 0.5 dB. Attaining 8 μm alignment accuracy of 2 nearly-hair-thin fibers in the crowded, dirty, often wet conditions that exist in manholes in metropolitan area seemed almost out of the question. Not only has this been done, but much lower loss performance has been attained, usually in the 0.1-0.4 dB range. This has been accomplished by clever

fixturing, using a variety of alignment techniques such as sleeves and V-grooves [32], to butt splice or fusion splice individual fibers. Some cable structures which have regular arrays of fibers, such as cylindrical V-groove cores and fiber ribbons, lend themselves to mass splicing, that is a number of fibers are spliced together simultaneously. This can avoid handling the tiny individual fibers and speed up the splicing job.

The splicing task becomes even more difficult in the case of SM fibers. Figure 14 shows that transverse offset needs to be of the order of 1 μ m to get low splice loss. This is one of the reasons that SM fiber systems followed the development of multimode systems. Because of the great accuracy required in an SM fiber splice, and because most practical splicing methods will likely require 'active core alignment', that is, adjustment of the alignment of the two cores to maximize transmission before completing the splice, it is likely that SM fibers will not be mass spliced. Both fusion and bonded butt splices of SM fibers have been reported [34,35] with losses of 0.1 dB or less.

High-strength SM splicing techniques, needed for undersea cable, which consistently have strengths > 200 Kpsi and losses of < 0.1 dB, have been reported [35].

Field Experiments and Systems

In order to establish the feasibility and practicality of optical fiber transmission, a number of multimode fiber experiments were conducted in the mid 1970's in Japan, the United States, France, the United Kingdom, Italy, and Germany. The first of these, which emphasized cabling and splicing, was carried out by Furukawa during the summer of 1974. It involved 400 meters of 4 fiber cable, of which 200 meters was installed aerially, the remaining 200 meters was placed underground. Splicing was performed using a sleevebased technique. Results of the experiment were reported by Murata [36,37]. Optical fiber field trials and early applications in North America, Europe, and Japan are described [38-40].

AT&T Bell Laboratories installed an experimental optical fiber trunk system in Atlanta in the latter part of 1975 [41]. The system used a 650m, 144 fiber cable that was configured in a loop which passed through underground ducts. Hence, optical signals could be sent through the cable many times to establish long transmission lengths by appropriately connecting different fibers of the cable with short jumpers at two single-fiber jack fields. The cable, of the ribbon type, was mass spliced using 144 fiber array connectors [42], with an average loss of 0.8 dB. A full range of system experiments was carried out at 44.7 Mb/s, which yielded unrepeated spacings up to 10.9 km at error rates of $< 10^{-9}$ and negligible crosstalk even with mass splicing.

The most significant aspect of the Atlanta experiment was that it established the viability and practicality of all aspects of optical fiber trunk transmission, including the optical cable medium, its installation, splicing, optical transmitters and receivers, electronics, optical jack fields and jumpers, and optical system performance. The success of the experiment led to the decision to install a similar system in underground ducts in the Chicago 'Loop' area. The system, which began carrying service in the spring of 1977, provided digital video transmission for use with experimental 45-Mb/s video terminals along with data and voice. The results of this effort led to the FT3 45MB/s lightwave trunk development, which began in 1978, and to the first standard service in September 1980 in the Atlanta-Smyrna area. Miller [32] reported that as of December 1982 more than 150000 km of cabled fibers had been installed in association with FT3 and FT3C, which are AT&T Technologies supplied lightwave transmission systems operating at 45Mb/s and 90 MB/s, respectively. As of December 1983, more than 300000 km of cabled optical fibers had been installed in what was the Bell System [43] for these same systems and for fiber loop carrier applications [44].

The first major field test using optical fibers to bring broadband services to individual residences was the Hi-OVIS project [45] in Japan, which began in 1978. It used LED's and plastic-clad step index glass core fibers and baseband transmission to provide a very

broad range of video services, including two-way video using channel selection signals. It involved 168 subscribers and was configured to help meet the social requirements and community needs set by the Ministry of International Trade and Industry (MITI).

At this time, optical fiber systems are more than 'interesting new technology'. In many places and instances around the world it has now become necessary to justify when anything other than an optical fiber system is proposed for trunk or long-haul right-of-way applications. This is the case in a number of Bell Operating Companies, in the United Kingdom and Canada, to name a few. Major long-haul routes in the United States include a 776 mile FT3C route along the east coast from Moseley, VA, to Cambridge, MA, and a 500 mile FT3C system in California linking Los Angeles and San Francisco.

SM system, with their inherently large bandwidth and longer repeater spacing capability, are the main thrust in new systems for long and short haul applications. NTT in Japan has sponsored a field trial of a 400-Mb/s SM fiber system between Musashino and Atsugi, and 80-km route passing through 11 cities with 4 intermediate repeaters [40]. The system operates at 13 μ m and uses a cable with 6 SM fibers, 6 graded-index multimode fibers (for comparison purposes), 2 power feeders, and 6 quads. The NTT trial was due to be completed in March 1983 and was to be introduced into the long-haul network in 1983. Announced plans indicated more than 60 such installations and 90000 fiber kilometers beginning in 1983.

In addition, both the United States and the United Kingdom have announced plans for major long-haul routes using SM fiber [46,47], and some short-haul systems are already in operation [48].

Undersea lightwave systems are being aggressively pursued in the United States, the United Kingdom, France, and Japan. A Deep Water Sea Trial of an undersea lightwave system was carried on by AT&T Bell Laboratories in September 1982 at a depth of 5.5 km [49,50]. The results of the trial include the following:

- The 18.2 km cable, which contained 12 low-loss high-strength fibers, performed as anticipated during laying, holding, and recovery operations.
- Error-free transmission at 274 Mb/s was demonstrated at 1.3 μ m in a concatenation of 3 regenerator spans (a length of 109 fiber km). The signal was looped through the cable 3 times (54.6 km) to 1 underwater regenerator, then looped 2 more times to a second underwater regenerator (36.4 km), from which it passed through the cable 1 more time (18.2 km) to a shipboard regenerator.
- The maximum change in loss due to temperature, tension, and pressure was less than 0.1 dB under all conditions.

In November 1983, it was announced that AT&T has been awarded a major portion of the first transatlantic lightwave cable system, known as TAT-8 [51]. The Deep Water Sea Trial previously referred to laid the groundwork for, and established the viability of, the technology AT&T will employ. AT&T will provide the segment of the system from a landing point in Tuckerton, NJ, to a branching device off the European continental shelf. AT&T will supply 3146 nautical miles (nml) of undersea cable, repeaters, and terminal equipment. Standard Telephone and Cables will supply 279 nml of cable as well as repeaters and terminal equipment to reach Widemouth, England from the branching point; Submarcom will do the same for the 167 mile link from the branch point to Penmarch, France. AT&T Communications was given the responsibility for ensuring the technical compatibility of the three parts of the TAT-8 system. The system, which is planned for service in June 1988, is expected to provide the equivalent of 40000 two-way telephone channels.

As a measure of progress in the experimental systems area, the 'world record for the longest unrepeated transmission distance' in a Laboratory demonstration changed hands three times last year. Early in 1983 a world record of 119 km was achieved at AT&T Bell Laboratories at a 420-Mb/s rate [52]. In June 1983, Nippon Telegraph and Telephone (NTT) succeeded in reaching 134 km at 446 Mb/s [53], in the spirit of 'can you top this', AT&T Bell Laboratories

reached 161-km spacing at 420 Mb/s [54]. These incredible spacings at such high bit rates are not practical today for real systems because such laboratory systems do not account for system margins, reliability, physical constraints on splices, and above all, costs. However, they do signify the tremendous rate of progress being made, and it is possible that in a five to ten year period these parameters will be achieved in commercial systems.

Outlook for the Future

Currently, fiber research efforts are moving to the longer wavelength range beyond $2\mu\text{m}$, where Rayleigh scattering losses can be much lower. Unfortunately, this means abandoning the high-silica glasses because of their infrared absorption. A number of material systems including germania, fluoride, and chalcogenide glasses are under investigation [55]. Thus far, fiber losses have been high due primarily to impurities. Although some of these systems have the potential for losses below 0.01 dB/km, it will take considerable effort to get down to the 0.16-dB/km minimum reported for high-silica fibers [56]. Even if the impurity problems are solved, there are significant physical-property issues and difficult cost problems to be solved before longer-wavelength systems become practical. Nevertheless, the payoff potential is so large that it is 'well worth the hunt'.

Other areas which appear to have significant potential, particularly for long wavelengths, are coherent transmission and detection. Coherent systems have the potential of achieving the quantum noise sensitivity limit, however, they require single frequency stabilized transmitters and local oscillators. Depending on the system parameters and choices, such as bit rate and type of detector, improvements in system sensitivity of the order of 20 dB are theoretically possible (smaller if a reasonably good avalanche photodiode (APD) is available). Recently, two techniques have been reported for injection locking a diode laser and attaining fullwidth half-maximum line widths of less than 10 KHz [57]. Using an injection-locked transmitter and an HeNe local oscillator to perform hetero-

dyne detection, a sensitivity improvement of 14 dB at 8 Mb/s was measured over 123 km of fiber relative to a p-i-n photodiode. Many issues remain to be resolved, such as laser stability, polarization preservation in fibers, and nonlinear propagation effects, but there is reason to be optimistic.

Much progress has also been made in sources and detectors. These developments will further enhance the ability of the new optical fiber technology to do old transmission jobs better and more cheaply than other guided transmission systems. Perhaps this will eventually lead to the same kind of qualitative effect that integrated circuits have had on electronic systems, that is, allowing society to do things that were inconceivable before the transistor and its descendant realizations. But, for a while at least. I suspect we will focus on the quantitative side, emphasizing higher speeds, longer distances, and lower costs. I dare say we will see much more of this in the next 20 years.

References

1. E. Risberg, 'A History of the Finnish Telegraph Administration, 1855-1955' General Direction of Posts and Telecommunications, Helsinki, 1955.
2. D. Hondros and P. Debye, 'Elektromagnetische Wellen an dielektrischen draethen', Ann Phys. vol. 32, pp. 465-476, 1970.
3. K. C. Kao and G.A. Hockham, 'Dielectric-fiber surface waveguides for optical frequencies', Proc. Inst. Elec. Eng., Vol. 113, pp. 1151-1158, July 1966.
4. (a) K.C. Kao and T.W. Davis, 'Spectrophotometric studies of ultra-low-loss optical glasses I. Single beam method', J. Sci. Instrum. vol. 1 (ser.2), pp. 1063-1068, Nov. 1968; (b) M.W. Jones and K.C. Kao 'Spectrophotometric studies of ultra-low-loss optical glasses II: double beam method'. J. Sci. Instrum. vol. 2 (ser. 2). pp. 331-336, April 1969.
5. F.P. Kapron, D.B. Keck, and R.D. Maurer, 'Radiation losses in glass optical waveguides'. Appl. Phys. Lett. vol. 17. pp. 423-425, Nov. 1970.

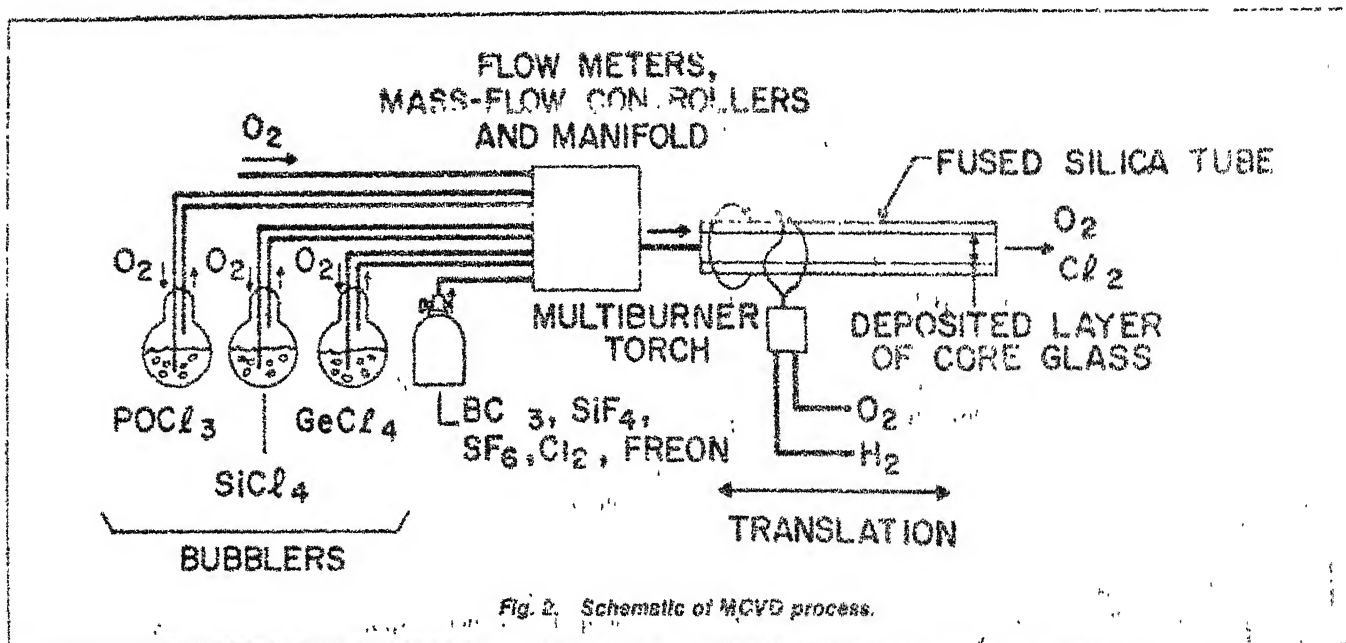
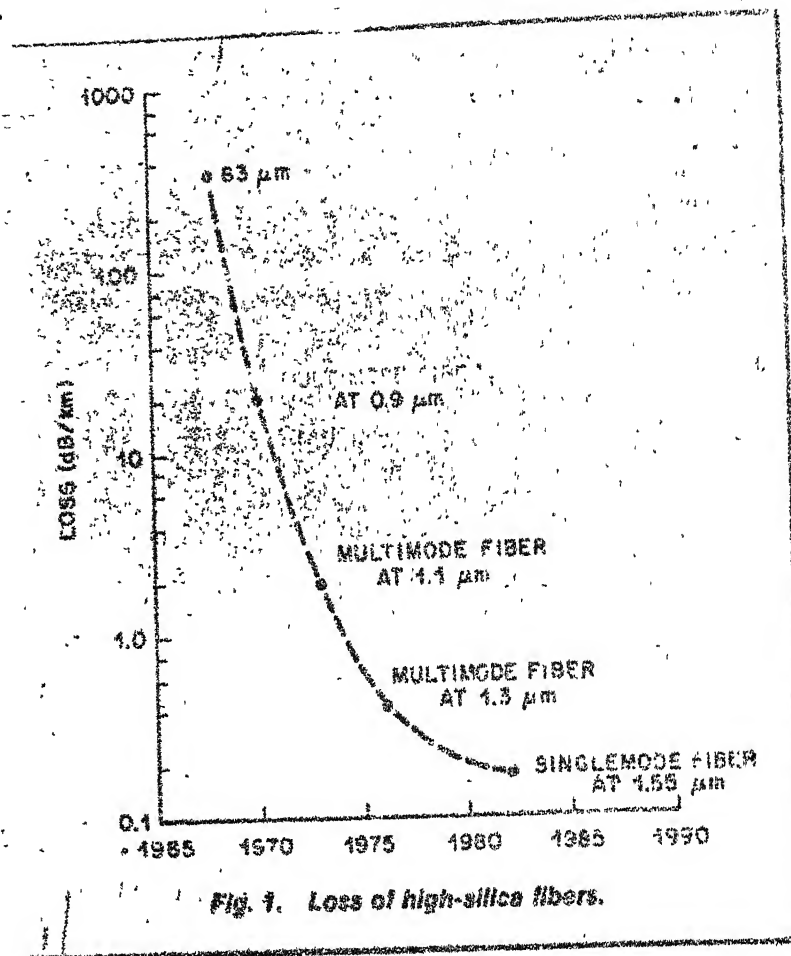
6. I. Hayashi, M.B. Panish, P.W. Foy, and S. Sumski, 'Junction lasers which operate continuously at room temperature'. Appl. Phys. Lett. vol. 17. pp. 109-111, Aug. 1970.
7. T. Li, 'Advances in optical fiber communications: an historical perspective'. IEEE J. Selected Areas in Commun. SAC-1. no.3. pp. 356-372 April 1983.
8. Private communication-United States Energy Information Administration, United State Department of Energy.
9. K.C. Kao, 'Optical fibers and systems: history and future'. Ericsson Rev., vol. 56, No.3, pp. 92-94, 1979.
10. R.D. Maurer, 'Optical fiber components: history and future'. Ericsson Rev. vol. 56. no. 3. pp.95-99.
11. D.B. Keck, P.C. Schultz, and F. Zimar, 'Method of forming optical waveguide fibers'. U.S. Patent 3 737 292, filed Jan. 3 1982 issued June 5, 1973: see also 'Method of forming optical waveguide fibers, 'U.S. Patent Re 28 029, filed June 21, 1973. issued June 4, 1974.
12. P.C. Schultz, 'Fabrication of optical waveguides by the outside vapor deposition process'. Proc. IEEE vol. 68 pp. 1187-1190. Oct. 1980.
13. J.B. MacChesney and P.B. O'Connor, 'Optical fiber fabrication and resulting product', U.S. Patent 4 217 027, filed Feb. 22, 1974. issued Aug. 12, 1980.
14. T. Izawa and N. Inagaki, 'Materials and processes for fiber perform fabrication-Vapor-phase axial deposition', Proc. IEEE: vol. 68, pp. 1184-1187. Oct. 1980.
15. D. Koppers, H. Lydtin, and L. Rehder, 'Method of producing internally coated glass tubes for the drawing of fiber optic light conductors', U.S. Patent 4 145 456, filed Nov. 16, 1977, issued Mar. 20, 1979.
16. (a) J.B. MacChesney, 'Materials and processes for perform fabrication Modified chemical vapor deposition and plasma chemical vapor deposition', Proc. IEEE vol. 68. pp. 1181-1184, Oct. 1980; (b) S.R. Nagel, J.B. MacChesney, and K.L. Walker, 'An overview of the modified chemical vapor deposition (MCVD) process and performance'. IEEE J. Quantum Electron. QE-18. pp. 459-475, April 1982.

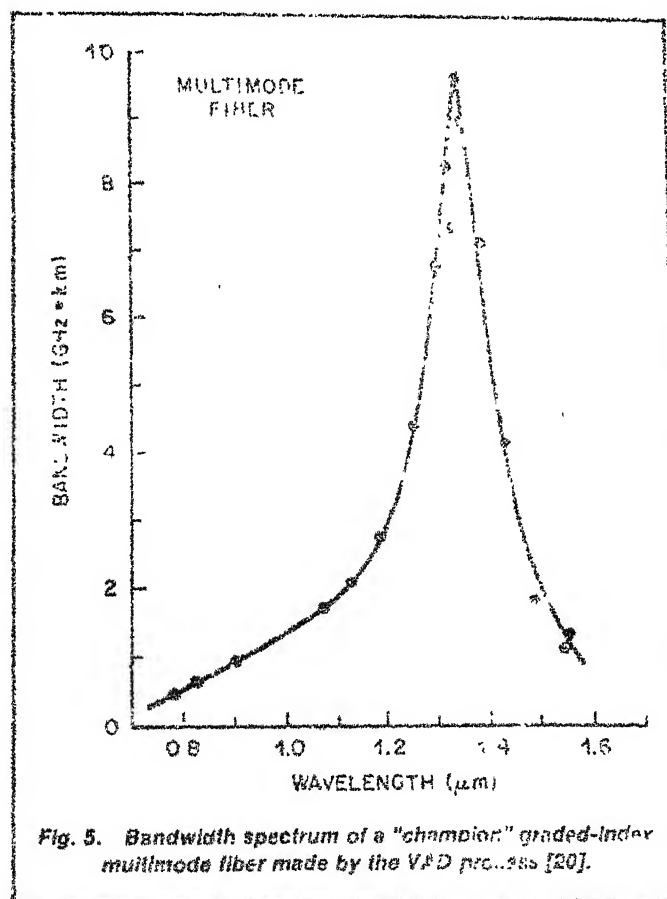
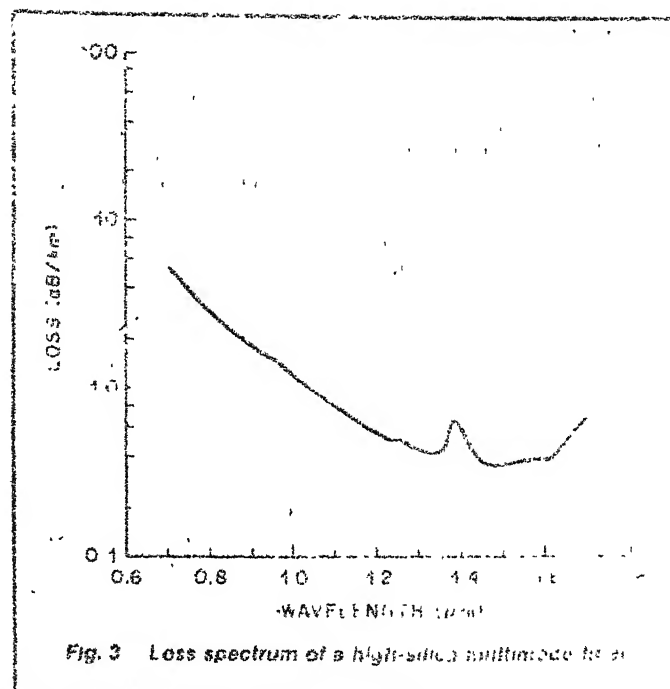
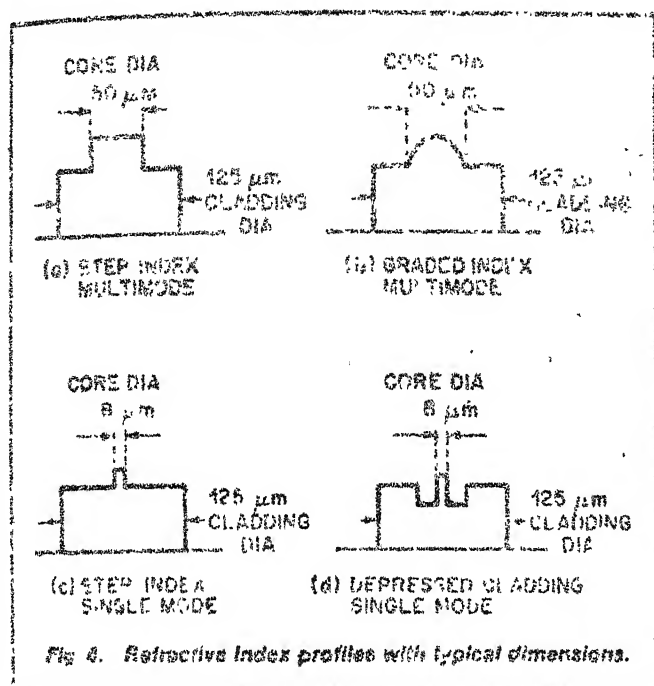
17. D.P. Jablonowski, D.D. Padgett, and J.R. Merten, 'Performance of the MCVD preform process in mass production conditions', paper TUEE2, Tech. Dig. 5th Topical Meet. Opt. Fiber Commun. Phoenix, AZ April 1982.
18. S.R. Nagel, 'Recent Advances in the MCVD Process Rate and Fiber Performance', 'Invited paper, Fourth Int. Conf. on Integrated Optics and Optical Fiber Commun. Tokyo, Japan, June 27-30, 1983.
19. S.E. Miller, 'Light propagation in generalized lens-like media', Bell System Tech. J. vol. 44, pp. 2017-2064, Nov. 1965, see also, 'Waveguide for millimeter and optical waves', U.S. Patent 3 434 774, filed Feb. 25, 1964, issued Mar. 25, 1969.
20. M. Horiguchi, M. Nakahara, N. Inagaki, K. Kokura, and K. Yoshida, 'Transmission characteristics of ultra-wide bandwidth VAD fibers', Paper AIII-4, Proc. 8th Euro. Conf. Opt. Commun. Cannes, France, Sept. 1982.
21. L.G. Cohen, W.L. Mammel, and S. J. Jang. 'Low-loss quadruple-clad single-mode lightguides and dispersion below 2 ps/km nm over the 1.28 μ m-165 μ m wavelength range. Electron. Lett. vol. 18. pp. 1023-1024, Nov. 1982.
22. G.R. Irwin, 'Fracture', Encycl. Phys. vol. 6, pp 551-590, 1968.
23. D. Kalish and M. I. Schwartz, 'Review of research and production of high-strength fibers', Proc. Optical Commun. Conf. Amsterdam, The Netherlands. Sept 1979.
24. D. Kalish, P.L. Key, C.R. Kurkjian, B.K. Turiyal, and T.T. Wang, 'Optical Fiber Telecommunication, S.E. Miller and A.G. Chynoweth, Eds. pp. 417-425, New York: Academic Press, 1979.
25. M.I. Schwartz, D. Gloge, and R.A. Kempt, Optical Fiber Telecommunication, S.E. Miller and A.G. Chynoweth, Eds. pp. 435-453, New York Academic Press, 1979.
26. M.I. Schwartz, P.F. Gagen, and M.R. Santana, 'Fiber cable design and characterization', IEEE, vol. 68, no. 10. Oct. 1980.
27. D.L. Brownlow, F.V. DiMarcello, A.C. Hart, Jr. and R. Huff, 'High-Strength Multikilometer Lightguides for Undersea Applications', post-deadline paper, 8th ECOC, Cannes, France, Sept. 21-24, 1982.

28. P.K. Runge, '101km lightwave undersea system experiment at 274 Mb/s', Optical Fiber Conf. Proc. Phoenix, AZ. April 1982.
29. W.B. Gardner, 'Microbending loss in optical fibers', Bell Syst. Tech. J. vol. 54. no.2, pp. 457-465, Feb. 1975.
30. D. Marcuse, 'Microbending losses of single-mode, step-index and multimode, parabolic-index fibers'. Bell Syst. Tech. J., Vol.55, no.7, pp. 937-955, Sept. 1976.
31. D. Gloge, 'Optical-fiber packaging and its influence on fiber straightness and loss', Bell Syst. Tech. J. vol.54, no.2, pp. 243-260, Feb. 1975.
32. C.M. Miller, 'Optical fiber cables and splices', IEEE J. Selected Area in Commun, SAC-1, no.3 pp. 533-540, April 1983.
33. P.K. Runge and P.R. Trischitta, 'Light in the depths of the sea with FO undersea cable system'. Telephony, pp. 32-37, August 23, 1982.
34. C.M. Miller, G.F. Devau, and M.Y. Smith, 'Low-loss single-mode fiber splices using ultraviolet curable cement', 4th Int. Cont. on Integrated-Optics and Optical Fiber Commun. Tokyo. Japan, 30A3-6, pp. 128-129, June 27-30, 1983.
35. J.T. Krause and C.R. Kurkjian, 'Improved high-strength flame fusion single-mode splices'. 4th Int. Cont. on Integrated Optics and Optical Fiber Commun. Tokyo. Japan, 29A4-6, pp. 96-97, June 27-30. 1983.
36. H. Murata, S. Inao, and Y. Matsuda, 'Step-index type optical fiber cable'. 1st European Cont. on Optical Fiber Commun. pp. 70-72 London, United Kingdom, Sept. 16-18, 1975.
37. H. Murata, S. Inao, Y. Matsuda, and T. Takahashi, 'Splicing of optical fiber cable on site'. 1st European Cont. on Optical Fibre Commun. pp. 93-95, London, United Kingdom, Sept. 16-18, 1975.
38. J.S. Cook and O.I. Szenteši, 'North American field trials and early applications in telephony'. IEEE J. Selected Areas in Commun. SAC-1, no.3, pp. 393-397, April 1983.
39. A. Moncalvo and F. Tosco, 'European field trials and early applications in telephony'. IEEE J. Selected Areas in Commun. SAC-1, no.3. pp. 398-403, April 1983.

40. H. Ishio, 'Japanese field trials and application in telephony', IEEE J. Selected Areas in Commun. SAC-1, no.3 pp. 404-412, April 1983.
41. R.S. Kerdock and D.H. Wolavel, 'Results of the Atlanta experiment'.-Bell Syst. Tech. J. vol. 57, no.6, pp. 1857-1879, July-August, 1978.
42. C.M. Miller, 'Fiber optic array splicing with etched silicon chips', Bell Syst. Tech. J. vol. 57, no.1, pp. 75-99. Jan.1978.
43. Private Communication
44. P.P. Bohn, M.J. Buckier, and T.N. Rao, 'Bringing lightwave technology to the loop, 'Bell Lab Rec. pp. 6-10, April 1983.
45. K. Sakurai and K. Asatani, 'A review of broadband fiber system activity in Japan, 'IEEE J. Selected Areas in Commun. SAC-1, no. 3, pp. 428-435, April 1983.
46. I. Jacobs, 'Lightwave communications in the Bell System-1982 and beyond'. 6th Topical Meet. Optical Fiber Commun. Tech. Digest. p.80, Feb. 28-March 2, 1983, also Recent Developments in Fiber-Optice Commun. Seminar sponsored by the IEEE Communications and Computer Societies, New York Chapters, pp.1-4, May 12, 1983.
47. J.E. Midwinter, 'Optical fiber systems: low-loss links', IEEE Spectrum, pp. 45-47, March 1980.
48. H. Sinnreich, E. Loytty, and K. Kamiyama, 'Advantages of single mode FO systems for short-hault links', Telephony. pp. 32-36, Nov.21, 1983.
49. S.M. Abott, R.E. Wagner, and P.R. Trischitta, 'SL undersea lightwave system experiments', IEEE Conf. on Commun. C3.5.1. pp. 695-697, Boston, MA. June 1983.
50. P.K. Runge and P.R. Trischitta, 'Future undersea lightwave communications system', Signal, pp. 30-35, June 1983.
51. AT&T Contract, New York Times, p. D-4, Nov. 17, 1983.
52. W.T. Tsang, R.A. Logan, N.A. Olsson, H. Temkin. J.P. Vander Ziel, I.A. Kaminow, B.L. Kasper, R.A. Linke, V.J. Mazurczyk, B.I. Miller, and R.E. Wagner, '119-km 420 Mb/s Transmission with 1.55 μ m Single-Frequency Laser', Topical/Meet on Optical Fiber Commun. post-deadline paper PD-9. Feb. 28-March 2, 1983.

53. 'NTT achieves longest optical fiber transmission', The Japan Times, July 1, 1983.
54. B.L. Kasper, R.A. Linke, J.C. Campbell, A.G. Dentai, R.S. Vodhanel, P.S. Henry, I.P. Kaminow, and J.S. Ko, 'A 161.5 km Transmission Experiment at 420 Mb/s'. 9th European Conf. on Optical Commun, Geneva, Switzerland, Post-deadline paper, PD 7, Oct. 1983.
55. S. Yoshida and H. Murata, 'Infrared optical fibers, optical fibers and devices', Japan Ann. Rev. in Electronics & Telecommun. vol.5, Amsterdam, The Netherlands: Nort-Holland, 1983.
56. M.G. Blankenship and C.W. Deneka, 'The outside vapor deposition method of fabricating optical waveguide fibers'. IEEE J. Quantum Electron, QE-18, pp. 1418-1423, Oct. 1982.
57. D.M. Smith, 'Coherent monomode optical systems in the 1500 nm waveband'. 4th Int. Conf. Integrated Optics and Optical Fiber Commun. 30C3-1, Tokyo, Japan June 27-30. 1983.





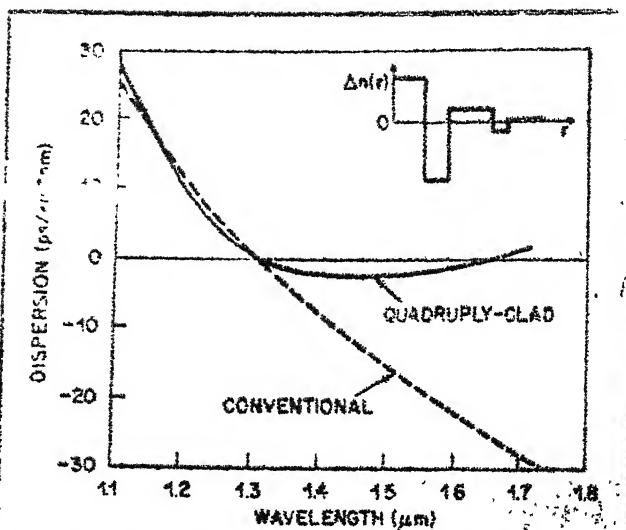


Fig. 6. Chromatic-dispersion spectra of SM fibers. The dashed curve represents a conventional step-index fiber; the solid curve is the measured dispersion of an experimental quadruply-clad fiber with a profile as shown in the upper right corner [21].

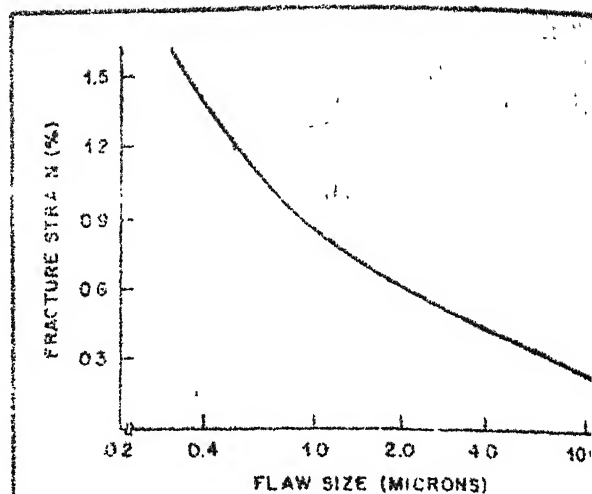


Fig. 7. Fracture strain vs. flaw size in high-silica fiber

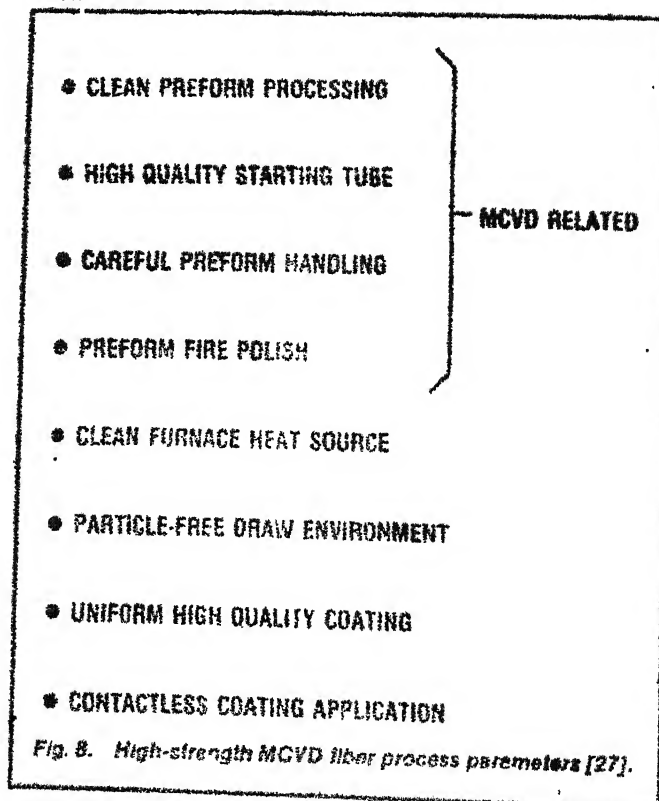


Fig. 8. High-strength MCVD fiber process parameters [27].

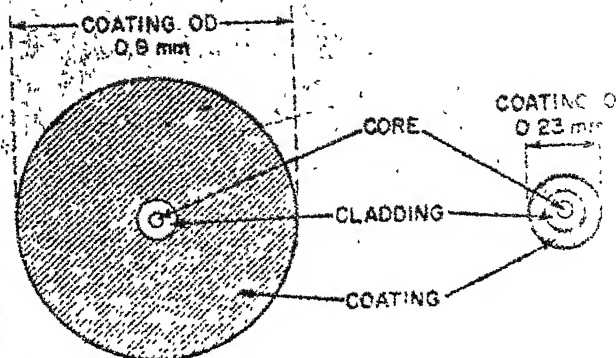
REPORTED EXPERIMENTAL RESULTS

- LABORATORY: 12.2 km AT 200 ksf (1.4 GPa)
4.5 km AT 500 ksf (3.5 GPa)
- PILOT PLANT: 10.5 km AT 200 ksf (1.4 GPa)

MCVD FIBER FOR UNDERSEA SYSTEMS

- CRITERIA: ≥ 2.5 km AT 200 ksf WITH HIGH TRANSMISSION PERFORMANCE
- DATA BASE: 54 PREFORMS, 557 km DRAWN
10.3 km AVERAGE LENGTH
- YIELD: 74% ≥ 2.5 km
AVERAGE LENGTH > 2.5 km, 6.1 km
50% > 8 km
22% > 10 km
MAX LENGTH — 12.2 km (TOTAL DRAWN)
- BEST REPORTED: 101 km ASSEMBLED LENGTH
200 ksf FIBER, 300 ksf SPLICES

Fig. 9. MCVD high-strength fiber [15].



(a) "Tight configuration" coating.

(b) "Loose configuration" coating.

Fig. 10. Cross-sections of typical coated fibers used in tight and loosely coupled cable designs.

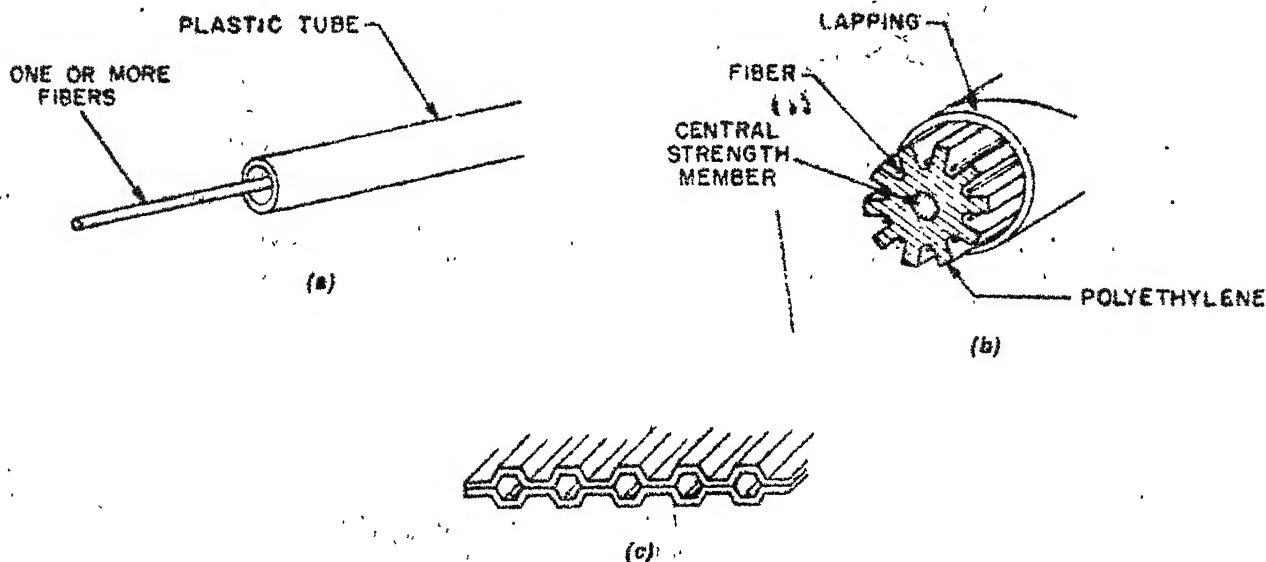


Fig. 11. Loose core structures: (a) loose tube; (b) loose cylindrical structure, (c) loose ribbon [32].

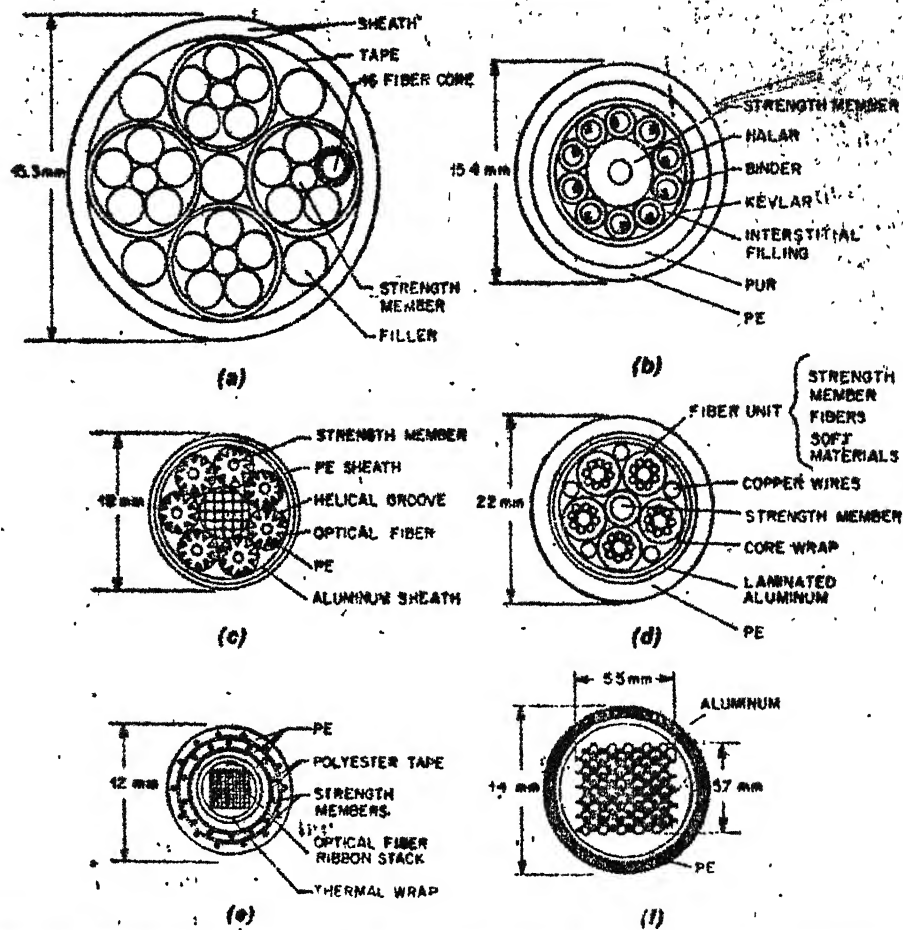


Fig. 12. High density cable designs: (a) 320 fiber—light stranded; (b) 70 fiber—loose bundles; (c) 70 fiber—loose cylindrical; (d) 40 fiber—tight stranded; (e) 144 fiber—light ribbon; (f) 50 fiber—loose ribbon [32].

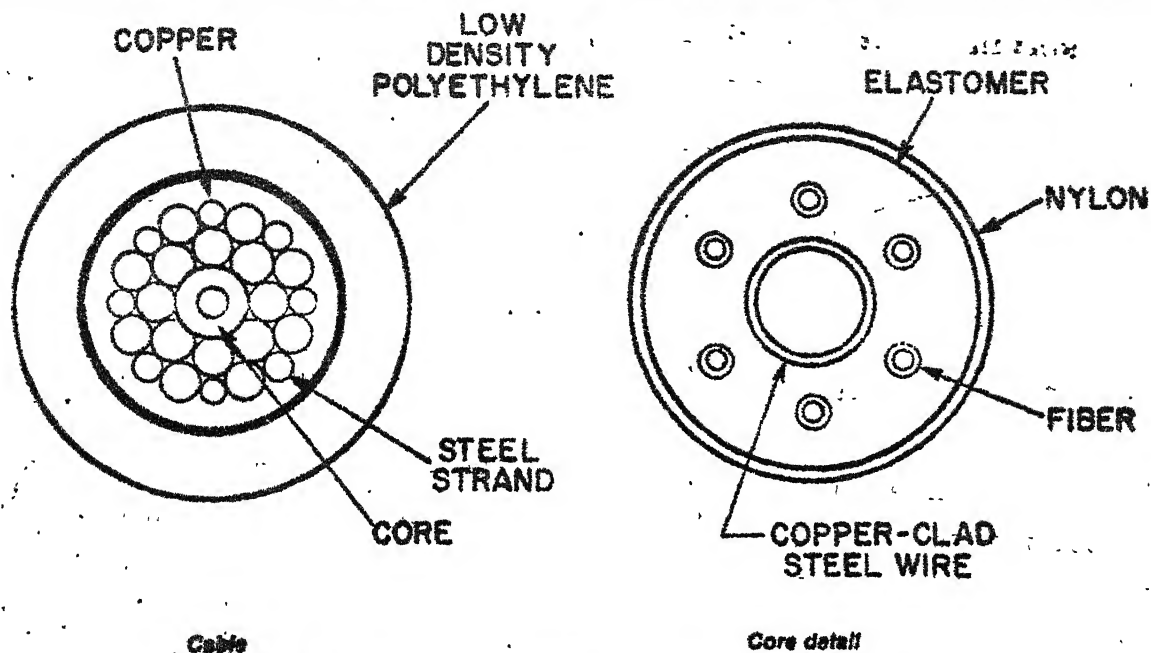


Fig. 13. Undersize cable—light coupled embedded fiber core [33].

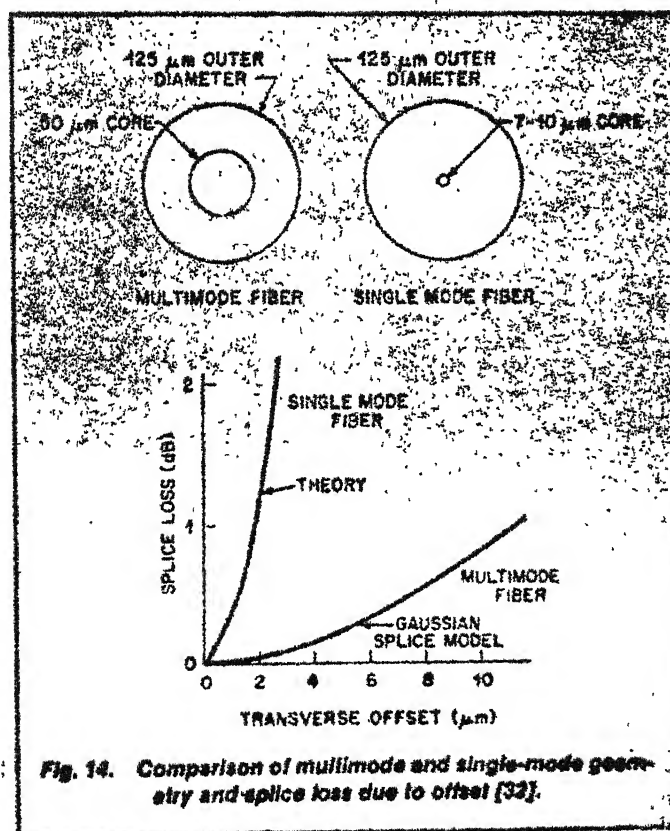


Fig. 14. Comparison of multimode and single-mode geometry and splice loss due to offset [33].

OVERVIEW OF TELECOMMUNICATIONS VIA OPTICAL FIBERS

ABSTRACT

Light-wave transmission on a glass-fiber transmission medium has reached a fully commercial stage, with carrier wavelengths in the 0.82-0.85 μm region. Second generation systems will operate with carrier wavelength in the 1.2-1.6 μm region where high silica fibers have more attractive loss and dispersion characteristics. Research continues at a high level, and will lead to continued rapid evolution of lightwave systems.

LIGHT WAVE

Light wave telecommunication systems using glass fiber guides are now being manufactured and installed on a regular commercial basis. The era of experimental and trial installations appears to be near an end, and customers are ready for standard commercial offerings.

Cables containing photon flow in glass fibers are superseding cables containing electron flow in copper pairs or coaxials. Applications are to undersea (intercontinental) communication systems, to domestic intercity systems, to metropolitan area trunking systems, to feeder links in the subscriber loop, and to on-premises or local links such as data bus in computers or switching machines. The breadth of these applications of optical fibers was anticipated in early reviews appearing in PROCEEDINGS OF THE IEEE [1]-[3]. The rapid evolution from research demonstration to commercial service is in part a reflection of intensive work in many organizations overseas as well as in the U.S. In part, it is also a reflection of the intrinsic soundness of the new art. Early field experience with fiber-guide systems in England, Japan, and the U.S. yielded essentially trouble-free operation and unexpectedly few 'problems'.

The driving force for putting fibers into long-distance systems is low transmission loss and attractive bandwidths. Installed cables have shown losses in the vicinity of 4 dB/km at wavelengths near 0.82-0.85 μm ; laboratory samples of spliced but uncabled fiber of 30 km or longer lengths have shown

1.3 μm , and system development objectives are less than 1 dB/km installed. For the multimode fibers now being produced, dispersion limits would permit a bit rate of 50 Mbit/s for repeater spans of at least 10 km. Larger bit-rate distance products should become feasible. For single-mode fibers a bit-rate distance product of 100 Gbit km is feasible (from the standpoint of dispersion) for a laser system near 1.3 μm . These numbers are reflected in so much lower repeater costs than for wire-pair or coaxial systems that the system economics for light wave is very attractive based on voice traffic alone, and wide-band services would increase the attractiveness.

The Bell System is installing a standard metropolitan trunk system in Atlanta (45 Mbit/s), has committed a 600 + mile longhaul system between Boston and Washington, DC, and has under exploration a transatlantic cable system targeted for service in the late 1980's. Plans are being developed in other countries.

The key new components needed for light-wave systems are the fibers, the carrier-wave sources (lasers and light-emitting diodes (LED's)), and the light detectors.

There are four processes for making the fibers that are likely to be used commercially: Corning Glass Works made the first low-loss fiber using a process called outside vapor-phase oxidation (OVPO), and they are still proponents of it. Bell Laboratories invented the modified chemical vapor deposition (MCVD) process which was widely adopted by others and which produced very-low-loss fibers. Nippon Telegraph and Telephone Public Corporation has recently shown that a process they extensively explored, called vapor-phase axial deposition (VAD), can also make very-low-loss fibers. These three processes all make fibers whose composition is mostly SiO_2 with relatively small amounts of Ge, P, and sometimes B as dopants to alter the index and to lower the working temperature somewhat below that for pure SiO_2 . The fourth process, extensively explored by the British Post Office, uses multicomponent glasses of much lower working temperature so that drawing from a crucible is feasible. The latter has the capability of being a truly continu-

ous process and, if the pure starting materials become suitably low in cost, may prove the least expensive. Currently, MCVD, OVPO, and VAD make the lowest loss fibers, and all three can also make wide bandwidth fibers.

Fiber-guide cable design differs in detail from metallic cable design because glass has notably different mechanical properties than copper, and because the fiber develops excess loss (called microbending loss) if it is distorted at points separated by the order of 1 mm longitudinally. Pressing against a rough surface could do this, for example. Nevertheless, by careful engineering many of the cable companies are finding viable designs. Similarly, splicing and making demountable connectors are now challenges that are being met with field-viable solutions.

Sources for light-wave transmission are an interesting and complicated challenge. Semiconductor lasers and LED's are the dominant candidates for fiber-guide transmission, but within that scope there are numerous options. Lasers are ideal and worth a premium price because they couple power more efficiently into the fibers and because their narrower spectral width reduces the effect of the intrinsic chromatic dispersion of the silica fibers. Present commercial systems for metropolitan area trunks use 0.82-0.85 μm lasers. Longer distance systems are also planned with laser sources. LED's are adequate for data links and are already extensively used. Longer wavelength LED's can also take on major transmission roles. Whereas at 0.82-0.85 μm wavelength, the LED fiber combination yields chromatic-dispersion-limited systems to a bit-rate distance product of about 100 Mbit-km, the second generation LED-fiber systems near 1.3 μm wavelength permit a bit-rate-distance product of 2000 Mbit km due to the minimal chromatic dispersion of SiO_2 near 1.3 μm . The laser-LED comparison takes on another dimension in the subscriber loop application. The environmental temperature range encountered by electronics used in the subscriber loop is large - which can be accommodated easily by LED's but is difficult for lasers. Lasers have an emission thre-

shold which is intrinsically temperature sensitive, leading to a need for circuitry to automatically adjust the driving current. At the present state of the art, this also leads to shorter device life at the higher temperatures. What emerges is a future in which both LED's and lasers will be needed, but for different applications.

Further laser research is needed not only to better control device life, but also to achieve a source with output in a single-transverse and single-longitudinal mode throughout the device life. Only with such a device can the SiO_2 fiber's lowest loss regions near $1.55 \mu\text{m}$ be used most advantageously in very high bit rate systems.

Detectors for first generation $0.82\text{--}0.85 \mu\text{m}$ systems are based on established silicon technology, and avalanche gain is advantageously employed. For the 1.3 and $1.5 \mu\text{m}$ regions, very satisfactory p-i-n detectors have been made in the laboratory using InGaAs and InGaAsP. There are excess-noise difficulties (probably fundamental) when attempting avalanche gain in these materials. The preferred form of receiver appears to be a p-i-n detector followed by a low-noise GaAsFET preamplifier.

Getting the new material systems InGaAs and InGaAsP into manufacture for lasers, LED's and detectors is one of the principal pacing elements in bringing about commercial utilization of the attractive long wavelength region.

The applications of fiber light guides in applications other than conventional transmission are often driven by other virtues of the fiber waveguide. In computer links, for example, the advantages are freedom from environmental electrical noise, small size, and of course broad bandwidth. Here fiber cost is not critical but device cost must be very low, reliability high, and digital error rate in the 10^{-11} $\text{--}10^{-13}$ region. Although laser-based configurations have received the most attention, LED device performance seems closer to meeting the requirements.

In Japan, the use of fiber for electric power system supervision, control, and protection has reached the commercial stage.

Here the key features are freedom from induction and noise due to the insulating nature of the medium. There are 35 km of system in place with 20+km planned. These users call for standardization of fibers and connectors to facilitate commercial growth.

In the subscriber loop some analog light-wave transmission has been used; because the fiber link is combined with other analog transmission systems, the cost of digital terminals is often not justified. For the longer term, however, the configuration of choice is likely to be digital transmission on feeder links from the central office to remote interfaces where some form of multiplexing or switching is likely to be used to allow a plurality of customers to use the large transmission capacity of each fiber. This is an area where the new capabilities of the fiber and of low cost digital electronics and memory will stimulate novel useful transmission-switching configurations. There also is needed innovation on the part of the business community to make use of the new broad-band possibilities. The growth in 'broad band', which almost certainly will occur at some time, will involve changes in people's living habits. Although the consumer will be the final arbiter of the attractiveness of such changes, the business community will play a key role in offering new service possibilities. The subscriber loop is the place where this action is. Against this backdrop of fluidity in the period ahead, suitable characteristics for the telecommunications facilities are adaptability and flexibility.

Military organizations find fiber-guide transmission attractive for telecommunications and as elements in special applications. For telecommunications, it is savings in weight and cost that fibers offer as compared with copper cables, along with freedom from electromagnetic interference in congested environments. Examples of specialized applications include hydrophones, rotation sensors, acceleration sensors, and (speculatively) even a communication tether for a guided missile.

Ionizing radiation increases the loss of silica fibers, by amounts ranging from many thousands of decibels per kilometer

within a millisecond of severe exposure to a few decibels per kilometer, ten or more seconds after exposure. In this respect, photons in fibers are less rugged than electrons in conductors.

The various communications uses of fibers require laser or LED powers no more than a few milliwatts, and at that power level the fibers are linear. At powers of the order of 100 mW, single-mode fibers begin to show nonlinearity-self-phase modulation, stimulated Raman scattering, and ~~stimulated~~ Brillouin scattering are possibilities. For multimode fibers a laser power of about 2.5W marks the onset of nonlinearity. Such power levels can be generated; where linearity is sought, they must be avoided. There may be the possibility of taking advantage of nonlinearity in future novel configurations.

The forward momentum of research as well as development of light-wave technology is great. The feasibility of using what has been called integrated optics in building multiplexing circuits for single-mode (and single-polarization) waves has been demonstrated in the visible wavelength region, and early realization of single-mode polarization-independent circuitry is expected. In this work lithographic techniques, analogous to those used in electronic integrated circuitry but including innovations needed to meet the requirements of lightwave circuits, have been created to make possible development of complex light-wave circuitry for future light-wave systems. Other work strives to combine light-wave detectors or sources on the same substrate with their associated electronic devices-i.e., preamplifiers or drives; here the lithography is straightforward but the semiconductor device work is new. Still farther in the future, the building of both electrical and optical circuits in the same substrate (InGaAsP on InP, for example) may become feasible, leading to monolithic integrated electrical-optical circuitry which intermix photonic and electronic effects. Finally, the application of new memory and large-scale integration circuitry to fiber system, manufacture, and characterization needs is certain to sustain the rapid evolution of this fascinating art for the indefinite future.

IEEE Transaction on Power Apparatus and Systems, Vol. PAS-99.
No. 3 May/June 1980.

THE USE OF FIBER OPTICS FOR COMMUNICATIONS, MEASUREMENT AND CONTROL
WITHIN HIGH VOLTAGE SUBSTATIONS

INTRODUCTION

One of the most important requirements of the ideal communications medium for high voltage environments is the ability to communicate between points of high potential and points of low potential without being susceptible to injected noise or dielectric breakdown. In High Voltage (HV), Extra High Voltage (EHV) and Ultra High Voltage (UHV), substations, Electromagnetic Interference (EMI) -- Radio Frequency Interference (RFI) and ground mat potential differences cause problems in collecting reliable, accurate high speed data using metallic cabling. As the nameplate ratings and the voltages increase the requirements for quality and quantity of data collection and analysis increase. To meet these data requirements sophisticated mini and microcomputer based Power System Control, Protection and Supervision Systems are used (1,2,3).

It appears that adaption of novel optical technologies to provide communications systems using fiber optics could provide (a) the required electrical isolation and freedom from injected noise, (b) faster and more reliable data transfer and (c) reduction of overall costs.

This paper provides an overview with various systems employing fiber optics in high voltage substations. The overview is divided into three major sections: (1) Communications (2) Measurement and (3) Control. Each discussion includes possible advanced design considerations.

COMMUNICATIONS

This section deals with communications as it relates to conventional point to point data, voice or video interconnections using "Free Space" optical or fiber optic links.

In the begining it was of interest to see the feasibility of using "Free Space" optical links for video and data transmission. Three such systems were bought and tested. The first was a LED-driven data set used to couple multiplexed data from the substation yard to control house. The second was a 5 MHz video link employing FM modulation of a HeNe Laser(4). The most recent was a laser diode 10K bit system. Each has its uses, however, poor visibility will knock this type of system out. With the advances in fiber optic systems, the free space approach has lost some of its appeal.

The following discussion on fiber optic link has been divided into four parts: (a) High voltage to ground (or high voltage), (b) test trailer to transducer, (c) relay house to control house and (d) control house to power house. The first is probably only possible using fibers as previous attempts at using radio frequencies were not too reliable. The latter three take advantage of fiber optics portability (very low weight), immunity to EMI/RFI and ground mat potential differences, high bandwidth, low installation costs and long distances between repeaters.

High Voltage to Ground (or High Voltage) Communications

Fiber optics have been used in high speed (six cycles or less) series capacitor insertion schemes. The first devices installed were control up-link only. In 1976 a more sophisticated device was designed by NOKIA of Finland and installed in a 500 kV line compensation station (5). Not only was an uplink capacitor bypass command channel provided but also 24 (time division multiplexed into three downlink fibers) channels were provided to a ground based converter. Conventional coaxial cables were connected from the converter to instrumentation in the control house. These channels provide information on the status of nine protective relays, seven breaker status points, five signal and power supply checks, one relay and channel continuity check, and two analog measurements of current channels. In addition, three uplink optical channels were included to provide multiplex address commands to the capacitor platform. This system is still in service.

BPA has recently installed, for test, a Westinghouse ZnO_2 (Zinc Oxide) non-linear resistor on one 500 kV capacitor platform. Its function is to absorb and dissipate high energy transients that could otherwise destroy one or more capacitor sections. However, if the resistor itself is in danger then it, along with the series capacitors must be bypassed. For this test, BPA designed, built and installed an energy monitoring device that integrates the energy stored in the resistor and issues a bypass command if the resistor is in danger. To do this it was necessary to measure the current into the resistor (using a conventional CT) and transmit that information to a microprocessor located in the control house. For that task a 4-channel 325 meter low loss fiber link using voltage to frequency-frequency to voltage conversion was designed. It was unique in that ± 0.1 full scale dc to 5 KHz accuracy was required. The three additional channels provided one voltage and two other current test readings. The capacitor platform was tested under system fault conditions, met design requirements and has been in service since late 1978. Other links are being designed for other platforms.

Test Trailer to Transducer Communications

Using the same modulation technique and similar equipment to that described in the previous discussion on capacitor platforms, BPA is proceeding to redesign the communications links to and from its portable test trailers. Previously, heavy triax cabling was used resulting in (a) difficulties in laying out the cables which attach to various precision transducers located throughout the high voltage yard and (b) problems of ground isolation. The ground differentials may exceed several thousand volts during fault conditions, which combined with induced EMI/RFI coupling, pose problems with accurate data collection and interpretation. Changing over to fiber optics and utilizing batteries at the transmitter site, in addition to good shielding of the transmitter, eliminates the problems with ground differentials and induced EMI/RFI. Fiber optic cable reels weigh only pounds as compared to the hundreds of pounds for triax; thus, storage facilities and laydown times are minimized. Two different systems are in the planning stage, both at $\pm 0.1\%$ accuracy; one with a response from dc to 40 KHz and the other to 5 MHz. The interface

units will be designed to allow for a variety of inputs. Inputs include Capacitive Potential Transformers (CPT's), Current Transformers (CT's), wirewound Potential Transformers (PT's), pressure and temperature transducers, etc. The ability to run the fiber optic cables directly to high voltage areas is an advantage not possible with the triax cables.

Relay House to Control House Communications

Substation cable tunnels and ducts between points within the switchyard and the control house, can be fairly expensive. Fiber optics with their inherent ability to communicate at high bandwidths, while requiring very little space, are expected to significantly reduce these expenses.

BPA is using sophisticated minicomputer based system to handle large quantities of station events data. If remote multiplexers located in relay houses in the yard are used, fiber optics can provide noise immune links to control house Substation Integrated Control Systems (SICS) with much less costly ductwork. BPA has experienced no major problems in pulling fiber optic cables through existing ductworks as present day fiber cables are very well constructed.

Control House to Powerhouse Communications

BPA substations are often located near the hydroelectric power houses or thermal generation plants. Large quantities of secure data are needed to and from these power plants. The more common data links have been hardwired multiconductor cable and microwave communications systems. The cables, at times, are plagued with noise and large ground differential voltages. They are also bandwidth limited, expensive and very difficult to install. Microwave links, without reflectors, are line of sight only and are subject to frequency spectrum availability. Incorporating fiber optics would allow for nearly unlimited bandwidth growth, ease of installation and freedom from noise and ground differential voltages. Repeater spacings of up to 32 km are feasible. Cables with internal strength members (messenger) are available for overhead routing.

MEASUREMENT

This topic is probably best separated into two parts : (a) Active (light source and electronic modulation at the measurement site) and (b) Optically passive (exclusively dielectric at the measurement side).

Measurement Using Active Transducers

One of the first systems using optical waveguides at BPA was the Allis-Chalmers "Traser" current transformer. This unit was tested in 1963 and was designed to measure current on a 230 kV bus. Using a toroidal winding around the bus, a small representation of the line current was used to frequency modulate a Light Emitting Diode (LED). This LED was close-coupled to a rigid, clad glass rod which was dielectrically connected to a phototransistor and demodulator some six meters away at ground level. The overall concept was sound, however, in the event the line was faulted the power supply, which relied on the bus being energized, could not become useful in time to enable the modulator to provide adequate information to link protection relays. This was a serious problem. It wasn't until 1978 when Westinghouse, under EPRI funding, installed for test a modified adaption of that device in a BPA 500 kV facility for evaluation purposes. This device had a startup time of 100 pS or better (which is fast enough for adequate protection), utilized Analog/Digital (A/D) conversion, realized a 10 KHz bandwidth and provided an optical path using low loss, ruggedized, graded index fiber optics continuous from site to control house (300meters). This technology is important as it offers possibilities of relief from the usually bulky conventional CT, provides better dynamic current range and frequency response. In terms of dollars it means lower construction and installation costs, especially as it relates to 1200 kV instrumentation.

Little work has been done in voltage measurement using similar techniques. However, it would be quite possible to employ fiber optics to eliminate the use of metallic cabling in the same manner. A divider (resistive or capacitive) to ground would be required which still leaves the problem of a bulky, expensive support device. Other, more sophisticated methods of measuring voltage and current are discussed

in subsequent paragraphs on optically passive devices.

Other applications which employ fiber optics include HV DC converter valve control. In such a device an optical system commands a positive pulse be applied to a control grid which counteracts the negative grid bias voltage thus triggering the valve. There are a number of such devices used in the Pacific Intertie, ± 400 kV DC Converter station at Celilo, near Dalles, Oregon. Also, an experimental Hughes-designed metallic return transfer breaker was installed for test at the Celilo DC facility which utilizes fiber optics for voltage and current measurement in conjunction with conventional CPT and Hall effect device transducers.

Other parameters to be measured within a HV facility may include temperature, pressure, positional status, field strength and gas or oil composition or level. It appears that all present methods of making these measurements could be adapted to employ fiber optics providing there was power available at the site to run the transducer and modulator. If power is not available or not practical, e.g., measuring temperature deep within a transformer, wirewound CPT, or breaker, then a more novel approach may be to power the circuitry with light derived power. In one approach, the photoreception properties of a LED could be used. Assuming that it is possible to time space the transmitted message, an optical source at the terminal end (i.e., LED, LD, HeNe Laser, etc.) could be used to transmit enough power to the site to charge a storage and regulation device. Then at a timed interval (e.g., triggered at the absence of the power beam) the transducer would send its message via the LED into the fiber optics to be received and decoded at the terminal end. With fiber losses very low and responsiveness approaching 0.5 amperes/watt a very efficient power transfer is possible. Of course, using a separate photodiode and fiber optic channel would also do the task.

Measurement Using Optically Passive Devices

In the ideal system no electronics at the measurement site would be best. The entire link outside the control House, including the transducer, could be dielectric, avoiding the need for power supplies, shielding and circuit maintenance. In 1968 BPA began looking into

such an approach. In 1971 practical methods of doing this were described and by 1975 a prototype was designed, constructed and tested in several 500 kV ac facilities and one +400 kV DC facility. The system was a non-contact voltage measurement prototype system which used an electro-optic crystal interrogated by a laser beam. While this prototype did employ electronics at the site, the dielectric sensor was completely isolated one meter distant. The sensor used was K^*DP (Deuterated Potassium Dihydrogen Phosphate) and its dynamic optical properties were the result of the Pockels effect. It essentially measured the electric field and thus the voltage on the bus could be derived. This device was designed as a method of detecting high speed (200 KHz to 1 MHz) transients for use in automatic fault location equipment and used a digital fiber optic data link from yard to control house.

Earlier in 1973 a materials search was conducted through a contract with the Oregon Graduate Center (OGC) - Beaverton, Oregon. This contract proved voltage, current and temperature measurement, could be performed. (6, 7). The results was a prototype installed at a 500 kV facility in 1977 which, using completely dielectric materials at the bus level, measured the voltage, current and ambient temperature. This was classified as a "Free Space" device (as was the former device) in that interrogation sources and detectors, including analysis electronics, were located directly below, at ground level (approximately seven metres from the bus and sensor module). Attempts to integrate fiber optics at this time were not made due to the unavailability of proper low loss fiber optics and source/detector coupling mechanics. However, a prototype voltage, current and temperature measurement system using long (up to 1 km) low loss fibers is being designed and constructed now (the sensors being supplied by the OGC, the rest of the system by BRA). Tests of the prototype are scheduled for early 1980. Figures 5 and 6 show block diagrams depicting this approach. In addition, a portable E-Field measurement device will be constructed to allow for quick field strength mapping instrumentation within and around energized facilities. This device will employ K^*DP , however, Lithium Niobate ($LiNbO_3$) will be used in the high accuracy ($\pm 0.1\%$), high bandwidth (up to 10-MHz) bus voltage measurement sensor. In the current measurement sensor, (same specifications)

the Faraday effect is used with a bar of Hoya FR-5 glass (originally used in the 1976 free space device).

These higher bandwidths and accuracies could provide a more efficient approach to fault locating and some protective relaying schemes. For example, two E modules spaced approximately one meter apart could provide information as to which direction a travelling wave from a power line fault was coming. At present this decision is deductive using other, slower methods.

This technology of measurement using optically passive devices could be significant in that not only can the devices be made faster and more accurate, but will require far less "Bulk" in the support structure. In 1200 kV applications this should result in significant cost savings. In addition the device could be included in instrumentation plans for compressed gas insulation (CGI) facilities.

Cost savings could be realized by incorporating many sensor modules in the same support structure, as shown in Figure 7. A typical substation distribution scheme (breaker and a half) is shown. An optimum system would allow measurement of current on each leg and voltage on each section. Using conventional technology this would require eight separate structures. With optically passive Electro-Optic/Magneto-Optic (E-O/M-O) technology, only two structures would be required. This provides redundancy and could result in a possible contraction of the physical layout size of a station.

Temperature measurement is important since the E and H-field crystals are affected by ambient temperature and therefore must be corrected by feedback circuits or other means. There are various methods to optically measure temperature including rotating another field sensitive crystal away from the field axis (null) and optically monitoring its change. This could also be done using the same crystal (See Figure 9). Other ways include utilizing the natural thermal birefringence properties of quartz. This method will be used in the fiber optic coupled E-O/M-O device (Refer to Figure 5). This technique was first used in the 1976 BPA free space device (6). Another method involves interrogating temperature sensitive liquid crystal solutions. Still another method involves using a

exhibit dynamic optical absorption. In this technique a material (i.e., gold doped ruby, YIG, etc.) is interrogated by a laser beam. The temperature change intensity modulates the inbound light which is detected and linearized remotely.

The temperature measurement device by itself would also be useful in other applications such as HV transformer overheating detection. Resolutions to 0.1°C are possible.

Measuring other conditions such as positional status, pressure, liquid level, density, and possibly even gas or oil composition or contamination, are possible. Several ideas are shown in Figures 9 and 10 to illustrate this point. Figure 9 shows a scheme in which pressure could be measured. Figure 10 shows how a 500 kV disconnect switch could be monitored for positional status.

CONTROL

Perhaps a more difficult task than the measurement of variables is the control of devices. Here the advantage of the "comforts" of the control house for optical detection are gone and replaced by the noisy, dirty HV environment. Fortunately most control functions will not require the large bandwidths and risetimes required in measurement so detection amplifier can be made more immune to noise.

At BPA, control using optics has been demonstrated in various devices including trigger functions on HV AC to HV DC convertor valves, (ASIA-1968) HV power circuit breakers (FUGI 1/2 cycle, 500 kV breaker - 1974) and in insertion of series capacitors at line compensation stations (Westinghouse - 1968, NOKIA - 1976). All such devices use energy derived from the HV platform to power reception, analysis and trip electronics at the site.

The design approach for optically passive control systems (completely dielectric) is not immediately obvious at this time. Furthermore, the use of optically active components for control does not appear practical because of the unavailability of ultra-high gain, high power photo-SCR's and TRIAC's.

One rather interesting control application that has been discussed at BPA is the use of a high energy laser beam to intentionally cause a line to ground fault for line and device testing. At present there are three normal methods for intentionally causing a power fault; bolted (closing into a fixed trap from line to ground or line to line), swinging wire (wire with a deadweight set up to fall into a line with the tug of a rope), and the use of a crossbow arrow and wire. Each has elements of danger, requires extensive time to set up, is not totally reliable, and each has the drawback of not being able to choose where on the voltage or current wave the arc will be initiated. Using a high energy laser beam, coupled through ultra low loss large diameter fiber optics, directed to the energized bus, air (perhaps with a dopant gas) can be ionized (up to 1 meter) almost instantly and conduction to ground made at any point in the cycle. This could be valuable in worst case testing of new power equipment, line characteristics, automatic fault location equipment, etc.

CONCLUSION

When the magic number of 20 dB/KM attenuation (now approaching 1 dB/KM) was attained in fiber design, it became apparent that fiber optic cables could play a significant role in future substation design plans. After industry solves existing problems, such as field splicing, universal connectors, more efficient LED's and LED coupling, longer lifetimes on laser diodes, and when designs on optically passive transducers are tested and perfected, then the unique advantages of this technology will be available to engineers in helping them reduce costs and provide more reliable communications, measurement, and control service within high voltage substations.

BIBLIOGRAPHY

1. J.L. Jones and L.S. Greco, "An Application of Minicomputers to the Control of EHV Substations", presented at CIGRE Committee 32, October 12-16, 1975.

2. L.C. Ames and W. Lofstrom, Jr., "Implementation of an Integrated Control System in an EHV Substation", presented at the Western Protective Relay conference, Spokane, Washington, October 19-23, 1976.
3. J.L. Jones, "The Application of Microprocessors to Power System Data Acquisition and Control", Control of Power Systems Conference and Exposition Record, March 14-16, 1977. IEEE Publication No. 77CH1168-4REG5.
4. D.C. Erickson, "Bonneville Power Administration Experience with Optical Communications Systems". National Telecommunications Conference Cat No. 73 GH0 805-2NTG Page 36 B1-5 1973.
5. A.L. Courts, N.G. Hingarani and G.E. Stemler, "A New Series Capacitor Protection Scheme Using Nonlinear Resistors" IEEE Trans. Power Apparatus and Systems, Vol. PAS-97, pp. 1042-1052, July/Aug. 1978.
6. G.A. Massey, D.C. Erickson, R.A. Kadlec, "Electromagnetic Field Components: Their Measurement Using Linear Electro-optic and Magneto-Optic Effects". Applied Optics, Vol. 14. No. 11, Nov. 1975.
7. G.A. Massey, J.C. Johnson and D.C. Erickson, "Laser Sensing-of Electric and Magnetic Fields for Power Transmission Applications". SPIE Vol. 88 Polarized Light 1976.
8. R.E. Heimer, R.A. Maleswki, F.C. Cassidy: "Optical Methods of Electrical Measurements at High Voltages Levels". Proceedings IEEE, Vol. 65, No. 11, Nov. 1977, pp. 1524-1548.

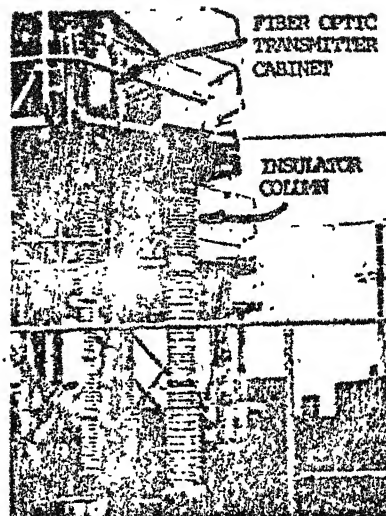


FIGURE 1. 500 kV CAPACITOR PLATFORM WITH FIBER OPTIC LINK. NOTE FIBER IS WRAPPED ON OUTSIDE OF INSULATOR COLUMN.

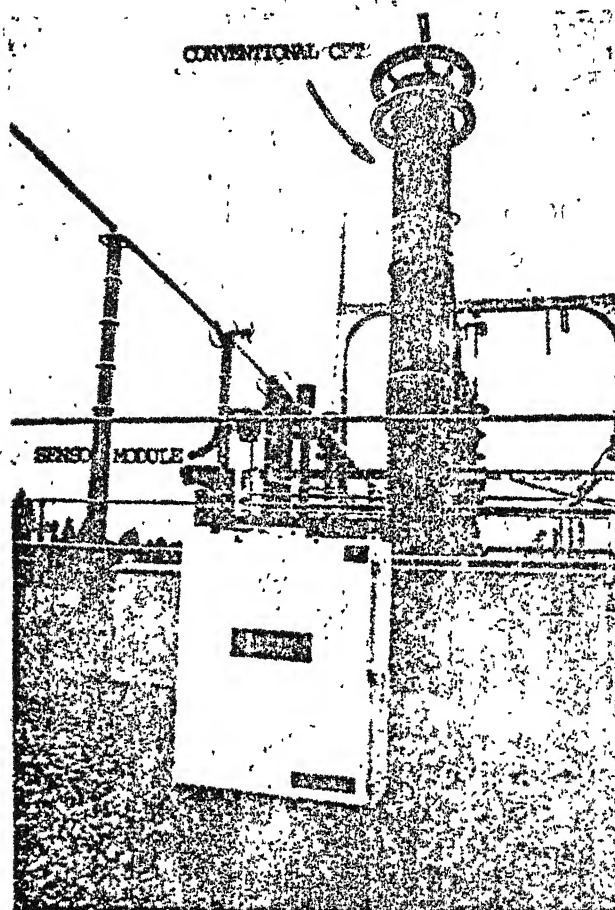
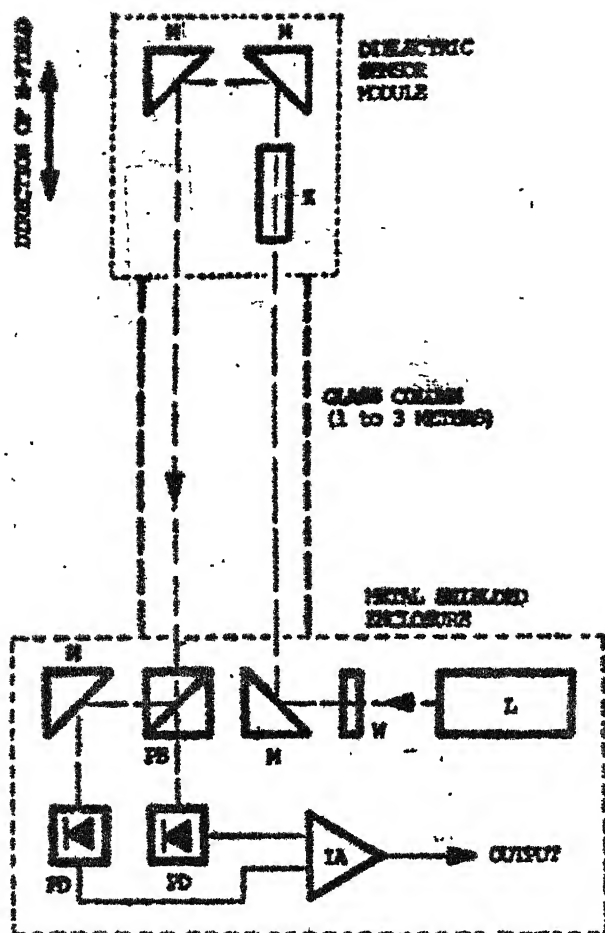


FIGURE 2. THE ELECTRO-OPTIC TRANSIENT DETECTOR.



- K = ACTIVE FIELD SENSITIVE MATERIAL (K*TP)
- M = BENDING MIRROR
- PB = POLARIZATION BEAMSPLITTER
- W = WAVEPLATE
- L = POLARIZED LASER (6328Å)
- PD = PHOTODIODE
- IA = INSTRUMENTATION AMPLIFIER

FIGURE 3. OPTICAL SCHEMATIC OF A FREE SPACE, E-FIELD TRANSIENT DETECTOR.

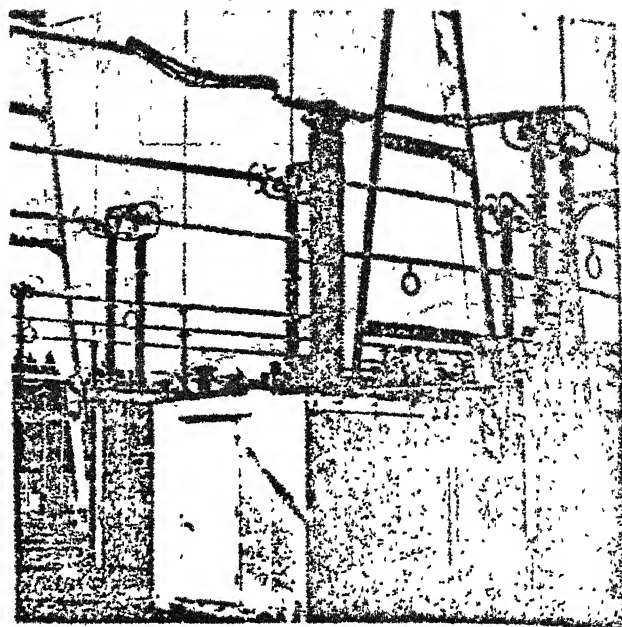


FIGURE 4. 500 KV BUS VOLTAGE AND CURRENT MEASUREMENT SYSTEM (FREE SPACE). THE BUILDING WAS USED FOR TEST EQUIPMENT.

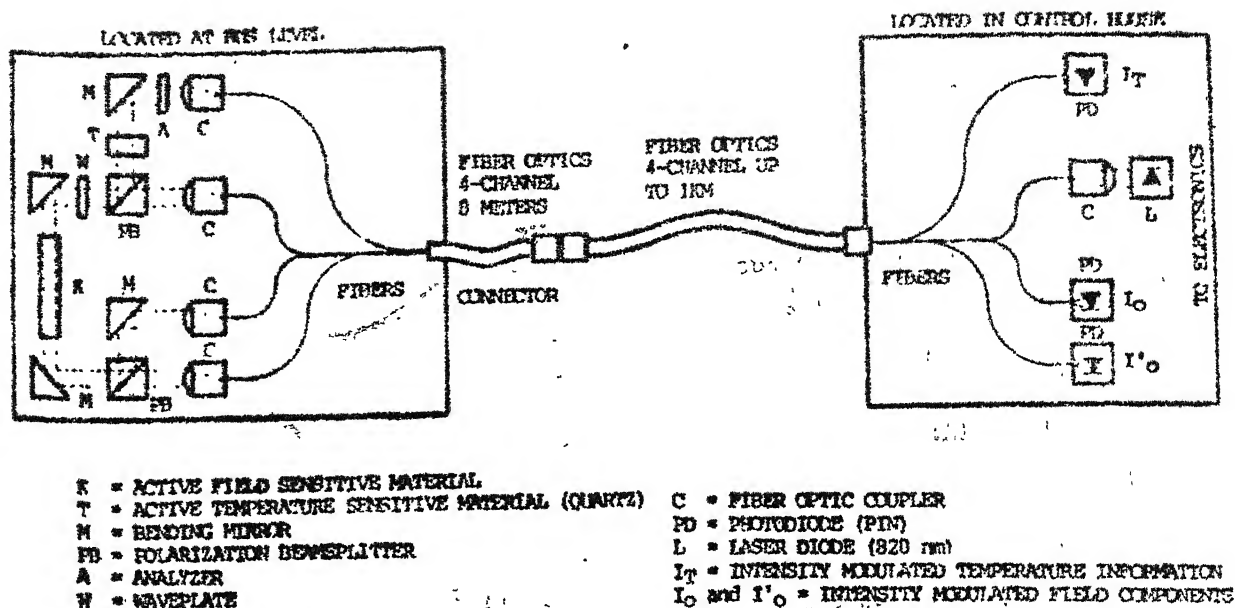


FIGURE 5. OPTICAL SCHEMATIC SHOWING FIELD MEASUREMENT SYSTEM.

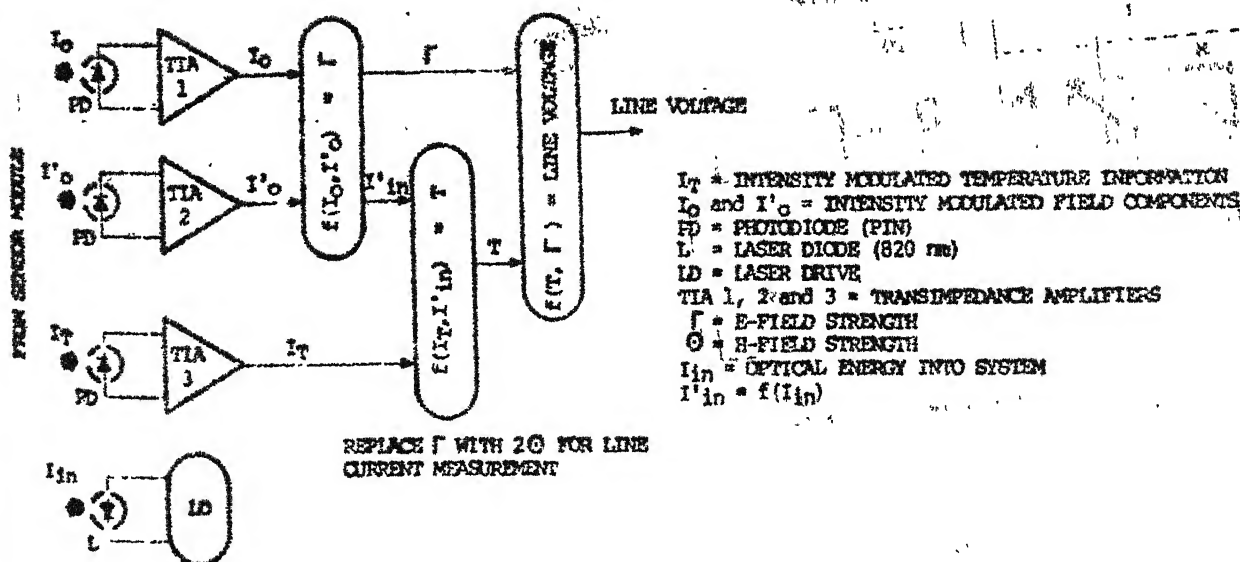


FIGURE 6. BLOCK DIAGRAM SHOWING CORRECTION PROCESS IN FIELD MEASUREMENT SYSTEM.

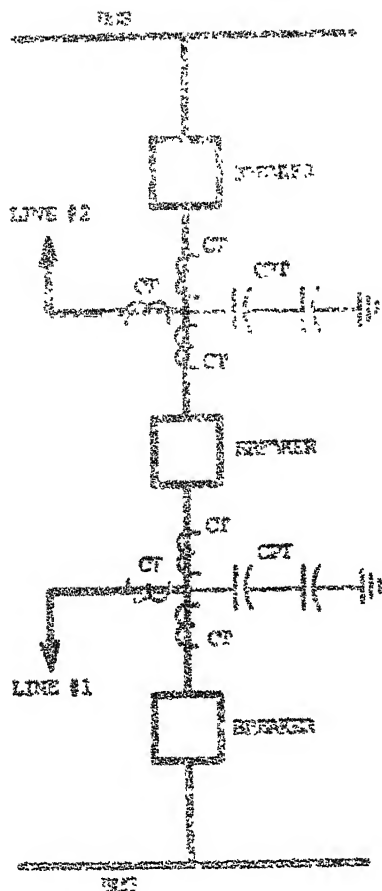


FIGURE 7. CONVENTIONAL (PUL) INSTRUMENTATION SUBSTATION DISTRIBUTION SCHEME.

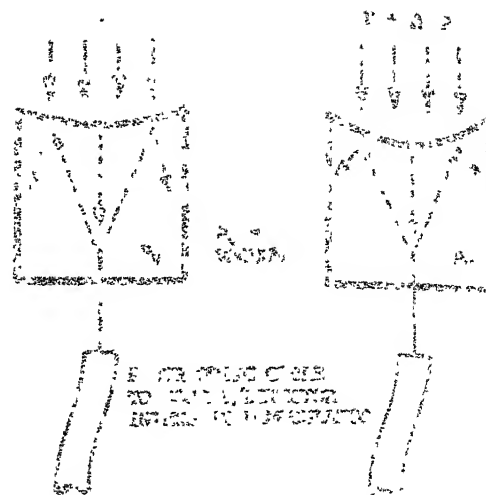


FIGURE 9. PERSPECTIVE DRAWING OF NON-COUPLED PACKAGES USING AN OPTICALLY TRANSPARENT BASE.

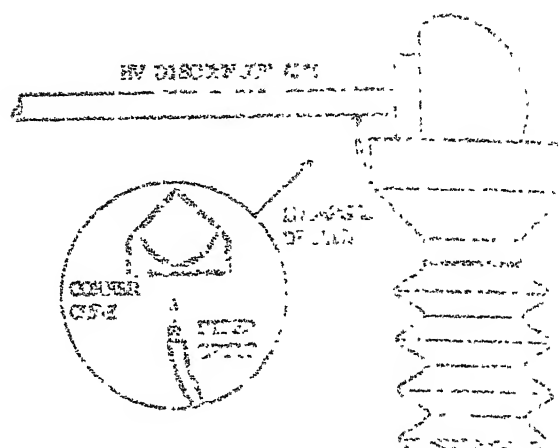
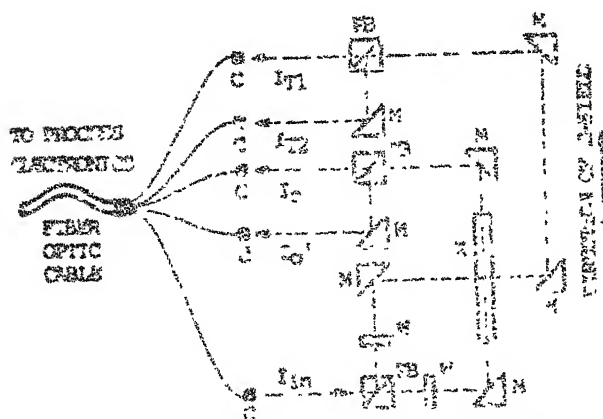


FIGURE 11. PERSPECTIVE DRAWING OF FIBER OPTIC CABLE TO TRANSMIT MULTIPLE SIGNALS OF A DISCONNECT. THE CORE CABLE IS TRANSPARENT AND THE CLAD IS TRANSPARENT. THE FIBER OPTIC CABLE IS TRANSPARENT. THE FIBER OPTIC CABLE IS TRANSPARENT. THE FIBER OPTIC CABLE IS TRANSPARENT.



- E = ACTIVE FIELD SENSITIVE CRYSTAL
- M = SIGNAL MIXER
- FB = POLARIZATION BEAM SPLITTER
- U = UNIDIRECTIONAL
- T1, T2 = TEMPERATURE COMPONENTS
- T3, T4 = E-FIELD COMPONENTS
- C = FIBER OPTIC COUPLER

FIGURE 8. OPTICAL SCHEMATIC SHOWING ONE METHOD OF MEASURING E-FIELD AND TEMPERATURE USING A SINGLE CRYSTAL.

Dr. S. GUPTA

High Voltage Transformers

2000 10 10

1

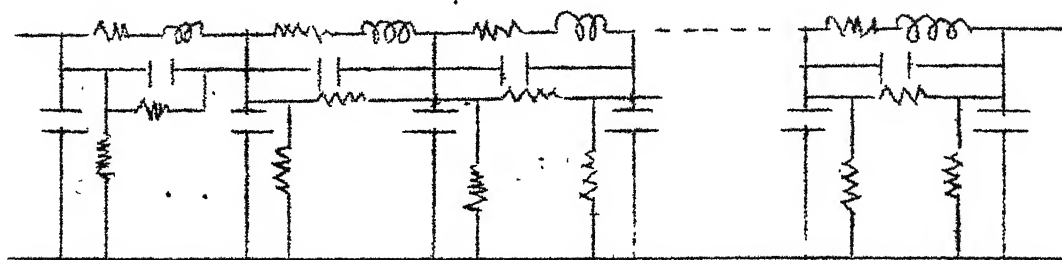
HIGH VOLTAGE TRANSFORMERS

There has been a tremendous increase in the unit sizes of transformers in the last 30 years. In spite of the fact that the basic materials have remained unchanged, a better understanding and better developed technologies have contributed to reduction in weight per MVA and improved efficiency. For example, CRGO was available in 1950s. In those days, to utilise the grain orientation of this material, cores were built up as shown in Fig.1. The laminations were secured through bolts and the flux path round these holes and the corners is as shown. In a 3 phase core, corners weigh 25 to 30% of the total and with the flux passing against the grain orientation, the iron losses may be upto twice the normal. In modern design the 90° joints have been replaced by 45° joints as shown in Fig.2 and the number of bolts have also been minimised. In order to permit interleaving they are arranged as shown in Fig.3. The study of the electromagnetic phenomena of such a structure is quite complex. For accurate analysis, the flux distribution is needed. This has been studied through an analogue employing an electrolytic tank. We are all familiar with the usefulness of the latter in high voltage engineering. Computer simulation has also been employed to calculate the flux distribution. In some modern designs the bolts have been dispensed with altogether and the core is held together by resin impregnated glass tape, which is heat cured. Such cores are not only magnetically superior but also mechanically. The achievement can be gauged by the fact that using the same core material and flux density the iron losses have been halved. This has been accompanied by significant noise reduction also.

WINDINGS

Results of advances in windings have also been quite spectacular although conductor material as well as insulation have remained virtually unchanged. Design factors that are critical are different for l.v./m.v. transformers and h.v. transformers. From

the point of view of the windings of high voltage transformers, the most critical problem is impulse response, which is a transient response. The windings for this purpose are represented as follows:



Each section represents one turn and the parameters in each section are equal. When a lightning/switching surge strikes it, the front of this impulse voltage is like a quarter cycle of a sinusoidal wave of very high frequency. Inductive elements under such conditions offer a very high impedance and large currents flow through the capacitive network. If the shunt capacitance, representing the capacitance between the winding and core/casing, were absent, the voltage distribution would have been uniform. The actual voltage distribution is as shown in Fig. 4. This is the initial voltage distribution as shown in Fig. 4(a). The voltage response with respect to time goes through oscillations, when the voltage may reach more than 150% and the final value shows a uniform V-distribution.

A disc type of winding gives highly non-uniform voltage distribution, as shown in Fig. 4. This type of winding has many advantages as follows:

1. It is comparatively easy to direct the flow of oil through each disc and the temperature rise in the winding can be minimised.
2. Mechanically it is easy to build and is robust.
3. There is no need for inter-layer insulation which also facilitates the production of a satisfactorily rigid and adequately braced winding.
4. The space factor is higher.
5. Better magnetic balance can be achieved and the calculation of reactance is simpler.

In the above cases the shields have been applied to reduce the shunt capacitance. Instead, it is also possible to change the voltage distribution by increasing the series capacitance. This can be done by connecting capacitors of suitable value. If it were possible to connect a large number of such capacitors, linear distribution can be obtained. A more practical method of increasing the series capacitance is to interleave the winding. This is done both radially and axially, as shown in Fig. 7. In this case the degree of improvement is a function of the extent to which it is considered advisable to distort the final distribution or to depart from the uniform steady state distribution.

In interleaved winding the turns which are connected consecutively in series are physically not adjacent to each other. In the figure a typical winding is shown. The turns are wound as a double conductor with the second set of turns connected back in series with the first. In this way the series capacitance may be increased more than 100 times. This may be done either for a part of the winding or the whole winding. However, this also increases the normal power frequency stress since a higher a.c. voltage appears across adjacent turns. As in other aspects of design, the advantages gained in transient performance have to be traded off against steady state performance.

The transient voltage response of the winding is a function of the ratio.

$$\frac{\text{shunt capacitance}}{\text{series capacitance}}$$

In the days of early development of transformers disc windings were extensively used, which were susceptible to impulse failure. In case of small low voltage transformers the shunt capacitance is relatively high making the response poor. On the other hand due to larger clearances of the high voltage winding w.r.t. the core and the low voltage winding, the shunt capacitance decreases. Due to the increase in radial depth of larger capacity high voltage transformer the series capacitance increases. This gives an inherently improved transient response.

The disadvantage of a disc winding is that impulse voltage response is very poor and its calculation is also more difficult. In addition, the radial clearance between windings is quite large for high voltage transformers.

The voltage response shows that in the axial direction the first few turns take almost the whole voltage, for which only inter turn insulation is available to withstand it. To reduce this electrical stress it was thought necessary to provide thicker insulation in this region. However, the consequently increased spacing reduced series capacitance and thereby the transient voltage further increased. A better solution was to reduce shunt capacitance by the use of shields.

For this purpose radial shields alone are not very useful, shown in Fig. 5(a). Addition of partial axial shields is very effective in pushing further the equipotential lines shown dotted in Fig. 5(b), and the voltage performance is very much improved. If full axial shields are provided in addition to radial shields, as shown in Fig. 5(c), almost ideal voltage distribution can be achieved.

In the case of a layer type of winding the arrangement of layers and equipotential lines are shown in Fig. 6(a) to (c). The voltage distributions are shown in (d) and (e) across each layer and across the winding respectively. As can be seen from these voltage distributions are better than for disc type of windings. However, this voltage distribution is also far from ideal. The application of shields can effect an improvement in it for layer type of windings also. In fig. 6 (a) an axial shield has been connected at the line end. The corresponding initial distribution of electrostatic field is shown in (b). The voltage distribution across each layer is shown in (c). This is distinctly improved from the previous case without a shield. The voltage distribution can be further improved by connecting a shield at the earth end also as shown in (e). The equipotential lines in this case are shown dotted in (f) and the voltage distribution is shown in (g) and (h).

Conductors

In the case of large current ratings of transformers it is necessary to take steps to reduce the stray load losses. For this purpose it is necessary to use continuously transposed multiple strip conductors. Within the area of the core window occupied by the windings, the majority of the leakage flux is parallel to the winding length. This results in stray eddy current losses in the conductor. This loss is proportional to $(a^2 b^4)$ where a is the total number of radial conductors in the winding and b is the radial depth of each conductor. Therefore reducing b has a substantial influence. In this case it is also necessary to equalise the induced e.m.f.s. in each strip so that the losses due to circulating currents can be minimised. This is achieved by transposition and each strand is insulated with a thin coating of enamel. The arrangement of conductors has been shown in Fig. 8.

Electro-mechanical Forces

From the point of view of system operation it is desirable to reduce transformer reactance. The lower limit for 500 to 750 MVA ratings is 10 to 12%. In such transformers very high current would result in case of short circuits. The radial electromechanical forces are proportional to I^2 and these forces are also getting critical from the point of view of design. In order to solve this problem two approaches are possible:

1. Develop materials which may be able to withstand these forces.
2. Develop windings to reduce these forces.

In practice both the above methods have been pursued. Shell type of construction is superior from this point of view, which gives higher axial stresses and lower radial stresses.

Testing of Transformers

In the early days if the transformer under test gave a kink in the oscillograms of applied voltage, the transformer insulation was considered to be faulty. Sometimes the cover blew off, when it was considered to be definitely faulty. However, there may be a fault even if none of the above is observed. Now it is recognised that oscillograms of neutral current or voltages transferred to other windings are good indicators. The latter are very sensitive to faults within the transformer. Now one looks for any change in response from the predicted response within the first few micro-seconds.

In these lecture a few important factors in the case of large high voltage transformers have been discussed. It will be in order to summarise the developments which have contributed greatly to the manufacture of these

1. Understanding how flux flows in complicated cores.
2. Understanding how leakage flux flows around windings.
3. How forces are developed as a result of these leakage fluxes
4. Developments in winding design.

The achievement can be gauged from the fact that in mid 1950s the MVA per active ton of a 120 MVA unit was 1.5. Now it is 1.5 or more.

TABLE 1

Per-unit field distribution in long rod-plane gaps

d (m)	z (in)	$E_z/V(m^{-1})$		
		Hemisphere (tip radius 0.3m)	Hyperboloid (tip radius 0.1m)	Cone (tip radius 0.01m)
5	0	2.54	4.48	32.27
	0.05	1.88	2.24	2.13
	0.15	1.16	1.11	0.785
	0.30	0.694	0.618	0.428
	0.50	0.429	0.388	0.275
	1	0.208	0.191	0.151
	2	0.103	0.0981	0.0849
	5	0.0586	0.0573	0.0530
	Measured at plane	0.055	0.054	0.049
10	0	2.21	3.92	28.37
	0.05	1.64	1.96	1.87
	0.10	1.27	1.30	0.990
	0.20	0.839	0.771	0.536
	0.50	0.376	0.335	0.242
	1.00	0.181	0.167	0.132
	3.00	0.0584	0.0567	0.0516
	5.00	0.0376	0.0370	0.0350
	7.00	0.0300	0.0297	0.0285
	10.00	0.0268	0.0266	0.0257
	Measured at plane	0.025	0.025	0.025

TABLE 2

Potential and field distributions for contributions for
conductor-plane gaps.

d/D		z/d					
		0	0.2	0.4	0.6	0.8	1.0
0.05	V'	1.0000	0.7976	0.5968	0.3972	0.1984	0.0000
	E'	20.3322	20.1509	20.0120	19.9140	19.8557	19.8368
0.10	V'	1.0000	0.7953	0.5938	0.3944	0.1969	0.0000
	E'	10.3312	10.1485	10.0108	9.9147	9.8580	9.8392
0.20	V'	1.0000	0.7907	0.5878	0.3895	0.1940	0.0000
	E'	5.3291	5.1439	5.0085	4.9161	4.8623	4.8446
0.50	V'	1.000	0.7779	0.5716	0.3758	0.1864	0.0000
	E'	2.3234	2.1315	2.0029	1.9201	1.8737	1.8587
1.00	V'	1.0000	0.7589	0.5488	0.3572	0.1761	0.0000
	E'	1.3152	1.1146	0.9964	0.9262	0.8886	0.8768
2.00	V'	1.0000	0.7274	0.5138	0.3299	0.1615	0.0000
	E'	0.8023	0.5899	0.4892	0.4360	0.4093	0.4011
5.00	V'	1.0000	0.6634	0.4510	0.2840	0.1378	0.0000
	E'	0.4775	0.2513	0.1837	0.1540	0.1404	0.1364
10.00	V'	1.0000	0.6017	0.3983	0.2479	0.1196	0.0000
	E'	0.3546	0.1267	0.0844	0.0682	0.611	0.0591
20.00	V'	1.0000	0.5367	0.3482	0.2150	0.1033	0.0000
	E'	0.2807	0.0610	0.0379	0.0299	0.0265	0.0255
50.00	V'	1.0000	0.4570	0.2920	0.1792	0.0859	0.0000
	E'	0.2205	0.0221	0.0130	0.0100	0.0088	0.0085
100.00	V'	1.0000	0.4058	0.2577	0.1579	0.0756	0.0000
	E'	0.1903	0.0100	0.0058	0.0044	0.0039	0.0037

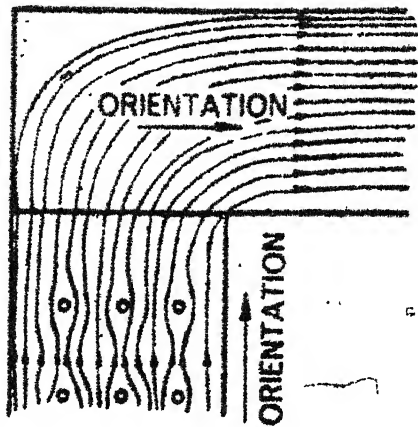
$$V = V_z/V$$

$$E' = DE_z/2V$$

TABLE 3

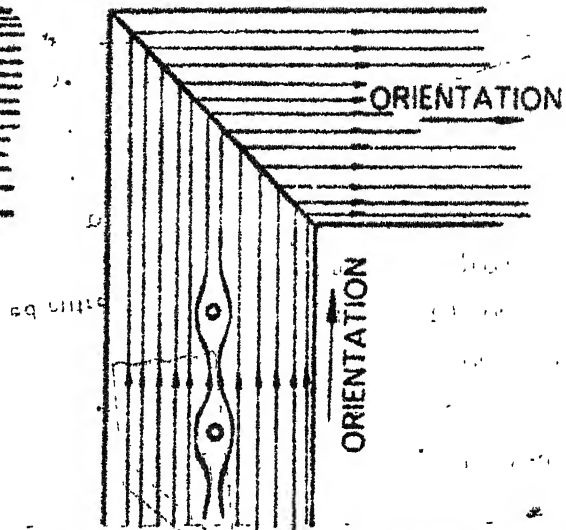
Gap factor for various configurations (positive impulse
120/4000 μ s)

Configuration	k
Rod-plane	1.0
Rod-rod (h = 3m)	1.3
Rod-rod (h = 6m)	1.4
Conductor-plane	1.15
Conductor-rod(h = 3m)	1.65
Conductor-rod(h = 6m)	1.9
Rod structure	1.05
Conductor-structure	1.3
Conductor-window	1.2



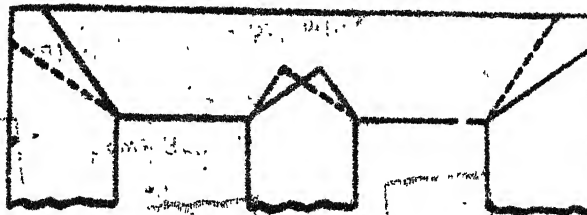
(a) CONVENTIONAL CORE

Fig. 1 Core Joints

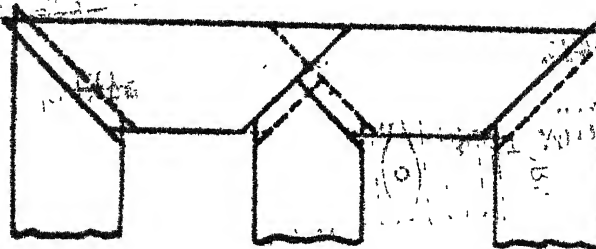


(b) MINIMUM BOLT MITRED CORE

Fig. 2 Mitred Joints

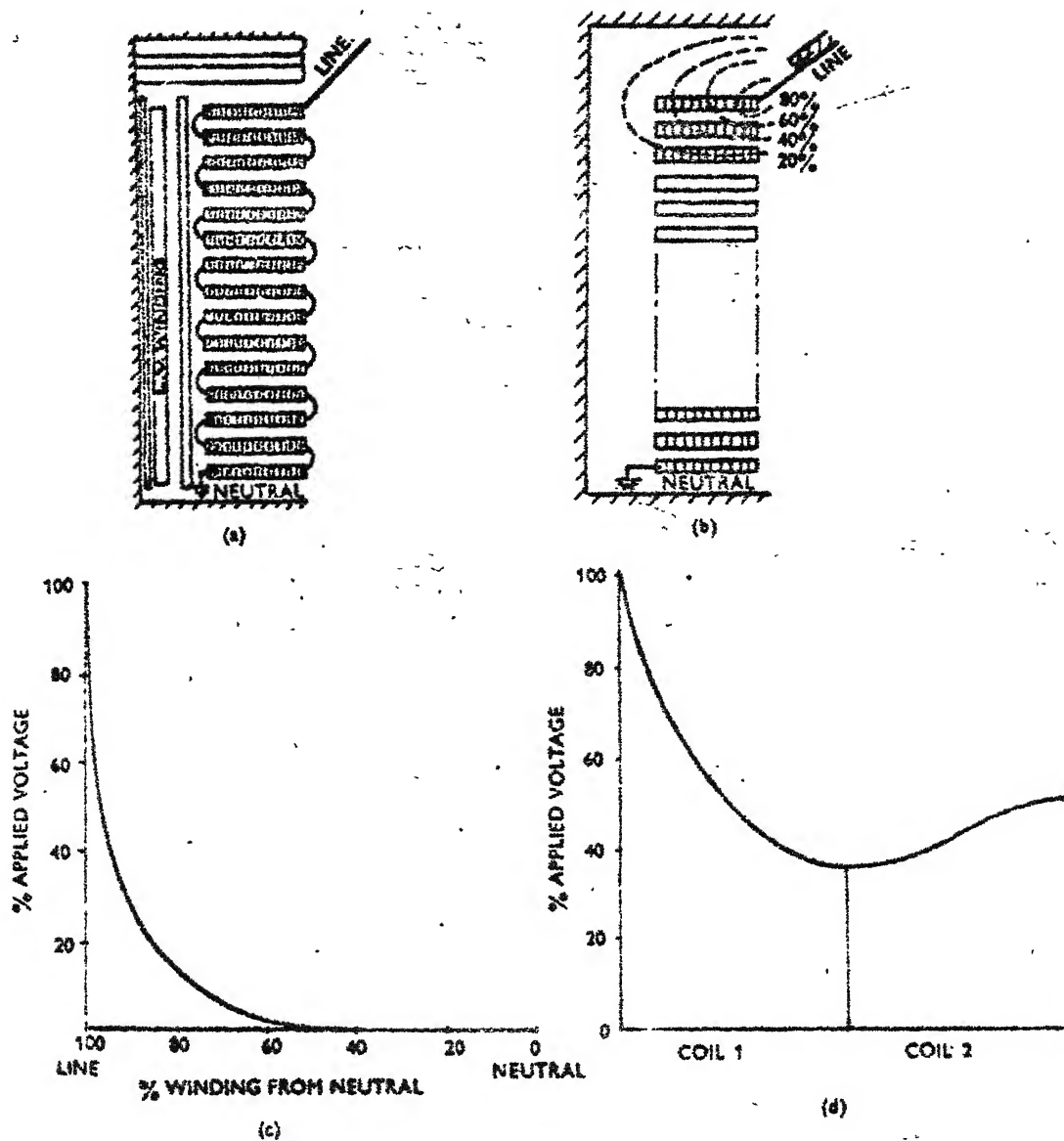


(a) shows 35° - 55° mitre



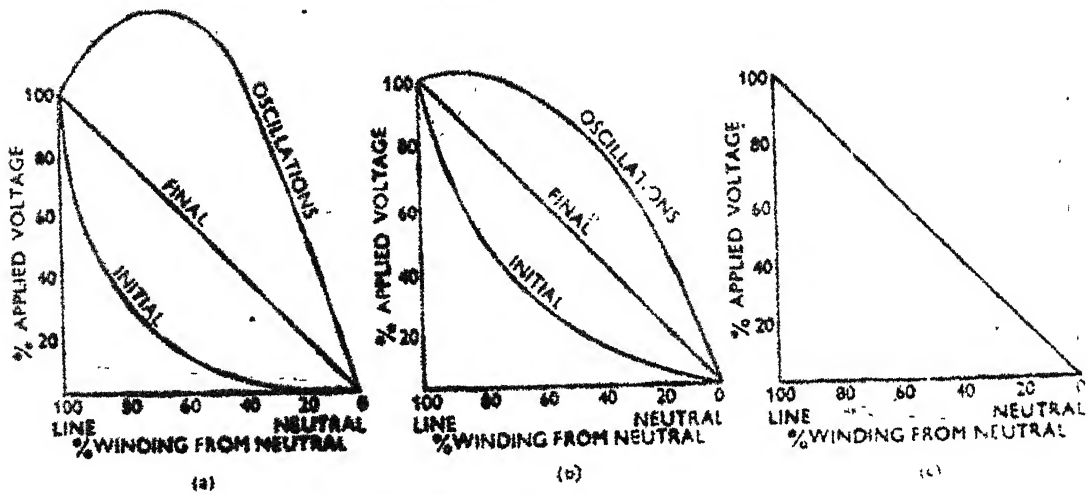
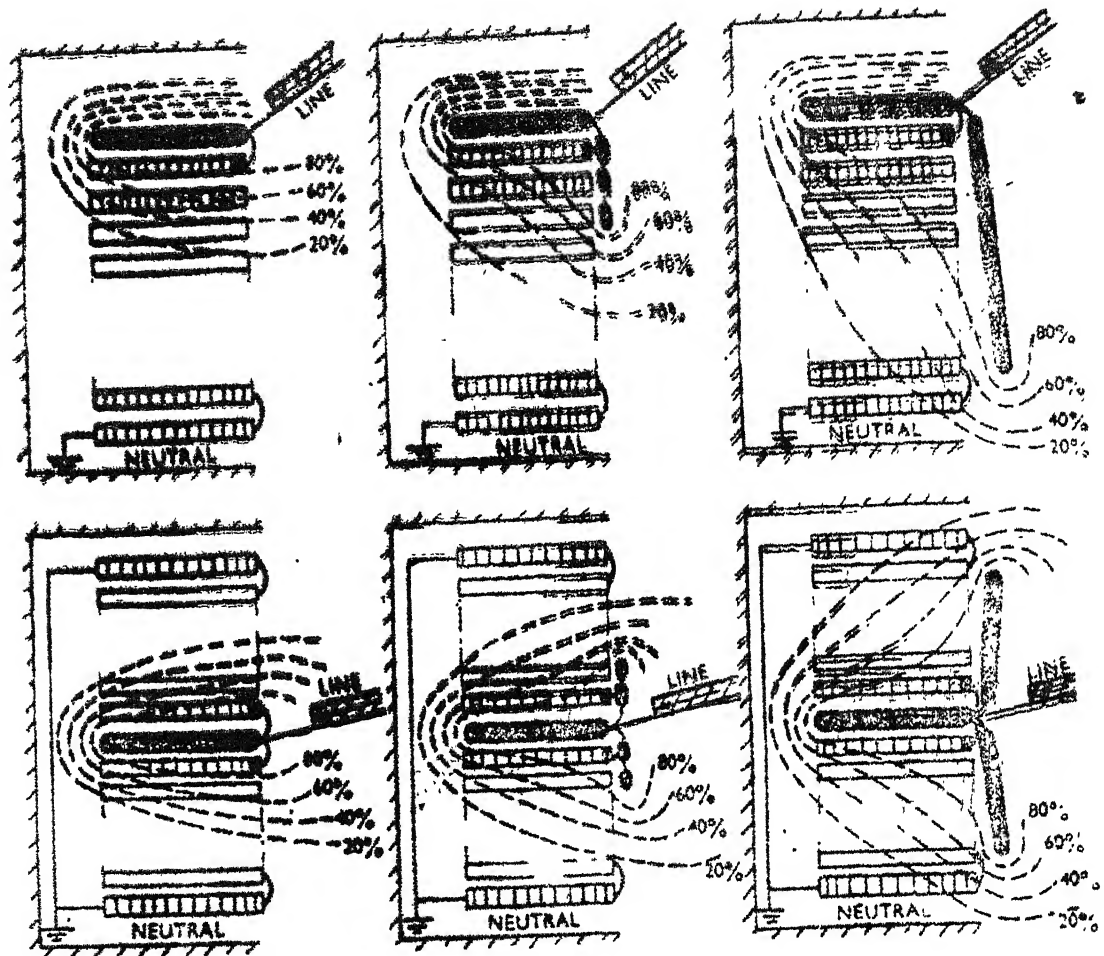
(b) shows 45° displaced mitre

Fig. 3 Mitred Joints with overlap



- (a) Winding arrangement.
- (b) Initial distribution of Electrostatic Field.
- (c) Envelope of axial mid-coil voltages.
- (d) Radial distribution of voltage in Line Coils.

Fig.4 Initial impulse voltage distribution in disc winding

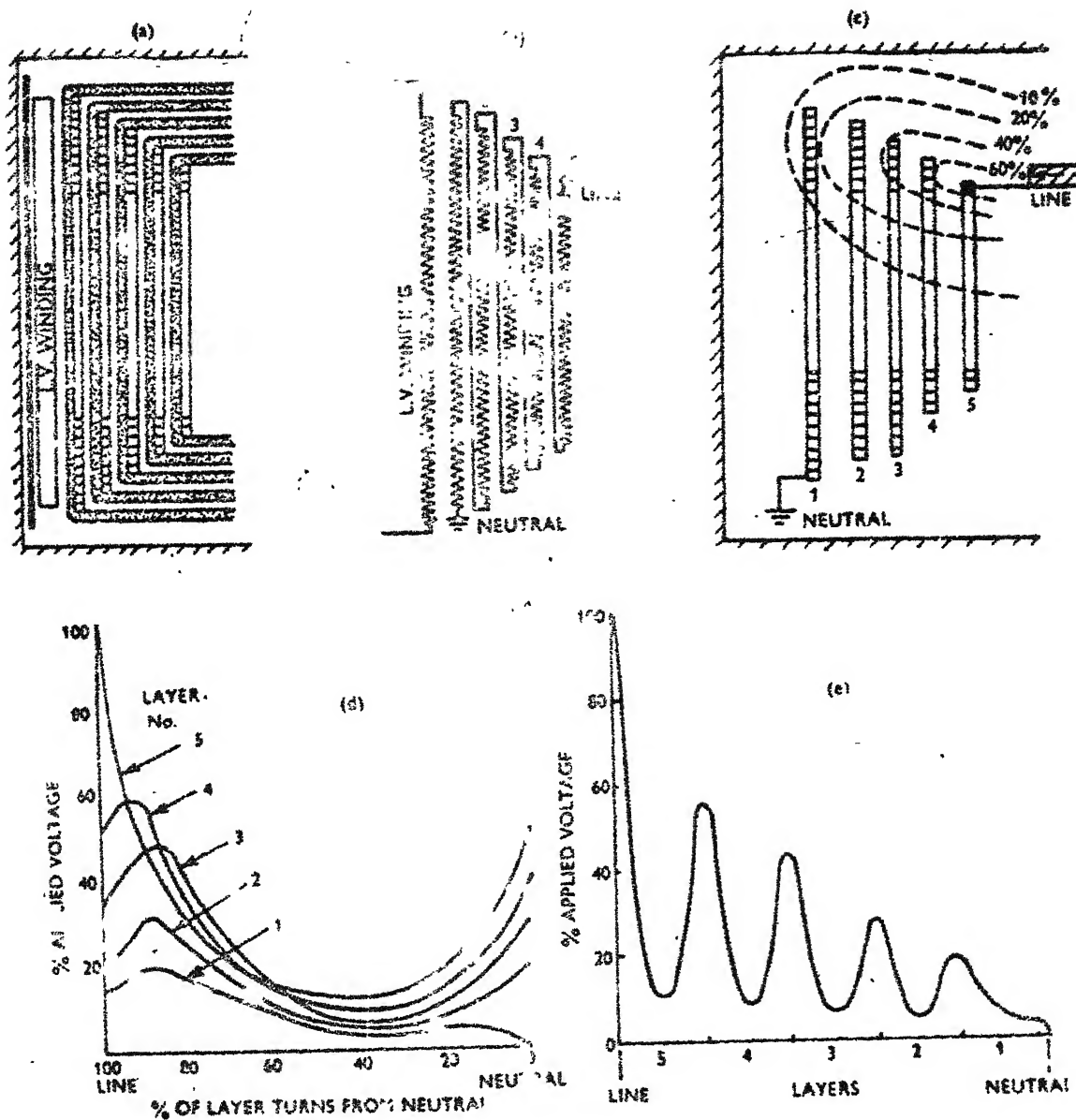


(a) Effect of Radial Shield.

(b) Effect of Radial Shield and Partial Axial Shield.

(c) Effect of Radial Shield and Complete Axial Shield.

Fig.5 Effect of shields on disc winding



- (a) Winding arrangement.
- (b) Interconnection of Layers.
- (c) Initial distribution of Electrostatic Field.
- (d) Distribution of Voltage across each Layer.
- (e) Distribution of voltage across Winding.

Fig.6 Layer type winding without shields

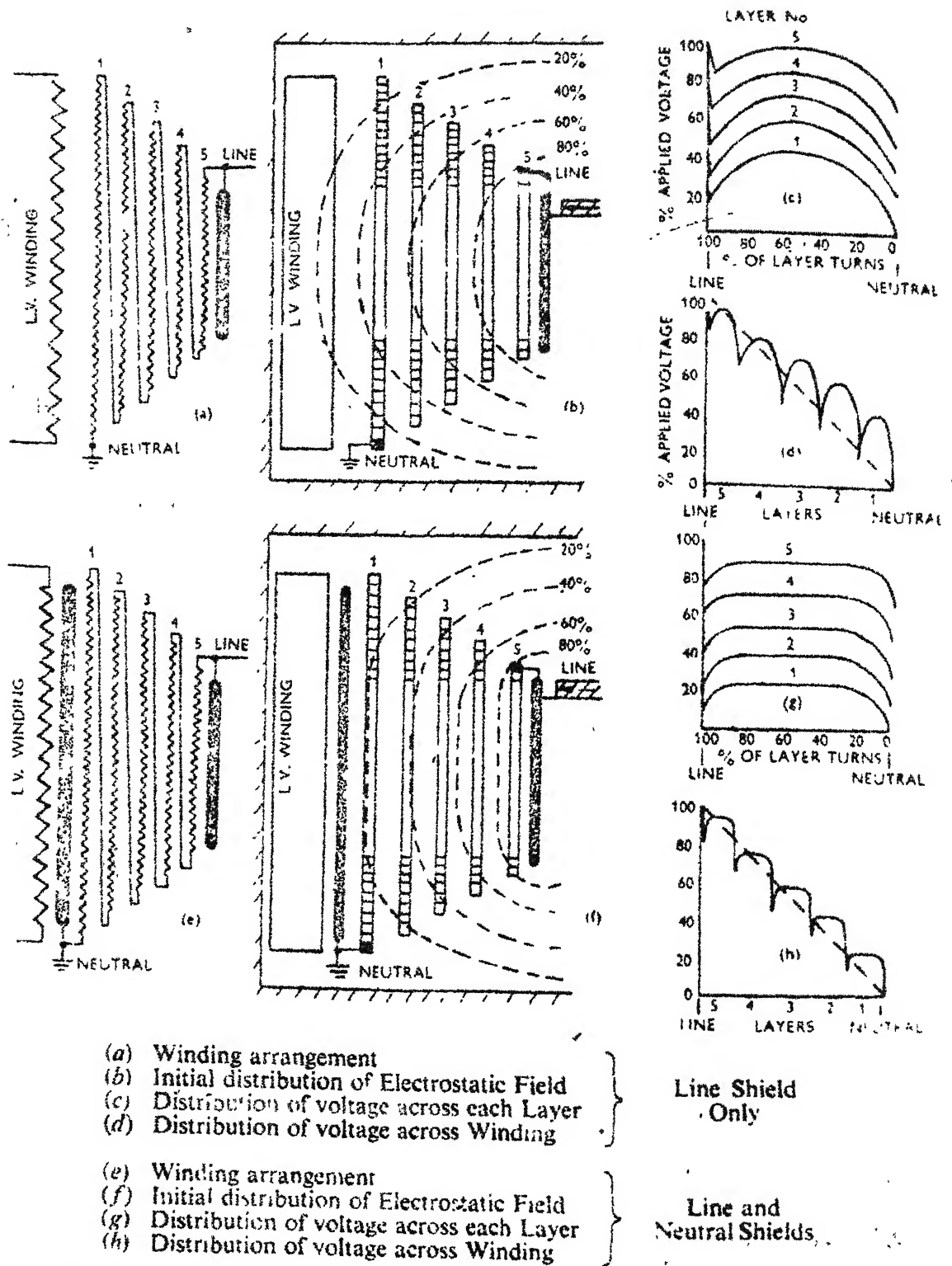
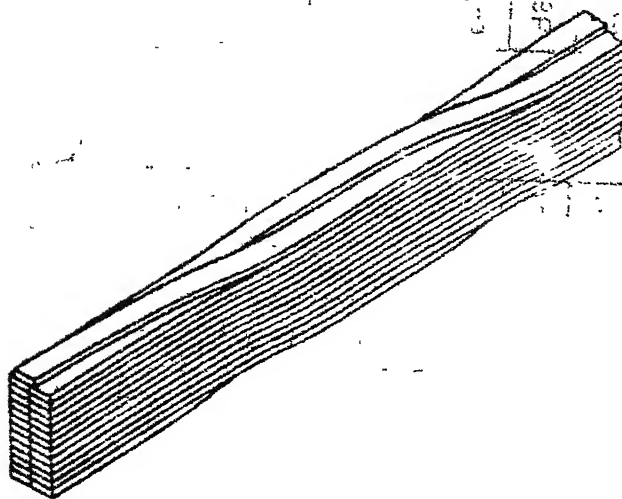


Fig.7 Layer type winding with shields



1		27		15		1	
27	2	26	1	14	16	27	2
26	3	25	2	13	17	26	3
25	4	24	3	12	18	25	4
24	5	23	4	11	19	24	5
23	6	22	5	10	20	23	6
22	7	21	6	9	21	22	7
21	8	20	7	8	22	21	8
20	9	19	8	7	23	20	9
19	10	18	9	6	24	19	10
18	11	17	10	5	25	18	11
17	12	16	11	4	26	17	12
16	13	15	12	3	27	16	13
15	14	14	13	2	1	15	14

Sections through conductor:

- a At start of transposition cycle
- b After first transposition
- c After 13th transposition
- d After 27th transposition

Fig.8 Transposed strip conductor

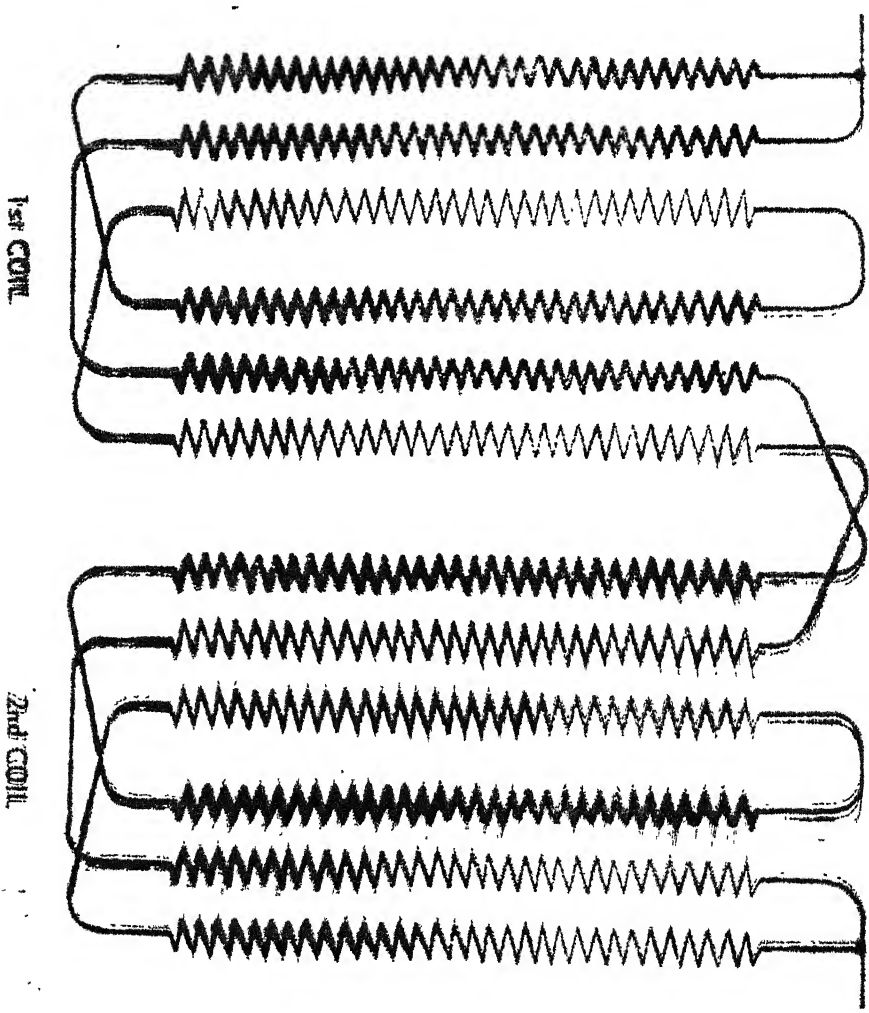
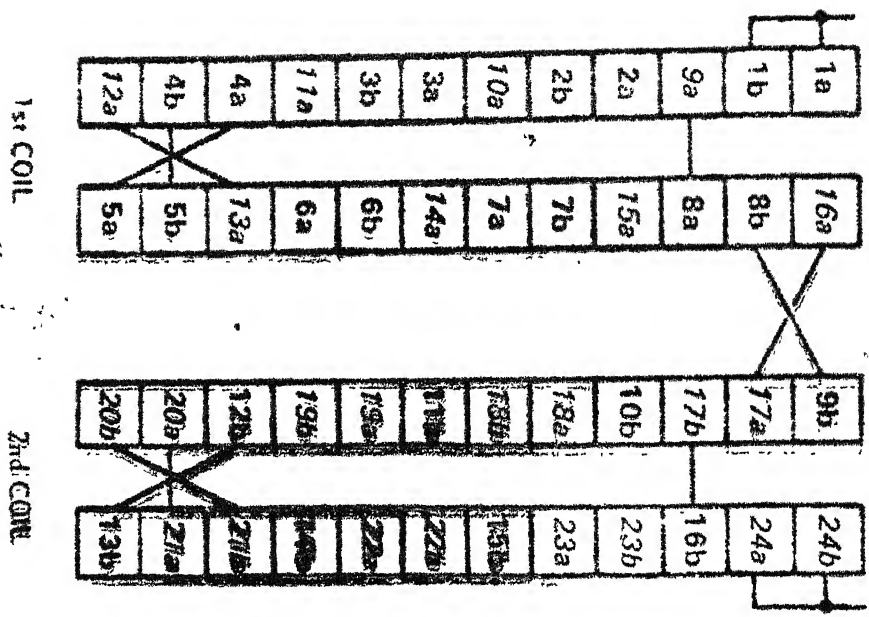


Fig. 9 Interleaved winding

Dr. K. R. Padiyar

Page Nos.	Topic
KRP-1-5	Modelling and Simulation of HVDC Links for Transients
KRP-6-12	Static VAR Systems

12

12

12

12

MODELLING AND SIMULATION OF HVDC LINKS FOR TRANSIENTS

INTRODUCTION :

The use of HVDC transmission as an alternative for long distance bulk power transmission from remote thermal and hydro plants as well as for interconnection of power systems is on increase. The planning, design and operation of the HVDC line requires a detailed study of the steady state and transient behaviour of the DC link and the interaction between the AC and DC system.

DESCRIPTION OF DC LINK

The schematic diagram of DC transmission link is shown in Fig.1 This shows a typical bipolar link with one 12 pulse converter unit per pole. Normally the two poles carry equal current and the ground current is zero. The major components of a HVDC link are described below.

1. Converter: The basic converter block is a three phase Graetz bridge shown in Fig.2. The valves carry current only in one direction and they are made of thyristor elements in series. A valve can be turned ON into a conducting state by applying a gate pulse, whenever the voltage across the valve is positive. The valve turns OFF at current zero. However a certain time (of the order of few hundred μ s) must elapse before it can regain its forward blocking capability. The average DC voltage across the converter can be varied by changing the instant of the application of gate pulse in relation to the sinusoidal voltage that appears across the valve before it starts conducting (called the commutating voltage).

2. Converter Control: The block diagram of a typical converter control system is shown in Fig.3. This consists of current controller, extinction angle controller, the firing angle controller. The reference of the current controller is derived from the slow acting power and auxiliary controllers. Normally, the rectifier

TRANSIENTS IN DC SYSTEM

These are caused by

1. DC line faults
2. AC line faults that can lead to commutation failure and shut down of DC link
3. Load rejection
4. Energization of converter transformers, filters
5. Blocking and deblocking of converters
6. Converter faults such as misfire

Some of the problems that can be caused by the transients are given below:

1. The line to ground fault in one of the poles can lead to a large transient overvoltage on the healthy pole. The design criteria for the air clearances of a bipolar line are often dictated by this overvoltage.
2. The transformer energization (with blocked converters) can lead to long duration dynamic overvoltages caused by saturation and inrush currents. These are particularly predominant when the DC system is connected to a lightly damped AC system such as isolated generation.
3. Self excitation can arise due to the interaction between AC filters and the isolated generator when the converters are blocked.
4. AC faults and blocking of converters (without by passing) can lead to injection of fundamental and second harmonic AC voltages in the DC line which is lightly damped.

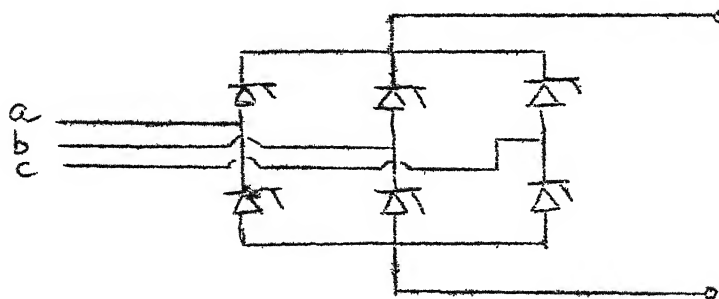
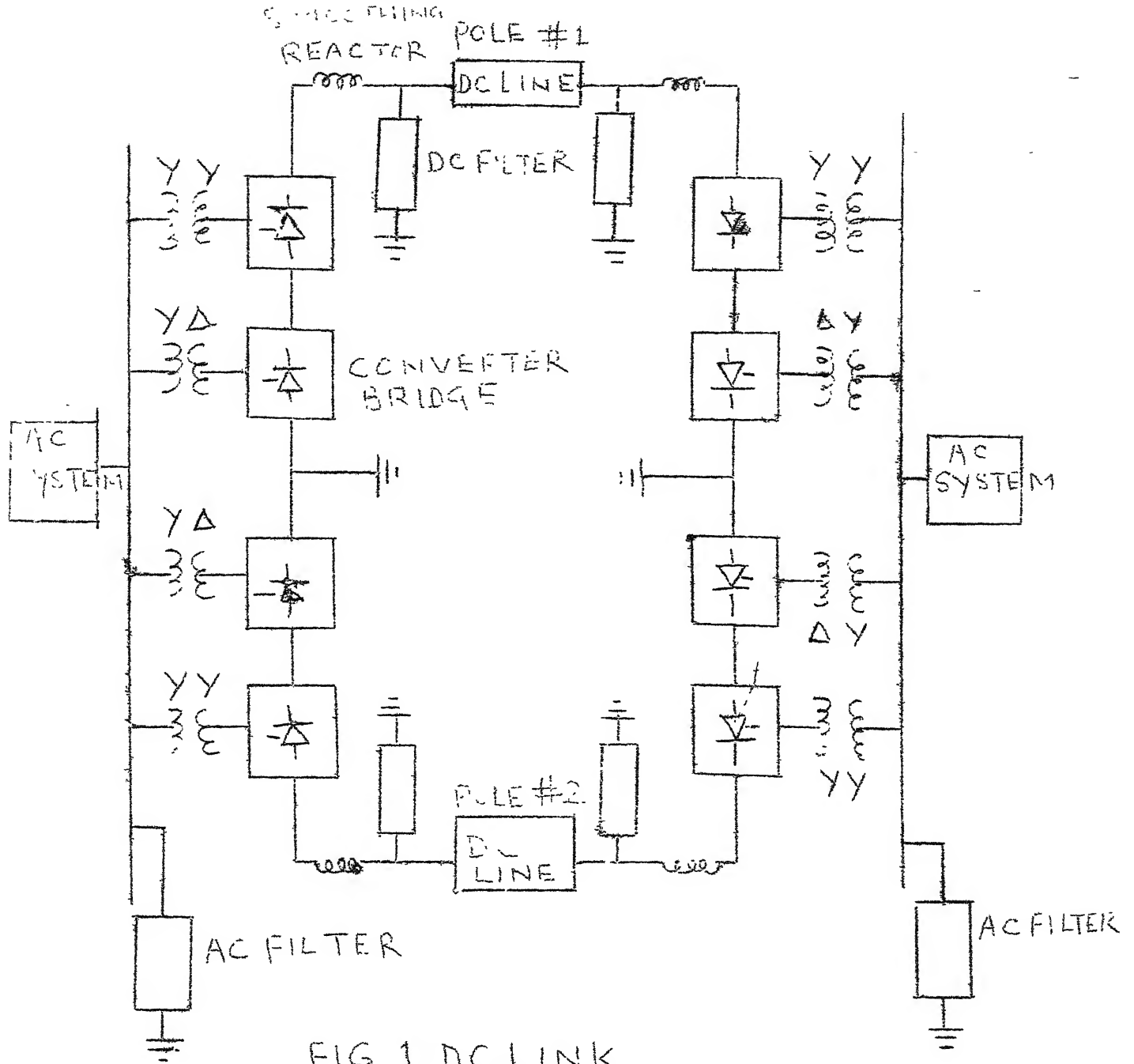
Highest overvoltages can occur in the case of prolonged misfire at the inverter valves. Large voltage and current oscillations on the DC line may cause current extinction at the inverter and severe overvoltage overshoot due to the rectifier continuing to feed energy to the system.

MODELLING OF DC SYSTEM

There are two approaches to simulation - (1) using physical or hybrid simulation using HVDC simulator, (2) using digital simulation. In what follows the second approach is considered.

Converter Model: The models depend on the degree of detail required to simulate a particular phenomenon. In the order of increasing complexity, these can be listed as follows:

1. Voltage source that is defined as a function of time.
2. Controlled voltage source in series with a resistance. The magnitude of the voltage source is determined by the delay angle which in turn is determined by the control system.
3. The valves are modelled as controlled switches. The switch is closed at the instant determined by the control system and opens at current zero. The grading /damping RC circuit across the valve is represented for simulating high frequency behaviour of the converter.
4. Controller : The knowledge of the transfer function of the various blocks in the converter control system can be used to simulate the controller response to given inputs.
5. Converter Transformer : Apart from leakage inductance and resistance of the transformer windings an accurate representation of the magnetization characteristic is essential.
6. DC Line: The dc line is either modelled as a lumped parameter line with a number of pi-sections or as a distributed parameter element. The two modes of propagation - ground and pole to pole have to be considered with different velocities and attenuations.



Filters and Reactors : These are represented as lumped elements with nonlinear characteristic if any. .

In addition, the surge arresters can also be modelled to determine their effect and energy absorption required.

AC System: In many cases, for the analysis of transients in the DC system, a simple representation of the AC system at each converter station may be satisfactory. The short circuit level at the converter bus and the damping in the system represented by the impedance angle at various harmonics are the important system characteristics that need to be considered.

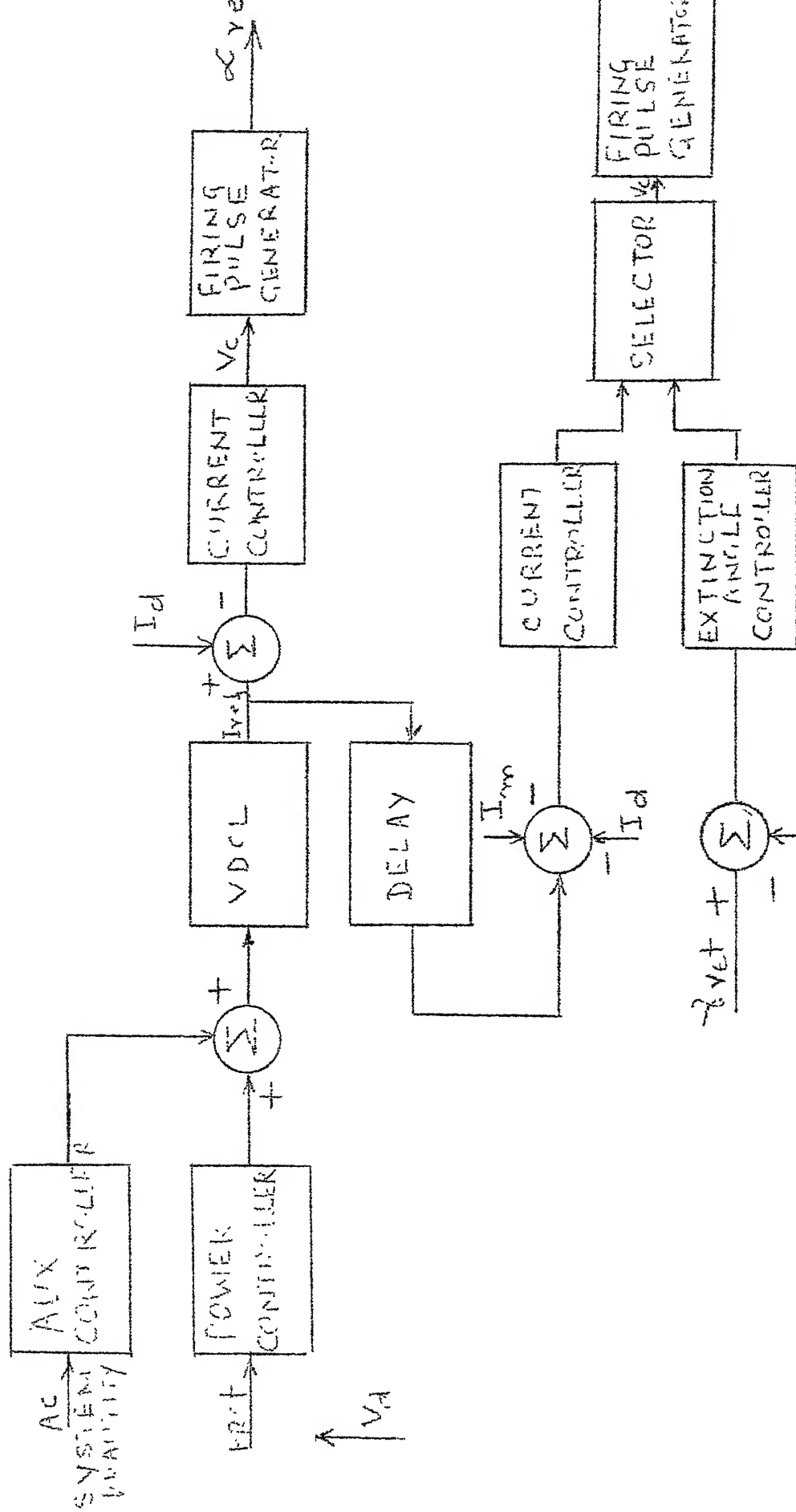


FIG 3. CONTROL SYSTEM FOR DC LINK

STATIC VAR SYSTEMS

The dynamic Var compensation where there is fast control of reactive power in response to system conditions, has many uses. Some of these are listed below :

- 1) to improve transient and steady-state stability of power systems
- 2) for better voltage and reactive power control in the system
- 3) dynamic compensation of first changing industrial loads such as arc furnaces, rolling mills etc.
- 4) to maintain voltage stability at HVDC converter terminals
- 5) Damping of loss frequency (0.5-2Hz) and subsynchronous frequency (10-40 Hz) oscillations in power systems
- 6) for control of overvoltages due to load rejection etc.

Switchable capacitors and reactors have too slow a response due to mechanical switching, to be considered for dynamic compensation. Synchronous condensers have a continuous control range and are reasonably fast, but have limitation due to maintenance and stability problems. Use of thyristor devices for power control initially for industrial drives and later in HVDC transmission has paved the way for the static var systems (SVS) with thyristor devices. They have a high speed response (1-2 cycles) and are capable of reliable performance.

The functions of a SVS can be divided into three categories.

- a) Voltage Support: Where the voltages at some specified points along a transmission line are regulated with SVS. For example consider a power station supplying a large system through a long transmission line, as shown in Fig.1



Fig.1.

By providing SVS at the midpoint of the transmission line to maintain the voltage, the following advantages accrue

- 1) Increase in transient and steady-state stability limits of power transfer
- 2) Control of overvoltages caused by load rejection
- 3) Reduction of line losses

b) Load Compensation : Here the function of SVS is to compensate for the variations in the load such that the net current flowing over the line feeding the load is a specified (say unity) power factor and balanced. This is required when the AC system is too weak to maintain the terminal voltage with load variations. Also it is not economical or desirable to supply the reactive power demand over long lines.

HVDC inverter stations, feeding AC systems with low SCR at the converter bus can benefit from the voltage stability provided by SVS.

c) Damping of Oscillations

By modulating the reactive power supplied by SVS in response to a control signal such as bus frequency, rotor velocity etc. it is possible to damp oscillations in the system. Use of a properly controlled thyristor controlled reactor at the generator terminals to damp ^{sub-}synchronous frequency oscillations has been suggested and implemented.

Static Var Systems :

These can have different operating principles and configurations; listed below

- 1) SVS with continuous, active control
 - a) Direct current controlled reactor (DCCR)
 - b) Thyristor controlled reactor (TCR)
 - c) Force commutated inverter (FCI)

- 2) SVS with discontinuous active control thyristor switched capacitor (TSC)
 - 3) SVS with combination of TSC and TCR
 - 4) SVS with inherent control
- Self saturated reactor with slope correcting Capacitor (SAR)

For power system applications, TCR with fixed capacitor or a combination of TSC with TCR is generally used. The basic configurations are shown in Fig.2.

Usually a SVS transformer is used to match the device voltage ratings to the line voltage. In such a case, for TCR with FC a specially designed reactor transformer can be used to eliminate separate reactor. To avoid the injection of triplen harmonics in the system, the reactors are usually connected in delta. Other harmonics can be eliminated by suitable filters. The fixed capacitor also serves as a filter. The filtering requirements can be reduced with 12 pulse operation. In this case a SVS transformer with two secondaries, one connected in star and the other in delta are used.

The advantages of TSC/TCR configuration are (i) low losses in the induction region (ii) reduction in the size of the reactor (iii) low harmonic currents. But the layout is more complex and the thyristor valve costs are increased.

Steady State SVS Characteristics :

The control characteristics (for steady state operation) are shown in Fig3. The control range of SVS is CD. The operating point is 'A' given by the intersection of the network and control characteristic. The control signal is obtained from the terminal voltage. However a positive slope (3-10%) is given over the control range to help in stabilizing the control system when SVS operates with large network impedances (with low short circuit level at the SVS bus).

The operating point can shift over a wide range with changes in the system operating conditions. In order to maintain a reserve for emergency conditions it is desirable to superimpose a constant reactive power control with slow response.

Steady State Analysis :

The analysis is applicable to a TCR. With the voltage and current waveforms for one phase, in steady state, are shown in Fig.4.

The current $i(t)$ over a half cycle is defined by

$$i(t) = \frac{\sqrt{2}V}{X_L} (\cos \alpha - \cos \omega t), \quad \alpha \leq \omega t \leq \alpha + \sigma \quad \left. \begin{array}{l} \\ \\ \end{array} \right\} \quad (1)$$

$= 0, \quad \alpha + \sigma \leq \omega t \leq \alpha + \pi$
 where α is the firing angle, σ is the conduction angle, X_L is the reactance of the reactor.

The fundamental component of the current I_1 , is given given by

$$I_1 = \left(\frac{\sigma - \sin \sigma}{\pi X_L} \right) V \quad (2)$$

$$I_1 = B_L(\sigma) V \quad (3)$$

where $B(\sigma) = \frac{\sigma - \sin \sigma}{\pi X_L}$, is the effective susceptance of the controlled reactor. Also.

$$\sigma = 2(\pi - \alpha) \quad (4)$$

The Fourier analysis gives the harmonic component I_n , as

$$I_n = \frac{4}{\pi} \frac{V}{X_L} \left[\frac{\sin(n+1)\alpha}{2(n+1)} + \frac{\sin(n-1)\alpha}{2(n-1)} - \cos \alpha \frac{\sin n\alpha}{n} \right]$$

$$n=3,5,7 \dots\dots\dots$$

SVS Control

The SVS control structure is shown in Fig.5. The network voltage and the compensator current are both measured, and the two values used as a basis for the voltage control with current drop. The correction of the network voltage for obtaining this drop is realized here on the AC side. The network voltage, after correcting for the drop is then rectified. On both AC and DC sides of the rectifier, filters are included. The filters on the AC side reduce the overvoltages arising in a consequence of low frequency ($<150\text{Hz}$) resonances in the system. They must be matched to the prevailing system conditions. The filters on the DC side serve to filter the ripple in the rectifier output or the harmonics introduced by asymmetry in the network voltage. The frequencies to be considered are pf_N , $2f_N$ and f_N , where f_N is the nominal frequency and p is the pulse number of the rectifier. The output voltage of the rectifier, after filtering, is proportional to the average value of the AC voltage, corrected for the drop.

The regulator used is a proportional integral (PI) controller and (if necessary) is equipped with a device which the gain specially when the AC system is weak. By limiting the output of the controller, it is possible to include other regulation and control devices such as for example current limiters and control equipment to allow the system to run up smoothly. A manual control system permits the SVS to be controlled manually during commissioning and for maintenance; or when extraordinary network states arise. Both voltage controller and manual control dictate the compensator susceptance B_{SVS} . The control logic realizes this by means of a combination of capacitor steps and appropriate control of the TCR. A linearizing function is also provided to make the regulator output proportional to the susceptance required. This ensures that the response of the

voltage controller has the same speed over the entire control range.

It is possible to supplement a voltage regulator by a var regulator. This can be coordinated with other switchable shunt capacitors/reactors.

During a transient subsequent to an unsymmetrical or asymmetrical fault, it is necessary to block the control action, otherwise overvoltage problem can worsen. This is because the natural control action of SVS is to switch on capacitors or reduce the inductive current when it sees a reduction in voltage. However this action is detrimental to the control of overvoltages.

References :

1. K. Reichart, 'Controllable Reactive Compensation', Electric Power & Energy Systems', vol.4. No.1. Jan. 1982, pp. 51-61.
2. H. Baker et al. 'Three Phase Shunt Reactor with continuously Controlled Reactive Current' CIGRE (1972) Paper 31-13
3. L. Barthold, 'Static Shunt Devices for Reactive Power Control' CIGRE (1974) paper 31-08.
4. L. Gyugyi and E.R. Taylor, 'Characteristics of Static, Thyristor-controlled Shunt Compensators for Power Transmission System Applications'. IEEE Trans., vol. PAS-99. No.5, Sept/Oct. 1980, pp. 1975-1804.
5. K. Reichart et al. 'Controllable Reactor Compensator for More Extensive Utilization of a High Voltage Transmission System' CIGRE (1974) Paper 31-04.
6. T.H. Putman and D.G. Ramey, 'A Modulated Inductance Stabilizer for Power Systems Subject to Subsynchronous Resonances' Int. Symposium on Static Var Compensation Montreal, Sept. 1979, pp. 269-289.

7. O. Waszynuk, 'Damping Subsynchronous Resonance Using Reactive Power Control', IEEE Trans. vol. PAS. 100 No.3, March 1981, pp 1096-1104.
8. R.L. Hauth and R. J. Morau, 'Introduction to Static Var Systems for Voltage and Var Control : the Performance of Thyristor-controlled Static Var Systems in HVAC Applications'. Tutorial Course presented at IEEE PES Summer Meeting (1978).
9. G. Romegialli and H. Beeler, 'Problems and Concepts of Static Compensator Control', IEEE Proc., vol. 128, pt c. No.6, Nov. 1981, pp 382-388.
10. S. Torseng, 'Shunt Connected Reactors and Capacitors Controlled by Thyristors', IEEE Proc., vol. 128 pt. C. No. 6, Nov. 1981 pp. 366-373.

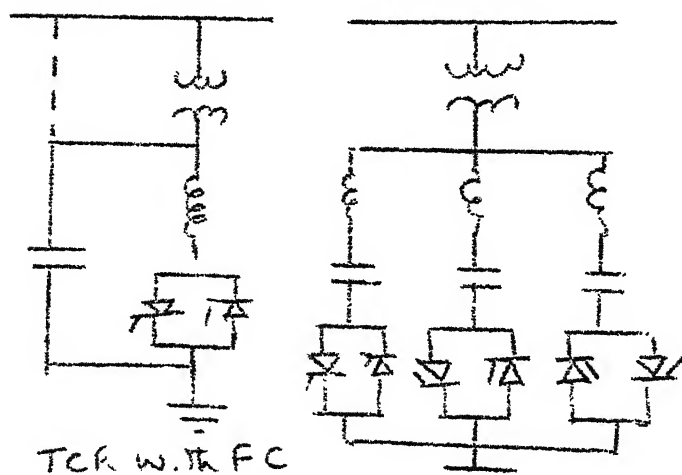


Fig. 2: Basic Configuration.

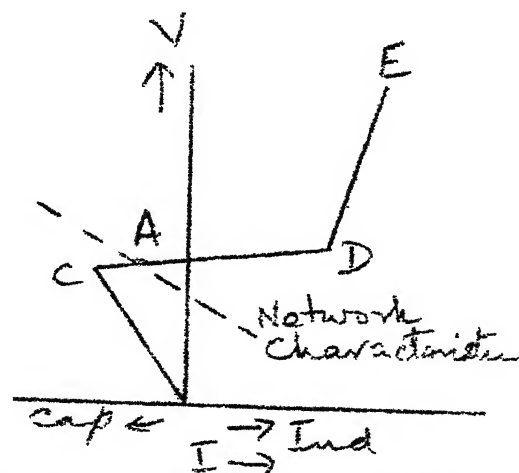


Fig. 3 steady state characteristic.

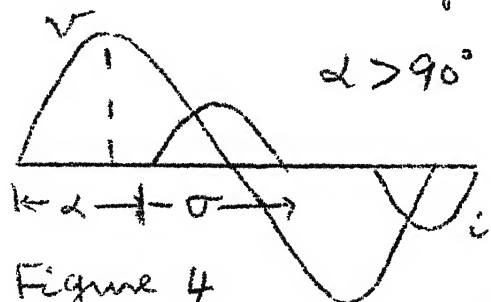


Figure 4

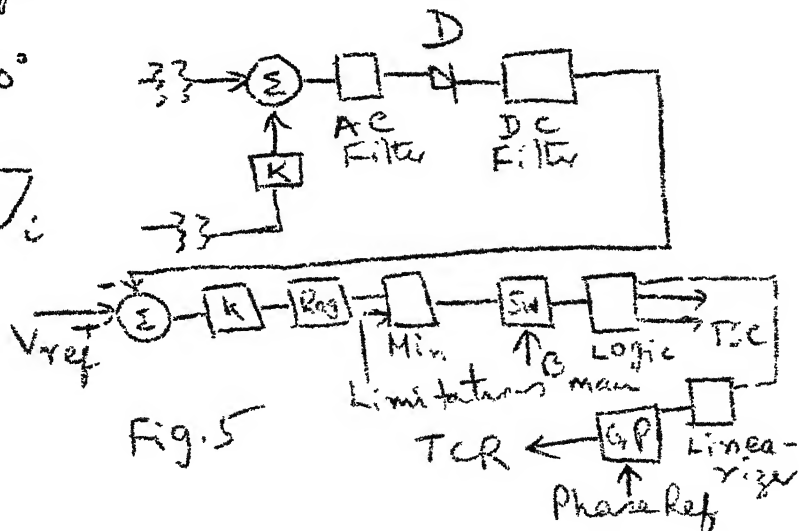


Fig. 5

DIGITAL SIMULATION OF HVDC SYSTEMS

Dr. SACHCHIDANAND

INTRODUCTION

HVDC simulators are widely used to study the dynamic performance of HVDC systems, although hybrid [8] and digital simulation [1-5] techniques have also been used. While a HVDC simulator is a versatile tool for simulating the dynamic performance under various conditions ranging from fundamental to high frequency, it is costly and less flexible compared to digital simulation. Thus the digital simulation can be used to supplement the HVDC simulator.

The major problem in the digital simulation is the converter representation because of the commencement and cessation of valve conduction. The converter topology varies with time. One way of handling this is to make the topology invariant by modelling the valve as a time varying impedance. But this leads to the system equations that require uneconomically small integration step size for their numerical solution. The varying topology of the converter has been considered using two methods. In the first method [3, 5, 6], also called the method of subroutines, the set of equations for all possible configurations of conducting valves are formulated so that a particular set of equation is chosen at any given time. This

method is suitable if only normal modes of converter operation are considered. In the second method [1,2,7] a transformation technique due to Kron [10] is used where the state equations corresponding to each state of the converter are generated using a transformation matrix.

In this report a novel converter representation based on graph theoretic analysis is introduced. The approach is conceptually simpler and leads to efficient formulation of the converter equations corresponding to all possible modes. There are in total 50 possible modes corresponding to 2,3 and 4 valve conduction. However, only 39 modes are of interest if the DC link current is assumed continuous. These can be handled using three simple cutset matrices which are easily generated. The topological analysis leads not only to the system state equations but also to the expression of dependent variables such as valve voltages.

A multiterminal HVDC system consists of i) the AC system feeding the converters, ii) converters with their associated controls and iii) the DC network consisting of transmission lines. The approach employed here is to model each component separately and in a modular fashion. These models are inter-

connected using appropriate interface variables. The dynamics of the converter controls are represented in detail. Both individual phase control and equidistant pulse control have been considered.

The results of the various test simulations under steady state and transient conditions for sample HVDC systems are presented to illustrate the capability of the computer program developed.

CONVERTER REPRESENTATION

A three phase bridge converter system is shown in Fig.1. This includes the leakage impedances of converter transformer (R_c, L_c) and the dc smoothing reactor (R_d, L_d). The effect of the ac system on the converter is represented by the source voltages (e_1, e_2, e_3). The dc network is also represented as a voltage source (V_c) at the converter terminals. It is to be noted that both the ac and the dc voltage sources are not constant and are actually determined as output (dependent) variables from the ac network and dc network models respectively. The effects of the converter on the ac and dc networks are represented by the injection of currents into the respective networks.

Fig.2 shows the graph of converter system. Elements 1 to 6 represent the valves. Elements 7 and 9 correspond to the equivalent circuit representation [10] of the ac system feeding the converter. The element 8 includes the series combination of R_d, L_d and V_c . In deriving the graph of Fig.2, the grading and damping circuits across the valves are ignored.

Fig.2 is the simplest graph representation of the converter system. There are 9 elements and 5 nodes. Correspondingly there are 4 tree branches and 5 links. For reasons that would be soon clear, the tree is chosen such that it includes elements 7,8,9 and one of the conducting valves (element S, where S can be valve 1 to 6). The constituent equations of element 7,8 and 9 are given by

$$\underline{V}_{B1} = Z \underline{i}_{B1} + \underline{e} \quad (1)$$

where

$$Z = R + \omega L p$$

$$R = \begin{bmatrix} 2R_c & C & R_c \\ 0 & R_d & 0 \\ R_c & 0 & 2R_c \end{bmatrix}; \quad L = \begin{bmatrix} 2L_c & 0 & L_c \\ 0 & L_d & 0 \\ L_c & 0 & 2L_c \end{bmatrix}$$

and

$$\underline{e} = \begin{bmatrix} e_3 & - & e_2 \\ & V_c & \\ e_1 & - & e_2 \end{bmatrix}$$

$$\underline{v}_{B1} = [\underline{v}_7 \ \underline{v}_8 \ \underline{v}_9]^T ; \underline{v} \text{ is element voltage}$$

$$\underline{i}_{B1} = [\underline{i}_7 \ \underline{i}_8 \ \underline{i}_9]^T ; \underline{i} \text{ is element current}$$

T denotes the transpose, $\omega = 2\pi f$ where f is the ac system frequency, $p = d/dt$.

For elements 1 to 6 following equations are applicable

$$v_k = 0 \quad k \in K : \text{set of conducting valves} \quad (2)$$

$$i_p = 0 \quad p \in L_2 : \text{set of nonconducting valves}$$

This assumes the valves to be ideal switches with zero forward impedance and infinite reverse impedance. The tree and cotree of the graph for $S = 1$ are shown in Fig.3.

For any network, branch and link variables are related by

$$\underline{i}_B = -B_L \underline{i}_L \quad (5)$$

$$\underline{v}_L = B_L^T \underline{v}_B \quad (4)$$

where subscripts B and L refer to branches and links respectively and matrix B_L is the component of the fundamental cutset matrix. This matrix for Fig.3, alongwith the matrices corresponding to various trees used in the analysis, is given in Appendix 1.

The tree branches are partitioned into two sets, one set B_1 (consisting of elements 7,8 and 9) and other B_2 (consisting of valve S). Similarly the links can be partitioned into two sets, L_1 (corresponding to conducting valves) and L_2

(corresponding to nonconducting valves). Thus matrix B_L can be partitioned as

$$[B_L] = \begin{matrix} & \begin{matrix} L_1 & L_2 \end{matrix} \\ \begin{matrix} B_1 \\ B_2 \end{matrix} & \begin{bmatrix} B_{L11} & B_{L12} \\ B_{L21} & B_{L22} \end{bmatrix} \end{matrix}$$

From (2), the following relations are evident

$$v_{L1} = 0, \quad v_{B2} = 0, \quad i_{L2} = 0$$

Substituting this in (1), (3) and (4), the following equations are obtained

$$(B_{L11}^T \text{ Z } B_{L11}) \dot{i}_{L1} = B_{L11}^T \underline{e} \quad (5)$$

$$v_{L2} = -(B_{L12}^T \text{ Z } B_{L11}) \dot{i}_{L1} + B_{L12}^T \underline{e} \quad (6)$$

$$\dot{i}_{B1} = -B_{L11} \dot{i}_{L1} \quad (7)$$

Equation (5) can be arranged in the form

$$\frac{d}{dt} \dot{i}_{L1} = -\omega L_1^{-1} R_1 \dot{i}_{L1} + \omega L_1^{-1} B_{L11}^T \underline{e} \quad (8)$$

where

$$L_1 = B_{L11}^T L B_{L11}$$

$$R_1 = B_{L11}^T R B_{L11}$$

Equation (8) describes the dynamics of the converter. From the knowledge of the voltage vector \underline{e} , (8) can be numerically integrated to solve for the state variables. The voltage across the nonconducting valves is given by (6). The dc and ac currents are given by (7).

DISCUSSION

Equations (6) to (8) are formed at each time the state of converter changes. The change in the status of valves in the link can be considered by rearranging the columns of matrix B_L . The matrix B_L has to be changed as the conducting valve S ceases to conduct. Although there are 6 possible matrices for the 6 valves, it is adequate to use only three such matrices corresponding to a valve group (1,3,5 or 2,4,6). This is under the assumption that atleast one valve is conducting in each valve group. The observation of matrices B_L^1, B_L^3 and B_L^5 reveal that two rows are invariant.

The procedure outlined above can be compared to the method described in [1,7] which are similar in objective. The method given here is simpler both conceptually and computationally. Also the valve characteristic can be assumed to be different than that of an ideal switch. The constituent equation in this case would be different than in (2). To give an illustration, the impedance of the valve during nonconducting period can be assumed to be finite (determined by the grading and damping circuit). Inclusion of this characteristic can be easily accomplished. In contrast, the references [1,7] implicitly assume the valve impedance to be infinite during nonconducting

period. The number of state equations per converter vary depending on the number of conducting valves (N) and is given by (N-1).

CONVERTER CONTROL REPRESENTATION

Each converter in a HVDC system is equipped with a controller that determines the instant of firing of each valve. The firing pulses are generated from a control signal which is the output of the current or extinction angle controllers. Normally current control is used at the rectifier and constant extinction angle (CEA) at the inverter. Basically there are two firing control schemes:

- i) Individual phase control (IPC), where the firing pulse for each valve is determined with respect to its own commutation voltage.
- ii) Equidistant pulse control (EPC), where the controller generates pulses at equal intervals in steady state, which is relatively independent of the distortions in the AC voltage.

Firing Control Scheme with IPC

The rectifier control signal obtained as the output of first order current controller is

$$E_{cr} = \frac{K_r}{1+T_{cr}s} (I_{refr} - I_{dr})$$

The inverter control signal is obtained as

$$E_{ci} = \sqrt{2} V_{LLi} \cos \beta_c - 2X_{ci} I_{ci} - V_{cc}$$

where

$$V_{cc} = \frac{K_i}{1+T_{ci}s} (I_{refi} - I_{ci})$$

The subscripts r and i denote rectifier and inverter quantities respectively. K is the controller gain, T_c is the controller time constant, I_{ref} is the reference current, I_c is the line current, V_{LL} is the rms value of line to line ac voltage, β_c is the extinction angle of the inverter and X_c is the commutating reactance. The firing pulse generator for a particular valve j compares the control signal with a signal E_{fj} corresponding to the commutation voltage of the valve advanced by 90° . A pulse is initiated at the instant when the following condition is satisfied.

$$E_{fj} > E_{ci} \text{ for inverter terminal}$$

and

$$-E_{rj} \leq E_{cr} \text{ for rectifier terminal}$$

The minimum delay angle (α_{min}) operation of rectifier is ensured by restricting the control signal E_{cr} from falling below $\sqrt{2} V_{LL} \cos \alpha_{min}$. In case of inverter, signal V_{cc} is clamped to zero while going negative to ensure the firing angle variation between $\pi/2$ and $(\pi - \beta_c)$.

Firing Control Scheme with EPC

An equidistant pulse firing scheme with pulse frequency control has been suggested to overcome the problem of harmonic instability which is inherent with EPC [9]. This necessitates feedback control of not only the current but also the extinction angle. In the present context of simulation, only rectifier terminal is considered to be equipped with this type of control. Fig.4 shows a simplified block diagram of the controller from which the state equations can be written down.

A constant slope ramp function is generated starting from zero at each firing instant. This ramp function is compared to the sum of the control signal (U_c) and the bias voltage proportional to $T/6$, and a pulse is initiated at each instant of equality. When $U_c = 0$, the firing pulses are generated at every 60° corresponding to steady state operation. The firing in the rectifier mode is prevented until the commutation voltage has reached a defined minimum positive value. This ensures the minimum delay angle operation of rectifier. The details of this firing pulse generation scheme are described in reference [11]

REPRESENTATION OF DC AND AC NETWORK

The DC network consists of transmission line which can be represented by a π circuit. The DC current of each converter,

which is obtained in terms of the state variables, is injected into the DC network at converter terminals. State equations for the dc network can be easily written down and are time invariant. The voltage V_c in Fig.1 is directly obtained as a capacitor voltage which is chosen as a state variable in the dc network equations.

The AC system can also be similarly modelled and the state equations are time invariant. The currents i_7 and i_9 (refer Fig.1) are treated as current sources in the derivation of AC network equations.

COMPUTER PROGRAM

Based on the procedures outlined in the previous sections, a computer program has been developed to simulate a controlled multiterminal HVDC system containing upto 10 monopolar terminals. The structure of the program is modular with each subsystem or control function described in individual subroutine. At a particular instant of time the states of all the converters are defined and the equations are formulated using the converter model described earlier. The converter state changes due to 1) cessation of conduction in a valve or 2) firing of a valve. The converter state is checked at the beginning of each integration time step. If necessary, the exact instant of cessation

of conduction in a valve is determined by linear interpolation using the valve current measurement. The presence of firing pulses is determined from the controller subroutine and the valve is put into the conducting state if it is forward biased and the voltage exceeds the defined minimum limit.

Some of the salient features of the program are given below :

1) Initial conditions:

The simulation can proceed from a) zero initial condition or b) initial conditions established from the steady state operating point. In the former case the system is started by putting all the converters under starting control. Here the firing angles are initially set at 90° and are changed linearly until the current builds up. For the second case the required steady state operating conditions are obtained from AC/DC load flow calculations [12] .

2) Converter Control:

At present there are three choices of the converter control as listed below:

- a) Constant α control
- b) Individual phase control
- c) Equidistant pulse control

Because of the modular structure of the program other control

strategies can also be incorporated, if necessary.

3) DC network equations are formed directly from the knowledge of line data and line to bus incidence matrix.

At present modified Euler's integration method is used for solving the state equations although trapezoidal or other methods can be used.

TEST SIMULATIONS

The capability of the program developed is illustrated by simulating a 2 terminal and a 3 terminal HVDC system [8]. The schematic diagrams of these systems are shown in Figs. 5 and 6. The details of the system parameters are given in Appendix 2. Various test simulations are carried out to investigate the system response both in steady state and transient conditions following a disturbance.

Fig.7 shows the steady state waveforms for a two terminal system with the operating condition B as given in Appendix 2. Individual phase control is assumed here. This establishes the terminal 1 (rectifier) operating on constant current control and terminal 2 (inverter) operating on CEA control.

The transient system response of a 2 terminal system with individual phase control is investigated with the following disturbances:

A. Change in current reference setting (with operating condition A)

- 1) at both the terminals, from $I_{ref1} = 0.65$ p.u., $I_{ref2} = 0.55$ p.u. to $I_{ref1} = 1.0$ p.u. and $I_{ref2} = 0.9$ p.u.
- 2) at both the terminals, from $I_{ref1} = 0.40$ p.u., $I_{ref2} = 0.3$ p.u. to $I_{ref1} = 1.0$ p.u. and $I_{ref2} = 0.9$ p.u.
- 3) at the rectifier terminal alone, from $I_{ref1} = 0.65$ p.u. to $I_{ref1} = 1.0$ p.u., thus increasing the current margin.
- 4) as in case 1 with source reactance at both the terminals increased by 2.5 times and the smoothing reactance doubled.

B. 30 percent dip in AC system voltage in one phase for 5 cycles (with operating condition B),

- 1) at the inverter terminal
- 2) at the rectifier terminal

The system performance for the above cases are shown in Fig.8 to 13 respectively.

For a three terminal system, the following disturbances are considered:

C. Change in current reference setting

- 1) at all the three terminals, from $I_{ref1} = 1.15$ p.u., $I_{ref2} = 0.57$ p.u. and $I_{ref3} = 0.46$ p.u. to $I_{ref1} = 1.45$ p.u., $I_{ref2} = 0.72$ p.u. and $I_{ref3} = 0.61$ p.u.

D. 30 percent dip in AC system voltage in one phase persisting for 5 cycles

1) at converter 1

2) at converter 2

3) at converter 3

Figs. 14 to 17 refer to the above cases respectively. All the above figures (8-17) show the variation of average DC current and voltage over 50 cycles of simulation. The disturbance is initiated at the beginning of the 20th cycle. All the above cases assume individual phase control for the converters.

Discussion of Results

The results demonstrate the operation of the converter control under both steady state and transient conditions. As the objective of this study is mainly to illustrate the program capability, the optimization of controller parameters was not attempted. Fig.7 shows the predominant 6th harmonic ripple in the line current. This probably is due to the fact that the control signal from the line current was not filtered.

The following observations are made from the results obtained.

Change in Current Reference

The responses for both two terminal and three terminal cases show that the current controller at each terminal comes into action as a step change in the current reference is applied simultaneously. The current settles down to the new value in a reasonably short time. Increase in the magnitude of the step change in the current reference leads to increase in the magnitude of dc voltage oscillations and increased settling time. Observation of case A.3 (refer Fig.10) shows that the current control is acting only at the rectifier and as expected, however, this leads to large oscillations in the current and voltage. This implies that the introduction of time delay in transmitting the current order to the inverter terminal leads to deterioration of the performance. Perhaps this can be improved with an optimized controller design.

It was observed that when the source reactance was increased, the system malfunctioned. This problem was overcome by doubling the value of smoothing reactance. This shows that the converter design is critically dependent on the system parameters.

Response following Disturbance in AC Voltage

With the dip in rectifier side ac voltage, the current

control shifts to the inverter and the rectifier operates with minimum delay angle. The variation of firing angles in the first cycle following the disturbance is shown in Fig.13.

For the three terminal system it is observed that the dip in the voltage at the terminal with CEA control is the most severe disturbance. Similar observations can be made for the two terminal system.

The equidistant pulse control has also been tested for the two terminal system. Fig.18 shows the response of the system when subjected to a step change in the reference current magnitude similar to the case 4.4. The rectifier terminal was equipped with equidistant pulse control and inverter terminal had individual phase control. The response shown in Fig.18 is similar to that shown in Fig.11 except for the fact that the oscillations in current and voltage are reduced in this case.

In all the test simulations presented here, the ac system was assumed to be represented by a voltage source. The detailed representation of the AC system including harmonic filters is feasible by augmenting the computer program. The detailed investigation of the equidistant pulse control will be undertaken alongwith the detailed model of the AC system.

CONCLUSIONS

A novel converter representation based on the graph theoretic analysis is described. The computer program is developed for dynamic simulation of multiterminal DC systems utilizing the converter model. The program also includes the representation of converter controls using in particular phase control and equidistant pulse control, and can be used in studying the performance of the controller under various system operating conditions. Results of various test simulations for a 2 terminal and 3 terminal sample systems are presented. Apart from illustrating the capability of the program, the results indicate the need for the optimal design of controllers, which is critically dependent on the system parameters.

APPENDIX 1

CUTSET MATRICES

The six cutset matrices B_L^j , each corresponding to the valve considered in the tree, are given below. The superscript j denotes the valve number S .

$$[B_L^1] = \begin{array}{c|ccccc} & 3 & 5 & 4 & 6 & 2 \\ \hline 7 & 0 & 1 & 0 & 0 & -1 \\ 8 & 0 & 0 & -1 & -1 & -1 \\ 9 & -1 & -1 & 0 & 1 & 1 \\ 1 & 1 & 1 & -1 & -1 & -1 \end{array}$$

$$[B_L^3] = \begin{array}{c|ccccc} & 3 & 5 & 4 & 6 & 2 \\ \hline 7 & 0 & 1 & 0 & 0 & -1 \\ 8 & 0 & 0 & -1 & -1 & -1 \\ 9 & 1 & 0 & -1 & 0 & 0 \\ 3 & 1 & 1 & -1 & -1 & -1 \end{array}$$

$$[B_L^5] = \begin{array}{c|ccccc} & 1 & 3 & 4 & 6 & 2 \\ \hline 7 & -1 & -1 & 1 & 1 & 0 \\ 8 & 0 & 0 & -1 & -1 & -1 \\ 9 & 1 & 0 & -1 & 0 & 0 \\ 5 & 1 & 1 & -1 & -1 & -1 \end{array}$$

$$[B_L^4] = \begin{array}{c|ccccc} & 1 & 3 & 5 & 6 & 2 \\ \hline 7 & 0 & 0 & 1 & 0 & -1 \\ 8 & -1 & -1 & -1 & 0 & 0 \\ 9 & 0 & -1 & -1 & 1 & 1 \\ 4 & -1 & -1 & -1 & 1 & 1 \end{array}$$

$$[B_L^6] = \begin{array}{c|ccccc} & 1 & 3 & 5 & 4 & 2 \\ \hline 7 & 0 & 0 & 1 & 0 & -1 \\ 8 & -1 & -1 & -1 & 0 & 0 \\ 9 & 1 & 0 & 0 & -1 & 0 \\ 6 & -1 & -1 & -1 & 1 & 1 \end{array}$$

$$[B_L^2] = \begin{array}{c|ccccc} & 1 & 3 & 5 & 4 & 6 \\ \hline 7 & -1 & -1 & 0 & 1 & 1 \\ 8 & -1 & -1 & -1 & 0 & 0 \\ 9 & 1 & 0 & 0 & -1 & 0 \\ 2 & -1 & -1 & -1 & 1 & 1 \end{array}$$

APPENDIX 2

SYSTEM PARAMETERS

Two Terminal System

The two terminal system, Fig.5, is synthesized from the three terminal system of reference [8] by neglecting the terminal 3 of Fig.6. System parameters used in this study are chosen on the basis of reference [8].

Commutating reactance:

$$X_{c1} = X_{c2} = 0.055 \text{ p.u.}$$

Smoothing reactor:

$$\text{Resistance } R_{d1} = R_{d2} = 0.003 \text{ p.u.}$$

$$\text{Inductance } L_{d1} = L_{d2} = 0.3 \text{ p.u.}$$

Transmission line:

$$\text{Resistance } r = 0.0508 \Omega/\text{mile}$$

$$\text{Inductance } l = 0.00324 \text{ H/mile}$$

$$\text{Capacitance } c = 0.0091 \mu \text{ F/mile}$$

$$\text{Length} = 800 \text{ miles}$$

Controllers:

a) Individual phase control

$$K_1 = K_2 = 19 \text{ p.u.}$$

$$T_{c1} = T_{c2} = 0.2 \text{ seconds}$$

b) Equidistant pulse control

$$K_1 = 1.0 \text{ p.u.}$$

$$T_1/T_2 = 2; T_2 = 0.005 \text{ seconds}$$

Operating condition:

A. Line-to-line AC peak voltage

$$E_1 = 1.15 \text{ p.u.}, E_2 = 0.95 \text{ p.u.}$$

$$\alpha_1 = 15.46^\circ, \gamma_c = 15^\circ, \alpha_{\min} = 5^\circ$$

$$I_{d1} = I_{d2} = 0.6 \text{ p.u.}$$

B. Line-to-line AC peak voltage

$$E_1 = 1.0 \text{ p.u.}, E_2 = 0.95 \text{ p.u.}$$

$$\alpha_1 = 15.46^\circ, \gamma_c = 15^\circ, \alpha_{\min} = 5^\circ$$

$$I_{d1} = I_{d2} = 0.6 \text{ p.u.}$$

Converter 1 (rectifier) operates on constant current control and converter 2 (inverter) on CEA control.

Three Terminal System (Fig.6)

Commutating reactance:

$$X_{c1} = X_{c2} = X_{c3} = 0.055 \text{ p.u.}$$

REFERENCES

1. N.G. Hingorani, R.H. Kitchin and J.L. Hay, 'Dynamic simulation of HVDC power transmission systems on digital computer,' IEEE Transactions on Power Apparatus and Systems, Vol.PAS-87, pp.989-996, April 1968.
2. N.G. Hingorani and J.L. Hay, 'Dynamic simulation of multiconverter HVDC systems by digital computer, Part I: Mathematical model,' IEEE Transactions on Power Apparatus and Systems, Vol.PAS-89, pp. 218-222, Feb.1970.
3. N.G. Hingorani, J.L. Hay and R.E. Crosbie 'Dynamic simulation of HVDC systems on a digital computer,' Proc. IEE, Vol.113, pp.793-802, May 1966.
4. J. Millias-Argitis, G. Giannakopoulos and G. Galanos, 'Dynamic simulation for multiterminal HVDC systems,' IEEE Transactions on Power Apparatus and Systems, Vol.PAS-97, pp.587-593, March/April, 1978.
5. A.M. El Serafi and A. Shehata, 'Digital simulation of AC/DC systems in direct phase quantities,' IEEE Transactions on Power Apparatus and Systems, Vol.PAS-95 pp.731-736, March/April 1976.
6. J.S.C. Htsui and W. Shopherd, 'Method of digital computation of thyristor circuits,' Proc. IEE, Vol.118, pp.990-998 Aug. 1971.
7. S. Williams and I.R. Smith, 'Fast digital computation of 3-phase thyristor bridge circuits,' Proc. IEE, Vol.120, pp.791-795, July 1973.
8. D.P. Carroll, 'Hybrid computer simulation of multiterminal DC power transmission system,' IEEE Transactions on Power Apparatus and Systems, Vol.PAS-89, pp 1126-1133, July/August 1970.
9. J.D. Ainsworth, 'The phase locked oscillator - A new control System for controlled static converters,' IEEE Transactions on Power Apparatus and Systems, Vol.PAS-87, pp.859-865, March 1968.

10. G. Kron, 'Tensor for Circuits', Dover, 59.
11. A. Ekstrom and G. Lins, 'A modified HVDC Control system,' IEEE Transactions on Power Apparatus and Systems, Vol. PAS-89, pp.723-732, May/June 1970.
12. K.R. Padiyar and Sachchidanand, 'Load Flow Analysis of multiterminal HVDC/AC systems,' accepted for presentation at IFAC Symposium on Theory and Application of Digital Control, New Delhi, January, 1982.

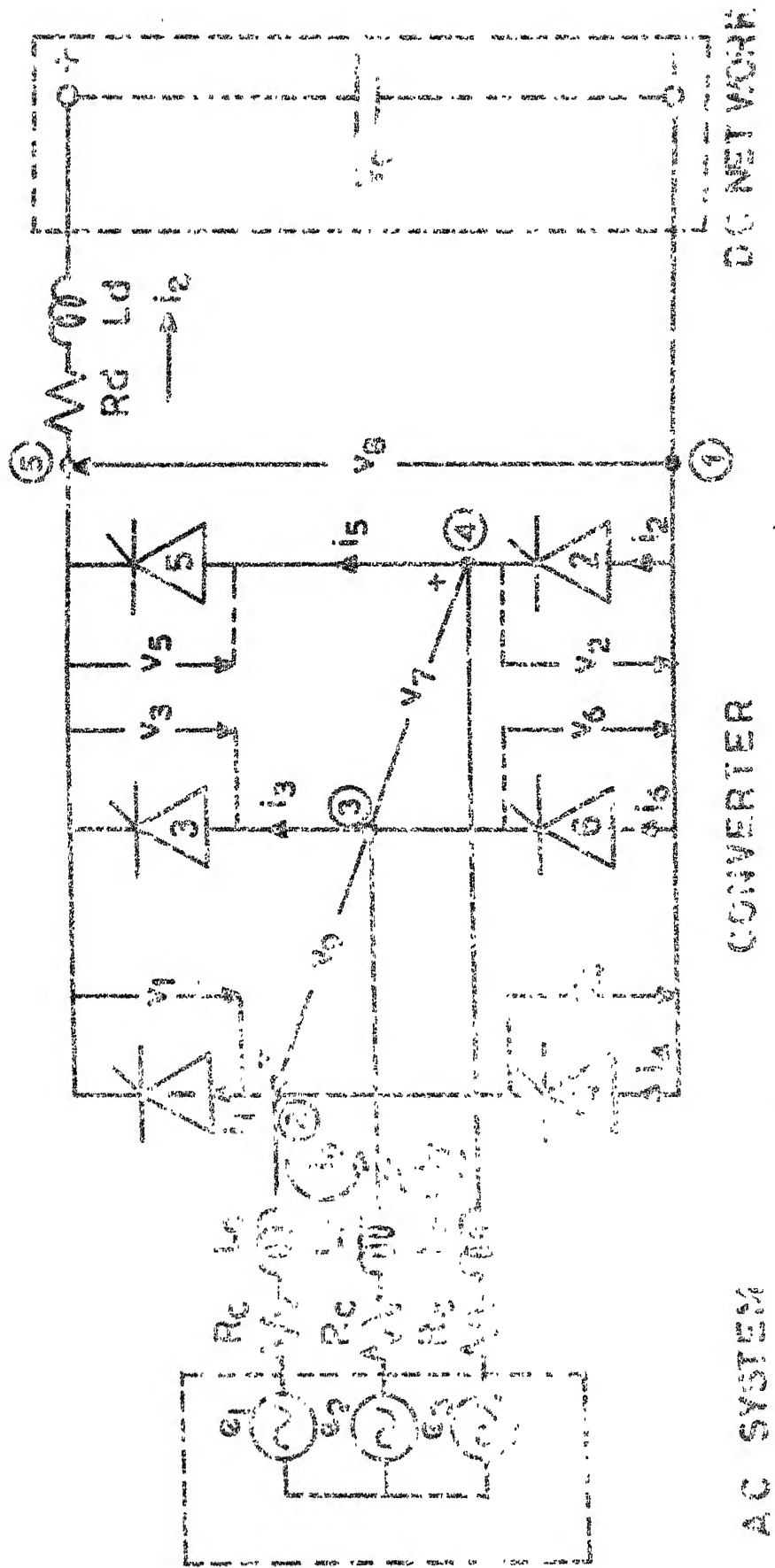


FIG. 1 THREE PHASE BRIDGE CONVERTER SYSTEM

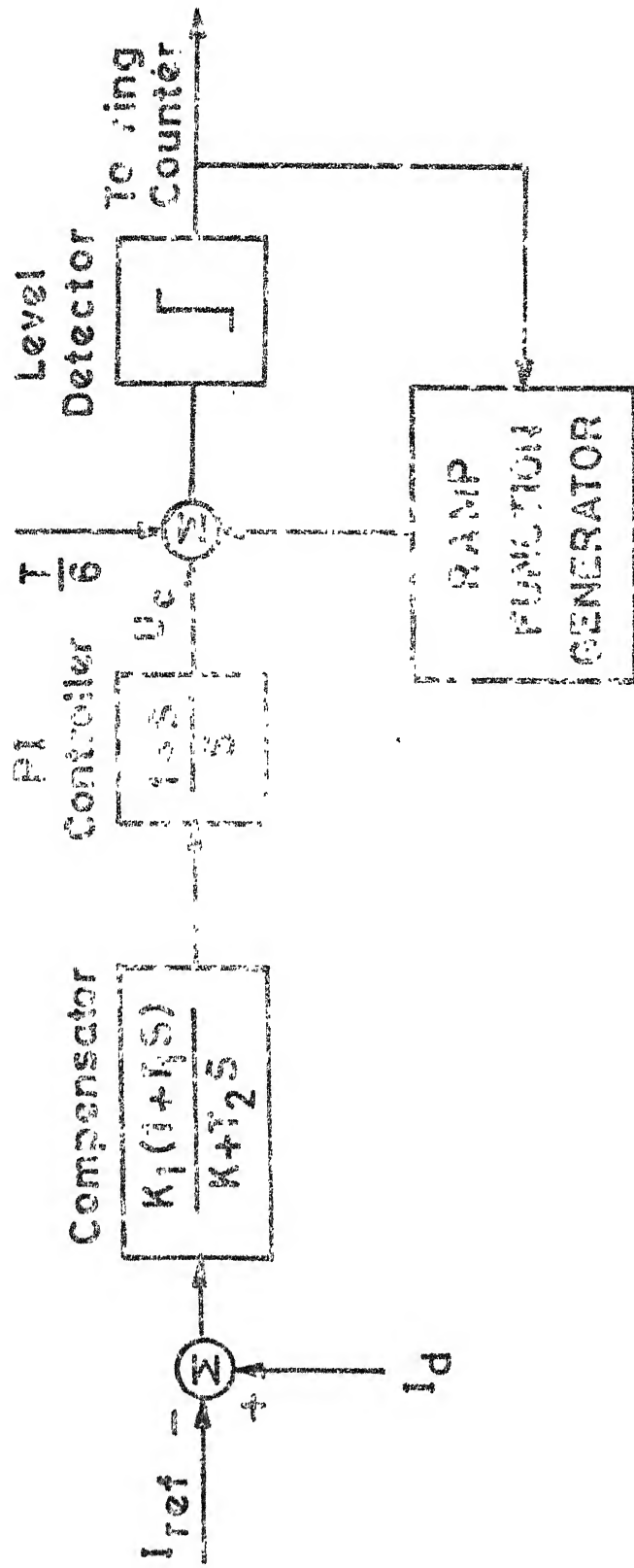


FIG. 4 EQUIDISTANT PULSE CONTROL

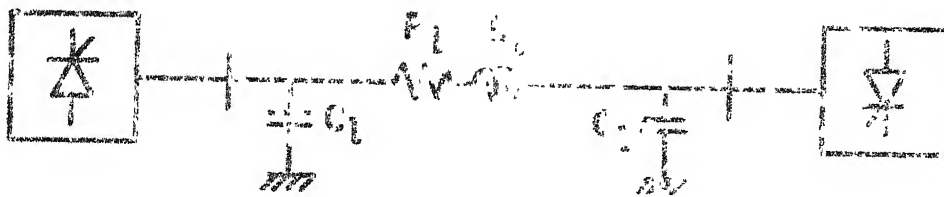


FIG. 5 TWO TERMINAL POWER SYSTEM

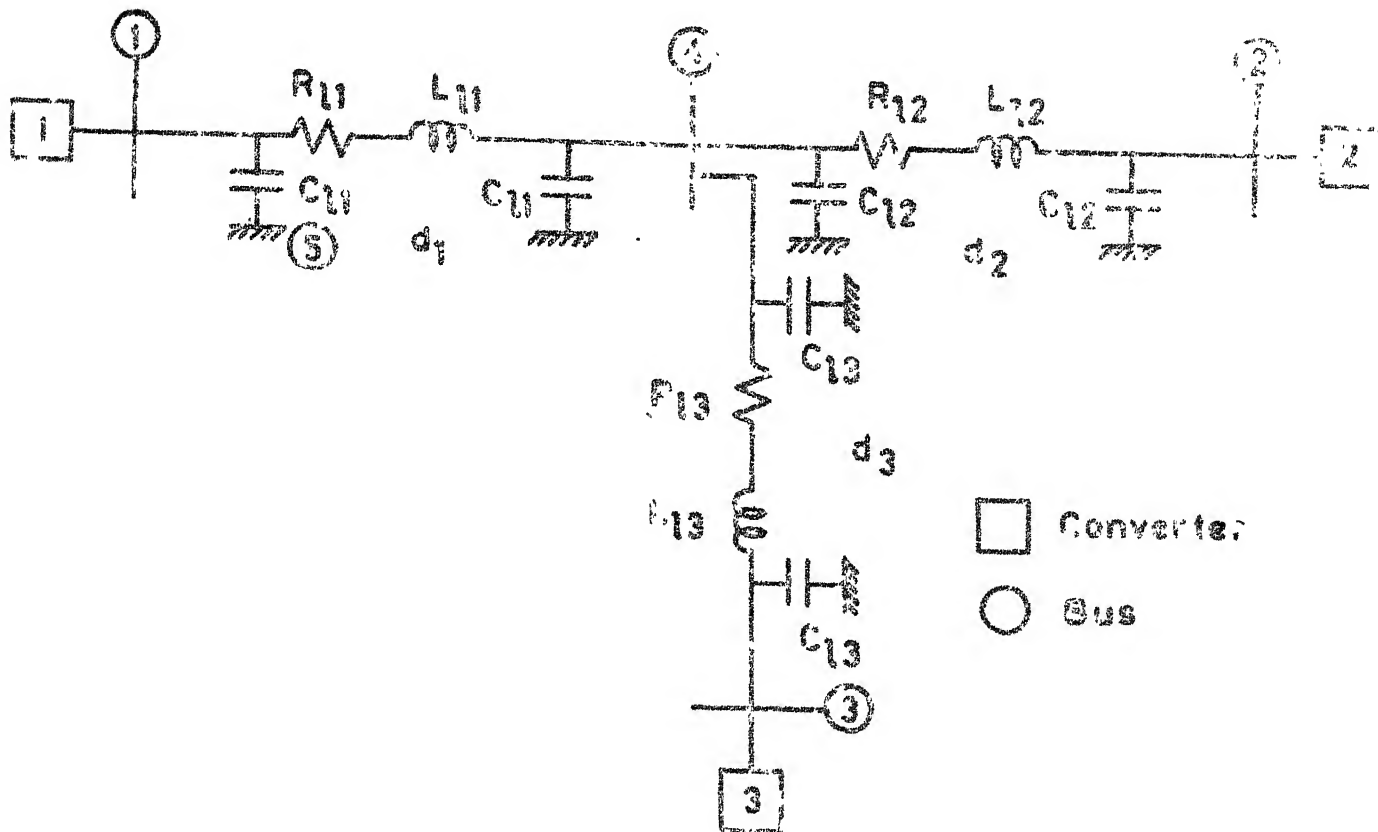


FIG. 6 THREE TERMINAL HVDC SYSTEM

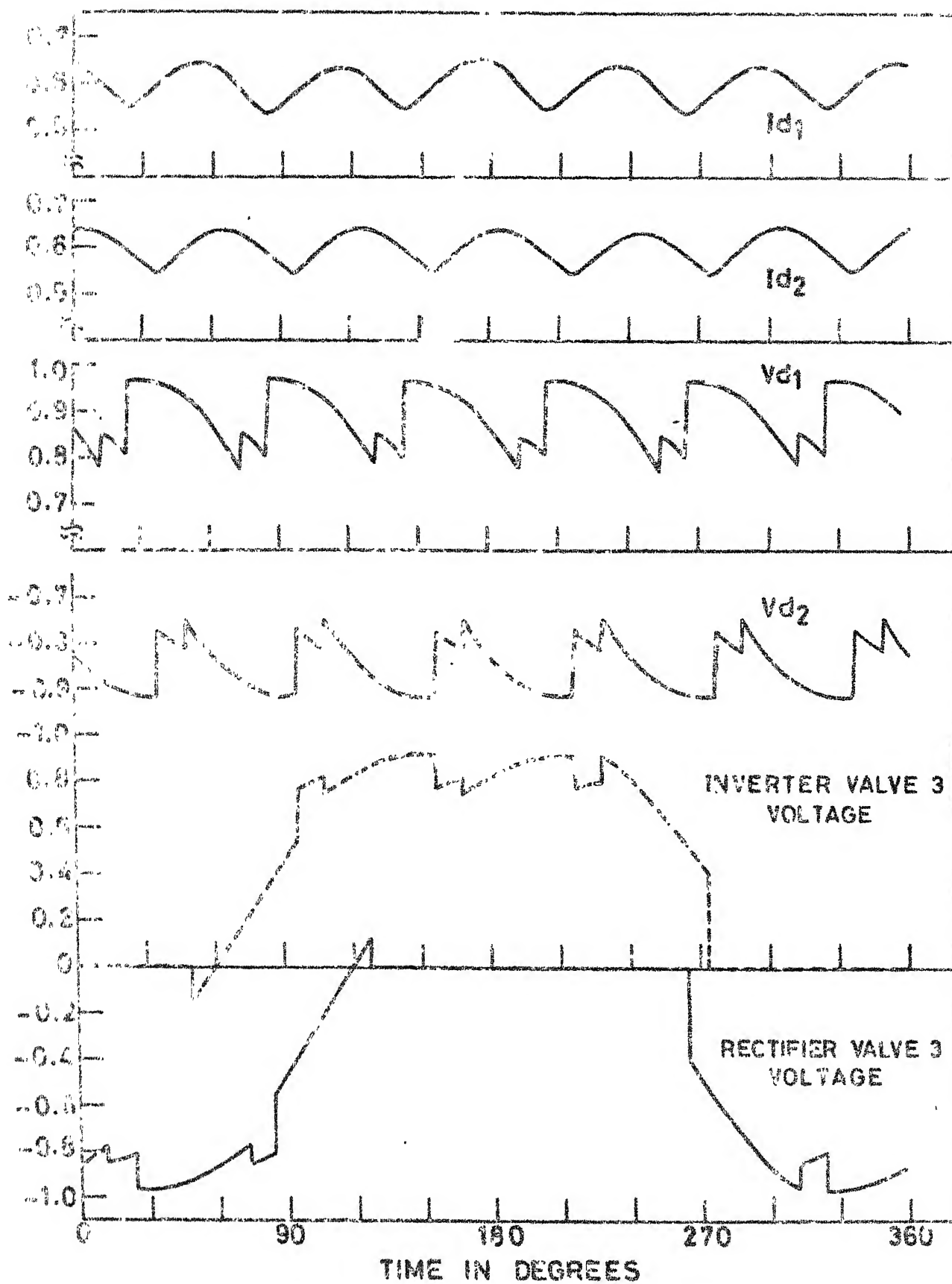


FIG. 7 STEADY STATE WAVEFORM (2 TERMINAL SYSTEM)

CASE A.1

Change in I_{ref}

$I_{ref_1} : 0.65 \text{ to } 1.0$

$I_{ref_2} : 0.55 \text{ to } 0.9$

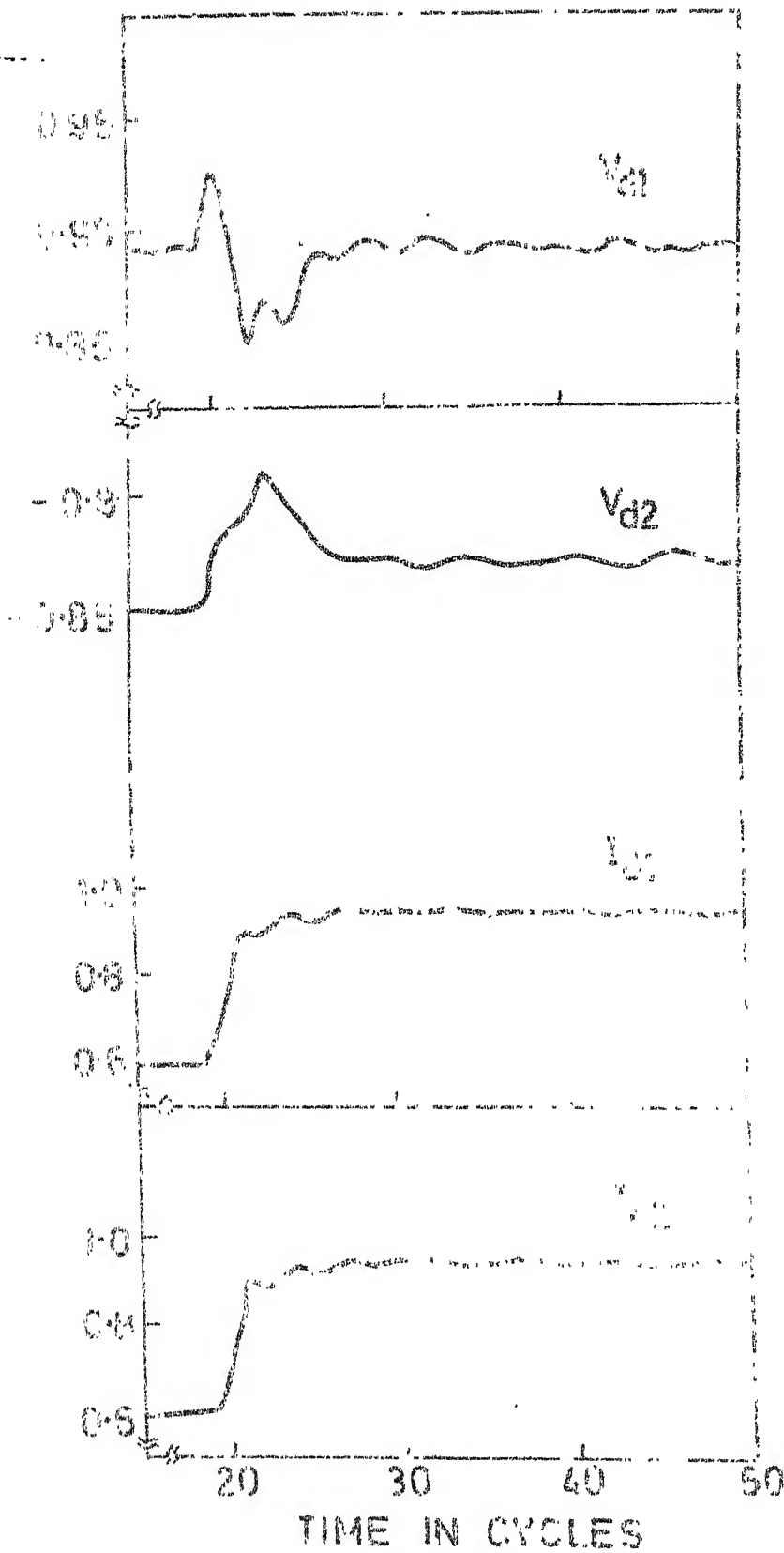


FIG. 8 RESPONSE FOR CASE A.1

CASE A.2

Change in I_{ref}

$I_{ref1} : 0.4 \text{ to } 1.0$

$I_{ref2} : 0.7 \text{ to } 0.9$

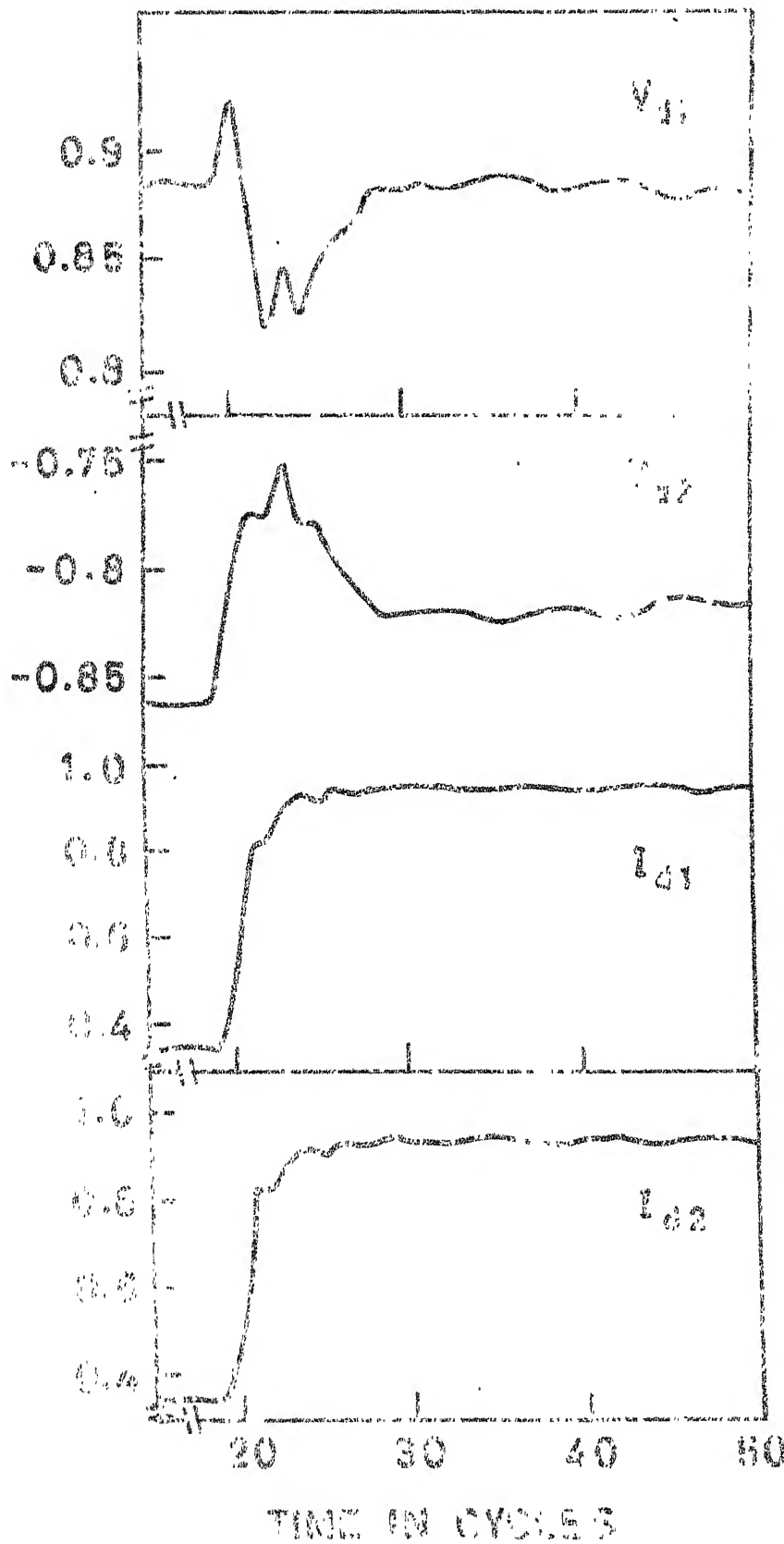


FIG. 8 REGULATION OF CASE A.2

Case A.3

Change in I_{ref}
(Rectifier only)

$I_{ref_1} : 0.65 \text{ to } 1.0$

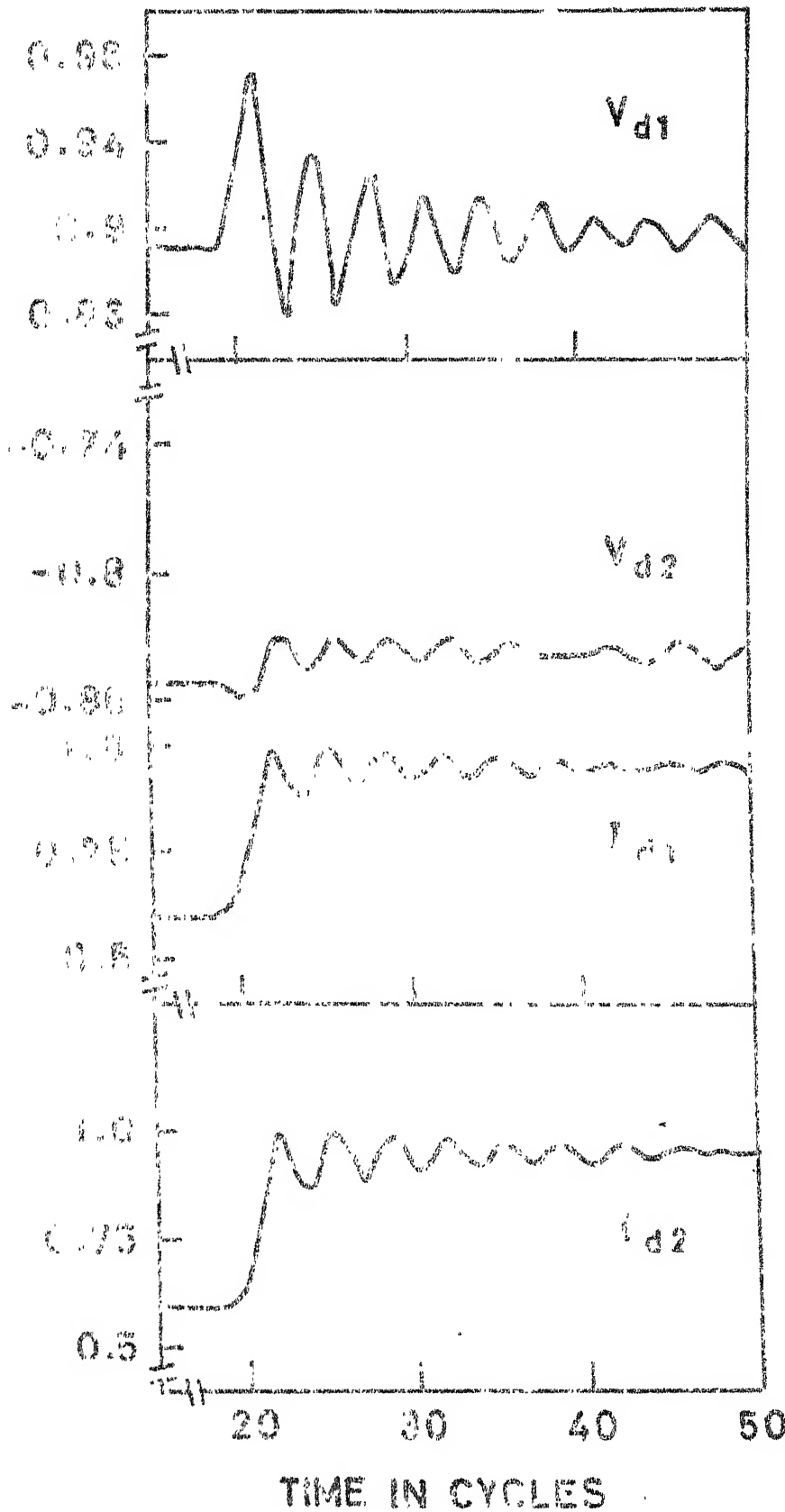
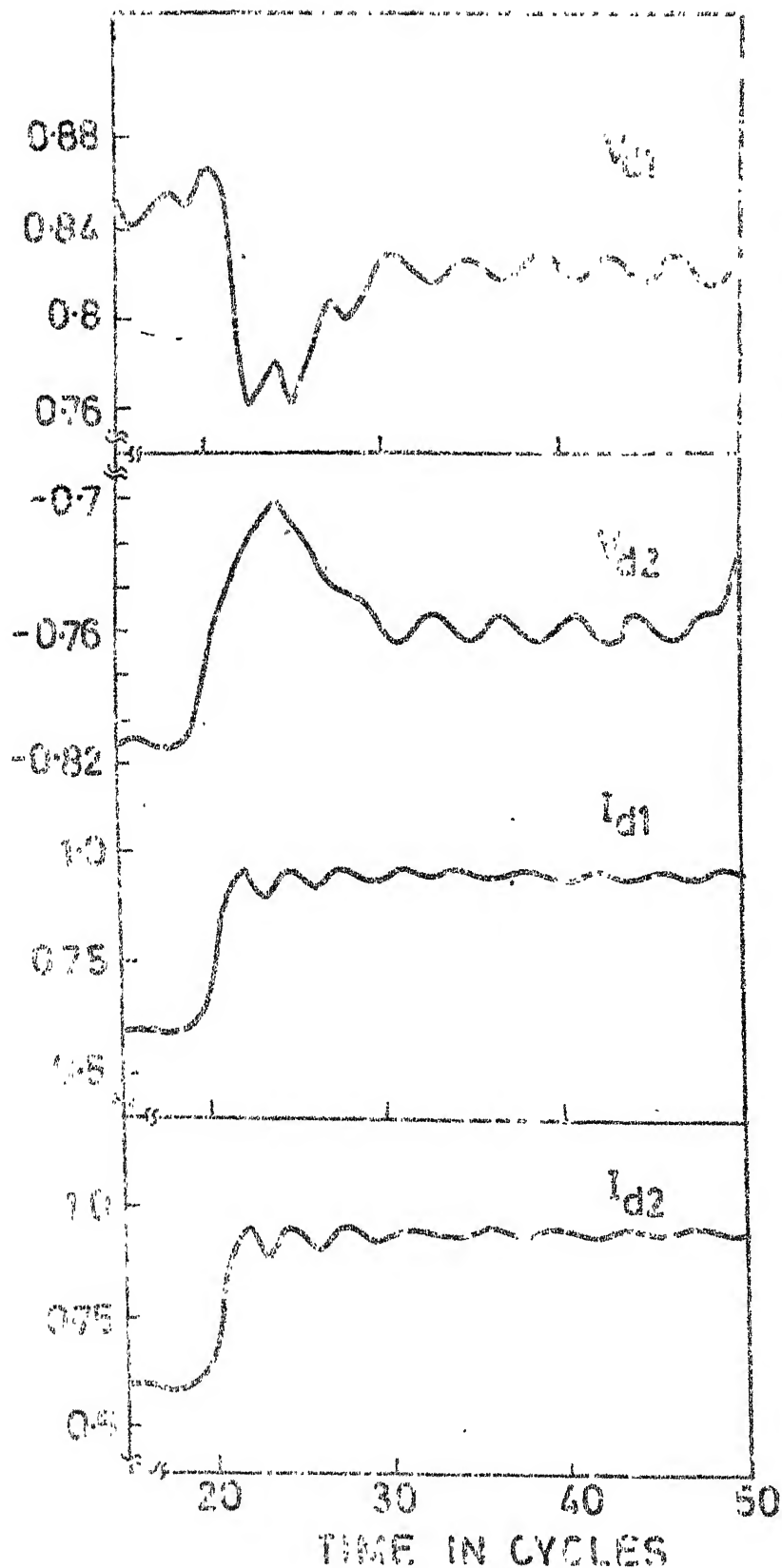


FIG. 10 RESPONSE FOR CASE A.3



Case A.4

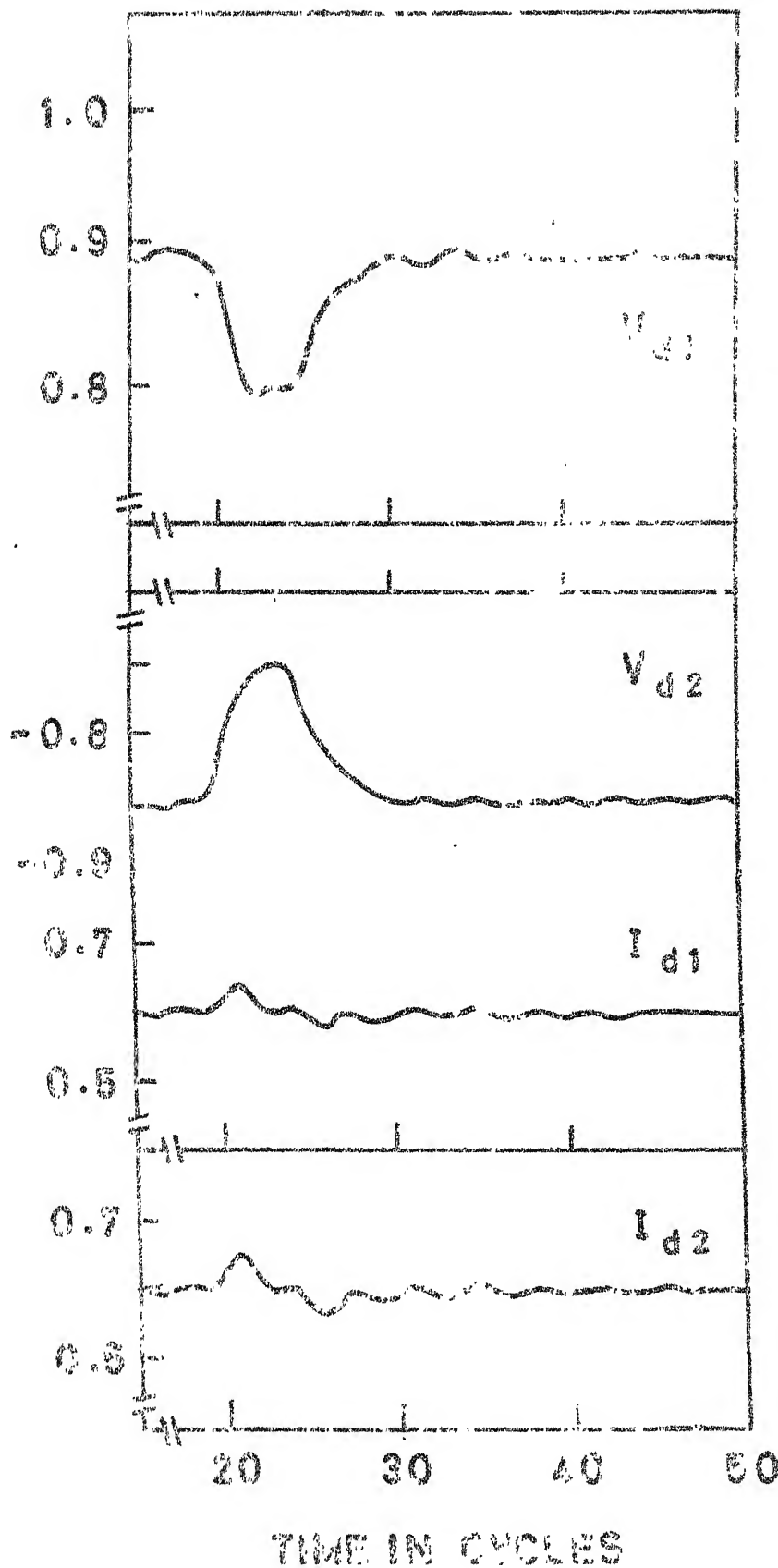
Change in I_{ref}

$I_{ref_1} : 0.65 \text{ to } 1.0$

$I_{ref_2} : 0.95 \text{ to } 0.9$

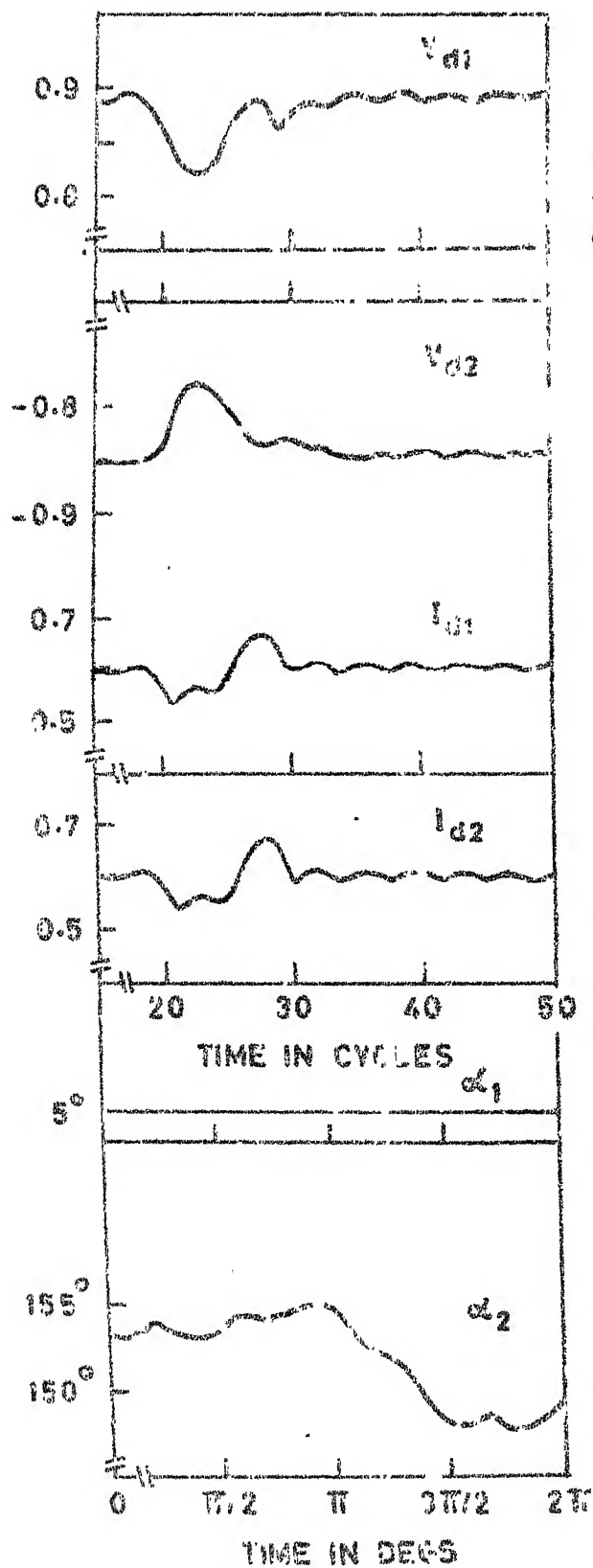
Source reactance
increased 2.5 times
 L_d doubled

FIG. 11 RESPONSE FOR CASE A.4



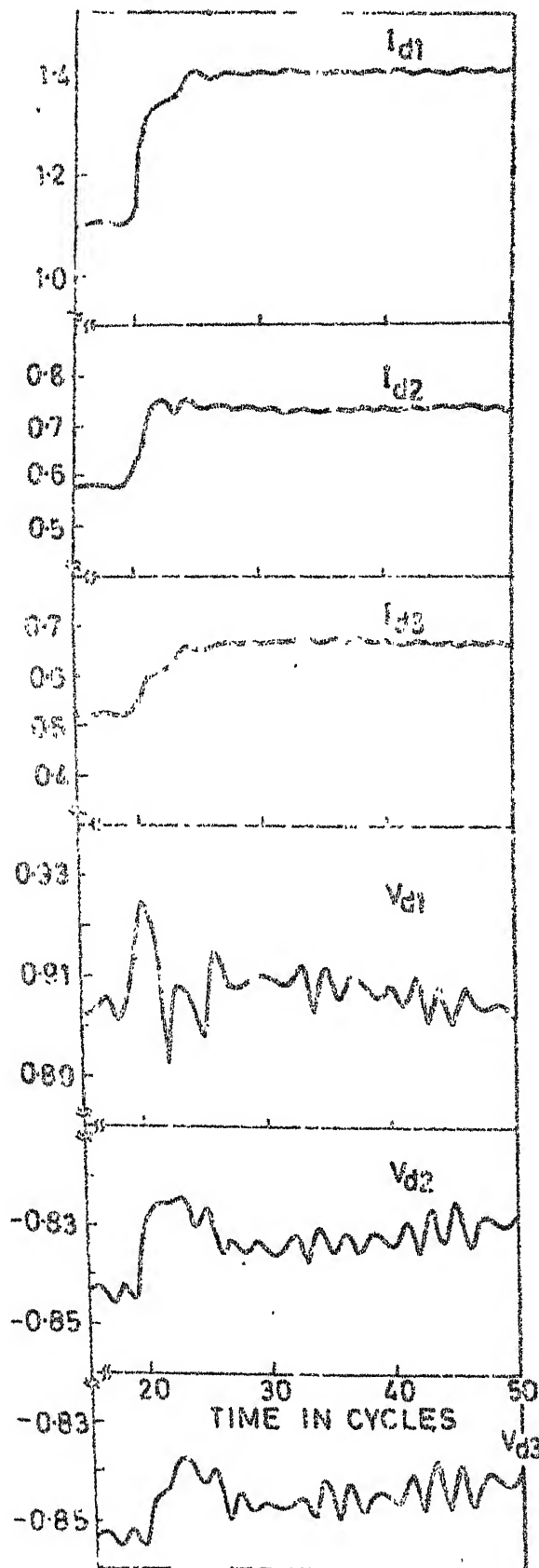
Case B.1
 30% Dip in AC
 voltage (5 cycle
 duration) at
 inverter

FIG. 12 RESPONSE FOR CASE B.1



Case B.2
30% Dip in AC
voltage (5 cycle
duration) at
rectifier

FIG. 13 RESPONSE FOR CASE B.2



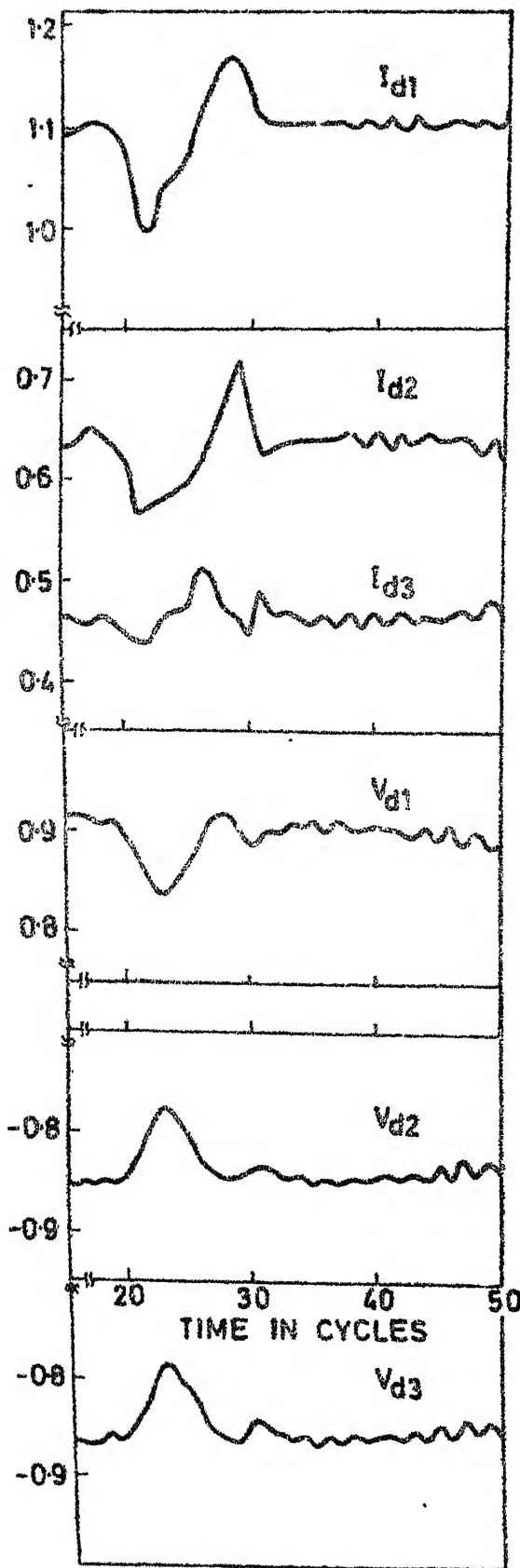
Case C.1

Change in I_{ref}

I_{ref1} : 1.15 to 1.45

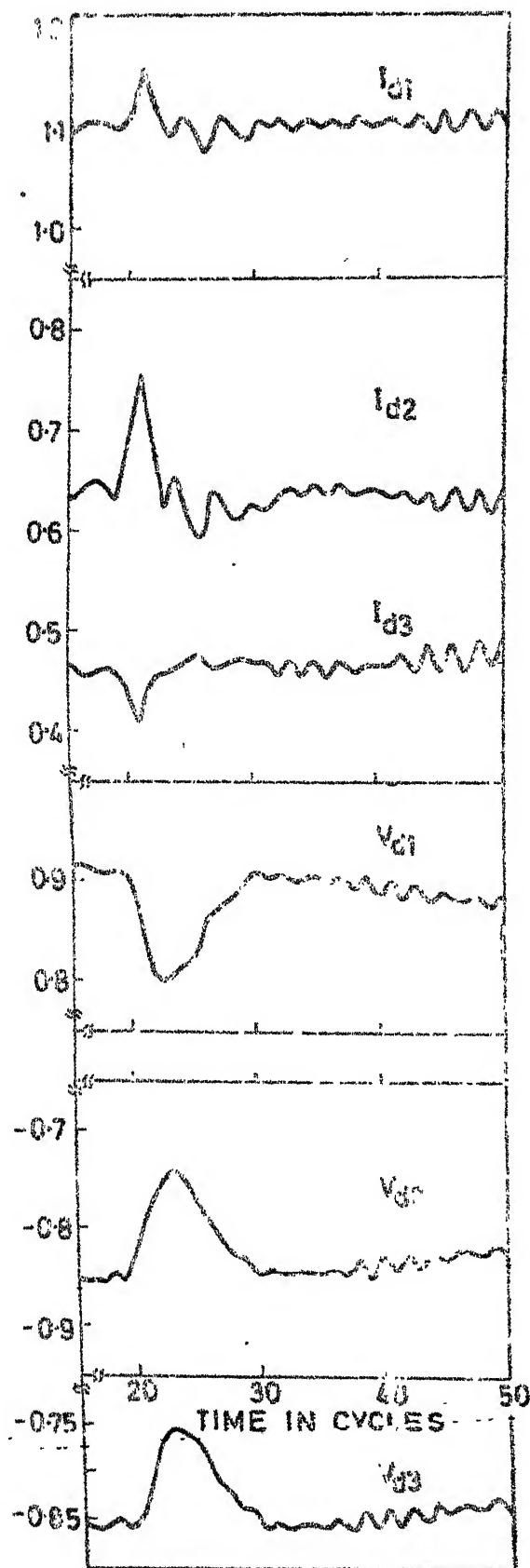
I_{ref2} : 0.57 to 0.72

I_{ref3} : 0.46 to 0.61



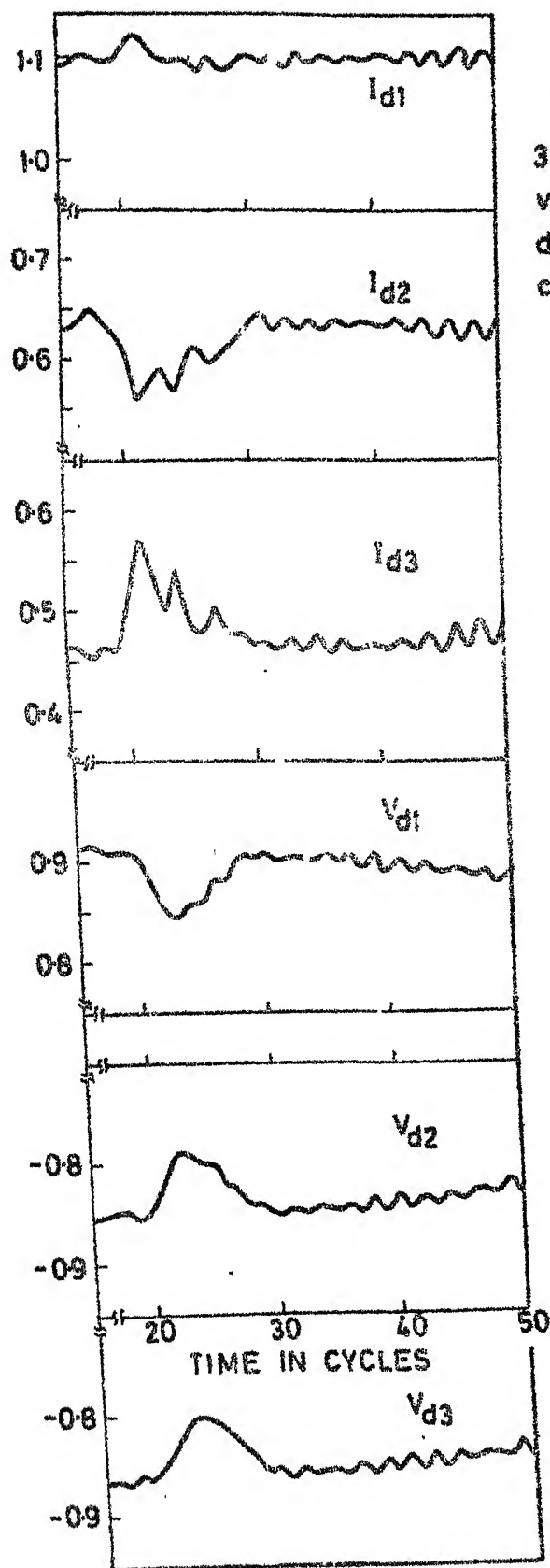
Case D.1
30 % Dip in A C
voltage (5 cycle
duration) at
converter 1

FIG. 15 RESPONSE FOR CASE D.1



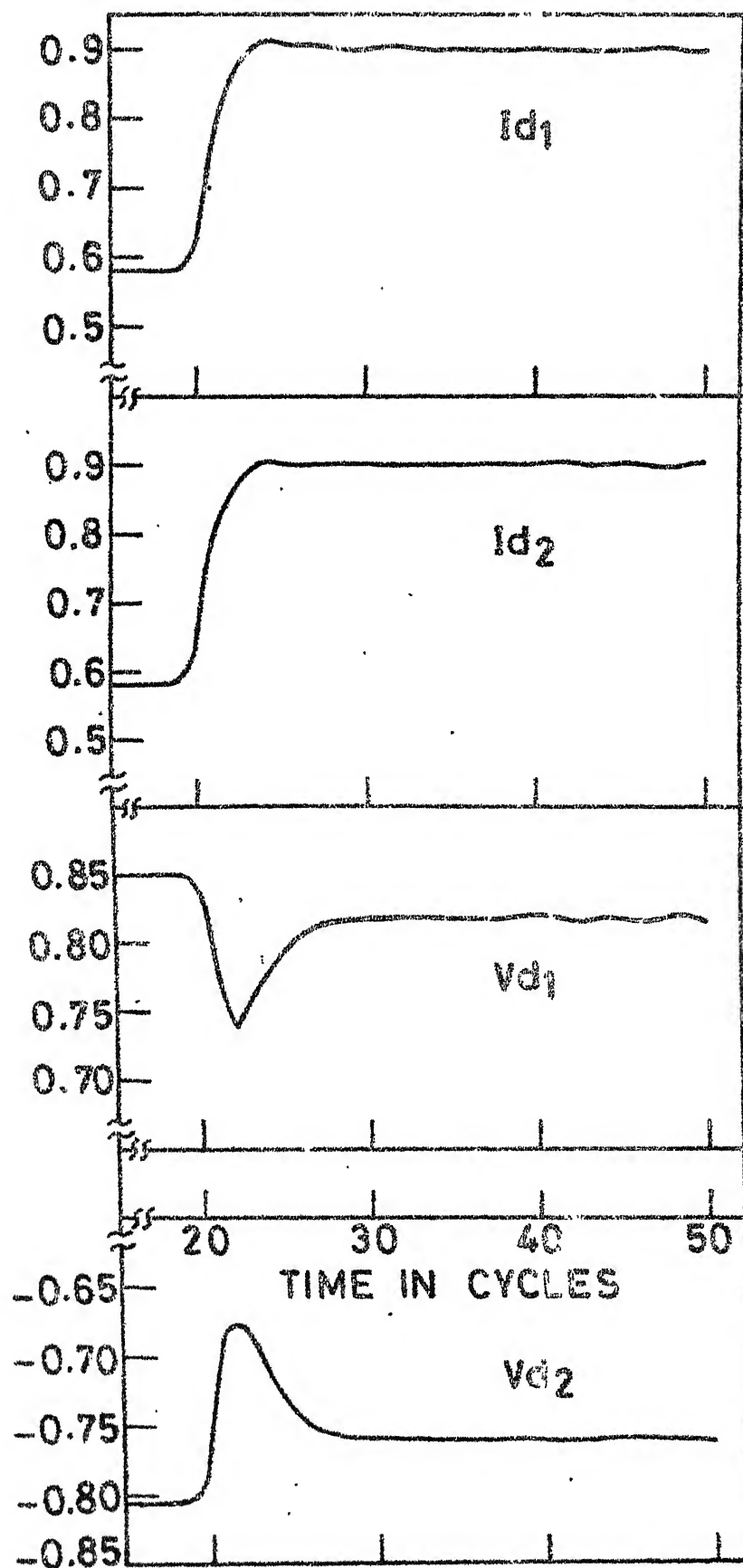
Case D.2
30% Dip in AC
voltage (5 cycle
duration) at
converter 2

FIG. 16 RESPONSE FOR CASE D.2



Case D.3
30 % Dip in AC
voltage (5 cycle
duration) at
converter 3

FIG. 17 RESPONSE FOR CASE D.3



Case A.4
with EPC
Change in I_{ref}
 $I_{ref_1} : 0.65$ to 1.0
 $I_{ref_2} : 0.55$ to 0.9
Source reactance
2.5 times
 L_d doubled

FIG. 18 RESPONSE FOR CASE A.4
WITH EPC

Dr. L.P. SINGH

Protective Relaying

I. Relays General Information

Introduction:

The importance of relays for apparatus and system (including transmission line) protection are well known. They work as **silent** sentinels guarding the system against abnormal operation. The purpose of relaying can be stated in the following manner:

1. By providing fast clearing of fault, damage to the apparatus is reduced.
2. Any subsequent hazards like fire, loss of life are reduced.
3. By removing the particular faulted section, the continuity of supply is maintained through the remaining healthy section.
4. By clearing the fault fast, fault arising time is reduced and therefore the system can be brought back to the normal state sooner.
5. Since the fault stays on the system for a very short period, by high speed relaying, the transient stability limit of the system is very much improved. Fig.1 shows the improvement in stability limit as a function of fault clearing time.

To achieve all these objectives the relays must satisfy the following requirements.

1. Since the faults on a well designed power system are normally rare, the relays are called in for operation once in a way. This means that the relaying system is normally idle and must reliably operate when faults occur. Thus the relay must be reliable.
2. Since the reliability partly depends on the maintenance, the relays must be easily maintainable.
3. There are two ways by which the relays mal-operates. One is the failure to operate in case of faults and the second one is relay operation where there is no fault. Relay must be immune from both.
4. Relay must be sensitive enough to distinguish between normal and faulty operation of the system.

1.1 Type of Relays:

A number of relays are used for power system protection. Some of them are primary relays meaning that they are the first line of defence. These relays sense the fault and send a signal to the proper breaker to trip and clear the faulted line. The fault may not be cleared if the breaker fails to open or the relay mal-operates. The breaker failures are for two reasons. Failure of the supply to the tripping coils or a stuck mechanical lever. In this case, a second line of defence to the power system is provided by the back up relays. These relays have a longer operating time even though they sense the fault along with the primary relays. Relay operating time is defined as the time interval between the sensing of fault and sending signal to the proper breaker for opening. Back up relays are arranged in two ways. They are located at the same place as the primary relays (local back up) and operate the same breakers. Or they are located at the another station and open a different breaker. In the latter case the reliability is more but a longer section of the system is disconnected due to the operation of the back up relays. Fig. 2 shows the location of the primary and back up relays. Here the remote back up is provided by multistep primary relays and local back up by a non-directional over current relay with delayed operation.

The likelihood of failure of protection equipment is as follows :

Relays	43 percent
Circuit breakers	26 percent
Supply of wiring	18 percent
Instrument transformers	10 percent
Misc.	3 percent

The relay failure is due to :

1. Contacts
2. Open circuit in relay coils
3. Wrong setting

Some times the local back up relays operate the breakers behind the bus. This is called the breaker back up. Local back up protection has the draw back that they use the same d.c. supply for breaker tripping.

Following are the common types of relays used for apparatus and line protection.

1. Over current relays
2. Directional relays
3. Under voltage relays
4. Frequency relays
5. Distance relays
6. Thermal relays
7. Phase sequence relays
8. Differential relays.

All the existing relaying schemes use either one or more of these relays with slight modifications.

Fig. 3 shows the basic connections of a relay. There are two ways in which the circuit breaker trip coil is energized. One method uses the station battery to supply the current after the relay contacts close. This is shown in Fig. 3. In the other method as soon as the relay operates the C.T. secondary current flows through the trip coil and energise it. This does not require a station battery and is used for protection of feeders.

Fig.4 shows the zones of protection usually defined for a power system. The relays in each zone are supposed to operate fault within that zone. This is called the unit type of protection. In this scheme the relays do not provide back up for the other zone relays. So internal back up is necessary for each zone. This is usually provided by non-directional high set time delayed over current relays. The zones overlap to avoid any blind zones. The overall system protection is divided into

- a) Generator protection
- b) Transformer protection
- c) Bus protection
- d) Transmission line protection
- e) Feeder protection

1.2 Relay Terminology:

Pick up - Min. value of operating quantity for which the relay operates.

Drop out- Min. value of operating quantity for which the relay resets after it has operated.

Sensitivity - Ability of the relay to discriminate between faulted and normal conditions.

Selectivity - To select faults only within the desirable zone of protection.

Reliability - Ability to perform its function when desired.

Reach - The set max. distance of fault from the relay location which the relay can detect.

Over reach - Ratio of the max. distance of fault from the relay location to the set distance for the relay.

Under reach - do -

Set impedance - Impedance of the line up to the reach of the relay.

Fault impedance - Impedance of the fault (impedances)

Instantaneous - No time relay involved in the relay operation.

Time delay - Time interval between the sensing of fault to the relay contacts close.

Inverse time - Time delay inversely proportional to the operating quantity.

Primary relay - Main relays

Back up relay - Supporting or supervisory relays

Comparator - Another name for relay

Phase comparator- Relay comparing the phase angles of input quantities

Amplitude comparator - Relay comparing the amplitudes of input quantities.

Instantaneous Comparator - Relay comparing instantaneous values of input signal.

Blocking relay - Relay operation produces blocking

Blinders - Make the relay immune for certain faults.

Dual input comparator - Has two input signals

Multi input comparator - Has more than two input signals

Seal in relay	- Relay contacts are by passed after the seal in relay operates.
Flag indicator	- Indicator to show that the relay has operated.
Burden	- V A Product of the relay coil
Transactor	- Air core coil which convert a current signal to voltage.
Transducer	- Which produces the proper relay signals from the power system.
N.C. contacts	- Normally closed contacts
N.O. contacts	- Normally opened contacts
Auxiliary contacts	- Contacts other than the main contacts in circuit breakers.
Threshold operation	- Relay is about to operate. Net torque is close to zero (i.e. fault has occurred at the balance point)

2.0 Circuit Breakers :

The function of the relays as earlier discussed is to sense the fault and energise the trip coil of the circuit breaker. Now a days circuit breakers are available with opening time of about 1 cycle. These are called one cycle breakers. Four types of breakers are normally used for equipment and transmission lines protections.

1. Air circuit breakers
2. Oil circuit breakers
3. Minimum oil circuit breakers
4. Air blast circuit breakers
5. Vacuum switches.

The first is used for apparatus protection at low voltages. The second is used for feeder protection. Three and four are used for high voltage lines. In the place of air, the SF_6 is also used. Air blast breakers for EHV lines has become standard practice. They have a clearing time of less than a cycle. These breakers produce what is called as current chopping which results in over voltage on the system. Switching resistances are normally used with these breakers. Vacuum switches for high speed fault interruption are being introduced now.

For important lines the breakers are provided with a reclosing feature. The breaker after opening closes again after a prescribed dead time. The reason for this practice is that the major percentage of faults on lines are transient in nature. They are called arcing faults and occur due to the conductor swining. Therefore the fault is automatically cleared. Even if the fault is not self-clearing, the arc gets extinguished when the line is opened. Fig. 5 shows the control circuit for the remote operations of the breakers.

3.0 Types of relays:

Following types of relays are used for various types of protection schemes:

1. Electromechanical type:.

Here the torque on the moving member is produced by electromagnetic action. Examples of these relays are

a) Armature attracted type. This is shown in Fig. 6(a). Normally used as an instantaneous relay for over current or under voltage detection. Since the torque is non-uniform there is contact chattering and it has a high pick up to drop out ratio.

b) Induction cup or disc type relays: This is shown in Fig. 6(b). The difference between the cup and disc in the fabrication of the stator and the rotor. The torque is more uniform here and the ratio and the operation of pick up to drop out is more closer to unity. This relay is widely used for a large type of relays. Most of the distance relays are of this type. We shall discuss these later in detail.

2. Thermal relays:

These relays use bimetallic strips and the relay operation is based on unequal expansion of the two strips. These are used for apparatus protection. They are not as sensitive as the induction cup type relays. Also their drop out value is very low because of large thermal time constant.

3. Transducer relays:

These relays use the nonlinear B - H characteristic of the magnetic core. Transducer implies variable inductance. When the core is not saturated, the coil offers a very high impedance and when the core is saturated the coil will be almost a short circuit. These relays are discussed in the following chapters.

4. Rectifier bridge relays:

These relays also use the electromagnetic action for the production of torque. The signals to these coils are obtained after full wave rectification. These relays can be used both as amplitude or phase comparator. Fig. 6(c) shows the rectifier bridge comparator using signal amplitudes for comparison. It can be observed that if $i_o > i_r$ the coil will have a net operating torque and the relay operates. Fig. 6(d) shows the operation of the relay as a phase comparator. If the phase angle between the signals i_1 and i_2 is less than $\pi/2$, the relay operates. In this case one of the signals i_1 acts as the polarising current and permits only one pair of diodes to conduct. By suitable choice of the input signals, different types of relay threshold characteristics can be obtained. These are used as multiple input distance relays. Details are discussed elsewhere.

5. Electronic relays :

The relays discussed above have moving parts. Due to these reasons, the electromechanical relays have some inherent drawbacks. These are listed below:

- a) High burden on CT_S and PT_S.
- b) High operating time due to inertia of moving parts.
- c) Contacts pitting. This results in bad contacts and relay mal-operation.
- d) Contact racing. This is the result of the inertia of the moving parts. Due to this, relay co-ordination becomes difficult.
- e) Require frequent maintenance.
- f) Affected by vibrations and shocks.

Moving contact relays operate due to external vibrations like seismic shocks.

Due to these drawbacks, power system engineers have tried to induce electronic components for fault detections in the place of moving elements. These are called static relays. The advantages of the electronic relays are:

- a) Low burden on CT_S and PT_S .
- b) No moving contacts. Therefore all problems due to inertia like high operating time, contact racing are avoided.
- c) Require less maintenance
- d) Not affected by vibrations and shocks etc.

A detailed treatment of the electronic relays is given in the following chapters.

After the advent of the solid state devices, electronic relays have given way to solid state relays. Solid state relays have all the advantages of electronic relays and in addition, they are compact, more reliable and do not require high voltage power supplies. Now a days, many relay manufacturers are making solid state relays. They are also enable to adoption of different types of protection schemes. By proper selection of relaying quantities, it is possible to obtain many desirable relay characteristics. These will be discussed later in detail.

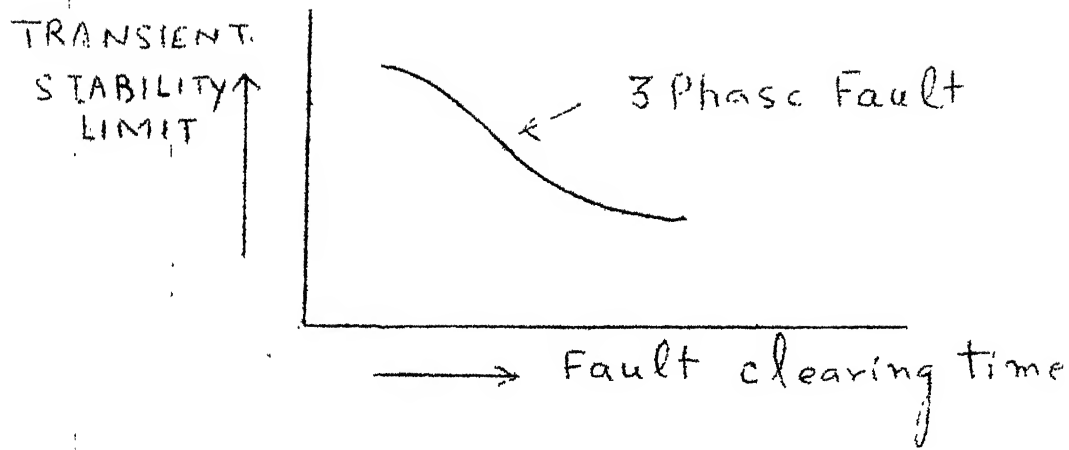


FIG.1. EFFECT OF HIGH SPEED RELAYS

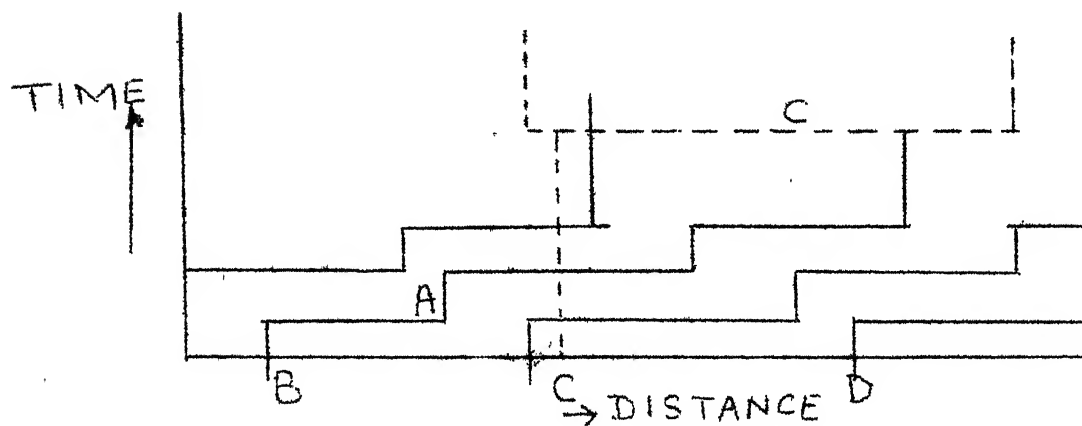


FIG.2. LOCAL RELAY BACKUP BY A DEFINITE TIME RELAY (DOTTED CHARACTERISTIC)

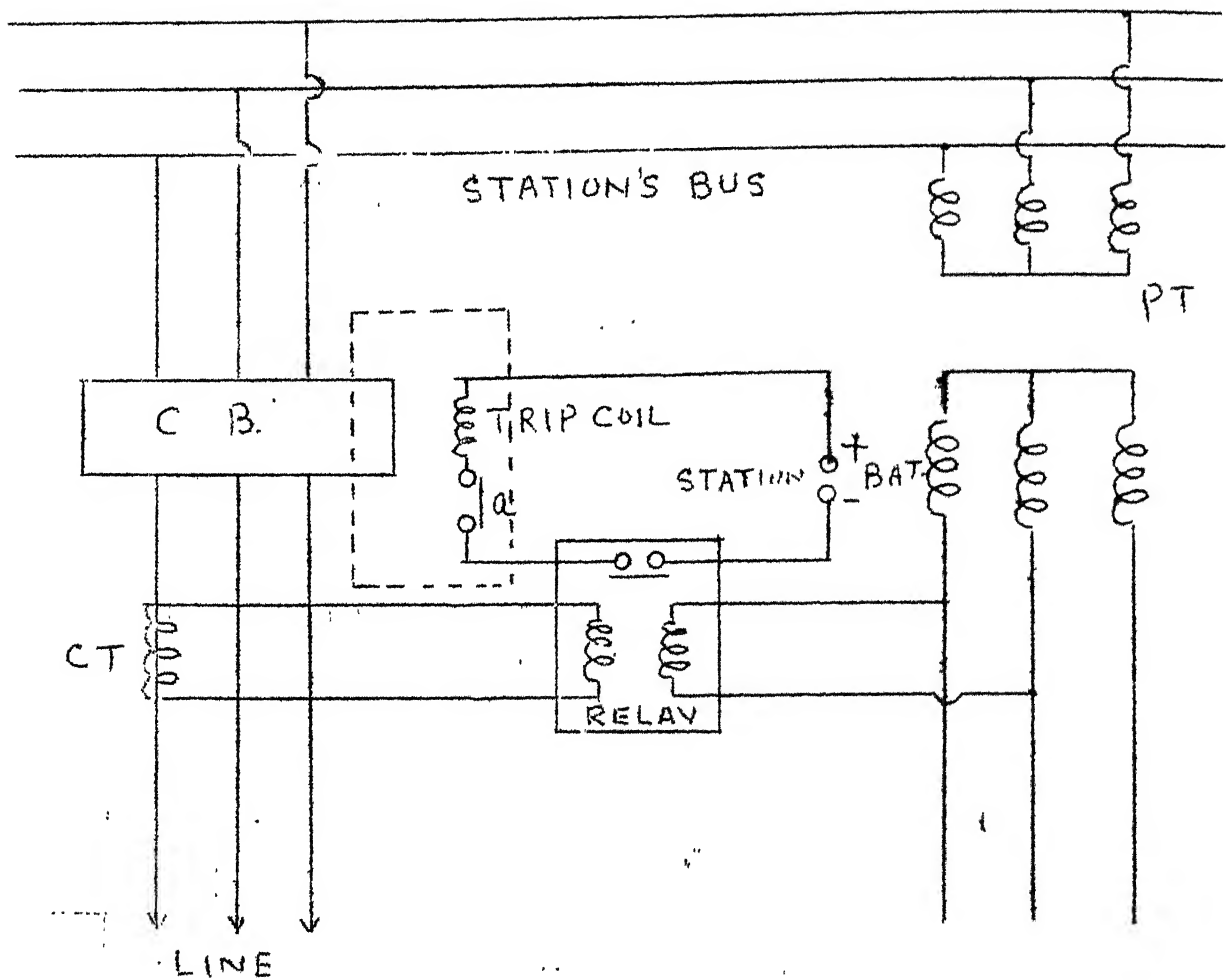


Fig3. RELAY CONNECTIONS

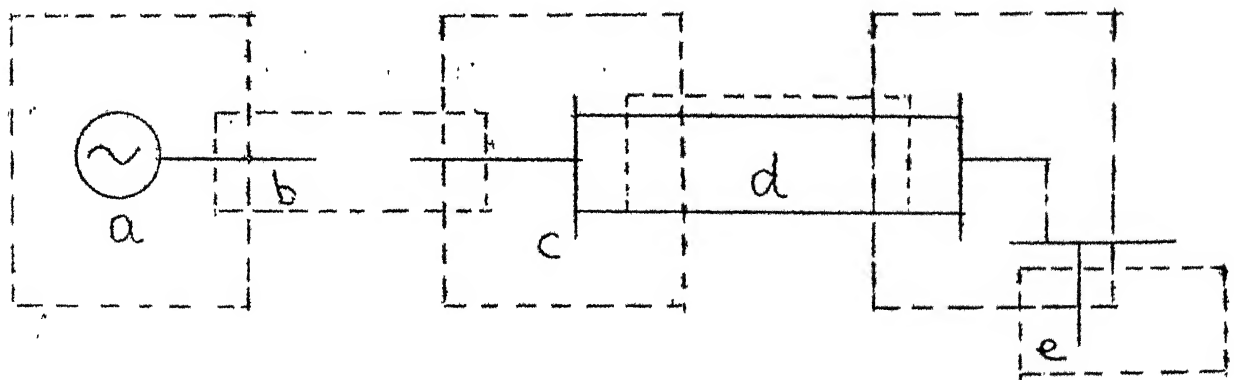
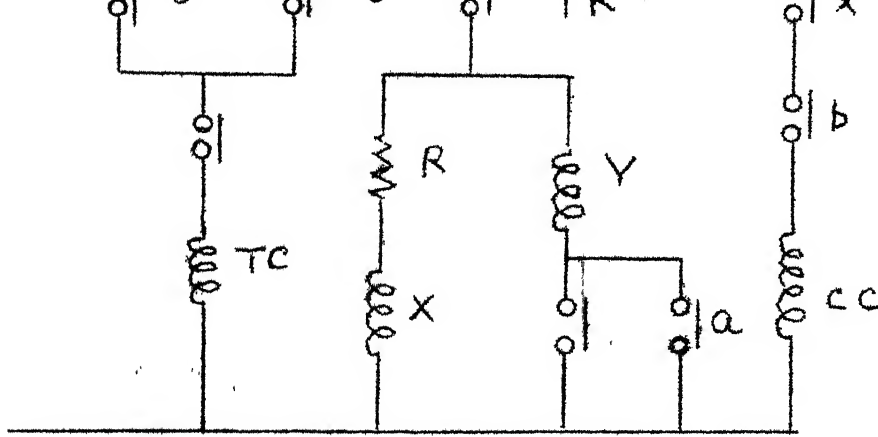


Fig4. PROTECTION ZONES



CC = CLEARING COIL

TC = TRIP COIL

Y = REVERSE RELAY FOR X X = CLOSING CONTACTS

CL = BREAKER AUXILIARY SWITCHES PR = RELAY CONTACTS

C = CLOSING SWITCH MANUAL T = TRIPPING SWITCH MANUAL

Fig. 5. CIRCUIT BREAKER CONTROL

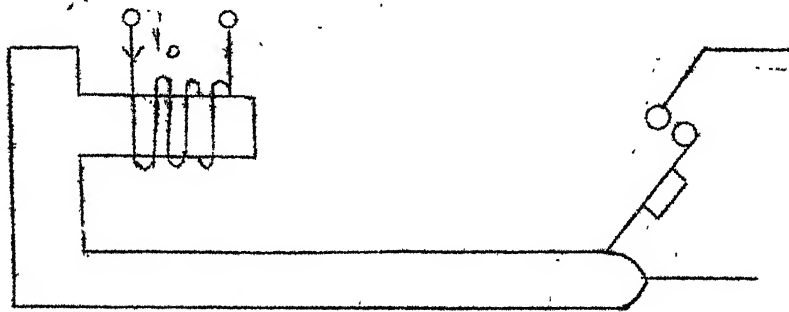


Fig 6(a) ARMATURE ATTRACTED TYPE RELAY

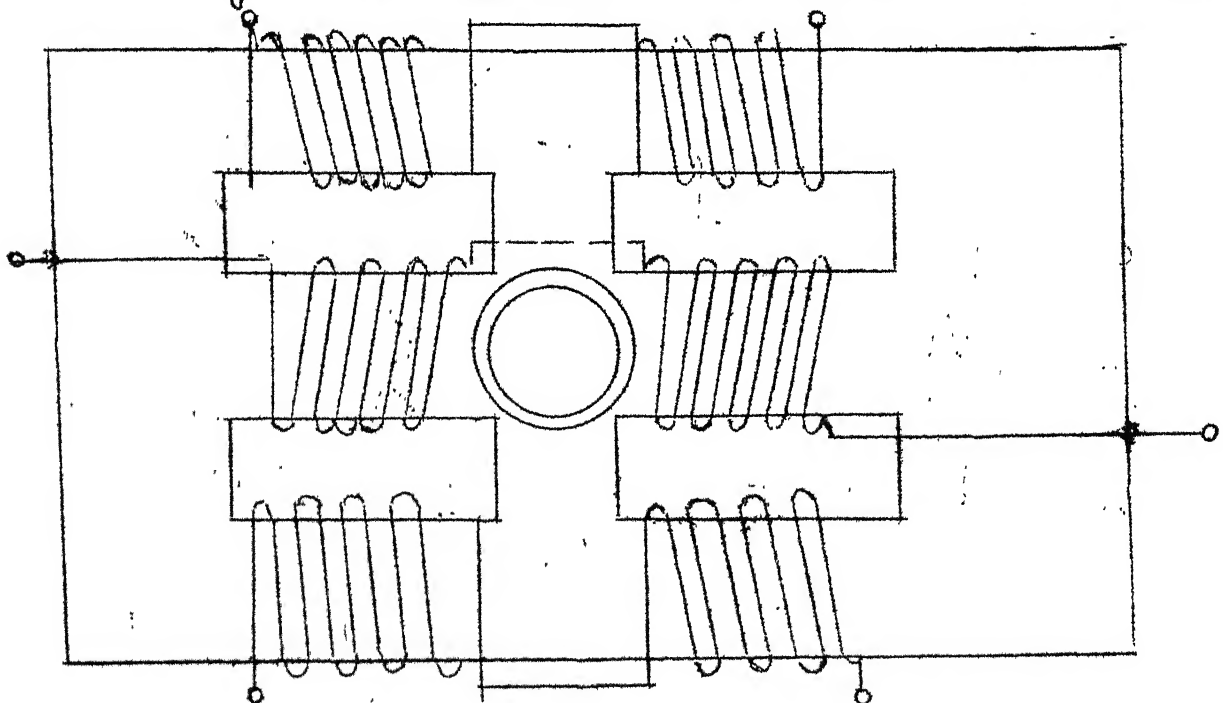


Fig 6(b) INDUCTION CUP TYPE RELAY

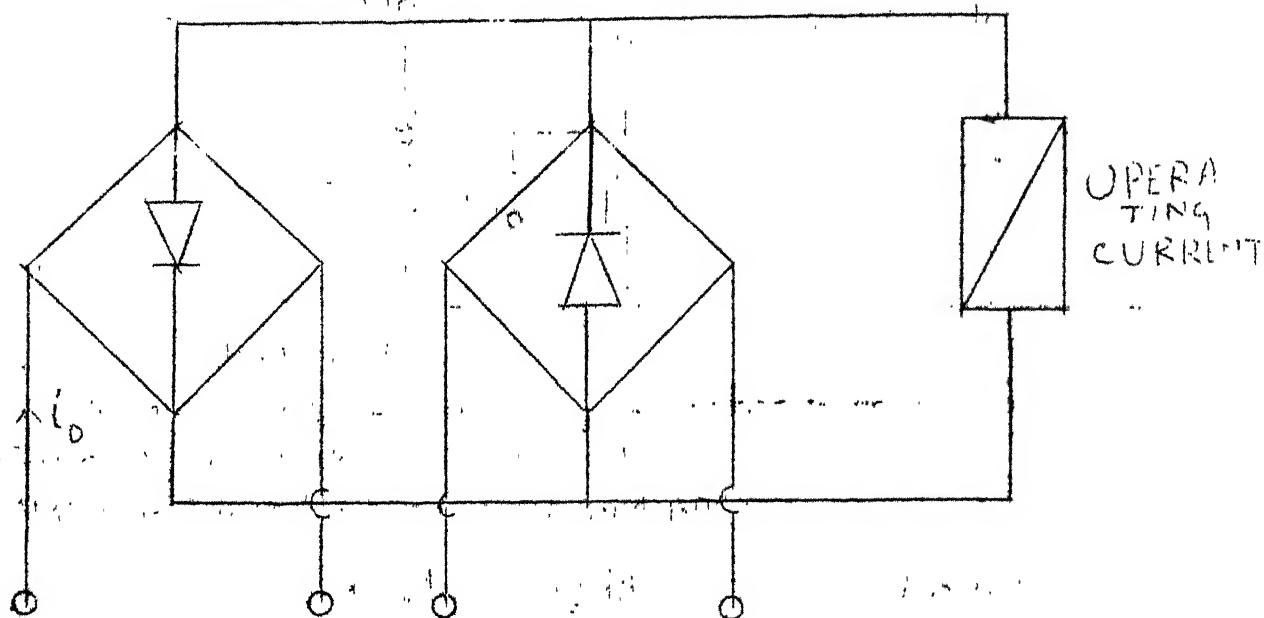


FIG 6(c) RECTIFIER BRIDGE AMPLITUDE COMPARATOR

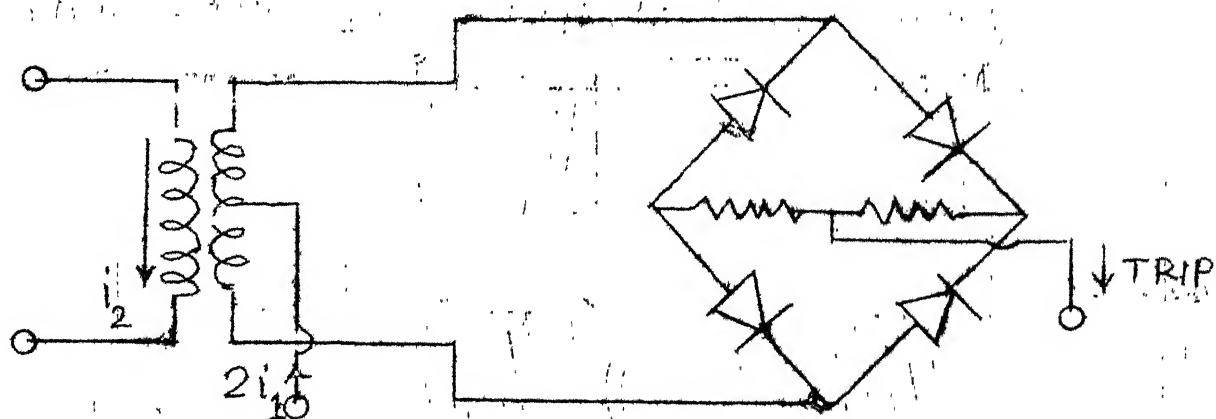


FIG. 6(d) RECTIFIER BRIDGE PHASE COMPARATOR

General Purpose Static Relay using Digital Techniques

A. J. Kellog, Non-member

Dr L. P. Singh, Member

Dr G. K. Dubey, Fellow

To achieve efficiency and economy in transmission, the transmission voltage is being stepped up to 400 kV transmission lines are already in operation in some states, such as UP, Maharashtra and MP, etc. For the protection of such EHV/UHV lines, reliable, fast operating and compact relaying scheme is needed. This paper deals with a new relaying scheme using digital circuits with CMOS logic for the protection of EHV/UHV lines. This relay has been designed, fabricated and successfully tested in the laboratory. This relaying scheme is expected to be better as compared to the existing ones.

NOTATIONS

- f = clock frequency
 f_n = normal operating frequency to give $\pm 90^\circ$ criteria
 f_d = desired frequency to give variable operating criteria
 I_L = system fault current referred to CT secondary
 k = voltage coefficient
 R_a = replica arc resistance (maximum value expected)
 S_1, S_2 = sinusoidally varying signals
 V_L = system fault voltage referred to PT secondary
 Z_L = impedance seen by relay (referred to secondary)
 Z_a = replica impedance
 α = phase angle between these signals
 β = angular criteria
 β_1, β_2 = angular limits of phase comparison
 λ = coincidence angle

INTRODUCTION

Static Distance relays are commonly used for the protection of EHV/UHV transmission lines. Due to

their high speed of operation, accuracy and reliability, practically no maintenance is needed once it is put into service. The relays¹⁻⁴, generally, use analog devices which give delayed operation at threshold condition. The operating time is a function of phase displacement and becomes infinity at the boundary condition. This creates a serious relay coordination problem⁵. This drawback was overcome by Ramanioorty and Lal⁶ by developing a comparator in which the response time was kept constant. The authors used digital techniques and TTL logic circuits. This relay was capable of generating many important characteristics such as ohms, directional, mho, restricted ohm and elliptical characteristics using variable angular criteria for operation. They also obtained quadrilateral characteristic, based upon multi-input coincidence principle but in a different way. The digital relay appeared to be good at first, but detailed study showed the following general drawbacks:

- (i) TTL gates used are sensitive to spurious signals due to low noise immunity, thus the relay could be prone to transients and line disturbances.
- (ii) The basic comparator circuit appears to be more complicated, using more components, hence less reliable, and also uneconomical and slow in operation.
- (iii) The same relay (comparator) may not be used to obtain quadrilateral characteristic.
- (iv) The same comparator cannot function both as cosine comparator and sine comparator.

These drawbacks of existing digital relay can be eliminated by using CMOS logic and simple relay circuit. This paper presents the development of an improved digital relay and techniques for obtaining different threshold characteristics. Efforts have been made

A. J. Kellog, Dr L. P. Singh and Dr G. K. Dubey are with IIT, Kanpur.

This paper was received on January 19, 1981, and was presented and discussed at the Semi-Annual Paper Meeting held at Delhi on August 19, 1982.

nomy and reliability with fast operation is provided so that the same relay could be used as sine comparator and can cater to additional requirements like power swing blocking, etc.

IMPROVED DIGITAL COMPARATOR

The comparator described is an integrating type average type with minimum operating time of 15 m sec under steady state condition and maximum operating time of 25 m sec under dynamic condition. It is free from the dc transient component appearing in the fault current and hence this is bound to give better performance under transient condition also. Power swing blocking can be applied through AND gate A_3 . The novel feature of the comparator is that it can be used as sine and cosine comparator and also as a multi input comparator giving any desired characteristic. Apart from being used as single phase relay with slight modifications, it can be used as a polyphase relay; thus giving additional advantage of economy and ease in relay coordination.

OPERATING PRINCIPLE

The two-input or multi-input phase comparator developed is symmetrical. In general, two-input phase comparator initiates relay tripping when the phase angle α satisfies the condition

$$-\beta_2 \leq \alpha \leq \beta_1 \quad (1)$$

The phase angle α is positive when signal S_1 leads S_2 , and is negative when S_1 lags S_2 . In majority of applications, the angular limit of phase comparison β_1 and β_2 are 90° and such comparators are called as 90° phase comparators or cosine comparator. This gives a directional characteristic, the trip area being on right side for the variable signal S_1 as shown by Fig 1(a). The coincidence of signals S_1 and S_2 ($180 - \alpha$), if more than 90° , initiates relay tripping. The tripping level is almost set to zero, and hence the response time is, more or less, the same up to $\pm 90^\circ$ of phase displacement.

The same tripping characteristics can be obtained by taking signal $-S_1$ and S_2 and measuring the anti-coincidence α' between them. Tripping occurs when,

$$\beta_1' \geq \alpha' \geq \beta_2'$$

If $\beta_1 = 90^\circ$ then $\beta_1' = 270^\circ$; thus $270^\circ \geq \alpha' \geq 90^\circ$.

Hence, the same comparator functions as sine comparator in which tripping occurs when $-S_1$ leads S_2 by more than 90° over a range of 0 to 180° . The waveforms are shown by Figs 1 (b) and (c).

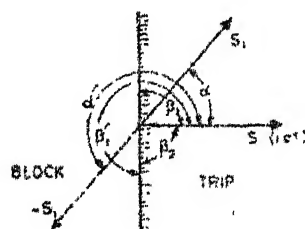


Fig 1 (a) Angular limits and tripping zone

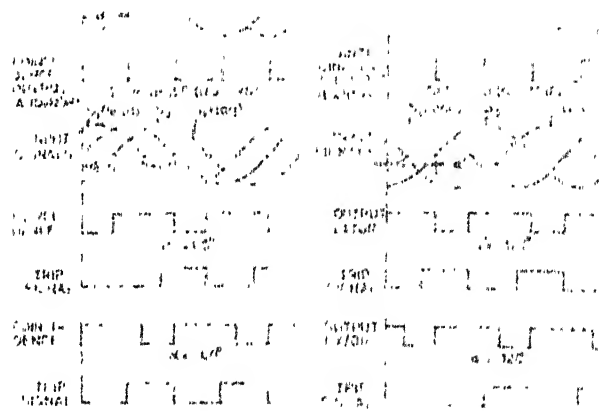


Fig 1 (b) Cosine comparator

Fig 1 (c) Sine comparator

DESCRIPTION OF COMPARATOR

The schematic diagram of digital phase comparator is shown in Fig 2. Flip flop F-1 is used as synchronizer whereas F-2 is in toggle mode. Hence, the first pulse of F-2 operates the monomulti M-1 and second pulse operates M-2 in such a way that, there exists a phase difference of 180° (10 msec duration) between the outputs of M-1 and M-2. Monomulti M-1 and M-2 are used as pulse stretchers whose outputs are AND compounded by gate A-2. Thus, the operation of comparator, due to dc offset current, is prevented during threshold condition. The AND gate A-3 is used to block the operation of relay during power swing. Namely, the control input of A-3 is set at logic (1) but becomes (0) due to the effect of power swing. Hence, the AND gate A-3 does not pass signal and so no output from final AND gate A-2.

The sinusoidal inputs S_1 and S_2 , after being converted to square pulse, are given to Exclusive-OR gate (Ex'OR). Thus, the Q output of F-1 is the measure of anti-coincidence (Ex'OR) whereas Q is the measure of coincidence (AND + NOR). The integrating capacitor is replaced by AND gate A-1 and binary counter BC-1 and BC-2. Two counters are used to measure the sensitivity of the comparator (zero level detection). The clock pulses are chosen that 64 pulses are received in 1 msec duration, at first, to give $\pm 90^\circ$ operating criteria. This gives the normal operating clock frequency f_0 as 128 kHz. The variable angular criteria can be obtained by change of clock frequency. Hence,

$$\frac{f_1}{f_0} = \frac{\lambda_0}{\lambda_1} = \frac{180 - \beta_2}{180 - \beta_1} = \frac{90}{180 - \beta_1}$$

$$f_1 = \frac{f_0}{2 - \frac{\beta_1}{90}} \quad (3)$$

The above relation can be used to find out new clock frequency so as to give different operating criteria β_1 . Hence, the relay can generate restricted directional, restricted ohm, and elliptical characteristics by using two-input comparator only. The same comparator can be used as sine comparator by inverting any one input (preferably S_1) and taking Q output of flip flop F-1. The operation of the relay as cosine comparator is shown in Fig 3.

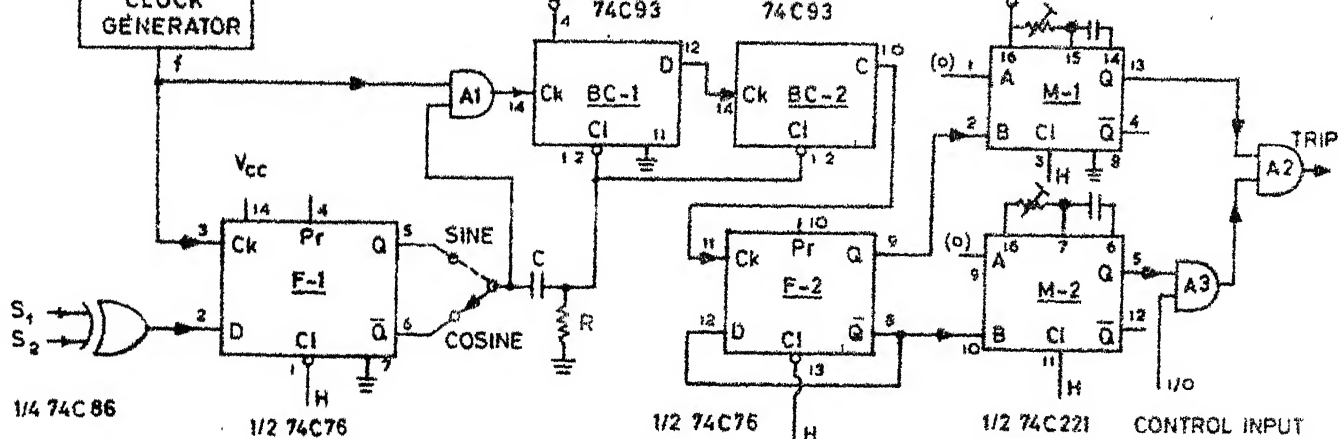
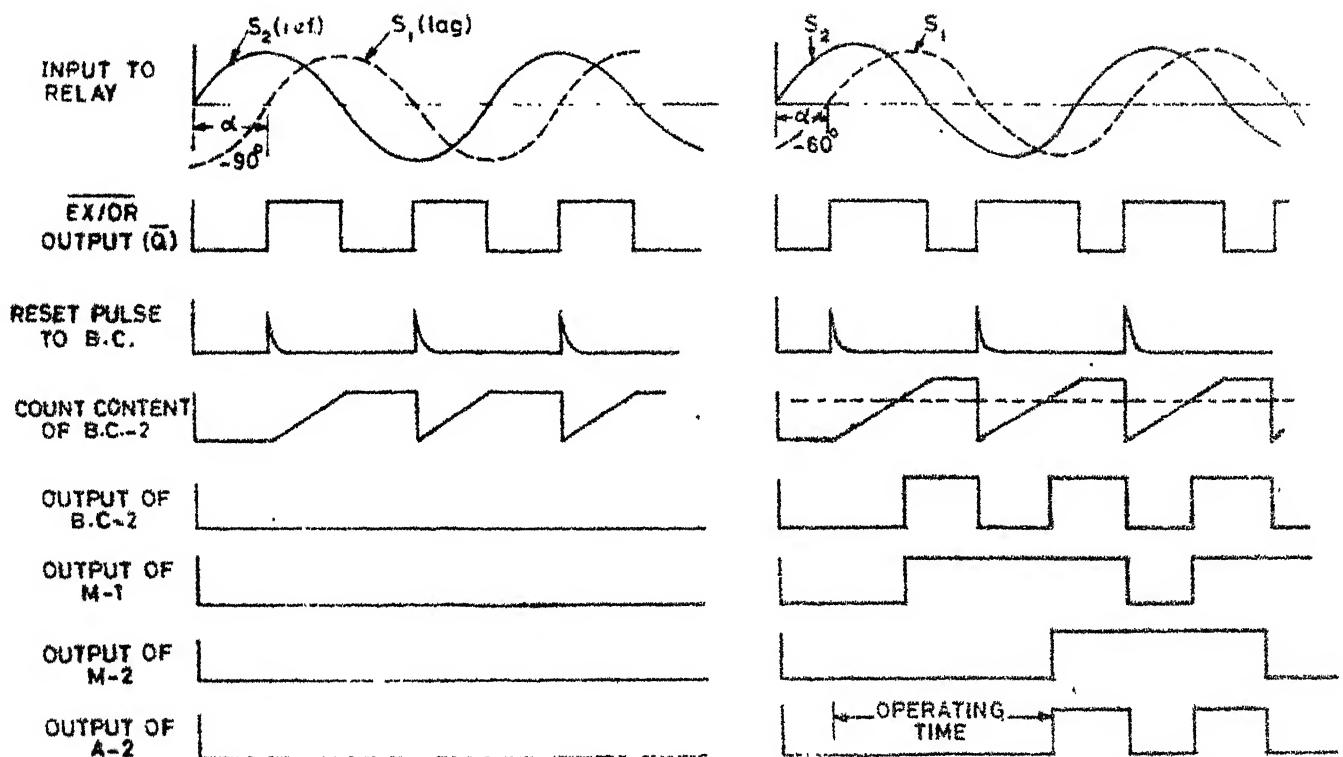


Fig 2 Schematic diagram of comparator



(a) Coincidence = Anticoincidence (Threshold condition)

(b) Coincidence > Anticoincidence (Operating condition)

Fig 3 Operation of comparator

APPLICATIONS OF COMPARATOR

The comparator can generate many important characteristics by giving suitable signals through measuring circuit. Transactors are used to simulate the line impedance. The following arrangement (Fig 4) is used to obtain different signals required to produce the desired characteristics.

RESTRICTED DIRECTIONAL RELAY

The inputs to the relay to obtain directional characteristic are

$$S_1 = V \text{ and } S_2 = IZ_R$$

This gives a straight line AOB, passing through origin O, as relay characteristic (Fig 5) with normal clock frequency f_0 and operating criteria of $\pm 90^\circ$.

Restricted directional characteristic can be obtained by same signals, by change of clock frequency from f_0 to f_1 and f_2 in such a way that:

$$f_1 = \frac{f_0}{2 - \beta_1} \text{ and } f_2 = \frac{f_0}{2 - \beta_2} \quad (4)$$

$$\beta_1 = 90 \left(2 - \frac{f_0}{f_1} \right) \text{ and } \beta_2 = 90 \left(2 - \frac{f_0}{f_2} \right) \quad (5)$$

Hence, any operating criteria and threshold characteristics can be obtained by change of clock frequency. The limit of change of clock frequency is from f_0 to $\frac{f_0}{2}$, which is easily obtained by frequency dividers or variable potentiometer. The restricted directional characteristics are shown in Fig 5.

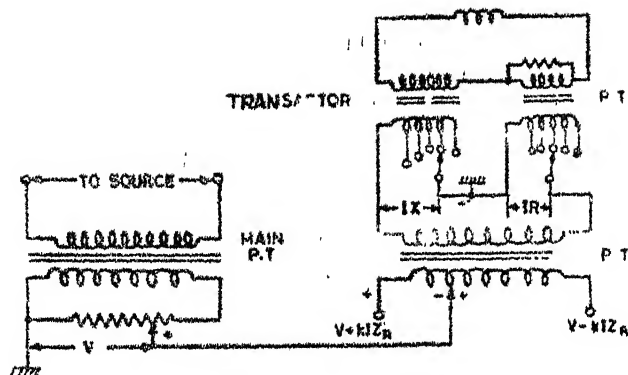


Fig 4 Measuring circuit

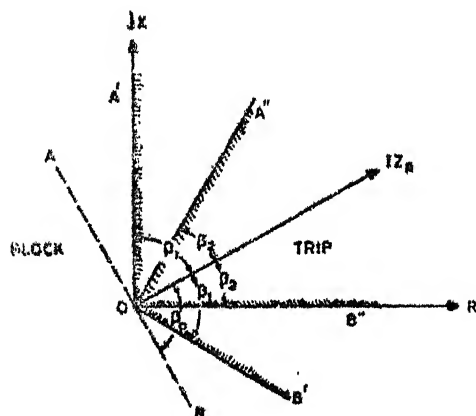


Fig 5 Restricted directional relay

If the inputs to relay are $-S_1$ and S_2 the relay functions as sine comparator with same operating principle.

RESTRICTED OHMS RELAY

The inputs to the relay, to obtain variety of characteristics, such as ohms, reactance and restricted ohms or angle impedance, are

$$S_1 = IZ_R - V \text{ and } S_2 = IZ_R$$

Characteristic APB is obtained if angular operating criteria β_0 is $\pm 90^\circ$. If the operating criteria is β_2 and β_1 , the characteristics $A'PB'$ and $A''PB''$ results. If the signal IZ_R has a phase angle of 90° with the horizontal axis, the resulting characteristics will be a reactance. Any type of characteristic can be produced by varying clock frequency in such a way that

$$\beta_1 = 90 \left(2 - \frac{f_0}{f_1} \right),$$

$$\beta_2 = 90 \left(2 - \frac{f_0}{f_2} \right)$$

$$\beta_1 < \beta_2 < \beta_0 \leq 90^\circ$$

For sine comparator, the inputs to relay are

$$S_1 = V - IZ_R \text{ and } S_2 = IZ_R$$

and the above theory holds good for this case also. The characteristics are shown by Fig 6.

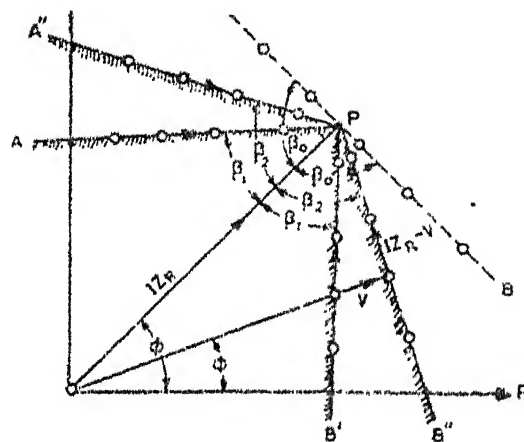


Fig 6 Restricted ohms relay

OFFSET ELLIPTICAL MHO RELAY

It is the starting element for a 3-step distance relay and avoids maloperation due to power swing. The inputs to relay are

$$S_1 = IZ_R - V$$

$$S_2 = k IZ_R + V, k < 1$$

This can give variety of characteristics by varying the operating criteria. If the operating criteria is β_0 ($\pm 90^\circ$), the resulting characteristic is offset mho as shown by curve (1) of Fig 7.

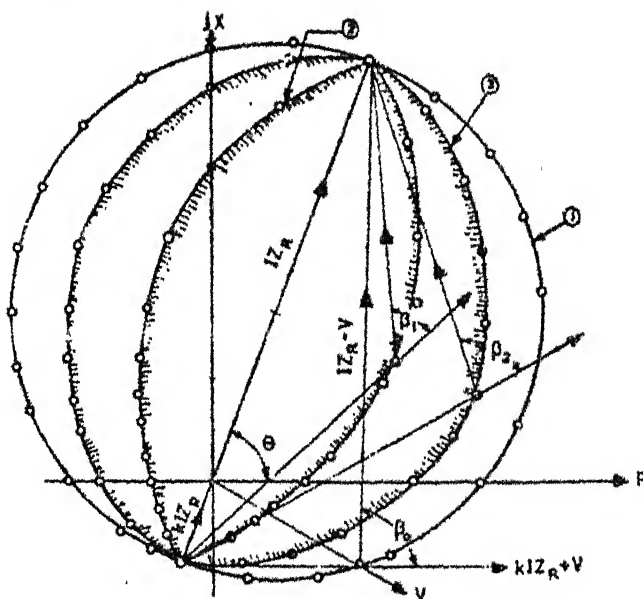


Fig 7 Offset elliptical relay

The offset elliptical characteristic can be obtained by varying clock frequency from f_0 to f_1 and f_2 to produce curve no (2) and (3) of Fig 7, with operating criteria as β_1 and β_2 . The relation

$$\beta_1 = 90 \left(2 - \frac{f_0}{f_1} \right),$$

$$\beta_2 = 90 \left(2 - \frac{f_0}{f_2} \right)$$

$$\beta_1 < \beta_2 < \beta_0 \leq 90^\circ$$

also valid for this case.

$S_1 = V - I Z_R$ and $S_2 = V + k I Z_R, k < 1$
and above theory holds good for this case also.

QUADRILATERAL RELAY USING TWO COMPARATORS

Fig 8 (a) shows the basic scheme for obtaining quadrilateral characteristic. Two comparators A and B are AND compounded to obtain the desired characteristic AOBP as shown by Fig 8 (b). The inputs to comparator A are,

$$S_1 = I Z_R - V \text{ and } S_2 = I Z_R$$

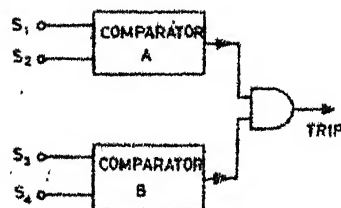


Fig 8 (a) Multi-comparator relay

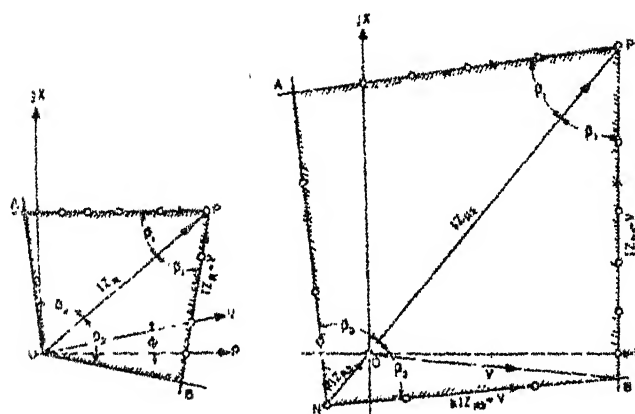


Fig 8 (b) Normal characteristics Fig 8 (c) Starting characteristics

which gives restricted ohms characteristic APB with β_1 as operating criteria. The input to comparator B are

$$S_3 = I Z_R \text{ and } S_4 = V$$

which gives restricted directional characteristic AOB with operating criteria of β_2 . The outputs of these comparators are, then, AND compounded to give final characteristic AOBP. By choosing appropriate value of Z_R and β_1 and β_2 , better threshold characteristic with any shape can be obtained.

The inputs required for sine comparator are

$$S_1 = V - I Z_R; S_2 = I Z_R; S_3 = I Z_R; S_4 = -V.$$

which will give same characteristics as discussed above. It can be seen that $I Z_R$ is common to both the comparators and thus, only three inputs are needed to produce quadrilateral characteristic.

OFFSET QUADRILATERAL RELAY USING TWO COMPARATORS

Offset quadrilateral characteristic is required for starting element of 3-zone distance relay which can be easily obtained by modifying one of the input of comparator B, hence, the input to comparator A are

which gives restricted ohms characteristic APB with β_1 as operating criteria. The range of this characteristic can be changed by varying the value of Z_R so that it lies in 3rd zone of the relay. The input to comparator B are

$$S_3 = I Z_R \text{ and } S_4 = k I Z_R + V, \text{ that is, } I Z_R' + V$$

which gives restricted directional characteristic ANB with β_2 as operating criteria. The output of these comparators are then, AND compounded to find characteristic ANBP as shown by Fig 8 (c). Any desired characteristic can be obtained by changing Z_R and β_1 and β_2 .

The sine comparator to produce the same characteristic with same theory of operation will have the inputs as

$$S_1 = V - I Z_R; S_2 = I Z_R; S_3 = I Z_R$$

$$S_4 = -(k I Z_R + V) = -(I Z_R' + V)$$

where $Z_R' = k Z_R$ and $k < 1$. $I Z_R$ is common to both the comparators, hence, only three inputs are needed to produce quadrilateral characteristic as with cosine comparator.

QUADRILATERAL CHARACTERISTICS WITH MULTI INPUT COMPARATOR

A two input comparator, using Ex/OR gate, can be modified to take any number of inputs, by using multi input Ex/OR gate [Fig 9(a-d)]. Four-input comparator is optimum which can give any type of quadrilateral characteristics. As multi-input Ex/OR gate is not available, it is substituted with AND + NOR logic and rest of the circuit remains unaltered. The inputs which are not used are, tied with available signals and the function of the comparator remains the same. The basic arrangement for multi input comparator is shown in Fig 10 (a).

The input signals needed for quadrilateral characteristic are (used only as a directional element)

$$S_1 = I Z_R - V; S_2 = I Z_R; S_3 = V;$$

$$S_4 = I$$

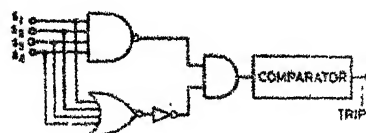


Fig 9 (a) Multi-input relay

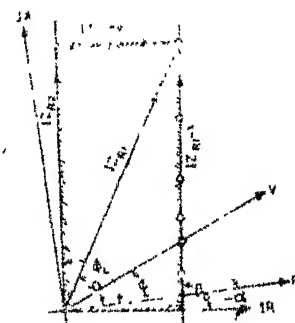


Fig 9 (b) Normal characteristic

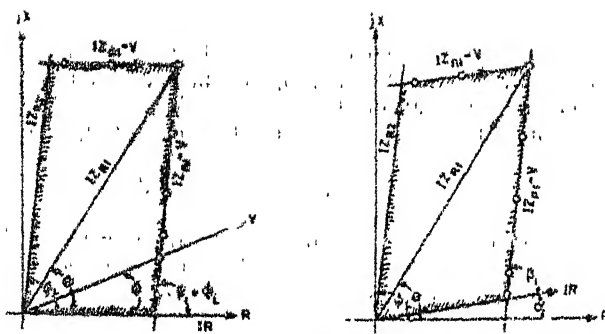


Fig 9 (c) Modified characteristics Fig 9 (d) Special characteristics

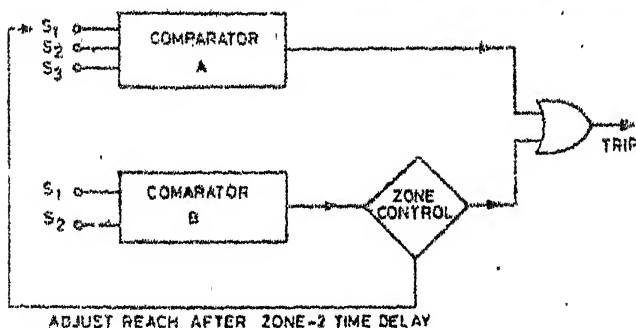


Fig 10 (a) Modified mho relay

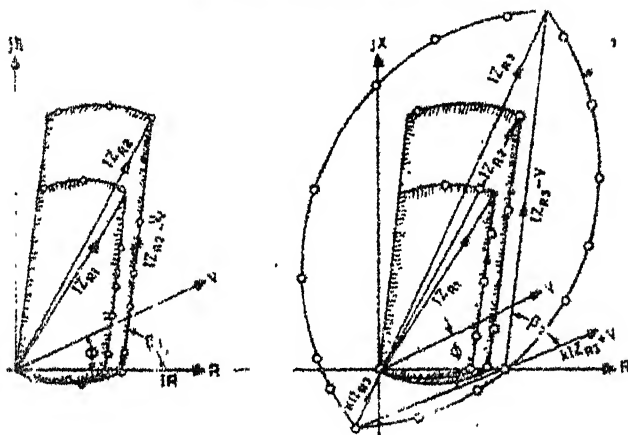


Fig 10 (b) Characteristics of comparator A Fig 10 (c) Final characteristics

Z_{R2} being replica of line impedance used only as a directional element. If $\alpha = 90 - \Phi_L$ and operating criteria β_2 is $\pm 90^\circ$, the resulting characteristic is as shown in Fig 10(b).

This characteristic can be made more compatible if the input signals to relay are

$$S_1 = IZ_{R1} - V; S_2 = IR \angle \alpha; S_3 = V; S_4 = IZ_{R2}$$

Here, angle α is set equal to zero by a pot only and the operating criteria $\beta_1 = \Phi_L$. This change yields the characteristic as shown by Fig 10 (c).

The resultant characteristic can be further modified if the inputs to comparator are

$$S_1 = IZ_{R1} - V; S_2 = IR \angle \alpha; S_3 = V; S_4 = IZ_{R2}$$

The operating criteria $\beta_1 < \Phi_L$ so that $\alpha = \Phi_L - \beta_1$ and the resulting characteristic is as shown by Fig 10 (d). This characteristic may be useful for bus bar protection, where arc resistance is generally absent. By proper

MODIFIED MHO RELAY

The classical mho characteristic can be modified and the effect of power swing can be completely eliminated by using blinders and adopting suitable operating criteria β_1 . Thus, the inputs to the relay are

$$S_1 = IZ_{R1} - V; S_2 = IR; S_3 = V; \text{ and } \beta_1 < 90^\circ$$

The modified impedance Z_{R1} can be changed to Z_{R2} after the zone-2 time delay, and the operating criteria β_1 are kept equal to Φ_L for shaping the characteristics as shown by Fig 10 (b). The resulting characteristics resembles quadrilateral characteristics.

A separate comparator could be used for 3rd zone protection in a normal way, but having operating criteria as β_2 which should be less than β_1 . If the inputs to this comparator are

$$S_5 = IZ_{R2} - V; S_6 = kIZ_{R2} + V; \text{ and } \beta_2 < \beta_1 < 90^\circ$$

then the resulting characteristic is as shown by Fig 10(c). The shape of the characteristic 3 is elliptical which is very narrow and hence immune to tripping due to power swing. This could be an ideal starting characteristic for carrier frequency to clear end zone fault quickly by simultaneous tripping.

The block diagram of modified mho relay is shown in Fig 10 (a).

RELAY TESTING AND PERFORMANCE

The digital relay was tested statically due to non-availability of Dynamic Test Bench. The different characteristics were plotted as shown and found to be very close to the theoretical characteristics. Hence, smooth curves are drawn passing through the test points.

The directional property of quadrilateral and modified mho relay was found by inverting signal IZ_{R1} , which made the relay inoperative in reverse direction. The relay remains operative down to very low input voltage; but does not operate when the voltage becomes zero for two input comparator. However, for multi input comparator, the relay remains operative even if the voltage becomes zero.

CONCLUSION

The paper describes the theory, principle of operation and applications of the improved digital phase comparator which could be used for variety of applications, specifically, in two-input mode, giving identical characteristics as obtained by cosine comparator. The resulting relay is fast in operation and at the same time no time coordination problem arises as the maximum operating time is of the order of 25 m sec at threshold condition. The relay construction is simple, using IC's and logic gates, which makes relay economical and reliable. The same relay can produce any desired characteristic, simply by change of input signals and operating criteria. This relay could be used as polyphase relay with slight modifications, giving economy and also ease in relay coordination.

REFERENCES

1. A J Kellogg, Dr L P Singh and Dr G K Dubey. 'Protection of EHV Transmission Lines by using Static Relays'. *Conference on Power System Protection, The Institution of Engineers (India), Madras, Paper B 5, April 1980.*
2. Hans Hoel, W D Humpage and C P Chapman. 'Composite Polar Characteristic in Multi-zonal System of Phase Comparison Distance Protection', *Proceedings of the IEE*, vol 113, no 10, October 1966 p 1631.
3. K Parthasarathy. 'New Static Three-Step Distance Relay', *Proceedings of the IEE*, vol 113, no 1, 1966, p 633.
4. L Jackson, J B Patrickson and L M Wedepobel. 'Distance Protection—Optimum Dynamic Design of Static Relay Comparators', *Proceedings of the IEE*, vol 115, no 2, February 1968, p 289.
5. A T John. 'Generalized Phase Comparison Technique for Distance Protection—Theory and Operation of Multi-Input Device', *Proceedings of the IEE*, vol 119, no 11, 1972, p 1595.
6. M Ramamoorthy and S N Lal. 'A Versatile Phase Comparator Relay using Digital Circuits', *Journal of the Institution of Engineers (India)*, vol 59, pt EL 6, June 1979, p 309.

Digital Travelling-Wave Protection of Transmission Lines

K. V. DESIKACHAR and L. P. SINGH

Department of Electrical Engineering, Indian Institute of Technology Kanpur 208016 (India)

(Received July 15, 1983)

SUMMARY

Almost all the algorithms proposed so far for the digital protection of transmission lines are of the distance type and involve the extraction of the fundamental components from the complex post-fault waveforms through the use of filters, whereas those based on the travelling-wave theory need only a short data window and no filtering. This paper presents two new algorithms of the latter type along with the results of digital simulation tests which confirm their viability.

1. INTRODUCTION

Because of recent advances in the field of minicomputers and microprocessors, digital protection of transmission lines is going to become a reality in the near future. Digital protection of transmission lines provides improved performance in terms of speed of operation as well as flexibility of obtaining, with ease, any desired composite threshold characteristics. With suitable software logic, the protective schemes can be made self-checking and, with modifications only to the software, any desired alteration of the threshold characteristics can be accomplished. A considerable amount of work in the field of digital protection of transmission lines has been reported since the late 1960s. This has been confined mainly to different types of algorithms for computing the impedance between the relaying and fault points as accurately as is tenable with high-speed requirements. The algorithms proposed up till now can be broadly classified into two groups: (1) distance relay algorithms and (2) travelling-wave relay algorithms.

The post-fault waveforms in the first one or two cycles after the occurrence of a fault comprise a power frequency fundamental, an exponentially decaying DC component and high-frequency transients. They also contain subtransient and transient power frequency components if the line fault is near a generating source. The first category of algorithms involve computation of the impedance between the relaying and fault points from the fundamental components of the voltage and current obtained by suppressing other components through filters and line modelling, whilst the second category utilizes the complex waveforms as they are for making relaying decisions. In this paper, a brief and critical overview of the distance-relay algorithms is given first in order to bring into focus their inherent limitations. Next, two new travelling-wave relay algorithms, whose viability has been tested on a digital computer with the fault data generated by the digital simulation of a sample power system, are presented.

2. OVERVIEW OF THE DISTANCE RELAY ALGORITHMS

These algorithms aim at extracting the fundamental power frequency components of voltages and currents from the complex post-fault waveforms and then determining the impedance between the relaying and fault points. Basically, there are four digital methods of determining the impedance from the fundamental components. In the first method, the magnitude of the impedance is calculated as the ratio of the peak voltage to the peak current and its argument as the difference between the phase angles of the voltage and current. The peak values of the

voltage and current and the phase angle between them can be determined either from samples of the fundamental components extracted from the ensemble of samples collected over one full power frequency period [1], or they can be predicted from a much smaller number of samples of the fundamental components by means of the values of the samples and their derivatives [2], or of their first and second derivatives [3], or of the samples and the sampling interval [4]. In the second method, the fundamental components of voltage and current are determined in the phasor form, from which the real and imaginary parts R and X of the pseudo-impedance seen by the relay can easily be evaluated [5-13]. In the third method, the line is modelled by differential equations, the numerical solution of which yields the values of R and X [14-19]. The advantage of this method is that it is necessary to filter out only those components not covered by the line modelling. For example, if the line is modelled by a series RL circuit, then there is no need to filter out the DC offset component. Also, this method allows one to deal with cases like series-compensated lines [16]. In the fourth method the impedance is determined directly in phasor form from the ratio of the frequency-domain values of the fundamental components of the voltage and current by the finite transform method [20]. All the methods which require samples over one full fundamental period for the computation of the pseudo-impedance offer no economic advantage in comparison with solid-state relays. The unwanted components of the post-fault waveforms are suppressed by various types of filters in order to obtain the fundamental components. Both analog and digital filters which have been proposed and/or used for this purpose are described in the following sections.

2.1. Analog filters

The mimic impedance used in the current transformer secondary plays the role of an analog filter inasmuch as it filters out the DC offset in the current signal. Complete suppression of the DC offset is, however, impossible since exact matching of the X/R ratios of the primary and secondary circuits is difficult owing to the fact that the X/R ratio of the

primary circuit up to the point of fault is a variable. Some algorithms [2, 3, 8] assumed employment of this filter. RC low-pass filters with a suitable cutoff frequency have been used to filter out the high-frequency components in the implementation of some of the algorithms [3, 6]. The fact that a single analog filter cannot suppress all the unwanted components and that these are slower than the digital filters led to the development and preferential use of the digital filters.

2.2. Digital filters

The various types of digital filters which have been proposed and tested are described below.

Notch filters

Two orthogonal notch filters with sine characteristics have been used to extract the fundamental components after elimination of the high-frequency components by an analog low-pass filter [2, 21].

Selected harmonic filter [17]

While the differential equations of the line are being solved by numerical integration, the integration is carried out over a certain number of overlapping subintervals, with required end points. This results in the elimination of certain harmonics and their multiples.

Least-square-error filters

In one type, the deficiency in modelling the line by differential equations is treated as an error and solution of the model parameters is obtained subject to minimisation of the mean of the squares of this error over the data window [15, 19]. In another type, a polynomial fit (for example, a straight-line fit over three points, a quadratic fit over five points or a cubic fit over seven points) is determined subject to the least-square-error criterion [2, 8]. By differentiating this polynomial, the necessary time derivatives can be found. In yet another type, a waveform containing a decaying DC offset, the fundamental and a desired number of harmonic components are assumed and the least-square-error criterion is applied to determine the unknown parameters of the fundamental component [10, 22, 23]. All these filters are rather slow and their accuracy depends on the data window

as well as the number of samples per cycle [24].

Orthogonal transform filters

Of these, the Fourier transform filter is the most widely used; it utilises sine and cosine functions as an orthogonal set [1, 5, 7-9, 12, 25, 26]. This filter suppresses all the unwanted components and therefore offers the best accuracy, but it requires a data window of one full fundamental period. However, filters employing data windows of half a cycle and less than half a cycle with tolerable errors have been proposed [8, 12]. Filters using odd and even square waves [7], Walsh functions [13], sample values and their derivatives [2], and the first and second derivatives of the samples [3] as orthogonal functions have also been proposed.

Finite transform filter [20]

The fundamental frequency impedance is determined over a finite data window by carrying out the filtering process in the frequency domain through the use of the finite transform method.

Kalman filters [11]

The non-fundamental components in the voltage and current waveforms are considered as noise signals. The noise signal in the voltage waveform is considered as a white noise sequence with decreasing variance, and that in the current waveform as an exponential process plus a white noise sequence with decreasing variance. Then, a two-state Kalman filter is used to extract the fundamental voltage phasor, and a three-state Kalman filter to extract the fundamental current phasor. The error in this filtering process has been reported to be less than 1% after half a cycle.

3. TRAVELLING-WAVE RELAY ALGORITHMS

This group of algorithms uses the complex post-fault waveforms as they are for making relaying decisions by means of travelling-wave techniques. Two distinct advantages are offered which lead to high-speed operation. First, there is no need for either analog or digital filters and consequently the time delays associated with them are eliminated.

Second, a very short data window can be employed. As a matter of fact, the sampling interval should be small enough to avoid aliasing errors. The sampling frequency should be at least twice as great as the cutoff frequency of the transducers in order to avoid aliasing errors. Thus with a current voltage transformer of cutoff frequency 2.5 kHz, the sampling frequency should be at least 5 kHz and the sampling interval 200 μ s. It is reported [27] that such a sampling interval may not be adequate to carry out the necessary digital implementation. However, it is believed by the authors that with the high-speed analog-to-digital conversion equipment and digital computers available at present, this sampling interval would be sufficient to derive and store the six digital samples of the phase voltages and line currents and to carry out the simple fault-detection algorithm described in this paper. Very few algorithms in this category have been proposed so far [28] most probably owing to the fact that the travelling-wave relaying concept is relatively new.

Two new algorithms in this category are presented in this paper. One is based on amplitude comparison of the relay inputs and the other on a fault-locating relay [29, 30]. Each algorithm can be split into two parts, fault detection and relaying. The fault detection algorithm is common to both and therefore is described first.

4. FAULT-DETECTION ALGORITHM

This algorithm is similar to that proposed by Morrison and Morrison [31]. One counter is provided for each phase voltage. The difference between the currently sampled instantaneous voltage of each phase and the corresponding one in the previous cycle (which has been stored) is computed and stored. These differences, up to one cycle after the occurrence of a fault, are the fault generated components and are used in the relaying algorithms described later. If for any phase this difference is greater than the previously stored value, then the counter of that phase is incremented by 1. Otherwise, the counter is decremented by 1, if it is not already zero. The latter ensures that no maloperation takes place due to spurious spikes. When the

counter of any phase reaches a preset value, a fault is assumed to have occurred. Then, the sampling is suspended, the transmitter is switched off from other jobs and the relaying program is executed. The setting of each phase counter is taken to be 5 for the amplitude-comparison relay and 10 for the fault-locating relay. A higher setting for the latter is necessary to collect an adequate number of samples of fault-generated voltage components in order to execute the algorithm. The setting for the difference of voltages one cycle apart is chosen as 0.05 p.u. for both the relays and is based on the assumption that load fluctuations do not lead to voltage variations of more than 0.05 p.u. The actual value for this setting can be determined by conducting digital fault-simulation tests on the power system. This is very simple and can easily be carried out within an intersampling period.

5. AMPLITUDE-COMPARISON RELAYING SCHEME

5.1. Principle of operation

After the occurrence of a fault, the voltages and currents at the relaying point, as at any other point in the power system, can be regarded as the sum of the pre-fault and fault-generated components [30, 32]. The fault-generated components during the first whole cycle after the fault occurrence are used for relaying and are computed by the cycle-to-cycle comparison method proposed by Mann and Morrison [31]. Although the fault data for testing algorithms are generated considering frequency dependency of the line parameters and without the assumption that the line is transposed, the inputs to the relays are computed on the assumption of a perfectly transposed line. To cater for all types of faults, three relays, one for each mode of propagation, are used. The inputs to the relays are as follows:

Mode 1

$$\begin{aligned} S_1^{(1)} &= v_f^{(1)} - R_{\text{set}}^{(1)} i_f^{(1)} \\ S_2^{(1)} &= v_f^{(1)} + R_{\text{set}}^{(1)} i_f^{(1)} \end{aligned} \quad (1a)$$

Mode 2

$$\begin{aligned} S_1^{(2)} &= v_f^{(2)} - R_{\text{set}}^{(2)} i_f^{(2)} \\ S_2^{(2)} &= v_f^{(2)} + R_{\text{set}}^{(2)} i_f^{(2)} \end{aligned} \quad (1b)$$

Mode 3

$$\begin{aligned} S_1^{(3)} &= v_f^{(3)} - R_{\text{set}}^{(3)} i_f^{(3)} \\ S_2^{(3)} &= v_f^{(3)} + R_{\text{set}}^{(3)} i_f^{(3)} \end{aligned} \quad (1c)$$

where $v_f^{(1)}$, $v_f^{(2)}$ and $v_f^{(3)}$ are the modal components of the fault-generated components of the phase voltages at the relaying point; $i_f^{(1)}$, $i_f^{(2)}$ and $i_f^{(3)}$ are the modal components of the fault-generated components of the line currents at the relaying point; $R_{\text{set}}^{(1)}$, $R_{\text{set}}^{(2)}$ and $R_{\text{set}}^{(3)}$ are the setting resistances equal, respectively, to what would have been the surge impedances of the three modes had the line been lossless and perfectly transposed. That is,

$$R_{\text{set}}^{(1)} = [(L_s + 2L_m)/(C_s - 2C_m)]^{1/2} \quad (2a)$$

and

$$R_{\text{set}}^{(2)} = R_{\text{set}}^{(3)} = [(L_s - L_m)/(C_s + C_m)]^{1/2} \quad (2b)$$

The propagation of travelling waves of voltages of each mode, upon the occurrence of a fault, is depicted in Fig. 1 for a fault ahead of the relaying point, and in Fig. 2 for a fault behind the relaying point. It is well known that the current and voltage of each mode have the following relationship: for backward waves,

$$v = -Z_0 i \quad (3a)$$

for forward waves,

$$v = +Z_0 i \quad (3b)$$

Accordingly, the relay signals for each mode for a few microseconds after the waves have reached the relaying point are given for an internal fault by

$$S_1 = -K_f(1 + R_{\text{set}}/Z_0)v_{ff} \quad (4a)$$

and

$$S_2 = -\rho_s K_f(1 + R_{\text{set}}/Z_0)v_{ff} \quad (4b)$$

where K_f is a factor which takes into account the effect of the fault resistance, Z_0 is the surge impedance of the mode concerned, v_{ff} is the corresponding modal component of the fault-generated components of voltages at the fault point, and ρ_s is the reflection coefficient at the relaying end of the line. Since $|\rho_s|$ is always less than unity under actual conditions, except when the relaying end is on open circuit, it can be seen that $|S_1| > |S_2|$. And, for a fault behind, the relay signals

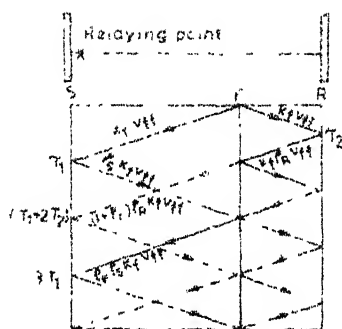


Fig. 1 Lattice diagram for a fault ahead of the relaying point.

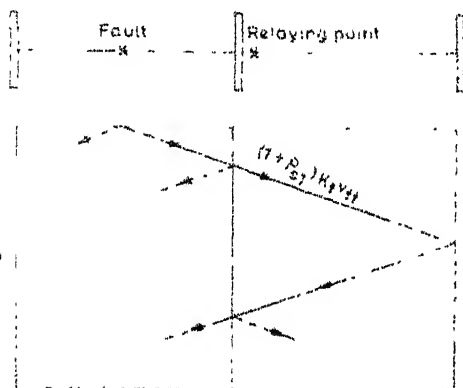


Fig. 2 Lattice diagram for a fault behind the relaying point.

for a few microseconds after the waves have reached the relaying point are given for each mode by

$$S_1 = 0 \quad (5a)$$

and

$$S_2 = -(1 + \rho_{s1})K_f(1 + R_{set}/Z_0)V_{ff} \quad (5b)$$

where ρ_{s1} is the reflection coefficient of the adjoining line. Therefore, for an external fault, $|S_1| < |S_2|$.

However, the modal components of voltages and currents are computed on the assumption of a perfectly transposed line and therefore the relations given in eqns. (3) will not be satisfied exactly. Accordingly, the conditions $|S_1| - |S_2| > 0.05$ p.u. and $|S_1| - |S_2| < -0.05$ p.u. are used to indicate, respectively, a fault ahead of the relaying point and a fault behind it. If, at both ends of the line, the fault is found to be ahead of the corresponding relaying points, then the fault is internal; otherwise, it is external. In the event of an internal fault, confirmed by an exchange of information between the ends of

the line through a carrier channel, the circuit breakers at both ends are tripped. Up on the occurrence of a fault, whether external or internal, the transmitter is switched off from other uses, if any. When the fault is ahead, the transmitter is started and a carrier is sent to the other end. Receipt of carrier from the other end and indication of a fault ahead of the local end indicate an internal fault. When the fault is behind, the transmitter is blocked from being started subsequently by the backward waves coming from the fault point and the remote end after reflection.

5.2. Relaying algorithm

The modal components of the voltages and currents are given by $x_1^{1,2,3}$, $T_m^{-1}x_1^{1,2,3}$ and $i_1^{1,2,3}$, $T_m^{-1}i_1^{1,2,3}$ respectively, where T_m is chosen to be the Karrenbauer transformation matrix:

$$T_m = \begin{bmatrix} 1 & 1 & 1 \\ 1 & 2 & 1 \\ 1 & 1 & 2 \end{bmatrix} \quad (6a)$$

Thus,

$$T_m^{-1} = \frac{1}{3} \begin{bmatrix} 1 & 1 & 1 \\ 1 & -1 & 0 \\ 1 & 0 & -1 \end{bmatrix} \quad (6b)$$

The computational effort is reduced by computing the modal components without division by 3; these are termed modified modal components in this paper. Consequently, the type-of-fault detection criteria are modified as follows:

for faults ahead of the relaying point,

$$|S'_1| - |S'_2| > 0.15$$

for faults behind the relaying point,

$$|S'_1| - |S'_2| < -0.15$$

S'_1 and S'_2 are the modified relay outputs evaluated with the modified modal components of the voltages and currents. With this modification incorporated, the relaying algorithm is as follows.

Step 1. Calculate, by the cycle-to-cycle comparison method, the fault-generated components of all the line currents for five sample sets backwards from the set at which

the fault detection algorithm had yielded a logical 'yes' output.

Step 2. Calculate the modified modal components of the fault-generated components of the phase voltages and line currents for the earliest sample set first.

Step 3. Calculate the modified inputs for all the modes.

Step 4. Check if $|S'_1| - |S'_2| > 0.15$. If so, a fault ahead of the relaying point has occurred and, therefore, start the transmitter. Also, if carrier signal is received from the other terminal, trip the circuit breaker. If not, proceed to the next step.

Step 5. Check if $|S'_1| - |S'_2| < -0.15$. If so, a fault behind the relaying point has occurred. Therefore, block the possible starting of the transmitter subsequently by the backward waves coming after reflection at the fault point and remote end of the line. If not, go to the next step.

Step 6. Take the next sample set and go to Step 2.

It can be seen that this algorithm is very simple and therefore, can be implemented even with a microprocessor system.

6 FAULT LOCATING RELAY SCHEME

6.1. Principle of operation

This scheme is also composed of three relays, one for each mode of propagation, and caters for all types of faults. The input signal pairs to the relays are the same as in the previous scheme. In this scheme, the signal S_2 of each mode is used to detect the forward waves. If $|S_2|$ exceeds a preset value, which is taken as 0.175 p.u. [33] in this work, the internal fault-detection program is bypassed and a transmitter, which sends information to the other terminal of the line to suspend the execution of the program there, is started. For a fault behind, the first travelling waves reaching the relaying point are forward and therefore, as can be seen from eqns. (5), $|S_2|$ exceeds the setting first and desired operation ensues. The program which implements this algorithm is termed the forward-wave-detection program.

Upon the occurrence of an internal fault, the value of $|S_1|$ increases rapidly from zero to $K_f(1 + R_{set}/Z_0)v_{ff}$ at the instant when the

travelling waves reach the relaying point. For a bolted fault, $K_f = 1$ and, with perfect matching between R_{set} and Z_0 , $1 + R_{set}/Z_0 = 2$. Under these ideal conditions, $|S_1|$ will be equal to $2|v_{ff}|$. Assuming that $v_{ff} = V_{ffm} \times \sin(\omega_0 t + \phi_0)$, the maximum slope of $|S_1|$ in between sudden or rapid increases may be equal to $2\omega_0 V_{ffm}$. The instant when the waves reach the relaying point for the first time is determined by computing the slope of $|S_1|$ and checking if it is greater than $2\omega_0 V_{ffm}$. Then, a signal is produced to block the starting of the transmitter subsequently by the forward wave. There will be a second rapid increase in $|S_1|$ when backward waves come again from the fault point after reflection [30]. The instant at which this takes place is determined as when the first derivative of $|S_1|$ exceeds $2\rho_s \omega_0 V_{ffm}$. The inclusion of ρ_s is due to the fact that the voltage and current magnitudes get reduced by this factor when the backward waves reach the relaying point the second time (Fig. 1). The time between these two instants, when multiplied with the velocity of propagation, gives twice the distance of the fault from the relaying point.

If the type of fault is not an internal fault, the above algorithm does not work. The procedure is then repeated with the second derivatives of $|S_1|$ and with settings of $2\omega_0^2 V_{ffm}$ and $2\rho_s \omega_0^2 V_{ffm}$ for detecting the first and second rapid increases, respectively. In the case of equal reflection coefficients at the two ends of the protected line and a fault resistance equal to one half of the surge impedance of the line, there will not be a second rapid increase in $|S_1|$ or in its first derivative for a fault at the middle of the line. Also for a close-in fault, the time interval between the first and second rapid increases would be too short to be evaluated by this algorithm. In the former case, a trip signal is issued after the first-derivative and second-derivative programs have been gone through and in the latter case after the detection of a rapid increase in either the first or second derivative of $|S_1|$ over a certain number of consecutive sampling intervals. The present scheme is an extension of an analog scheme proposed by the authors [30].

6.2 Relaying algorithm

Division by 3 in evaluating the modal components of the voltages and currents is

eliminated by using the modified inputs S'_1 and S'_2 as in the previous scheme. Accordingly, the condition $|S'_2| > 0.525$ p.u. is used for each mode to detect the forward waves reaching the relaying point first. The first and second derivatives of $|S'_1|$ at any sampling instant t_i are computed using the following numerical differentiation formulae [34].

$$\frac{d}{dt} [|S'_2|]_{t=t_i} = \frac{|S'_{1,i+1}| - |S'_{1,i}|}{\Delta t}$$

$$= \frac{\Delta S'_{1,1}}{\Delta t}, \text{ say}$$

$$\frac{d^2}{dt^2} [|S'_2|]_{t=t_i} = \frac{|S'_{1,i+1}| - 2|S'_{1,i}| + |S'_{1,i-1}|}{(\Delta t)^2}$$

$$= \frac{\Delta S'_{1,2}}{(\Delta t)^2}, \text{ say}$$

where $S'_{1,i+1}$, $S'_{1,i}$ and $S'_{1,i-1}$ are the modified signal inputs computed from $(i+1)$ th, i th and $(i-1)$ th sample sets of voltages and currents and Δt is the sampling interval. The first and, if necessary, the second derivatives are to be computed repetitively, and hence it is imperative that the computational effort be reduced. This is accomplished by modifying the criteria used to detect the first and second rapid increases in $|S'_1|$, as $\Delta S'_{1,1} > 6\omega_0 V_{\text{fthm}} \times \Delta t$ and $\Delta S'_{1,1} > 6\rho_s \omega_0 V_{\text{fthm}} \Delta t$ respectively, and the criteria to detect the first and second rapid increases in $d(|S'_1|)/dt$, as $\Delta S'_{1,2} > 6\omega_0^2 V_{\text{fthm}} (\Delta t)^2$ and $\Delta S'_{1,2} > 6\rho_s \omega_0^2 V_{\text{fthm}} (\Delta t)^2$ respectively. Also, a rapid increase in $|S'_1|$ or $d(|S'_1|)/dt$ may span two or three consecutive sampling intervals, in which case the fault-location computation goes wrong. This difficulty is surmounted by a suitable logic described in the algorithm given below. With the above modifications incorporated, the relaying algorithm is as follows.

Step 1. Calculate, by the cycle-to-cycle comparison method, the fault-generated components of all the line currents for twelve sample sets backwards from the sample set at which the fault-detection algorithm yielded the logical 'yes' output. The two extra sample sets are used to partly cover the interval immediately preceding the arrival of waves at the relaying point.

Step 2. Calculate the modified modal components of the fault-generated components of the voltages and currents.

Step 3. Calculate the modified signal inputs for all the modes and for all the sample sets.

Step 4. Check if $|S'_2| > 0.525$ p.u. for each mode. If yes is so for any mode, stop further execution of the relaying program at this end and start the transmitter which sends information to the other end in order to stop execution of the relaying program there also or to block tripping. If not, proceed further.

Step 5. Calculate, for each mode, $\Delta S'_{1,1}$ and check if it is greater than $6\omega_0 V_{\text{fthm}} \Delta t$. If not, take the next set of modified inputs and execute Step 4. If so, do not go again to Step 4, set the time counter to the value of the time corresponding to this sample set. The time counter setting and rapid-increase detection criterion remain the same if the above condition is satisfied over consecutive sampling intervals. If this happens for four consecutive sample sets, an indication that the fault is close-in is output. Otherwise, change the rapid-increase detection criterion to $6\rho_s \times \omega_0 V_{\text{fthm}} \Delta t$. When the latter condition is satisfied, set the time counter to the current time minus the previous setting. Stop further execution of the algorithm, compute the distance of the fault and output this value as well as a logical 'yes' for tripping. When this step yields no results, go to the next step.

Step 6. Repeat the algorithmic procedure of Step 5 with the second derivatives of the signal $|S'_1|$ for each mode with the rapid-increase detection criteria of $6\omega_0^2 V_{\text{fthm}} (\Delta t)^2$ and $6\rho_s \omega_0^2 V_{\text{fthm}} (\Delta t)^2$. If this step also fails to yield a result, go to the next step.

Step 7. Under these conditions, the fault will be at the middle of the line. Output an indication to this effect.

7. TESTING OF ALGORITHMS BY DIGITAL SIMULATION

In order to test the proposed algorithms, fault data are generated for a desired type of fault for two cycles, one pre-fault and one post-fault, by employing the digital simulation techniques described in an earlier paper by the authors [30]. The amplitude-comparison relaying algorithm is tested using the fault data computed for an internal fault at

the remote end (marked F_1) of the protected line and for an external fault (at the point marked F_2) in the four-bus power system shown in Fig. 3. Each source is represented by an equivalent lumped-parameter model with phase inductances calculated from the fault level specified and neutral impedance, from an assumed ratio of Z_0/Z_1 of 0.5 at power frequency. All the lines are 128 km in length. A three-phase fault through a fault resistance of 100Ω with a fault initiation angle of 0° is considered. The quantity $|S'_1| - |S'_2|$ is calculated for each mode and the results are given in Figs. 4 and 5. The fault-locating algorithm is tested using the fault data evaluated for a single line-to-ground fault on phase a at the remote end of the protected line of 200 km in length in the power system shown in Fig. 6. In this case, the sending-end (SE) and receiving-end (RE) sources are considered to be composed solely of transmission lines and cables and to have net surge impedances equal, respectively, to $1/9$ and $1/4$ of the power frequency surge impedance of the

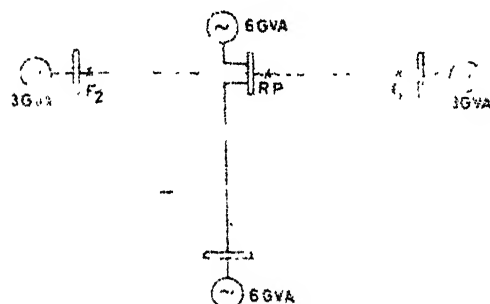


Fig. 3. A four-bus sample power system. R.P. = relaying point; values in units of GVA refer to short-circuit levels.

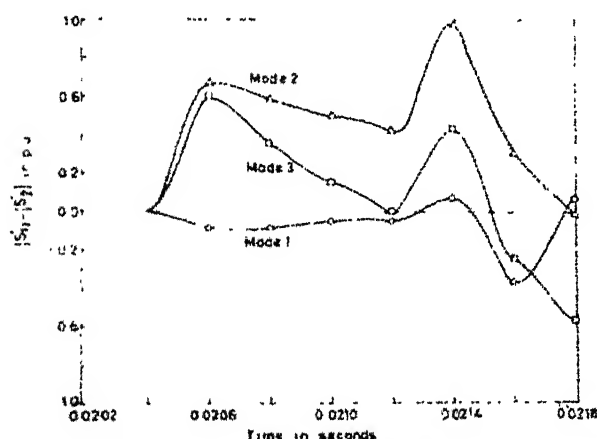


Fig. 4. Three-phase internal fault: $R_f = 100 \Omega$ and $\phi_0 = 0^\circ$.

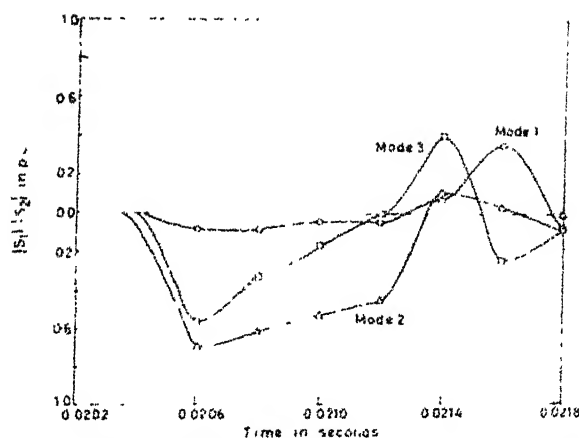


Fig. 5. Three phase external fault: $R_f = 100 \Omega$ and $\phi_0 = 0^\circ$.

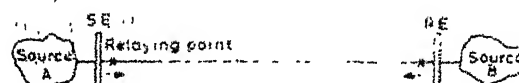


Fig. 6. A transmission line interconnecting two power systems.

protected line. A fault resistance of 100Ω and a fault initiation angle of 90° are considered. The signals $|S'_1|$ and $|S'_2|$ are computed and the results are given in Figs. 7 and 8. In both the sample power systems considered, each transmission line is a typical 400 kV quad-conductor single circuit of untransposed construction. An earth resistivity of $100 \Omega \text{ m}$, and frequency dependency of all line and earth parameters are assumed. The remaining data for each line are those given in Table 1 of ref. 30. The sampling interval is taken to be $200 \mu\text{s}$ and the peak value of the pre-fault voltage at the fault point is assumed to be 1.0 p.u.

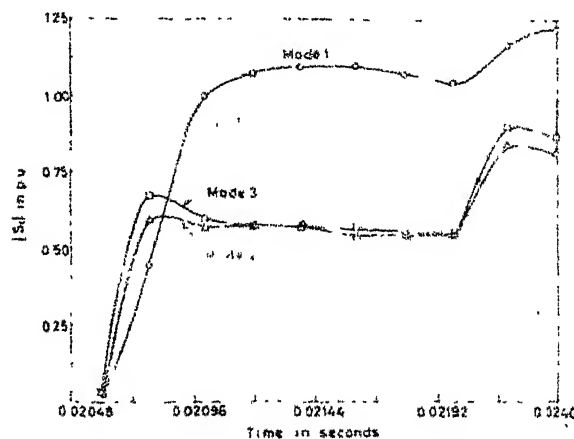


Fig. 7. Single-phase line-to-ground fault on phase A. $R_f = 100 \Omega$ and $\phi_0 = 90^\circ$.

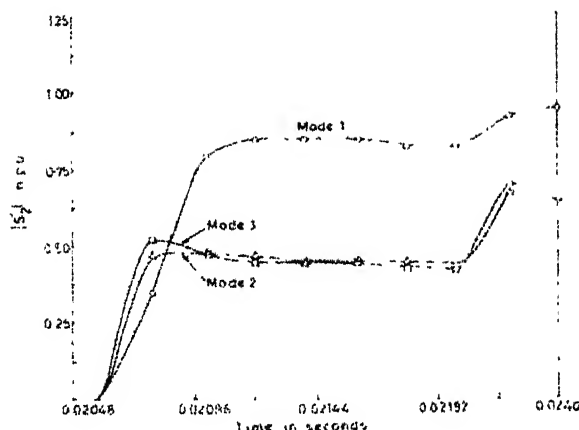


Fig. 8 Single-phase line-to-ground fault on phase A. $R_f = 100 \Omega$ and $\phi_0 = 90^\circ$.

Using the fault data, the fault-detection and relaying programs were run on the DEC 1090 computer system at the Indian Institute of Technology, Kanpur. In both cases, the CPU time was found to be less than 1 ms. However, eight sample sets in the first scheme and fourteen in the second were required to detect the fault. So, the total time of operation was about $8 \times 0.2 + 1 = 2.6$ ms in the first case and $14 \times 0.2 + 1 = 3.8$ ms in the second. Since the object of the paper was only to test the algorithms, only one type of fault is considered in each case.

8. CONCLUSIONS

The digital simulation tests carried out on the two new digital travelling-wave algorithms proposed in this paper established their feasibility. The heart of these digital schemes is the fault-detection algorithm, which is quite simple. With this fault-detection algorithm, not only the relaying algorithms employed in this paper, but also the analog travelling-wave relay schemes proposed by others [33, 35, 36] can easily be implemented digitally. There being no need for any filtering, the travelling-wave relay algorithms are superior both in terms of accuracy as well as speed, and therefore will ultimately supplant the digital algorithms in the digital protection of transmission lines.

NOMENCLATURE

C_s, C_m	self and mutual capacitances of line
L_s, L_m	self and mutual inductances of line
R_{rel}	relay setting resistance
S_1, S_2	relay input signals
Δt	sampling interval
V_{fsm}	amplitude of fault-generated component of voltage at fault point
v_f, i_f	fault-generated components of voltage and current
Z_0	surge impedance of line
ρ	reflection coefficient
ϕ_0	fault initiation angle
ω_0	nominal system angular frequency

Superscripts

1, 2, 3 components of modes 1, 2, 3

REFERENCES

- 1 M. Ramamoorthy, 'A note on impedance measurement using digital computers', *IEE Trans. (India)*, 9(6) (1971) 247-249.
- 2 B. J. Mann and I. F. Morrison, 'Digital calculation of impedance for transmission line protection', *IEEE Trans., PAS 90* (1971) 270-279.
- 3 G. B. Gilerest, G. D. Rockefeller and E. A. Udren, 'High-speed distance relaying using a digital computer Part I: System description', *IEEE Trans., PAS 91* (1972) 1235-1243.
- 4 J. G. Gilbert and R. J. Shovlin, 'High speed transmission line fault impedance calculation using a dedicated minicomputer', *IEEE Trans., PAS 94* (1975) 872-883.
- 5 G. R. Slemmon, S. D. T. Robertson and M. Ramamoorthy, 'High speed protection of power systems based on improved system models', *CIGRE, France*, 1969, Paper No. 31-09.
- 6 J. Carr and R. V. Jackson, 'Frequency domain analysis applied to digital transmission line protection', *IEEE Trans., PAS 94* (1975) 1157-1166.
- 7 G. S. Hope and V. S. Umamaheswaran, 'Sampling for computer protection of transmission lines', *IEEE Trans., PAS 93* (1974) 1522-1534.
- 8 A. G. Phadke, T. Hlibka and M. Ibrahim, 'A digital computer system for EHV substations: analysis and field tests', *IEEE Trans., PAS-95* (1976) 291-301.
- 9 G. S. Hope, O. P. Malik and M. E. Rasmy, 'Digital transmission line protection in real time', *Proc. Inst. Electr. Eng.*, 123 (1976) 1349-1353.
- 10 M. S. Sachdev and M. A. Baribeau, 'A new algorithm for digital impedance relays', *IEEE Trans., PAS-98* (1979) 2232-2240.

- 11 Adly A. Girgis and R. Grover Brown, Application of Kalman filtering in computer relaying, *IEEE Trans., PAS-100* (1981) 3387 - 3397.
- 12 A. Wiszniewski, How to reduce errors of distance fault locating algorithms, *IEEE Trans., PAS-100* (1981) 4815 - 4820.
- 13 J. W. Horton, Walsh functions for digital impedance relaying for power lines, *IBM J. Res. Dev.*, 10 (1976) 530 - 541.
- 14 A. D. McInnes and I. F. Morrison, Real time calculation of resistance and reactance for transmission line protection by digital computer, *Trans. Inst. Eng. Aust.*, EE7 (1971) 16 - 23.
- 15 R. Poncelet, The use of digital computers for network protection, CIGRE, France, 1972, Paper No. 32-08.
- 16 J. V. H. Sanderson and A. Wright, Protective scheme for series-compensated transmission lines, *Proc. Inst. Electr. Eng.*, 121 (1974) 1377 - 1384.
- 17 A. M. Ranjbar and B. J. Cory, An improved method for the digital protection of high voltage lines, *IEEE Trans., PAS-94* (1975) 544 - 550.
- 18 W. J. Smolinski, An algorithm for digital impedance calculation using a single PI section transmission line model, *IEEE Trans., PAS-98* (1979) 1546 - 1551.
- 19 P. Bornard and J. C. Bastide, A prototype of multiprocessor based distance relay, *IEEE Trans., PAS-101* (1982) 491 - 498.
- 20 A. T. Johns and M. A. Martin, Fundamental digital approach to the distance protection of E.H.V. transmission lines, *Proc. Inst. Electr. Eng.*, 125 (1978) 377 - 384.
- 21 G. K. Laycock, P. G. McLaren and M. A. Redfern, Signal processing techniques for power system protection applications, *Modern Developments in Protection*, Publ. No. 125, Institution of Electrical Engineers, London, 1975, pp. 284 - 290.
- 22 R. G. Luckett, P. J. Munday and B. E. Murray, A substation based computer for control and protection, *Modern Developments in Protection*, Publ. No. 125, Institution of Electrical Engineers, London, 1975, pp. 252 - 260.
- 23 A. W. Brooks, Jr., Distance relaying using least squares estimates of voltage, current and impedance, *Proc. IEEE PICA Conf.*, IEEE Publ. No. 77CH 1131-2-PWR, May 1977, pp. 394 - 402.
- 24 J. G. Gilbert *et al.*, The development and selection of algorithms for relaying of transmission lines by digital computers, in B. D. Russell and M. E. Council (eds.), *Power System Control and Protection*, Academic Press, New York, 1978, pp. 83 - 127.
- 25 A. G. Phadke, M. Ibrahim and T. Hlibka, Fundamental basis for distance relaying with symmetrical components, *IEEE Trans., PAS-96* (1977) 635 - 645.
- 26 G. Tirupathiah, A. Varshney and L. P. Singh, On line digital protection using microcomputer - a decentralized approach, Paper presented at the National Conference on Large Scale Power Systems, India, June 1982.
- 27 M. Kezunovic, Digital protective algorithms and systems - an overview, *Electr. Power Syst. Res.*, 4 (1981) 167 - 180.
- 28 T. Takagi and Y. Yamakosi, Digital differential relaying system for transmission line primary protection using travelling wave theory - its theory and field experience, IEEE PES Winter Meeting, February 1979, Paper No. A79 096-9.
- 29 K. V. Desikachar and L. P. Singh, Protection of EHV/UHV transmission lines using travelling wave phenomena. Paper presented at the National Power System Conference, India, December 1981.
- 30 K. V. Desikachar and L. P. Singh, Fault analysis of multinode power systems for designing ultra-high-speed protective relays along with a proposed relaying scheme, *Electr. Power Syst. Res.*, 6 (1983) 13 - 25.
- 31 B. J. Mann and I. F. Morrison, Relaying a three phase transmission line with a digital computer, *IEEE Trans., PAS-90* (1971) 742 - 750.
- 32 A. T. Johns and R. K. Aggarwal, Digital simulation of faulted e.h.v. transmission lines with particular reference to very high speed protection, *Proc. Inst. Electr. Eng.*, 123 (1976) 353 - 359.
- 33 A. T. Johns, New ultra high speed directional comparison technique for the protection of e.h.v. transmission lines, *Proc. Inst. Electr. Eng.*, 127 (1980) 228 - 239.
- 34 J. M. McCormic and M. G. Salvadori, *Numerical Methods in Fortran*, Prentice-Hall of India Private Ltd., New Delhi, 1979.
- 35 M. Chamia and S. Liberman, Ultra high speed relay for EHV/UHV transmission lines - development, design and application, *IEEE Trans., PAS-97* (1978) 2104 - 2116.
- 36 M. Vittins, A fundamental concept for high speed relaying, *IEEE Trans., PAS-100* (1981) 163 - 173.